



HAL
open science

Two proton radioactivity and other exotic decays in the ^{48}Ni region measured with ACTAR TPC

Aurora Ortega Moral

► **To cite this version:**

Aurora Ortega Moral. Two proton radioactivity and other exotic decays in the ^{48}Ni region measured with ACTAR TPC. Physics [physics]. Université de Bordeaux, 2023. English. NNT: 2023BORD0323 . tel-04482368

HAL Id: tel-04482368

<https://theses.hal.science/tel-04482368>

Submitted on 28 Feb 2024

HAL is a multi-disciplinary open access archive for the deposit and dissemination of scientific research documents, whether they are published or not. The documents may come from teaching and research institutions in France or abroad, or from public or private research centers.

L'archive ouverte pluridisciplinaire **HAL**, est destinée au dépôt et à la diffusion de documents scientifiques de niveau recherche, publiés ou non, émanant des établissements d'enseignement et de recherche français ou étrangers, des laboratoires publics ou privés.

THÈSE PRÉSENTÉE
POUR OBTENIR LE GRADE DE

**DOCTEUR
DE L'UNIVERSITÉ DE BORDEAUX**

ECOLE DOCTORALE SCIENCES PHYSIQUES ET DE L'INGÉNIEUR
ASTROPHYSIQUE, PLAMAS, NUCLÉAIRE

Par **Aurora ORTEGA MORAL**

Étude de la radioactivité 2-protons et autres modes de décroissance
exotiques dans la région du ^{48}Ni avec ACTAR TPC

Two proton radioactivity and other exotic decays in the ^{48}Ni region
measured with ACTAR TPC

Sous la direction de : **Jérôme Giovinazzo**

Soutenue le 24 Novembre 2023

Membres du jury :

M. Navin ALAHARI	Directeur de Recherche	GANIL	Rapporteur
M. Elias KHAN	Professeur	Université Paris-Saclay	Rapporteur
Mme. Christine MARQUET	Directrice de Recherche	LP2i Bordeaux	Examinatrice
Mme. Marine VANDEBROUCK	Chercheuse	CEA Saclay	Examinatrice
M. Jérôme GIOVINAZZO	Directeur de Recherche	LP2i Bordeaux	Directeur
M. Thomas ROGER	Chargé de recherche	GANIL	Invité

*A mi madre,
por enseñarme a ver los problemas como oportunidades.*

Acknowdlegments



Acknowledging for everything that I have experienced during four years of thesis is at once the most complex part of this manuscript and the most pleasant one. I have tried to go step by step, making a kind of location-division, trying to do not forget anyone, but of course I will, so first, I wanted to thank absolutely everyone that has been part of this adventure during 4 years during my thesis at Bordeaux, no matter in which moment.

My five stars jury

First I will like to thank the "5*" members of the jury, for accepting the invitation to participate to my thesis: Navin Alahari and Elias Khan (reporters), Marine Vandebrouck and Christine Marquet (examinators) and Thomas Roger (guest). Your comments and advices before and during my thesis defense have helped me a lot progressing as a scientist.



I had the chance to have met all of you during these four years in different moments, from the very beginning (Christine, who was present as an external advice the day of my PHD interview) to the very end of my thesis during the double alpha experiment, where I met Elias and told him that I had no idea about theory (I hope he didn't remember that when he accepted to join the jury). I also had the chance to meet Thomas, Marine and Navin quite early, in the first years of my thesis, during our experiments at GANIL. Thanks all for our interactions along these 4 years.

There are some people that were just there from the beginning, a bit on the side, in the "shadow", pushing me further away in science, without me noticing it. Navin, is one clear example of that. I am very very grateful for each of our interactions (even though they were a bit scary at the beginning). Now I appreciate each "weird" question that opened my mind, that made me think further and further. I also appreciated the 6+5 hours meeting before my thesis. It really helped me to look outside my topic, to understand the importance of my work in the nuclear physics field and how challenging it was. Thanks for pushing me further in science and for being there, present, during these four years.

Mes (insulating) pillars

Jérôme

S'il y avait quelqu'un de plus stressé que moi pendant la thèse, c'était très certainement toi. Merci beaucoup pour ta patience, pour ta disponibilité, pour ta réactivité. Merci de m'avoir transféré cette ÉNORME quantité de connaissances sur plusieurs aspects. Tu m'as converti, sans doute, en une meilleure physicienne, ou même, en une vraie physicienne (beaucoup plus précise et, surtout, spécialiste dans le traitement des erreurs). Ensemble, on forme une équipe très particulière, un peu comme le Yin et le Yang *-opposite but interconnected, mutually perpetuating forces*. On a très certainement eu des moments difficiles pendant cette thèse, mais on a réussi à tout surmonter et à continuer. On a également réussi à mieux se comprendre, et ça nous a fait grandir aussi du point de vue personnel. Ce travail est, à mon avis, une belle preuve de la qualité de cette équipe très particulière. Merci également d'avoir été, outre mon directeur de thèse, un vrai ami tout au long de ces années. Je garderai fortement dans mes souvenirs nos moments ensemble, des moments du quotidien au labo aux moments extraordinaires (comment notre discussion au milieu de la mer dans une planche de paddle et un kayak à Saint-Jacques ou les soirées à GANIL). Ça ne sera, malheureusement, jamais un bon moment pour la binomiale.



Thomas



Merci d'être très très présent pendant ma thèse dans toutes les étapes et aspects (expérience, analyse, rédaction, personnel). Merci pour l'énorme quantité des connaissances que tu m'as transférées, pour m'expliquer tous les secrets de ACTAR, pour me montrer parfois le côté facile des choses (honnêtement, je ne sais pas si je ne serais pas restée complètement perdue dans une des librairies de Jérôme sans toi pendant ma thèse). Merci aussi pour me faire mesurer/faire des tests avec ACTAR TPC (avec vraiment pas assez de stat) juste pour m'amuser et pour m'enseigner. Merci aussi de m'avoir encouragé avec mon idée d'écrire/illustrer cette thèse de manière un peu "différente". Merci de m'avoir apporté beaucoup de positivité, de m'avoir poussé loin, très loin, de croire en moi plus que moi-même, de m'équilibrer juste avec ta présence. On a sans doute une complicité extraordinaire, et ça a été juste trop cool de pouvoir travailler avec toi (et parfois pas tant que ça, voir les compétitions de lancement des noyaux cerise dans la salle d'acquisition...). J'ai également adoré tous les moments hors travail, à l'escalade ou autres, qu'on a eu la chance de vivre ensemble. En résumé, merci de avoir partagé cette étape de ma vie avec moi et tout ton support, ça aurait été beaucoup plus compliqué (voir pas possible) sans toi.

Ma vie sûr Bordeaux

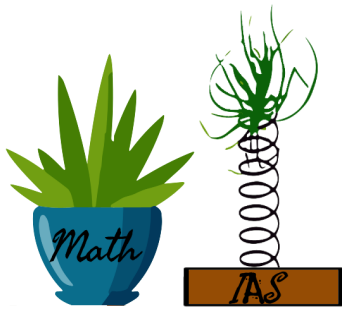


- NEX group
- Non permanents
- Lab
- La vie hors labo

Le groupe NEX

Je me sens vraiment très heureuse d'avoir eu la chance de rejoindre le groupe NEX. À l'intérieur, j'y ai trouvé des chercheurs/chercheuses exceptionnels desquels j'ai appris énormément des choses, mais j'ai aussi trouvé un groupe de personnes extraordinaires. On a toujours eu une atmosphère tellement incroyable (et amusante) que travailler avec vous tous ne ressemblait pas à du travail. J'ai pu le ressentir dès le début, lors de notre entretien très exotique.

Danke schön à Bertram, d'avoir été présente dès le début, pendant mon expérience de thèse où on a découvert ensemble LE événement deux-protons du ^{48}Ni . Merci aussi d'avoir répondu à toutes mes questions sur la *physique*, pour avoir pris le temps de lire et de corriger cette histoire de ~ 200 pages et pour m'apporter un peu de positivité quand j'en avais vraiment besoin. Un merci tout spécial également pour avoir emballé tout le "travelling set-up" pendant qu'on profitait de la montagne au CERN.



Je n'aurais jamais pu finir ma thèse sans mon coloc de bureau, Mathias. Tout d'abord parce que tu étais une sorte de source-de-concentration-pour-travailler-très-dur, ensuite parce que tu as compilé ma thèse quand j'étais complètement à l'arrache et stressée. Avoir la meilleure encyclopédie à pâtes dans mon bureau a été également très utile pendant ces années. Merci pour toutes tes réponses et ton implication dans mon travail, pour toutes tes blagues et pour être parfois là juste parce que tu sais que je travaille mieux

quand je ne suis pas toute seule.

Merci aussi à Stéphane, même si tu réponds jamais quand je dis Bonjour le matin. J'ai beaucoup apprécié ta présence (les très rares jours où tu étais au labo). Merci pour ta (presque toujours) bonne humeur et "good mood", et pour avoir répondu à toutes mes questions LISE (et autres!). Merci aussi à ma ^{44}Cr - γ -mate Pauline, de pas avoir écrit la partie de théorie de ma thèse, car finalement, j'ai beaucoup appris en l'écrivant moi-même. Merci également à la mangeuse de desserts professionnelle du groupe: Maud, pour faire des efforts pour souder un peu plus le groupe en dehors du labo. Merci aussi à Teresa, même si tu as laissé le groupe et qu'on n'a pas pu partager beaucoup de temps ensemble, tes conseils m'ont beaucoup aidé professionnellement et je sais que je peux compter sûr toi. Enfin, je tiens à remercier Beatriz, de m'avoir mis en contact avec Jérôme, car sinon je n'aurais jamais commencé cette aventure.

Merci à tous pour toutes les connaissances que vous m'avez transmises et pour votre énorme soutien pendant ma thèse. Vous m'avez appris l'importance et le sens d'être un groupe. Ensemble, on est plus forts et je suis heureuse de faire partie de ce noyau exotique qu'on forme ensemble.

Merci aussi aux non-permanents du groupe. Certains d'entre vous sont partis un peu trop tôt dans cette étape: merci Antoine, pour presque me renverser avec ton vélo le premier jour de mon arrivée au labo et pour partager énormément d'aventures (je me rends compte qu'on n'est pas allé à la plage aussi souvent qu'on l'aurait souhaité, mais il n'est jamais trop tard... on va à la plage?). Merci Audric, pour être très présent dans ma vie au labo et hors labo et pour tout ton soutien. J'ai beaucoup appris de toi (en physique, en français et +!). Merci aussi à Julien avec qui j'ai partagé la plupart de mon temps au début de ma thèse et qui m'a montré comment jouer au squash. Merci à vous trois pour votre patience au début quand je ne parlais pas vraiment français (même si vous ne vous en souvenez pas) et pour m'avoir appris les expressions les plus françaises au cours de mes premières années à Bordeaux. Merci aussi à Michele, qui a commencé la thèse en même temps que moi et avec qui j'ai partagé toutes les premières expériences en France et sur Bordeaux.

Je voulais également remercier à la deuxième génération des non-permanents NEX:



Merci à mon NEX-mate, ACTAR family mate, GANIL-mate, party-mate, massage-mate, karaoke-mate and (even!) climbing-mate, Quentin. Tu es devenu très vite un de mes plus grands supports au labo depuis ton arrivée et j'ai vraiment apprécié notre temps ensemble (peu importe où et peu importe quoi), des discussions sur des analyses à nos moments de danse les plus fous (La pepas, Moskow!). On a tout simplement trop d'histoires drôles ensemble, merci pour tout ça.

Merci également à Matthieu, pour tous les moments au labo et hors labo et pour m'avoir donné le meilleur conseil avant ma soutenance de thèse. Grâce à toi, j'ai pu vraiment profiter du moment. Merci aussi à Dinko, j'ai énormément apprécié chaque discussion avec toi, et tu m'as donné un peu plus de confiance en moi-même pendant nos conversations, merci pour ça.

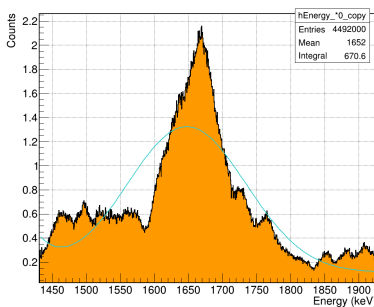
Finalement, je voulais aussi remercier à la troisième génération des non permanents NEX qui ont partagé avec moi la fin de la thèse et qui se sont beaucoup impliqués avec moi également: Camille, Emmanuel et Samuel (qui a même lu toute ma thèse!).

En général, merci infiniment au groupe NEX, permanents et non permanents. Je suis certaine que chacun a eu un rôle important dans différents moments de ma thèse, du côté scientifique ou personnel. Tout ce que j'ai appris pendant ces années et tout ce que je suis devenue, c'est, en partie, un mélange de vos connaissances, et nos interactions.

Les non permanents

Grand remerciement aux non-permanents d'être toujours là (même dans les périodes de vacances quand il n'y avait personne). On a vécu sans doute une période parfois très difficile pendant la thèse, mais on a toujours trouvé un moment pour discuter, faire la pause goûter, des afterworks, des activités hors labo, faire beaucoup de squats, aller courir à midi (running at 12?), faire des randonnées, des raclettes, aller faire du surf, faire des repas des déprimées... Si on a commencé cette dynamique de groupe entre les non-permanents c'est très probablement grâce à Vincent. Merci pour ça, et merci d'avoir passé la première partie de ma thèse avec moi, physiquement, et le reste en distance, parce que je ressentais que t'étais toujours là.

Un très grand merci spécial à Antoine, Julien, Audric, Guillaume, Xalbat, Loïc, Quentin, Mathieu, Pierre C, et Pauline avec qui j'ai passé la plupart de ma thèse et qui ont été un énorme support pour moi au quotidien. Vous avez rendu ma vie sur bordeaux et mes journées (et soirées) beaucoup plus agréables.



Je voulais remercier énormément à mon stagiaire du pic chinois, Loïc. Merci d'avoir suivi mes analyses de très prêt, merci pour tous tes conseils, pour tous les cours de stat que tu m'as donnés et surtout pour tous les super moments qu'on a passés ensemble (voir installation de ma guirlande). Merci d'avoir profité avec moi de la vie hors labo, du soleil (quand il y avait!), de l'escalade, des pique-niques... Merci pour avoir pris soin de moi quand j'avais vraiment besoin, de m'avoir rendu la vie sûr Bordeaux plus facile et plus complète.

Merci à tous d'avoir rendu possible ce magnifique groupe de non-permanents. Vous avez été un vrai support pour moi pendant ma thèse.

Le labo

Merci à tout le reste des gens du labo qui rendent en général plus agréable mes moments au quotidien. En particulier, je voulais remercier à Jérôme Piernat pour m'ouvrir la porte les 80% des fois où j'oublie ma carte, pour avoir passé une journée entière ou deux à m'expliquer comment fabriquer mon propre plan de pads (on ne sait jamais). Merci aussi à Fred pour les cafés-massage, sa bonne humeur et toutes les activités qu'on a faites hors labo. Merci aussi à Nadine, pour organiser mes dix millions de missions, à Pascal qui m'a aidé à rassembler ma thèse pour l'envoyer à Navin l'arrache à la fin de la thèse...

Merci, en général, à tous les gens du labo que j'ai eu la chance de rencontrer et connaître pendant ces années. Je me suis senti très accueillie parmi vous. Je ressens que chaque petit détail que vous avez eu avec moi et chaque petit échange qu'on a eu a été important dans le cours de ma thèse. J'ai ressenti énormément votre support, et je vous remercie pour ça.

Je garderai très profondément tous les moments de cette belle étape sur Bordeaux avec vous tous, ou le "souvenir de couverture" c'est le moment où on a tous levé nos verres ensemble pendant mon pot de thèse. À cette superbe période parmi vous, merci à tous!



La vie hors labo

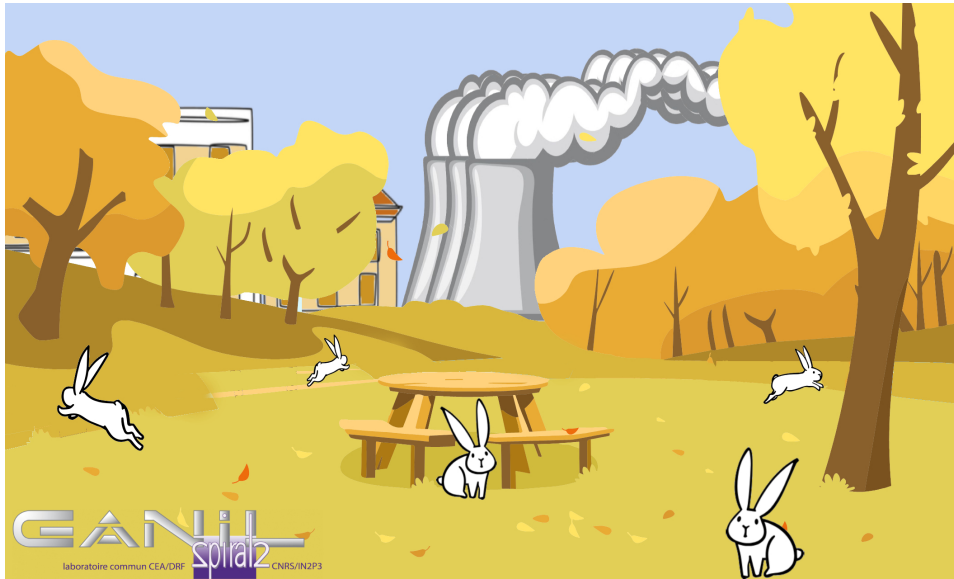
Merci à ma famille adoptive de Bordeaux: Kevin, Charlotte, Alex, Alice, Lucile, Laurence, Julien, Matthieu, Jordan, Le Belge, Momo, Aurelie, Hicham... qui m'ont adopté pendant ces années sans même savoir trop parler français et avec qui j'ai partagé les meilleures soirées et BBQ sur Bordeaux. Vous avez rempli de bonheur, rigolades et expériences ma vie hors laboratoire. Merci de m'avoir aidé m'intégrer complètement dans la culture française et de me faire sentir chez moi sur Bordeaux. Vous avez tous été un grand support pendant ces années de thèse.

Merci à mes amis de l'escalade, avec qui j'ai passé la moitié de mes soirées au Climb up et des weekends extraordinaires en falaise. Je dois aussi résumer ici trois pages de remerciements à mon binôme Anatole: merci, de me supporter les mauvais jours (après des calculs non réussis des angles) et les jours brillants (ou j'ose me jeter de 1 cm dans les voies). Merci aussi de me rendre plus forte à l'improvisation, de me faire sentir libre chaque fois qu'on est partis en weekend en montagne ou en falaise. Je rentrais, à chaque fois, avec les batteries hyper chargées et un énorme sourire. Un remerciement aussi spécial pour mon voisin Étienne, qui n'a jamais voulu grimper avec moi, mais qui a été toujours là pour vérifier que je travaillais pendant le weekend ;) (et pour m'obliger parfois à faire une pause pour voir un peu le soleil).

Merci aussi à Reda et Houda, avec qui j'ai partagé le tout début de cette période sur Bordeaux et qui m'ont énormément aidé à me sentir chez moi très vite.

Merci, en général, à tout le monde qui a participé à la construction de ma nouvelle vie à Bordeaux dans n'importe quel moment. Je garderai de cette étape de ma vie plein des bons souvenirs très profondément dans mon cœur.

My parallel life in Caen



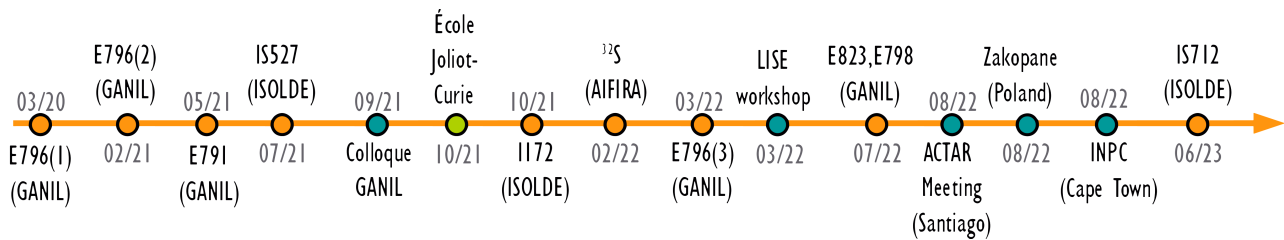
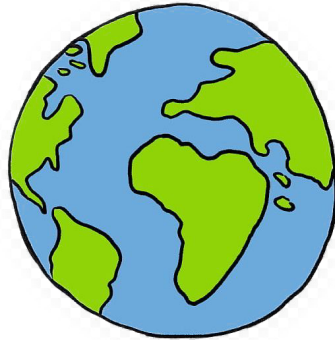
During my thesis, I spent that much time at GANIL that some people actually thought that I was working there. During my stays at GANIL I had the chance to meet too many people and I even managed to build a "parallel life" there.

The interactions with all people at GANIL were quite enriching for me. I want to thanks to the LISE team and the E791 experiment collaboration, for making their best during the experiment of my thesis, for teaching me a lot of things during and after the experiment. I (sometimes) also had some life outside the lab: I want to thank all the PHD students from GANIL which whom I enjoyed my time there: Alex, Mukul, Julien, Jekabs, Nishu and my gym-mates Laura and Marina, who I met randomly in the gym and became a part of my life in Caen.

During my periods in Caen, I also had the chance to have a family, the ACTAR family: Thomas, Julien, Jérôme, Juan, Quentin and Anastasia. When I remember our times together at GANIL I just feel lucky. Working with all of you was just amazing. Thanks for coming with me to climb and for all our crazy moments together outside GANIL.

I had the chance to meet Juan quite early during my first stays at GANIL. You became my super ACTAR-mate since the beginning and someone really important, at present, in my life. I just cannot imagine this stage of my life without you. We became inseparable (Pin y Pong!) quite fast and spent almost all the hours of the day with each other. Together we were stronger (we even managed to survive a confinement at GANIL, and to become professional tennis players in the meanwhile).

"Worldwide" interactions



I also had the chance to meet amazing people all around the world during conferences, summer schools and experiments.

I think that the tiniest interaction with any of the people I met was worthed and helped me to grow as a scientific and as a person. I feel really lucky to have met you all, and to have shared funny, (and also boring) moments with you. The list is just too big, but I wanted to thank all people that I just crossed during this adventure. Such as the "Leuven team", with whom I shared a lot of hours of shifts, the "local" people I meet at ISOLDE, or the 2-alpha experiment collaboration, which I met at the very end of my thesis and gave me a final boost.

I had the chance to meet some of you several times in different situations and I become friends with you. Thanks for showing me all your amazing projects, for example the crazy PUMA project (Alex) or the cousin of ACTAR (Oleskii). Thanks also for teaching me some theory along long night shifts (Louis Heitz), or for deep conversations that made me trust myself a bit more (Louis Lalanne).

Special thanks to the people from the USC Santiago (Juan, Bea, Dani R, Dani F, Cristina, Manu, Diego) because you have adopted me in your family during our periods together at GANIL, the collaboration meeting or the week I spent with you at the end of my thesis. I felt that I could really count on you during these four years. Thanks for making me feel this way.

Cómo llegué hasta aquí



No se desde dónde comienzan los agradecimientos en una tesis, pero me gustaría agradecer a varias personas que me hicieron a llegar hasta mi tesis en Burdeos.

Gracias en primer lugar a mis padres, que aunque les pareciera la locura más grande del mundo, eso de estudiar física, me dieron la posibilidad de vivir cuatro años en Granada. Gracias también a los profesores y compañeros que me han motivado a seguir este camino desde el instituto hasta la carrera.

Gracias a David (Shuff) que me “obligó” a irme de Erasmus. Gracias al Erasmus, y a toda la gente que crucé en ese año maravilloso, porque eso me motivó a acabar la carrera de física. Gracias a Marta, con quien tuve la suerte de escribir mi (tercer) proyecto de fin de grado en Granada y quien ha estado siempre ahí para ayudarme y darme un empujón hacia la aventura de la investigación.

Gracias a mis compañeros y amigos de Granada, con quien di mis primeros pasos de investigadora. Infinitas gracias a mis patos del máster, que me ayudaron cuando no entendía NADA de la teoría, que me apoyaron a seguir en el mundo de la investigación y a “cambiarme bando” al de la física experimental. Gracias también a Fran y Lluís por compartir un super viaje por Tailandia que me ayudó a estar en el mejor “mood” posible en mi entrevista para la tesis.

Por último infinitas gracias a Ismael, mi compañero de aventuras, quien compartió conmigo los momentos más duros del inicio de la tesis desde la distancia, quien escuchó mis movidas de física loca cada día, con quien tuve la suerte de pasar el mejor “corona-vairus” del mundo y de comenzar una pasión que cambiaría mi vida para siempre, la escalada. Gracias por apoyarme y hacerme sentir que podía llegar donde quisiera con esa “cabecita mía”, aquí estoy.

Mi familia, mi pueblo, desde la distancia



Gracias a mis amigos del pueblo, por vuestro apoyo a pesar de la distancia y por hacerme sentir que el tiempo no existe mientras estoy fuera, porque cuando vuelvo todo es como antes. Gracias por aguantar mis explicaciones de cosas que no se entienden muy bien y por creer siempre en vuestra amiga la física loca.

Por último y más importante, gracias a mi familia más cercana: Mamá, Papá, Ana, Abuela, Abuelo, Tito, por apoyarme y cuidarme desde lejos (¡y desde muy lejos!) en cada momento, por recargarme las pilas cuando más lo necesitaba, por seguir de cerca cada uno de mis pequeños logros del día día, sin entender muy bien dónde estaban los protones en mis gráficas. Gracias por educarme enseñándome que puedo llegar donde quiera, sin límites, y por ayudarme a ello. Gracias por vuestros consejos, vuestro cariño y nuestras locuras de familia. Gracias por aguantar esa parte negativa de mi que los demás no ven, por darme el empujón que me falta a veces, por hacerme volar lejos, aun queriéndome cerca. Gracias porque sin vuestro apoyo, nada de esto habría sido posible.

Preface (explanation of illustrations)

Along this thesis, there are multiple illustrations (photo-montages¹) which I created myself. In particular, the chapter cover ones, are sometimes not easy to understand, so I wanted to explain them. I encourage the reader to go through the thesis and come back to this preface, if desired, to understand the parallel story behind these illustrations.

Thesis cover: $Z=28$ region close to the proton drip line

The introduction image, the cover of this thesis, is a representation of the nuclear chart at the proton drip line. On the cliff, the main nuclei studied in this region are represented by different squares, each of them with a particular color, with the protagonist (^{48}Ni) in the foreground, represented in orange, which is THE color of this thesis. There are some quickdraws on the cliff, representing at once my passion (climbing), which I discovered during my thesis and that greatly helped me along these years. Also, this climbing path represents somehow the difficult way along these four years. The original design was made by hand by A. Moral (my mother) and was later digitalized and treated by myself. Two different versions with different combinations of colors were created, and I even made a poll to choose the final one. Thanks to all people that participated in that poll!. The results were that tight that finally I choose to put both pictures along the thesis at different moments, as suggested by Jordan (thanks for that!).

Context and motivations: *understanding the nuclear force*

In this image, an alpha particle is teaching the protons and neutrons how to behave within the nucleus. Could we, attending to this course, understand the mysteries of the nuclear force?. This image has some particularities, for example, the two plants in the self (Math and IAS) which are real plants in my office, that replace my office-mate Mathias when he is not there. The equations and the potential design in the blackboard have been drawn by Louis Heitz (a real theoretician!) during the two-alpha experiment in 2023. Finally, two of the protons are a bit far away from each other, due to the Coulomb repulsion.

ACTAR TPC: *the CoBo alignment party*

This is, most likely, the hardest illustration to understand. Different elements of the ACTAR TPC detector having a party are represented on it. Each of them is, at the same time, one member of the ACTAR family: from left to right: MuTanT module: Jérôme, Field cage: Julien Pancin, (crazy) CoBo module: Anastasia, Silicon Wall: Juan, Source support: Quentin, Mesh: Thomas and Pad plane (myself). This special party "the CoBo alignment party" makes reference to a very tuff process to carry out each time the acquisition gets blocked, due to a problem in the clocks of the different CoBo modules. This image aims to represent our times together at GANIL, which was just one of the most incredible stages during my thesis and my

¹base images are often taken from <https://www.freepik.es/>

life.

E791 experiment: *a real mess*

This image was the first one to be created, it is inspired by a game of my childhood (Hercules) which I used to play with my sister. It represents the huge mess and how difficult it was to run this experiment: implanting the ^{48}Ni nuclei (the arrow on the left) in the ACTAR TPC detector (on the right). Although originally, some of the elements did not have special sense, when discussing with people I realize that they could. The huge magnet can represent the magnets in the LISE spectrometer, the fire, some of the fire-alarms that eventually made stopping the experiment, the moving axe, the slits on the spectrometer, the shark and the water, all the water leak problems during the experiment. In summary: a real mess.

Calibrations

This image just represents the different processes (a bit complicated) to pre-treat all the signals from ACTAR TPC and other detectors with a colorful and a bit crazy machine.

Analysis: *the emotive finding of two-proton emission from ^{48}Ni*

In this image, the implantation-decay correlation process is represented². My analysis code (Analysis.C) is classifying the different proton events into "boxes", after an energy measurement (device in purple). The different boxes correspond to the different nuclei implanted during the experiment. There are a lot of protons emitted from ^{41}Ti (the most produced isotope during the experiment) that fill the corresponding box on the right. The program is completely moved because of the event that he is just classifying: a two-proton event from ^{48}Ni . The mountains and the rainbow in the back are actually different graphs obtained during the analysis. The grass, the sun and the clouds are the same ones represented in the portrait of the thesis, this analysis is indeed happening in the nuclear-chart cliff.

Results: *sunset at the proton drip line*

In this image, a sunset version of the nuclear chart at the proton drip line is represented. After the huge efforts of analysing these data (~50 pages of analysis) it has certainly become a bit dark. This image leads to the result chapter, in which each of the nucleus (represented by the different squares) will descend to be analysed. All graphs and tables will match their specific square colors in the cliff, and this is the reason for the "colorful" and a bit crazy result chapter.

Further analysis and perspectives: *"le fameux chapitre du futur"*

This is a futuristic version of the analysis program (C+++) and process in an undefined space-time. Several issues encountered during the analysis and some of the proposed solutions are represented in the

²I came out with this crazy idea with the help of Pierre C, thanks a lot for that!

image: the identification process using a crystal ball function on the left. The classification of the emissions from the cathode or the window (nuclei that are moving towards the first "mountain" (emissions from the window), the second one (emissions from the cathode) or that are decaying "on flight" (flying nuclei in the region at the middle). The "mountains" themselves are a representation of the dispersion of the initial point of the protons, obtained in the analysis chapter, which served to characterize the non-neutralization problem. The strange sun on the right is also a result which showed a small shift between stopping point and starting point of implantation and decay events. Finally, at the back, some crystals can be observed. This represents the future of ACTAR TPC: the coupling with γ detectors for full proton spectroscopy measurements.

Conclusions: *proton fireworks or "Fuegos protoficiales"*

This image is a representation of the proton-drip-line-cliff at night. After the analysis process, all the nuclei have decayed and have been analysed. The only thing left are the emitted protons, and this is what is represented by the fireworks, that are actually real proton tracks from ACTAR TPC. This image was designed by A(na).Ortega Moral (my sister) because I was certainly in a rush by then (thanks for that!)

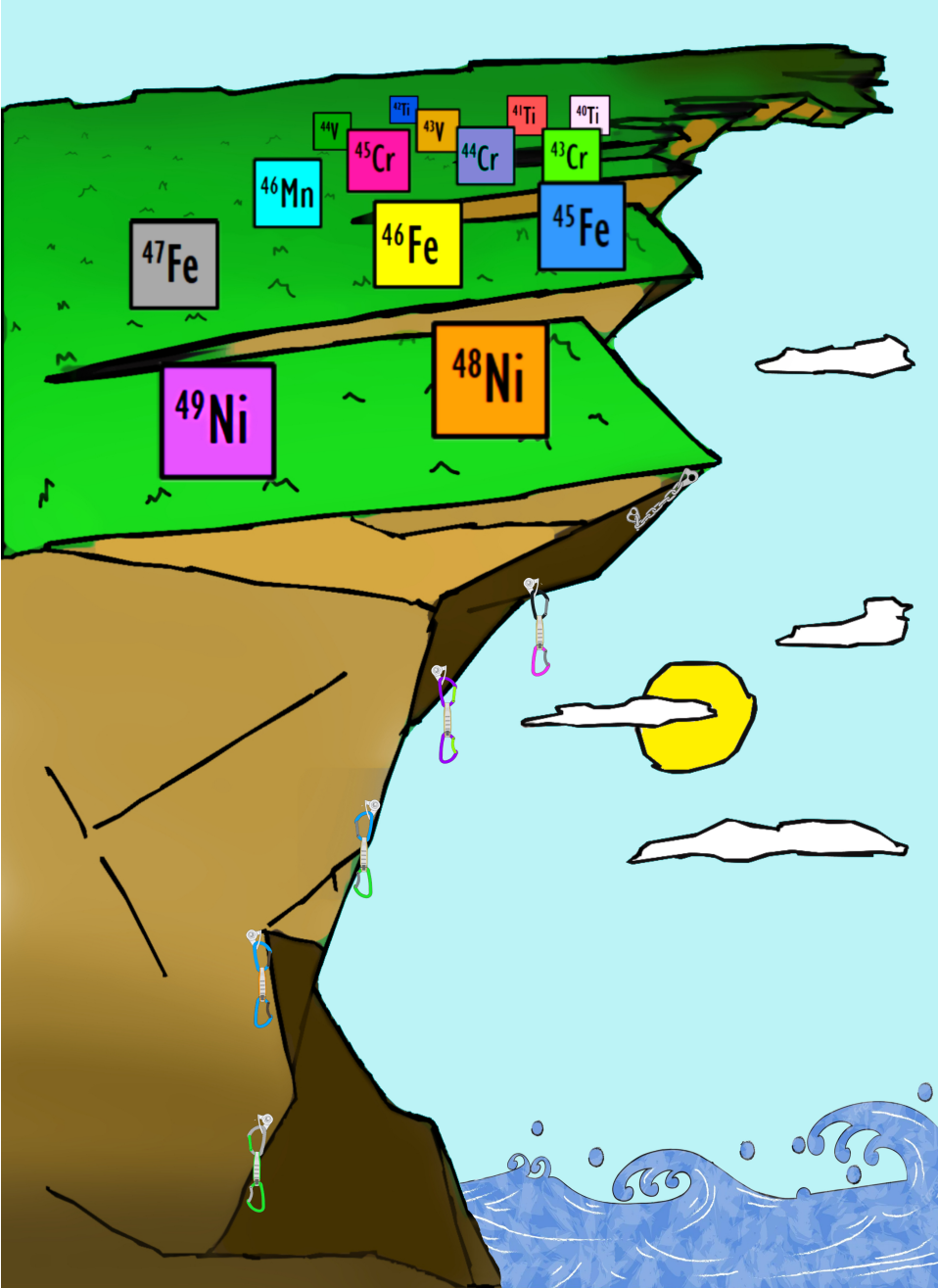
Contents

Introduction	20
1 Context and motivations	25
1.1 Atomic nucleus	26
1.2 Nuclear structure	28
1.3 Decay processes	29
1.4 Region of measurement in E791 Experiment	32
1.5 β^+ /EC delayed proton(s) emission.	32
1.5.1 β^+ and electron capture decays.	33
1.5.2 Delayed proton emission	33
1.5.3 Isobaric Analogue State and Isobaric Multiplet Mass Equation (IMME)	35
1.6 Ground State proton emission	37
1.7 Two proton radioactivity from ground state	38
1.8 Two proton emission mechanisms	39
1.9 Two proton studies	41
1.9.1 Two proton experiments	41
1.9.2 Two proton decay models	42
1.10 Motivation of the study of the ^{48}Ni decay products	49
2 ACTAR TPC	51
2.1 Gaseous detectors in nuclear physics	52
2.2 Recent TPC developments in nuclear physics	54
2.3 ACTAR TPC	56
2.3.1 ACTAR TPC chamber	58
2.3.2 Effective volume: drift region, detection plane	58
2.3.3 Extraction of the signal: metallic-core PCB and connection to the electronics (ZAP! boards)	60
2.4 GET electronics	61
2.4.1 AGet chip	62
2.4.2 GET trigger.	64
2.4.3 GET decision logic for E791	64
3 E791 Experiment	67
3.1 Introduction	68
3.2 Primary and radioactive beam	69
3.3 Selection process (LISE spectrometer)	69
3.4 Additional detectors for identification purposes	71
3.5 ACTAR-TPC: gas and pressure choice	73

3.6	Trigger and time logic	74
3.7	Towards the final settings	76
3.7.1	Online Identification	76
3.7.2	ACTAR TPC "online" measurements	77
4	Pre-treatment of signals and drift velocity measurements	81
4.1	ACTAR TPC signal corrections and calibrations	82
4.1.1	Baseline Correction	82
4.1.2	Fixed Pattern Noise (FPN) Correction	83
4.1.3	Pad signal amplitude gain-matching	84
4.1.4	Pad time signal alignment	86
4.1.5	Input signal reconstruction	87
4.2	CATS detector calibrations (CATibrations)	89
4.3	Drift velocity measurements	90
4.3.1	Procedure	91
4.3.2	Alpha source tests	92
4.3.3	Drift velocity from proton tracks	94
4.3.4	Discussion and comparison of drift velocity results.	95
5	Analysis	97
5.1	Implantation and decay events, observables	98
5.2	Identification of the nuclei	100
5.2.1	Experimental parameters for identification.	102
5.2.2	Extrapolation of parameter values for exotic nuclei	103
5.2.3	Identification radius	103
5.2.4	Probabilities	104
5.2.5	Limitations and use of the 4D identification analysis	105
5.3	Proton track analysis	106
5.3.1	Number of tracks and initial fit values	106
5.3.2	Signal fitting	109
5.3.3	Proton energy determination	116
5.3.4	Interpretation and cleaning of the energy proton distributions: escaping protons	122
5.4	Implantation-Decay correlations	124
5.4.1	Time condition	124
5.4.2	Spatial condition	125
5.5	Non-neutralization of the ions, track dispersion parameter.	127
5.5.1	Fraction of emissions from the cathode	128
5.5.2	Drifting time of ions	132
5.6	Observables: half-life, proton energies, branching ratio	133
5.6.1	Half-life measurements	133
5.6.2	Proton Energies	135
5.6.3	Branching Ratio	142
6	Results	147
6.1	⁴¹ Ti	150
6.2	⁴⁵ Cr	154
6.3	⁴⁴ Cr	158

6.4	^{43}Cr	165
6.5	^{46}Mn	172
6.6	^{47}Fe	177
6.7	^{46}Fe	182
6.8	^{45}Fe	186
6.9	^{49}Ni	189
6.10	^{48}Ni	193
6.11	Summary of main results	197
7	Further analysis and setup upgrade	201
7.1	Identification of the nuclei	202
7.2	Drift of ions	204
7.3	Fitting of the implantation event and escaping protons	204
7.4	Proton Fitting in 3D	204
7.5	Setup upgrade (γ and β detection)	205
	Conclusions and Perspectives	206
	Bibliography	210
	Résumé/Summary	216

Introduction



The atom has been considered to be the indivisible smallest unit of matter along the centuries. From 1896, when the radioactivity was discovered by Henri Becquerel, multiple studies started to be performed around a new hypothesis: atoms being themselves compound objects. In 1911 this theory was proved by Rutherford, when he interpreted the Geiger and Mardens experiment, in which alpha particles were fired at a thin gold foil. The experiment showed that most of the alpha particles were passing through with minimal deflection (as it was expected for an indivisible atom with a constant density) but some of them were being deflected at large angles. This finding led Rutherford to interpret the atom having a small, dense and positively charged nucleus surrounded by negatively charged electrons in orbits, giving rise to a new science: nuclear physics.

At the present time, around 100 years later, the nucleus itself is known to be composed by protons and neutrons (nucleons) that are also not indivisible units of matter but made of quarks. The aim of nuclear physics is to understand the forces that maintain the nucleus together and how the nucleons are arranged in the nucleus (nuclear structure). Explaining nuclear structure from nucleon interactions is already quite challenging, and the connection to a deeper level interaction (quark interaction) is even more complex. Strong theoretical and experimental efforts have been done to understand the nuclear strong interaction by studying and modeling the structure of the different existing nuclei in Nature (mainly stable) and the unstable ones, that have been created artificially by the use of particle accelerators, living for a while until they decay transforming themselves into a more stable nuclei by emitting decay products. There exist several theoretical models describing nuclear structure that have been established to work well under some assumptions, by comparison with experimental information, but none of them is able to reproduce the characteristics of the more than 2500 nuclei that are currently known. Further theoretical considerations are needed for the understanding of the different nuclear processes, and new experimental information is required to pursue this aim, in order to validate the different theoretical hypotheses.

Experimentally, information about the structure of the nucleus can be obtained in different ways, for example, by exciting the nuclei and studying the de-excitation process or by induction of nuclear reactions. In the case of unstable nuclei, information about the structure can also be obtained by studying the decay products. This latter possibility constitutes in some cases, for very unstable nuclei, the only possibility to explore the structure of the nucleus.

Since the discovery of the radioactivity in 1896, several radioactive decay processes have been discovered, allowing for a better understanding of nuclear structure. Electron capture, spontaneous fission, β and alpha decays, discovered from 1899 to 1938 constitute the "classical radioactivity processes". New rare decays were experimentally evidenced when the production of nuclei far from the stability became possible by the use of particle accelerators: β/EC delayed particle emission, direct single or two proton emission, cluster radioactivity or with the improvement of detection techniques: double β/EC decays. These decay modes constitute the "exotic radioactivity processes" and the only way for the study of the nuclear structure of nuclei far from the stability.

In particular, the two proton radioactivity, predicted at the beginning of 1960 by Goldansky and experimentally evidenced only in 2002, is a very rare decay in which the emission of a single proton from the nucleus is energetically forbidden, indicating a correlation of the two proton subsystem inside the nucleus. Different theoretical approximations have been proposed to try to describe this process and to predict the different available observables of such a decay: half life, energy and angular correlations between the protons. Theoretical descriptions were able to reproduce the measured half-life for the few known ground-state 2-proton emitters: ^{45}Fe , ^{48}Ni and ^{54}Zn , but not anymore when the two proton radioactivity was established for ^{67}Kr in 2016 with a half-life of the order of twenty times lower than expected. Two

hypotheses have been recently proposed to explain this discrepancy for ^{67}Kr : either a transitional situation between a direct and a sequential emission of the protons or the influence of the nuclear deformation in the measured half-life. These hypotheses, and the corresponding theoretical frameworks, need to be tested, which requires measuring the correlations (angular and energy) of the emitted protons for the different two proton emitters.

In parallel, important detection developments were achieved concerning gaseous detectors, historically used since the beginning of nuclear physics and the most suitable ones for tracking purposes. The measurement of the two proton radioactivity observables is one of the main motivations that boosted the most recent developments of gaseous detectors based on the principle of the Time Projection Chambers (TPC).

An experiment (E791) was performed at GANIL (Grand Accélérateur National d'Ion Lourds) in 2021 aiming to produce the (two proton emitter) ^{48}Ni nucleus to study the characteristics of the two proton radioactivity by using the ACtive Target and Time Projection Chamber (ACTAR TPC) gaseous detector. In addition, some other exotic decay modes in the ^{48}Ni mass region were measured. The current work addresses the analysis of this experiment, structured in seven different chapters.

The opening chapter is first devoted to explain some important basic concepts, the context and motivations in which this work is addressed in the nuclear physics field and a brief description of the different decay modes known up to date. Then, the main decay modes in the ^{48}Ni mass region (β -delayed proton emission and two proton emission), are described. Finally, a summary of experimental and theoretical works concerning the two proton radioactivity is presented.

The second chapter comprises a brief report about the experimental context of gaseous detectors and the characterization of the Active Target Time Projection Chamber (ACTAR TPC) device, a state-of-the-art gaseous detector used to study the decay products of the nuclei of interest during the experiment.

In the third chapter, the E791 experiment is described, covering different key points such as the production of the nuclei of interest, the selection process using the LISE3 spectrometer and the explanation of the different setting choices. Also, other ancillary detectors used for identification purposes and the acquisition decision logic of the experiment are described.

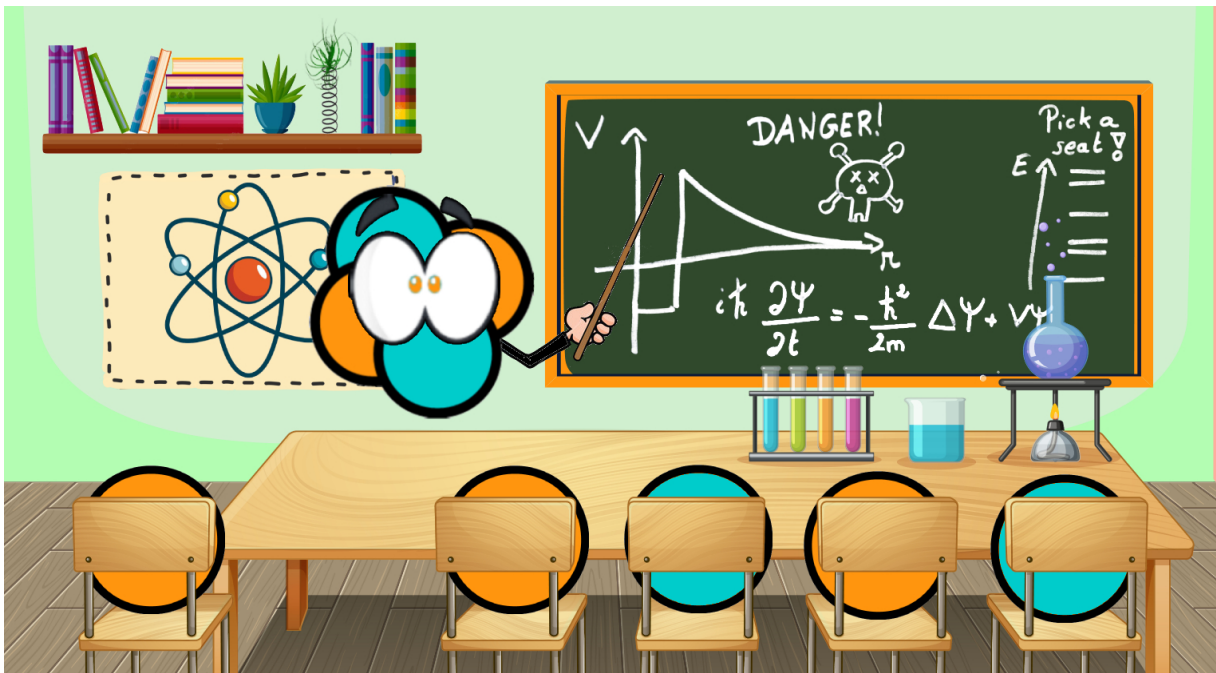
The fourth chapter is dedicated to explain the different processes applied for the extraction of the information from raw detector(s) signals to improve the quality of the data. Besides, the experimental measurement of an important parameter for determining the energy of the protons, the drift velocity, is detailed.

The fifth chapter covers the different stages of the analysis, the encountered problems and the strategies to obtain the main observables: half-lives, proton energies and branching ratios from the data.

In the sixth chapter, the results are presented nuclei per nuclei. Due to some encountered problems, result of an optimization of the experimental settings to increase the number of implantations of the ^{48}Ni nucleus, some of these results are still preliminary.

Finally, in the seventh chapter, some further analysis ideas, aiming to solve the main encountered problems and to improve the quality of the results, are briefly discussed.

Chapter 1: Context and motivations



Contents

1.1	Atomic nucleus	26
1.2	Nuclear structure	28
1.3	Decay processes	29
1.4	Region of measurement in E791 Experiment	32
1.5	β^+ /EC delayed proton(s) emission.	32
1.5.1	β^+ and electron capture decays.	33
1.5.2	Delayed proton emission	33
1.5.3	Isobaric Analogue State and Isobaric Multiplet Mass Equation (IMME)	35
1.6	Ground State proton emission	37
1.7	Two proton radioactivity from ground state	38
1.8	Two proton emission mechanisms	39
1.9	Two proton studies	41
1.9.1	Two proton experiments	41
1.9.2	Two proton decay models	42
1.10	Motivation of the study of the ^{48}Ni decay products	49

This chapter comprises the context and motivations of the current work. Important basic concepts and the main radioactivity processes of interest in the measured region are explained in sections 1.1 to 1.6. The last four sections include the description of the two proton radioactivity decay mode, the different experimental and theoretical studies performed to understand this rare decay mode and the motivation of the study of the ^{48}Ni nucleus.

1.1 Atomic nucleus

The word "atom" has been used along the centuries to represent the indivisible smallest unit of the matter until the discovery of the atomic nucleus in 1911 [1]. Different models and hypotheses of the structure of the atom have been proposed since then.

The atom is known to be composed of an atomic nucleus surrounded by an electron cloud. The atomic nucleus, is composed by protons and neutrons. The nuclear strong interaction (principally attractive in nature, rather short range, saturating and being charge-independent), maintains the nucleons together despite the Coulomb repulsion of the charged protons. This complex balance, responsible for the large amount of existing nuclei in Nature, depends on the size of the nucleus, the proton to neutron ratio (Z/N) and other effects such as the pairing energy or the shell structure of the nucleus.

This balance between forces maintaining the nucleons together can be quantified with the binding energy, characteristic of each nucleus. The binding energy corresponds to the amount of energy needed to separate the nucleons from the nucleus. The larger this value, the

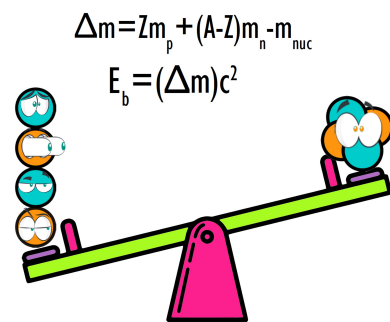


Figure 1.1: Mass deficit (Δm): The sum of the mass of the components (Z protons m_p and $(A-Z)$ neutrons m_n) is higher than the mass of the nucleus (m_{nuc}) which results into a positive binding energy. The binding energy E_b of the nucleus is related to the mass deficit via the Einstein equation.

more stable a nucleus will be. The binding energy can be determined by comparing the mass of the nucleus with the sum of the masses of its constituents, which results to be different from zero and positive for bound nuclei, as illustrated in Figure 1.1.

When the binding energy is not enough to hold the nucleons together, the nucleus becomes unstable, living only for a certain amount of time and then transforming into a more stable nucleus. The nuclei are usually classified in a bi-dimensional graph representing the number of protons (Z) as a function of the number of neutrons (N) (Ségre chart) (See Figure 1.2). The stable nuclei (around 260 out of 2500) existing

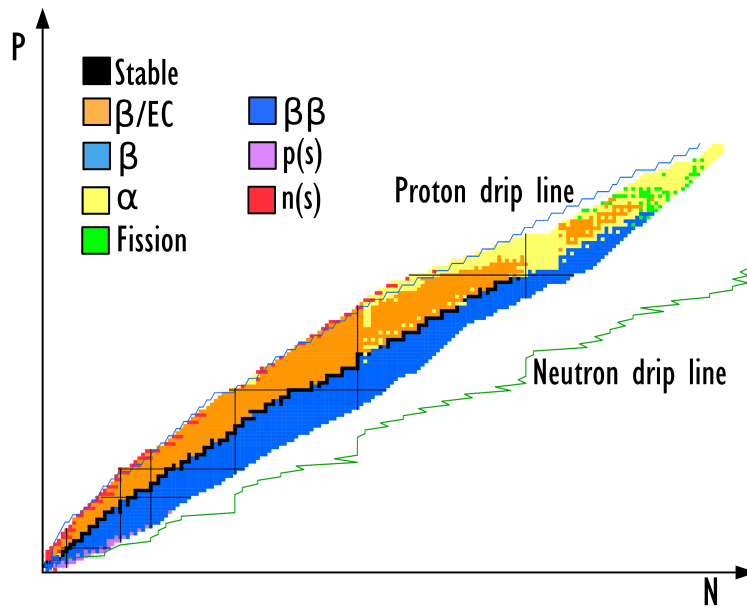


Figure 1.2: Ségre chart. The stable nuclei with large binding energies are shown in black, constituting the valley of stability. This group of nuclei divides the chart in two: neutron deficient region (top) and neutron rich (bottom). The colors of the nuclei correspond to the main decay modes, as shown in the legend. The proton and neutron drip lines are represented by the blue and green lines respectively.

in Nature are placed in the "valley of stability" and roughly divide in two regions the nuclear chart: the neutron deficient region and the neutron rich one. Apart from some long-lived radioactive species present in Nature or products of nuclear reactions occurring naturally (i.e. nuclear spallation in the atmosphere), the known unstable nuclei have been created artificially in the laboratory to study their characteristics.

There are some limits from which the nucleus cannot longer exist, for example too massive ones in which the short range nuclear force cannot hold the nucleons anymore (except from the predicted islands of stability [2]). For a given nucleus with Z number of protons, there exists also a limit on the number of neutrons N from which the nuclear force cannot longer maintain the nucleons together. These limits are called the proton and neutron drip lines for neutron deficient and neutron rich regions, respectively. They are represented in Figure 1.2 by the dashed lines.

1.2 Nuclear structure

The aim of nuclear physics is to understand how the protons and neutrons are arranged in the nucleus (nuclear structure) in order to be able to extract information about the fundamental nuclear forces between nucleons, which are responsible for the nuclear existence. Besides, nuclear physics also aims to find out the connection from these interactions with even deeper ones at a quark level. There exists several directions to follow for the study of nuclear structure: explaining the patterns and symmetries between the different existing nuclei (i.e. neutron rich against neutron deficient), understanding how the structure evolves when going away from stability and interpreting the different limits of existence mentioned in previous section: too massive nuclei or nuclei beyond the proton and neutron drip lines.

The shell model, proposed by M. Goeppert-Mayer in 1949 [3], is an approximation for the description of nuclear structure that is able to reproduce quite well many of the nuclei known at the present time. In this model, some of the nucleons are supposed to lay in different energy levels of a potential (produced itself by all the nucleons), forming an inert core, and only some of them (valence nucleons) being able to move between higher energy orbitals (valence space), as illustrated in Figure 1.3. This model reproduces quite well the shell closures of nuclei, happening when the number of nucleons is equal to 2, 8, 20, 28, 50, 82, 126 (magic numbers) which are more stable configurations of the nuclei. Despite the success of this model, it cannot be used to explain the structure of the more than 2500 known nuclei at present.

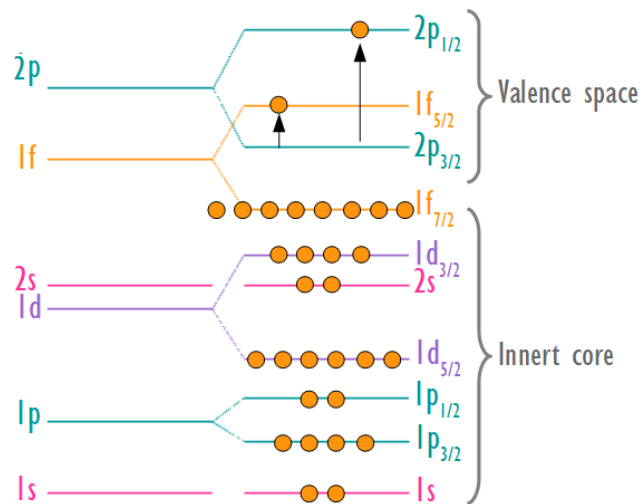


Figure 1.3: The different energy levels predicted by the shell-model are represented by the color lines. The filling of the protons (represented in orange) for a $Z=29$ nucleus show a completely filled shell ($f_{7/2}$) shell and the two protons are able to move in the valence space.

As a simplified image, there exists three different kind of models that work well for different kind of nuclei under some assumptions:

- *ab initio* models: which literally means "from the beginning", are approximations of nuclear structure obtained from the study of the interactions between the nucleons and some of them even taking into account chiral effective field theories (χ EFTs) of QCD [4]. Some of the lightest nuclei and heavier magic ones can already be explained using these models.
- Shell model: when dealing with more nucleons, the use of the *ab initio* models becomes complicated. The shell model, explained in the previous paragraph, works quite well for medium masses or for nuclei close to magic numbers in which the valence space and the number of valence nucleons is reduced.
- (Beyond) mean field models: when treating nuclei far from magic numbers or very massive ones, the

valence space becomes quite large, and even the approximation of an inert core and some valence nucleons is no longer adapted to describe them. A powerful approximation in these cases is to convert such a many-body system into a non-interacting system of quasi-particles using a suitable external mean field potential created by all the nucleons as a whole and treating the remaining interactions as a perturbation potential [5].

These theoretical models have been established to work well under some assumptions by the comparison with experimental information. This has been achieved over the years, by studying the structure of the different existing nuclei in Nature (mainly stable) and the unstable ones, that have been created artificially by the use of particle accelerators. Unfortunately, any of the existing models is able to reproduce the characteristics of the structure of all nuclei at once. Further theoretical considerations are needed for the understanding of the different nuclear processes, and new experimental information is required to pursue this aim, in order to validate the different theoretical hypothesis.

From the experimental side, there exist several techniques to obtain information about the structure of the nuclei:

- Mass measurements with ion traps (measurement of oscillation frequencies of ions in magnetic and/or electric fields).
- Excitation of the nucleus and study of the de-excitation processes (mainly by emission of gamma rays) (Coulomb excitation)
- Induction of nuclear reactions and study of the final products (i.e. transfer reactions, fission processes)
- Laser excitation, studying the interaction of the electron cortex with the nucleus.
- Study of decay products (in the case of unstable nuclei).

The study of exotic nuclei near the drip lines is of great importance for a better understanding of nuclear structure. In these regions, several important aspects in nuclear physics can be explored at once, such as the study of the evolution of the structure when moving away from stability or the limits of nuclear existence. The drip lines are experimentally difficult to reach. In particular, for the proton drip line, low production cross-sections and short half-lives (order of ms) are the main experimental limitations.

The current work focuses on the study of unstable nuclei very far from stability, close to the proton drip line. In this region, information on the structure of the nuclei is only accessible by studying the decay products. The low production cross-sections make their study impossible with any of the other experimental techniques mentioned above. In-beam studies by reaction are not possible at such low intensities.

1.3 Decay processes

The transformation of a nucleus into a more stable one is called "radioactive decay". It can occur in different ways depending on the force responsible for the transformation (weak, electromagnetic, strong) as it will be further discussed. The prediction of the exact moment in which a single nucleus decays is impossible, since the decay is a stochastic process. However, the half life ($t_{1/2}$), defined as the time required for a quantity of an unstable species to reduce to half of its initial value, can be estimated. This overall decay rate is characteristic of each nucleus, constituting one of the main observables of the decay

processes. The half-lives values have a huge range, from nearly instantaneous (${}^7\text{H}$, 23×10^{-24} s) to very long half-lives as it is the case for ${}^{40}\text{K}$, ${}^{232}\text{Th}$ and ${}^{238}\text{U}$, three unstable nuclei that can be found in nature with half-lives of the order of 10^9 years.

During the disintegration process, other particles or radiation are emitted. The emission of particles in the course of a decay is called radioactivity, and it was first discovered by Henri Becquerel in 1896 [6] when he left uranium salts near of a photographic plate wrapped in black paper for some days. Despite no exposure to visible or ultraviolet light, the plate resulted to have radiation evidences. He could then conclude that other invisible radiation from uranium was going through the paper, resulting in the discovery of radioactivity. Some years after that, Ernest Rutherford first distinguished two different radioactivity processes in 1899 [7] beta and alpha radioactivity:

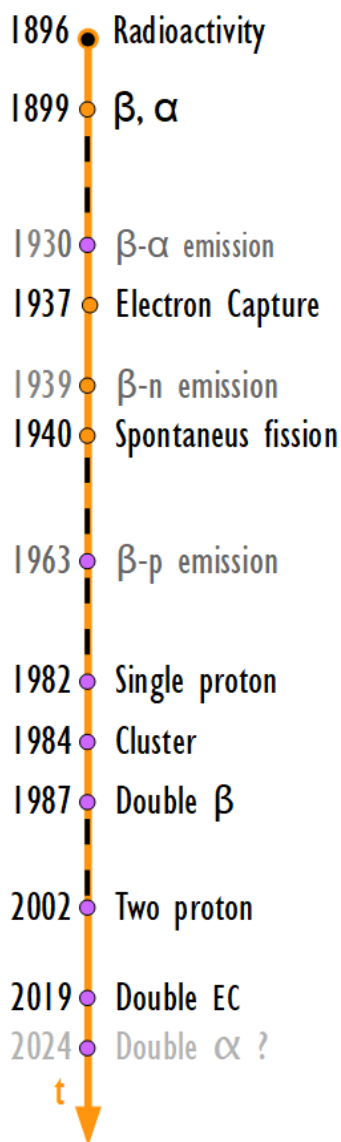


Figure 1.4: Discovery dates of different radioactivity processes. Classic radioactivity processes are represented in orange and rare decays in purple.

The β decay is a result of the weak interaction, it consists of a transformation of a proton into a neutron with emission of a positron and an electron neutrino (β^+) or the conversion of a neutron into a proton with emission of an electron and an electron antineutrino (β^-). These processes occur for unbalanced nuclei with a neutron deficiency (β^+) and neutron excess (β^-).

The **alpha decay** is a type of radioactive disintegration in which an alpha particle is emitted from the nucleus.

Other radioactivity processes were found in 1937, and 1940 respectively: The electron capture decay [8] and the spontaneous fission [10].

The **electron capture** is a process in which the nucleus captures an e^- from the electronic orbitals, transforming a proton into a neutron and emitting an electron neutrino in the process.

Induced and spontaneous fission, consists in the breaking apart of a massive nucleus into mainly two smaller fragments with similar (within 30% difference) masses. The induced fission was discovered in January 1939 by Otto Frisch and Lise Meitner [9] after an experiment taking part in December 1938. The existence of the spontaneous fission decay mode was established one year later in 1940 [10] and further studied in 1942 [11].

The electron capture and the spontaneous fission, together with β decay and alpha emission, constitute the "classical radioactivity processes".

New rare decays were experimentally evidenced when the production of nuclei very far from the stability became possible by the use of particle accelerators: β /EC delayed particle emission, single and two proton emission and cluster radioactivity or with the improvement of detection techniques (double β /EC decays). These decay modes constitute the "exotic radioactivity processes" [13] – [19].

β /EC delayed particle emission: consists of the emission of secondary particles after the β /EC process. For nuclei close to the valley of stability, the daughter nucleus of the β /EC decay can be produced in the ground state or in low-energy excited states. In these cases, the de-excitation to the ground state happens by the emission of γ ray(s) or electromagnetic interaction with an orbital electron (internal conversion (IC)). For nuclei with more and more proton/neutron (Z/N) unbalanced ratio, it becomes possible to produce decay products in higher and higher excited states. Sometimes, the energy of these excited states can be enough to allow for the emission of other particles. These particles are "delayed" since they are emitted by the daughter nucleus after the first β emission. The secondary emitted particles can be proton(s) [12] or alpha particle(s) [13] and neutrons [14] for β^+ , and β^- emissions respectively.

Ground State Direct Proton(s) emission(s) decay modes along the proton drip lines were predicted in the beginning of 1960. In this extreme Z/N ratio conditions, the strong force cannot longer bind the nucleons together, allowing for the possibility of a direct emission of protons from the nucleus. Due to the pairing effect (higher stability for nuclei with an even number of protons), a direct **single proton emission** for nuclei with an odd number of protons and a **double proton emission** for the ones with even Z were predicted. The single proton emission from ground state was first observed in 1982 [15]. The first experimental evidence of the two proton emission came later, in 2002 at GANIL [16] and GSI [43].

Cluster radioactivity: this decay mode, in competition with spontaneous fission, consists of a splitting of the nucleus by one favorable configuration in a non-symmetric way resulting into important mass differences between the fragments, in contrast to the spontaneous fission decay products. It was first evidenced in 1984 [17].

The last observed "exotic" decay modes are the **double β and double electron capture decays**. The double β decay is a process consisting in a simultaneous two-proton to neutron conversion ($\beta^+\beta^+$) with emission of two positrons and two neutrinos or ($\beta^-\beta^-$) emission, consisting in two-neutron to proton conversion with emission of two electrons and two anti-neutrinos. The first evidence of this decay mode was found in 1987 for β^- [18] and it has not yet been found for the β^+ case.

The double electron capture consists of a capture of two electrons, transforming two protons into two neutrons and emitting two electron neutrinos in the process. The probability of a double electron capture is quite small and challenging to measure, as discussed in [19]. Nevertheless, this decay mode was evidenced in 2019 [19].

A new decay mode, the double alpha decay (without formation of ^8Be cluster) has been recently predicted in 2021 [20]. Two experiments have been already performed at GSI (source experiment) and ISOLDE (ISOL-beam study) [21] in February 2022 and June 2023 respectively. The analysis of these data may lead to the discovery of this new exotic decay mode.

1.4 Region of measurement in E791 Experiment

In the current work, the nuclei in the neutron deficient side around $Z=28$, $N=20$ are studied (see Table 1.1 and Figure 1.5). In this mass region the main decay modes are β^+ emission or electron capture, followed by single or multiple proton emissions from the daughter(s), (β delayed proton emission). In the case of ^{48}Ni and ^{45}Fe , that are nuclei beyond the proton drip line, this decay mode is in competition with the direct two proton emission. These two main decay modes are discussed in detail in the following sections.

Z	28	26	25	24	22
Isotopes	^{48}Ni , ^{49}Ni	^{45}Fe , ^{46}Fe , ^{47}Fe	^{46}Mn	^{43}Cr , ^{44}Cr , ^{45}Cr	^{42}Ti , ^{41}Ti , ^{40}Ti

Table 1.1: Nuclei studied within this work classified by charger number.

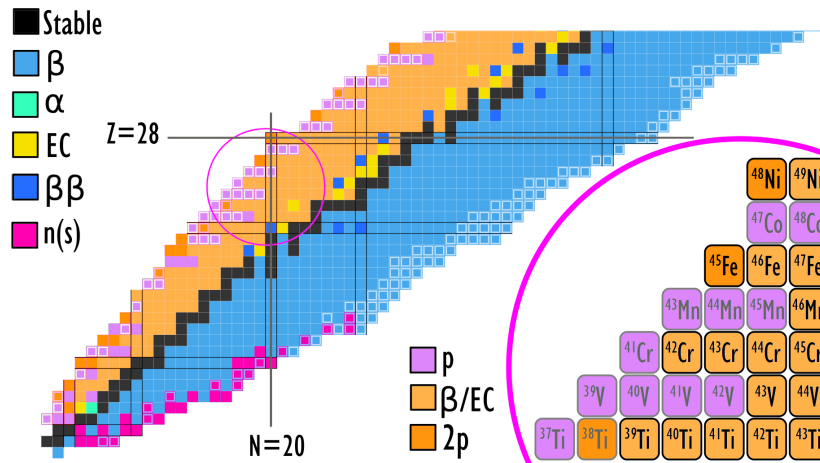


Figure 1.5: Zoom of the nuclear chart in the region of interest around $Z=28$ and $N=20$. The nuclei in orange decay mainly by β -p(s), the ones in darker orange (^{48}Ni , ^{45}Fe , ^{38}Ti) are predicted to decay also by two proton emission. The violet ones are unbound to single proton emission. Furthermore, the grey color of the boxes and nucleus names in the zoom of the region on the right, indicate a too-short half-life of the nuclei to be observed.

1.5 β^+ /EC delayed proton(s) emission.

The β^+ /EC delayed proton emission is a decay process happening in different stages and governed by the three microscopic interactions: the weak interaction, responsible for the first step of this decay (β^+ /EC), the strong interaction, accounting for the second step (emission of protons) and the electromagnetic interaction, responsible for the emission of γ rays (in the case of a filling of the excited state of the daughter). The β^+ /EC and the further emission of protons are explained along the section 1.5.1 and 1.5.2.

1.5.1 β^+ and electron capture decays.

The β^+ (Equation 1.1) and electron capture (EC) decay (Equation 1.2) processes are analogous processes in the sense that they both result into a transformation of a proton into a neutron. They constitute the main decay modes for neutron deficient nuclei.



The amount of energy released in the decay process is the Q value. It is proportional to the difference between masses of the initial and final products in a reaction. For the electron capture process, considering a negligible mass for the neutrino, it can be calculated from the difference of masses of the initial particles (M_X, m_{e^-}) and the decay products (M_Y), as defined in Equation 1.3.

$$Q_{EC} = (M_X + m_{e^-} - M_Y)c^2 \quad (1.3)$$

In the case of a β^+ decay, the Q value is defined :

$$Q_{\beta^+} = (M_X - M_Y - m_{e^-})c^2 \quad (1.4)$$

For an available decay energy (Q value) above $2m_{e^-}$ (1022 keV), the two processes are in competition. For energies below that value, only electron capture is allowed.

The feeding of the nuclear states of the daughter depends on its structure and on the available energy Q_β . The process must fulfill some selection rules concerning the change of the total angular momentum J , the total isospin T and the parity π . Two different types of transitions are defined depending on the allowed values for ΔJ , $\Delta\pi$ and ΔT : Fermi transitions ($\Delta J=0, \Delta\pi=0$ and $\Delta T=0$) and Gamow-Teller transitions ($\Delta J=0, \pm 1, \Delta\pi=0$ and $\Delta T=0, 1$, excluding the $0^+ \longrightarrow 0^+$ transition). The study of the β decay allows determining the level structure of the daughter nucleus and to characterize the different transitions, which is a unique way for testing the validity of different Shell model assumptions.

1.5.2 Delayed proton emission

The β delayed proton emission is a two-step process involving three different nuclei. The initial nucleus (precursor) decays by β or EC to the emitter nucleus, usually in an excited state, that decays emitting a proton to the final nucleus (daughter).

This type of decay is energetically possible when the mass of the precursor is larger than the sum of the masses of the daughter and the emitted particles. The emitter needs to be populated by β decay in an excited state of energy above its proton separation energy S_p (defined as the minimum energy required to remove a proton from the atomic nucleus) as shown in Figure 1.6. For lower energies, the emitter decays by emission of γ ray(s) to its ground state.

The emission of the proton occurs almost spontaneously if the filled excited states have energies above the Coulomb and centrifugal barrier. For lower energies, the emission can happen by tunnel effect with a probability that depends on the penetrability of the Coulomb and centrifugal barriers, depending on the proton energy.

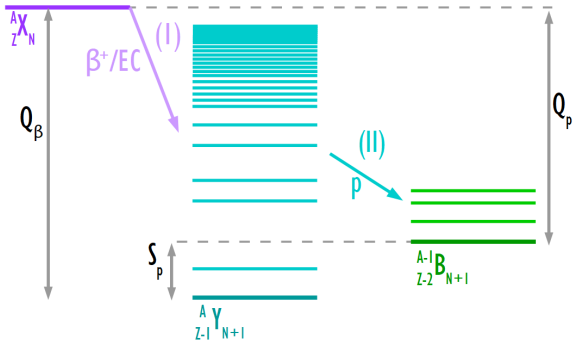


Figure 1.6: Example of the two-steps β delayed proton emission process. The three different nuclei involved: precursor, emitter and daughter are illustrated in purple, blue and green respectively. After the β or electron capture decay (I), if the populated excited state of the emitter has an energy higher than the proton separation energy (S_p) a proton (II) can be emitted.

The probability of a β delayed proton emission is higher as the nucleus becomes more exotic: the available energy Q_β for the feeding of the states of the intermediate nucleus increases when moving away from the valley of stability (which translates in a higher possibility of populating higher excited states). Inversely, the energy binding together the nucleus and the proton separation energy decreases for more and more unstable nuclei.

Precursors whose Q_β is large compared to the S_p energy ($Z > N$) and fulfilling equation 1.5 are called light precursors. For these nuclei, discrete states below the high level density region are unbound to proton emission. This translates into discrete experimental proton spectra.

$$Q_p = Q_\beta - S_p \gg S_p \quad (1.5)$$

The β -p decay was experimentally evidenced in 1963 [12], and since then, more than 160 nuclei have been identified to decay by β delayed proton emission [24], [28]. The known nuclei exhibiting such a decay mode have been evaluated recently in [29] to provide recommended values for their nuclear properties.

From the measurement of the proton energies in the β -p process, valuable information about the involved states of the emitters can be inferred, not accessible through other means in the case of the most exotic nuclei, where the proton emission decay dominates over γ decay, as illustrated in Figure 1.7.

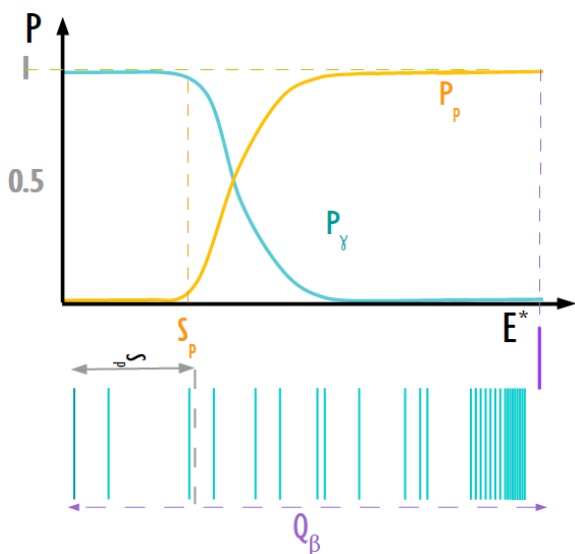


Figure 1.7: Top part: probability of emission P as a function of the energy E^* of the excited state of the emitter (populated by β decay) for γ and proton emissions in blue and orange, respectively. Above the S_p value, the proton emission starts to dominate over the γ emission. Bottom: example of the emitter level scheme: states below the S_p value can be studied only by γ emission. On the other hand, the characterization of states at high excitation (right) requires the detection of protons.

This decay mode is also of special interest in astrophysics for the study of inverse reactions (proton capture) occurring in stellar processes for nuclei along the astrophysical rp (rapid proton capture [30]) and p (proton capture [31]) paths.

For the most exotic nuclei, an emission of multiple protons (x) becomes possible, as illustrated in Figure 1.8. This is a consequence of the increase of the available energy Q_β and the decrease of the separation energy S_p when moving away from stability, which makes these nuclei fulfilling the condition 1.6.

$$Q_\beta - S_{xp} > S_{xp} \quad (1.6)$$

The emission of the protons occurs typically in a sequential way: multiple single proton emissions from the excited states of ${}_{Z-1}Y$, ${}_{Z-2}B$... ${}_{Z-n}D$ nuclei respectively. The β -2p emission was first evidenced in 1983 for ${}^{22}\text{Al}$ [26] and confirmed with a higher statistics in 1984 [27]. Since then, nine other β -2p emitters have been observed [32].

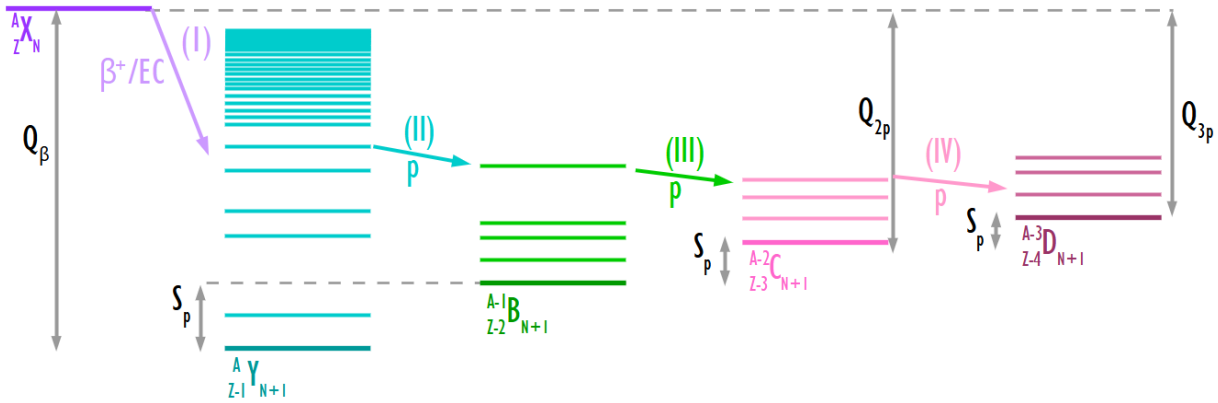


Figure 1.8: Example of a β delayed three proton emission process. The process happens sequentially in four different steps: β or electron capture decay (I) and proton emission of the first, second and third emitter nucleus (II, III and IV steps respectively).

In the mass region studied in this work, far from stability, the nuclei have large Q_β and small S_p values, and the β delayed proton(s) emission is a common decay mode. All the studied nuclei are classified within the light precursors framework: neutron deficient ($Z > N$) and fulfilling equation 1.5, meaning that the proton energy spectra that are obtained experimentally are discrete. Furthermore, for some of them, the available decay energy is predicted to be enough for a multiple proton emission. *First evidences of such processes are found in this work for some of the most exotic nuclei, as further discussed in Chapter 6.*

1.5.3 Isobaric Analogue State and Isobaric Multiplet Mass Equation (IMME)

The measurement of the proton energies from β delayed proton emissions can allow for a determination of the mass of the parent nucleus, as already estimated by Dossat *et al.* for proton rich nuclei in [24]. Two concepts (Isobaric Analogue State and Isobaric Multiplet Mass Equation) are introduced in this section to explain this process.

Isobaric analogue states (IAS) are states which differ only by a single quantum number from each other: the isospin projection T_z . According to their isospin quantum number T , they form a multiplet of $2T + 1$ members. One member is "generated" from its neighbour by replacing a proton (neutron) in a

certain quantum state by a neutron (proton) in exactly the same state, with the sole difference being the T_z quantum number. The masses of these multiplet members are very similar, once the Coulomb-energy contribution to the mass is corrected for. Figure 1.9 shows a schematic representation of the masses in an example multiplet as well as other states in the nuclei involved.

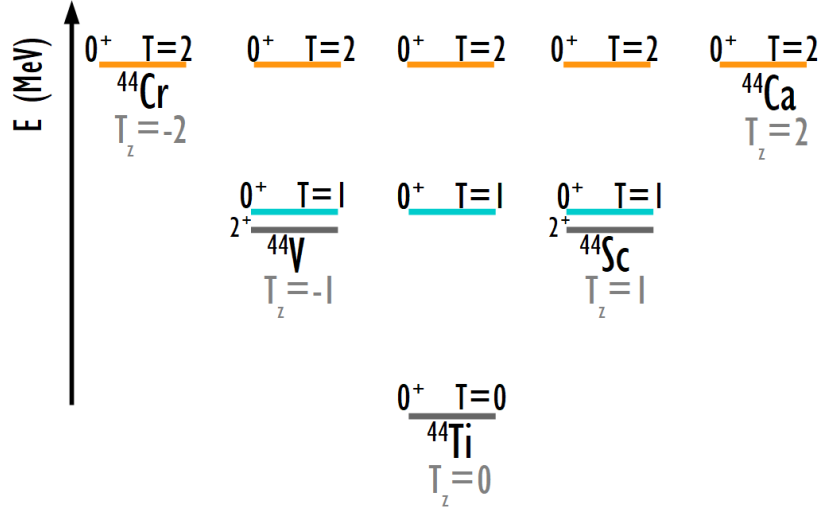


Figure 1.9: Energy levels of states in the multiplet of $A = 44$, $T = 2$, $I^\pi = 0^+$ from $T_z = -2$ to $+2$, i.e. ^{44}Ca , ^{44}Sc , ^{44}Ti , ^{44}V , and ^{44}Cr (in orange). For this representation, the Coulomb energy differences between the nuclei have been removed. The states in black are the ground states of the nuclei (except for ^{44}Cr and ^{44}Ca , represented in terms of T_z), in blue the $T_z=1$ 0^+ states and in orange the $T_z=2$ states.

As proposed first by Wigner in 1957[22], these different masses can be linked to each other via perturbation theory if the electromagnetic interaction is treated as a small perturbation of the strong interaction (assuming that it is small with respect to the main strong interaction force). This approach is valid only if there is no significant isospin impurity in the states of interest and the three-body terms in the strong interaction are negligible.

Under these conditions, the Isobaric Multiplet Mass Equation (IMME)[23], linking the masses of the states in different nuclei with same quantum numbers except T_z is obtained:

$$\Delta m = a(\alpha, T) + b(\alpha, T) \cdot T_z + c(\alpha, T) \cdot T_z^2 \quad (1.7)$$

where α represents all quantum numbers except T .

Beyond the test of validity of this equation, it can also be used to predict the ground-state mass. If three members of a multiplet are known experimentally, the coefficients a , b , c of the IMME equation can be determined and the mass of other members of the multiplet can be estimated. The measurement of the proton energies from β delayed proton emissions allow for a determination of the mass excess of the IAS state. If the mass of the daughter (less exotic) is also known, the mass of the parent nuclei (very exotic) can be calculated using the IMME equation as determined by Dossat *et al.* in [24].

1.6 Ground State proton emission

Rare decay modes at the proton drip lines (single and double proton emission from ground state) were predicted from the beginning of 1960 by Goldansky [25], Zeldovich [33], Karnaukhov [34] and Jänecke [35]. In extreme conditions, for nuclei beyond the proton drip lines, the separation energy S_p becomes negative as shown in Figure 1.10, meaning that the nucleus becomes unbound to direct proton emission from its ground state. If this separation energy is just slightly negative, due to the effect of the Coulomb and centrifugal barriers, the protons can stay in a quasi-bound state for a while until escaping by tunnel effect, as illustrated in Figure 1.11. The time until the proton escapes from the nuclei, related to the probability of penetration of the barriers, allows for the observation of the so-called proton radioactivity.

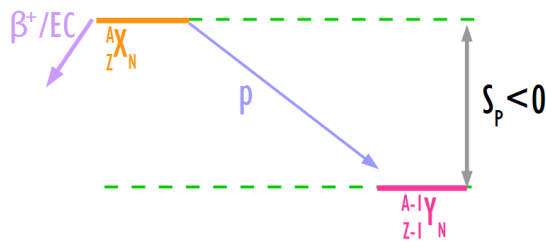


Figure 1.10: Energy scheme for the proton radioactivity process in competition with β decay.

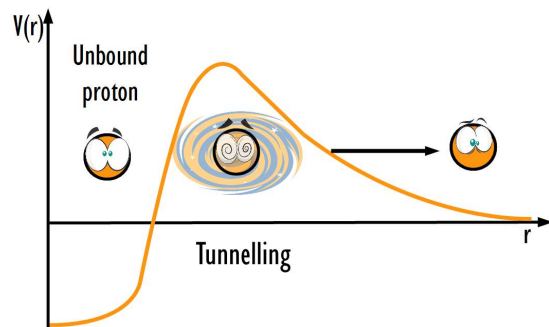


Figure 1.11: One proton, located in an unbound state, escaping from the nucleus by tunnel effect through the Coulomb and centrifugal barrier.

This exotic decay mode is in competition with the β delayed proton emission process previously described. The ideal conditions for the observation of a direct proton decay are found for proton energies Q_p below the Coulomb barrier but large enough so that the branching ratio with respect to a $\beta - p$ process becomes non-negligible (separation energies typically below -1 MeV). First experimental evidences for the single proton emission from ground state were found in 1982 [15] [36]. From then, more than 30 new nuclei beyond $Z=53$ have been measured [28]. This decay mode has allowed for a better understanding of nuclear structure at the proton drip lines and to study the tunneling process, from which information about the width and height of the coulomb and centrifugal barrier could be obtained. The half-life and the Q_p value are measured to obtain the proton orbital angular momentum, leading to a characterization of the state from which the particle was emitted in the parent nucleus.

1.7 Two proton radioactivity from ground state

In some special cases, the direct emission of two protons from the ground state becomes possible. Such a process occurs when the nucleus becomes unbound to two proton emission ($S_{2p} < 0$) and the emission of one single proton is forbidden ($S_p > 0$) as shown in Figure 1.12. The candidates for this very exotic decay

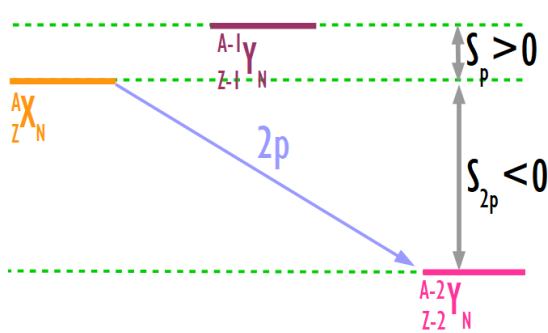


Figure 1.12: Energy scheme illustrating the conditions needed for the two proton radioactivity process.

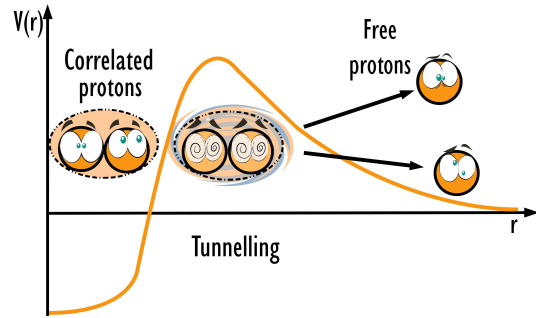


Figure 1.13: Two protons (correlated inside the nucleus) and further escaping through the Coulomb and centrifugal barrier by tunnelling.

mode are found in the proton rich region, beyond the proton drip lines and for nuclei with an even number of protons. In this particular case, due to the pairing energy effect [39], the initial nucleus ${}^A_Z X_N$ with even Z , has a larger binding energy than if a proton is removed from it. In other words, the system is more stable if the number of protons in the nucleus is even. An emission of two protons, leading to a product with even Z , remains therefore a possibility.

The fact that the protons cannot go through the barrier individually is an evidence of the subsystem correlation of the protons inside the nucleus. The two proton radioactivity, as predicted by Goldansky, assumes the two protons composing a ${}^2\text{He}$ system inside the nucleus and escaping together through the Coulomb and centrifugal barrier by tunneling. The di-proton system further splits due to the Coulomb repulsion. For the observation of such a process, the energy of the two proton system Q_{pp} needs to be, as in the single proton emission, smaller than the Coulomb barrier created by the protons in the nucleus but large enough to make the transition relatively fast to compete with β decay. Some first descriptions of this rare transition process were proposed at the beginning of the 60's ([37]-[41]). A full comprehension of the process is yet not achieved. Section 1.9.2 addresses an overview of the main theoretical approaches.

From this exotic decay process, two more observables, apart from the total energy of the system and the half-life, are available: the angle of emission between the protons and their individual energies, which are predicted to be affected by the structure of the initial nucleus. Theories able to predict these observables together with their experimental measurement can help for a better understanding of the two proton radioactivity and the nuclear structure beyond the proton drip lines.

The first experimental evidence of a two proton emission from the ground state was found for ${}^{45}\text{Fe}$ in 2002 from two independent experiments performed at GANIL [16], [42] and GSI [43]. Only three other emitters have been experimentally evidenced since then: ${}^{54}\text{Zn}$ [44] and ${}^{48}\text{Ni}$ [45] in 2005 and ${}^{67}\text{Kr}$ in 2016 [46].

1.8 Two proton emission mechanisms

In the previous sections, two different possibilities for the emission of two protons from the nucleus have been presented: the emission from an excited state (β -2p) and from the ground state (2p).

The emission from an excited state can happen, as explained before, directly or sequentially via an intermediate state as illustrated in Figure 1.14. In the same way, for some light nuclei, an emission from the ground state via an intermediate state is possible. Such a process can occur if the Coulomb barrier is small and the states of the $Z-1$ daughter (unbound) are large enough to allow for a single proton emission, as shown in Figure 1.15. This decay mode was first established for ${}^6\text{Be}$ [47], ${}^{12}\text{O}$ [48] and ${}^{16}\text{Ne}$ [49]. When the (broad) intermediate state has an energy below S_p the decay is called "democratic". No real distinction between simultaneous and sequential emission is possible, and no strong correlations between the particles are expected. Further studies suggest establishing the democratic decay as decay modes for ${}^6\text{Be}$, ${}^{12}\text{O}$ and ${}^{16}\text{Ne}$. A review of 2p emission from light 2p-unbound nuclei can be found in [32]. The current work addresses the study of nuclei of higher masses and longer half-lives in the $Z=28$ region, for which the emission of a single proton is forbidden.

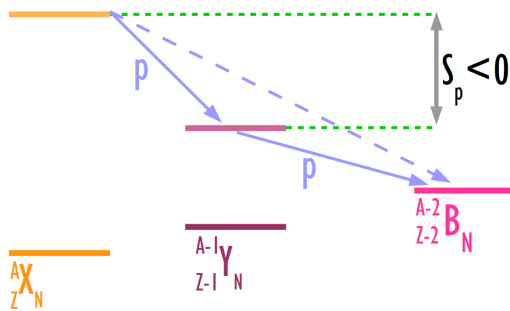


Figure 1.14: Sequential emission of two protons from an excited state via an intermediate state.

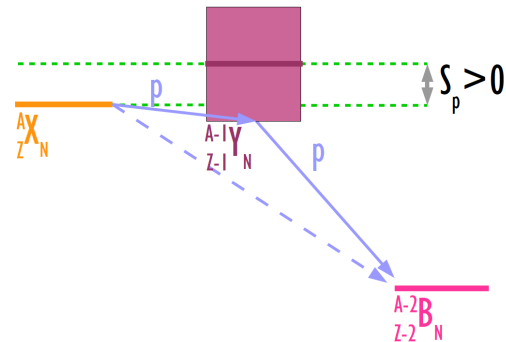


Figure 1.15: Sequential emission of two protons from the ground state via a broad intermediate state.

Within this context, there exists mainly two different approaches:

- The two proton radioactivity as defined by Goldansky, predicting the emission of a di-proton from the nucleus under the assumption of the two protons traversing the barrier together.
- The three-body simultaneous emission approach, that assumes a 3-body interaction between the protons and the nucleus, without the assumption of the pre-formation of a di-proton subsystem.

The main experimental goal in order to prove a "pure two proton emission" is first to distinguish it from the rest of the possibilities: sequential proton emission and "democratic" case. Secondly, in the case of a pure two proton emission, the experimental results may also clarify the decay characteristics (di-proton or three body approaches). The two proton decay mechanism can be disentangled by using two observables: the energies and the angle correlation between the protons.

The proton energy distributions: in the sequential case, the proton energies depend on the intermediate state from which they were emitted, translating into two well-defined energy peaks. In the sequential case via an intermediate state, these peaks may be larger due to the width of the intermediate state. Inversely, in

the case of a simultaneous emission, the available energy is shared between the protons. This configuration optimizes the penetrability of the barrier. (The emission of a first proton with higher energy than the second one will disfavor the emission of the second one.)

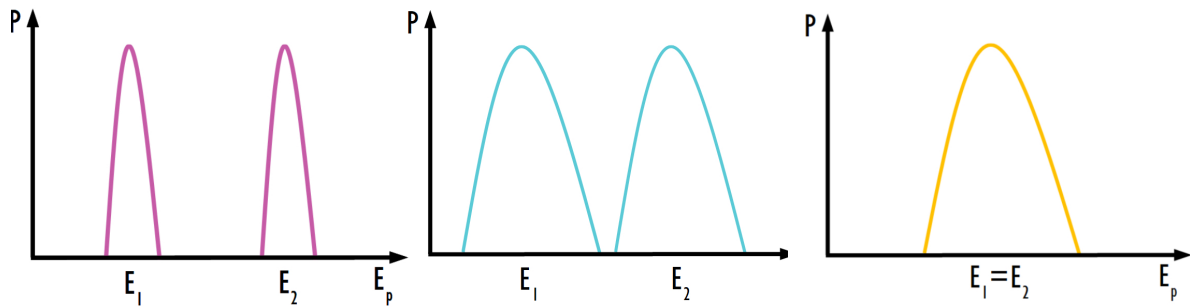


Figure 1.16: Schematic probability as a function of the energy of each proton in the different two proton decay hypotheses. On the left, the sequential decay case, in which the energy peaks are well-defined. In the middle, the case of sequential decay via a large state, due to the width of the state the energy peaks are broader. On the right, the real two proton decay in which the energy is shared between the protons.

The angular distribution: in the case of a sequential emission, no angular correlation between the protons is foreseen (isotropic distribution). In a pure two proton emission, in both cases (di-proton and three-body decay approaches) a strong correlation between the proton angles is expected. In the first case, since the protons are traversing the barrier together and split when escaping the nucleus, the angular distribution may be centered at small angles, as illustrated in Figure 1.17. In the three body decay case, the angular distribution may depend on the characteristics of the nucleus and the three-body interaction approximations taken into account, as further explained in Section 1.9.2.

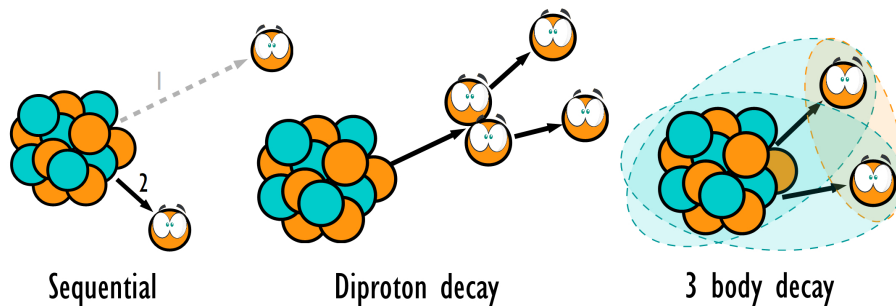


Figure 1.17: Proton angular distributions for the different 2p emission mechanisms. On the left the sequential emission is shown whose angular distribution is isotropic. The two different hypothesis for a real two proton decay (di-proton and 3-body decay hypotheses) are represented at the center and on the right respectively. The di-proton case may lead to small angle distributions (Coulombian repulsion once escaping the nucleus). In the 3-body decay a strong correlation is expected due to the interaction between protons inside the nucleus, but the shape of the angular distribution may vary depending on the theoretical approach used to describe the decay, as further discussed in section 1.9.2.

1.9 Two proton studies

Since the two proton radioactivity was predicted, experimental efforts have been made, first to prove the existence of such an exotic decay and then to improve the detection techniques to be able to get more information about the individual energies and the angles of emissions of the protons. The two proton radioactivity (three-body decay) taking place for nuclei beyond the proton drip lines (unbound systems), makes the description of the process very complex, as further explained in 1.9.2. Multiple theoretical studies have been developed to describe the two proton radioactivity and to reproduce the main observables. Both experimental and theoretical studies about this decay mode are discussed in this section.

1.9.1 Two proton experiments

The first experimental evidence of a two proton decay was found in 2002 for ^{45}Fe at two different facilities (GANIL and GSI) as mentioned in section 1.7. In both cases, the ^{45}Fe nuclei were produced by fragmentation of a ^{58}Ni beam of 75 MeV per nucleon (on a ^{nat}Ni target) and 650 MeV per nucleon (on a beryllium target) respectively, in order to study the decay products using very similar setups.

In the GANIL experiment, the setup consisted of a sequence of four silicon detectors, as shown schematically in Figure 1.18. The two first silicon detectors were used for fragment identification, the third silicon detector (with 16x16 x-y strips with a 3mm pitch) was used to stop the fragments and the last one, to identify high energy decay products. The implantation events were triggered by the two first silicon detectors, whereas radioactive decay events were triggered by S3 or S4. In the case of a two proton radioactivity, the emitted protons are stopped and detected in the stripped silicon detector (S3) in which the total energy can be measured. In the case of a β delayed proton emission decay, the proton may be detected in S3 together with some energy of the β particle, broadening the measured energy peak in S3, which, due to its longer range, is detected as well in S4. By imposing decay events with no signal in the last silicon detector (no β detected) and comparing the width of the energy spectra measured in the striped silicon detector (S3), the two proton emission events could be identified, resulting in the first evidence of the two proton radioactivity.

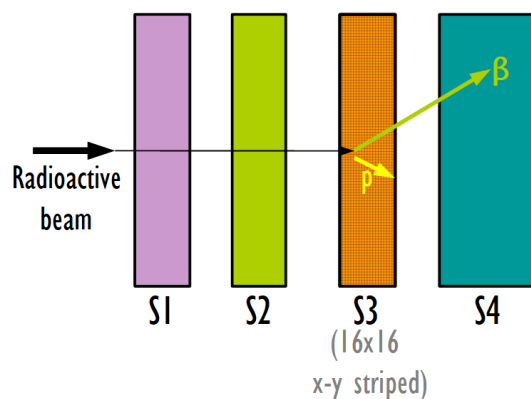


Figure 1.18: Schematic illustration of the detection setup used at GANIL to observe two proton decay events from ^{45}Fe . The two first silicon detectors (S1 and S2) are employed for identification of the incident nucleus. The fragments are stopped in the third detector S3 (16x16 x-y striped). The decay products are then measured in the same detector (for protons) and in S3 and S4 for longer range particles (β).

In the case of the GSI experiment, the setup consisted of a 8-silicon telescope mounted inside a NaI(Tl) "split barrel" composed by 6 NaI(Tl) crystals for γ rays detection, as illustrated schematically in Figure 1.19. The first silicon detector is used to trigger the acquisition by the incoming fragment. The signals from all the other detectors are then measured within 10 ms. The non-observation of γ rays (annihilation of e^+ from β decay) in coincidence with the dominant decay of ^{45}Fe not being compatible with a β decay but with a two proton emission scenario, allowed to state for the first evidence of this exotic decay. More details of both (GANIL and GSI) experiments can be found in [16] and [43] respectively.

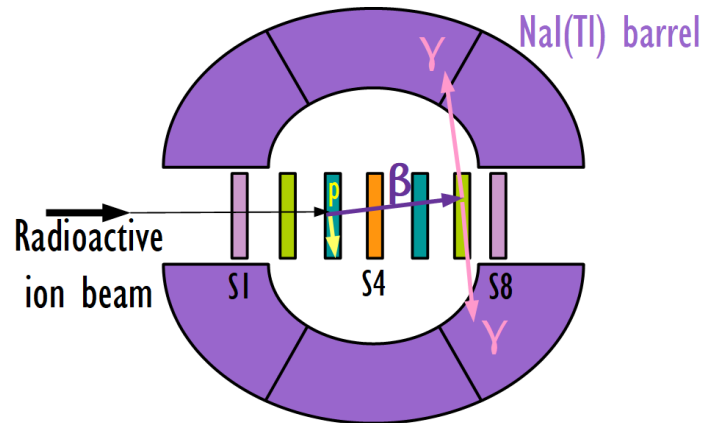


Figure 1.19: Schematic illustration of the detection setup used at GSI to distinguish two proton decay events from ^{45}Fe . One example of β delayed proton emission, measured within the 10 ms time window after the trigger in S1 by the incident nuclei, is illustrated. The proton is detected in S3 in coincidence with the β particle and the two back to back γ rays. In the two proton emission scenario, there is no β and γ detection. As explained in the text, this allowed to establish the two proton emission decay.

In the described experimental setups, no measurement of the individual energies of the protons nor any information about their angle of emission is achievable. Only the total energy Q_{2p} and the half-life can be measured. The first evidence of a two proton emission from ^{54}Zn [44], ^{48}Ni [45] and ^{67}Kr [46] were found in an analogous way.

The measurement of individual proton energies and angles between the particles requiring new detection techniques led to the construction of several time projection chambers, further discussed in Chapter 2. Measurements of the angle between emitted protons and their energies have been performed for ^{45}Fe [52], [53], ^{54}Zn [54] and ^{48}Ni [55] with 75, 7 and 4 total number of events respectively. These nuclei are still difficult to produce by the current techniques, and only in the first case the statistics is enough to lead to a more advanced comparison to the theoretical predictions.

1.9.2 Two proton decay models

The two-proton decay, happening beyond the proton drip lines, as mentioned in 1.9, is very complex to describe. Three different aspects need to be taken into account for a complete explanation of this radioactivity process: inner structure of the nucleus, coupling with the continuum, since the system is already an unbound system, and the three-body decay dynamics. The description of each of these features for a system very far from the stability is already quite challenging itself: the description of internal structure needs, very often, experimental data to constrain the models, which is not possible for such exotic nuclei. Since the system is beyond the proton drip line, a consistent description of the internal and external

wave functions is needed to reproduce the interplay between bound states and continuum regions of the nucleus. Finally, the three-body nature of the decay adds up an extra complexity to the description of the 2-proton emission process, because interaction between the three-bodies need to be taken into account at once. Some models have been developed, focusing on one or several aspects of this decay mode, as it is schematically shown in Figure 1.20.

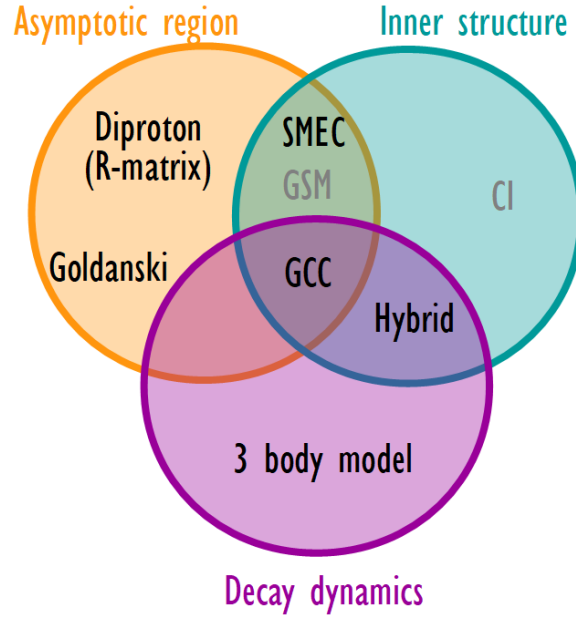


Figure 1.20: Schematic classification of the main theoretical models used to describe the two proton decay process (labelled in black) depending on the described main features: structure of the nucleus, asymptotic behaviour and decay dynamics. The models labelled in grey are used to develop new approximations, but not directly for the two proton decay description (See text). (Scheme inspired from Figure 7 in [50]).

Some models have been developed, focusing on one or two of the three main aspects of this decay mode: inner structure, coupling with the continuum (treatment of the asymptotic region) and decay dynamics, as it is schematically shown in Figure 1.20. Depending on their nature, they allow for the prediction of different observables. The different approaches proposed for this complex problem have already been reviewed in [32] and more recently in [50] and [56]. Some of the most important theoretical models are summarized and described in this work following a chronological order, trying to keep a connection with the experimental observables.

First description by Goldanski

Apart from predicting the two proton decay in 1960, Goldansky provided the first theoretical description of the process. He considered a potential barrier $V(r)$ (represented in Figure 1.21 with nuclear $V_{nuc}(r)$ and Coulomb $V_{coul}(r)$ components). The centrifugal term $V_l(r)$ was assumed to be zero.

The nuclear term is approximated by a potential well ($V_{nuc}(r) = -V_0$) for $r < r_N$ where r_N is the potential range and the Coulomb term is written:

$$V_{coul}(r) = \frac{(Z-2)e^2}{r_N} \quad (1.8)$$

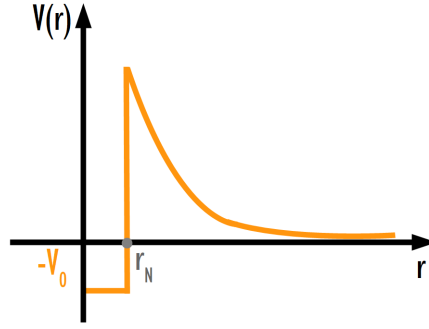


Figure 1.21: Potential approximation made by Goldanskii, composed by a potential well for $r < r_N$ and a Coulomb term for $r > r_N$. (Schematic, the nuclear term is in reality around ten times bigger than the height of the Coulomb barrier (6 MeV height) for ^{48}Ni).

Using this simplified potential, he calculated the penetrability factor $w(E)$ of the Coulomb barrier as the product of the relative penetrability factors for the individual protons. Under this calculation, the penetrability of the barrier becomes maximal when the two protons have equal energy. This can be easily understood in terms of individual penetrability factors: if a first proton p_1 with energy E_1 escapes the barrier, the available energy for the second proton becomes $E_T - E_1$, where E_T is the available energy neglecting the recoil energy of the nucleus. The emission of a first proton with large energy will then disfavor the emission of the second one.

The obtained penetrability corresponds to a penetrability factor of a particle with $M=2m_p$ mass, E_T energy and charge $2e$: a di-proton particle (^2He). This simple approach predicts the asymptotic observables of the "pure" $2p$ decay process: the sharing of the energy between the emitted protons and a strong angular correlation between them: the protons are considered to cross the barrier together and split afterward due to Coulomb repulsion, translating into small angles between them, as mentioned in subsection 1.8.

The penetrability factor $w(E)$ is related to the decay width Γ as:

$$\Gamma = \gamma^2 w(E) \quad (1.9)$$

Where γ^2 is the matrix element relating the initial and final states of the process. The decay width is related to the half-life $t_{1/2}$ of the nuclei by the Heisenberg's uncertainty principle:

$$\Gamma t_{1/2} \sim \hbar \quad (1.10)$$

So the higher the penetrability factor (high probability of crossing the barrier) the smaller the half-life of the nuclei and the bigger the decay width value.

Goldansky provided a first list of candidates in the $Z=8-36$ mass region [25] by calculating their half-lives. He estimated a lower limit for the half-life from which the process can be observed (order of 10^{-12}s).

This first qualitative description of the "pure" two proton radioactivity made by Goldansky already claimed that the observables may be affected by the inner structure of the initial nucleus. Since then, multiple theoretical approaches have been proposed aiming to provide a self-consistent explanation for such an exotic process.

Three-body decay (decay dynamics)

At the beginning of 2000 a model focused on three-body decay dynamics of the 2p process was proposed by Grigorenko et al. [57] using the hyperspherical harmonics method. Under a simultaneous emission hypothesis, the system is considered to be formed by a core (daughter nucleus) and the two emitted protons (3-body problem). The proton-proton interaction is approximated using a Gaussian potential, and the proton-core interaction is defined with a Woods-Saxon potential. Although no explicit internal structure of the emitter is taken into account in the model, by varying the orbital momentum l in the defined proton-nucleus ($p-N$) and proton-proton ($p-p$) potentials, the structure of the emitter can be artificially modified. Different calculations are thus performed for several values of l (different configurations) aiming to study the induced effects on the calculated observables and the emission dynamics. The three-body model is the first one predicting the fraction of energy of each emitted proton with respect to the total available energy E_T (E_p/E_T) and the angular distribution between them Θ_{pp} depending on the initial configuration of the emitter. By comparing the different 3-body calculations with experimental values, the configuration mixing in the wave function can be inferred. Such an estimation has been performed for ^{45}Fe and ^{54}Zn in [52] and [54] respectively.

The three body decay approach provides a valuable theoretical input, although the structure and the continuum effect of the two proton decay are not fully taken into account in the model. The theoretical calculation of new observables motivated further advanced experimental measurements of the two proton decay process.

Di-proton emission (asymptotic region)

Other calculations of 2p decay widths (Γ) were performed by Barker in 2001 using the R-matrix formalism [58]. Within this framework, the decay process is considered as an interaction of a (frozen) core and a system formed by the two protons (di-proton mechanism of emission assumption). The space is further divided in two regions: an internal region in which all potentials (nuclear, Coulomb and centrifugal components) are taken into account and an external region, defined from the potential range (r_N) in which the short-range nuclear contribution is neglected. An extra factor taking into account the relative energy of the two protons (needed energy to form a di-proton) is also added to the model. Solving the Schrödinger equation under these assumptions, the 2p decay width can be calculated.

The comparison of experimental half-lives with the predictions made with the R-matrix model serve, first, to validate the hypothesis of the di-proton emission and to study the relative energy of the system. This model providing a good description of the asymptotic region does not take into account the internal structure of the nucleus nor the 3-body decay dynamics because of the initial assumptions.

Shell Model Embedded in the Continuum (inner Structure + asymptotic region)

At the beginning of the 2000 the Shell Model Embedded in the Continuum (SMEC) was introduced as an extension of the interacting shell model or Configuration Interaction (CI). Although CI is a very successful model in nuclear theory, it cannot be used for the description of open quantum systems like the two proton decay. The SMEC approach [59] was consequently introduced to extend the CI model to the continuum, aiming to study weakly bound systems. The interaction with the continuum is quantified in the model with a parameter called the coupling constant to the continuum that it is inversely related to the half-life value: for a stronger coupling with the environment, the probability of interaction (decay) is bigger, so that the half-life becomes smaller.

In 2005, it was employed for the first time for the description of two particles in the continuum [60] and further applied to the two proton decay from the ground state in 2006 [61] allowing for the calculation of decay widths of different nuclei (^{45}Fe , ^{54}Zn and ^{48}Ni). The calculations were performed for different approximations of the coupling constant to the continuum and individually for direct emission and sequential emission hypotheses. The experimental comparison of the estimated values allowed to find the coupling constant and the mechanism of emission, reproducing better the experimental decay widths.

GCC model (inner structure + asymptotic region + decay dynamics)

The Gamow Shell Model (GSM) [62], [63] approach has been widely employed for the description of weakly bound systems along the drip-lines. This model belongs to the continuum-embedded framework: internal structure and asymptotic behaviour of the system are considered for the description of the studied processes.

The Gamow coupled-channel method (GCC) [64], developed in 2017, is an approach of the GSM in which three-body correlations are included. It is therefore the first model that takes into account the three main aspects of the two proton emission decay: internal structure, asymptotic behaviour and three-body decay dynamics. Separation energies, decay widths and nucleon-nucleon angular correlations for ^6He , ^6Li and ^6Be were predicted in [64] in order to benchmark the GCC approximation with the GSM model. Within this model, the decay width and the angular correlations between the nucleons are calculated for different strengths of the interaction between the protons. By comparing with experimental results, this interaction can be quantified.

Hybrid model (Structure+3 body dynamics)

To take into account the detailed structure of the nucleus and the three-body dynamics of the two proton decay, a hybrid model was developed in 2019 [65] as a combination of configuration-interaction (CI) calculations and the emission dynamics from the three-body approach by studying the penetrability of the barrier. The calculation is performed for different initial configurations (calculated decay widths from 3-body model). For the same configuration, the results are obtained by summing coherently or incoherently the different amplitudes (calculated from CI model) contributing to the emission. By comparing the different calculations with the experimental data, the best agreement is found for the results obtained by the incoherent sum of the different nucleon decay amplitudes contributing to the emission process with a s^2 contribution. As in the three body model, the comparison to experimental data allows inferring the mixing in the wave function. The half-lives of 2p emitters evaluated with the hybrid model agree with experimental data for ^{45}Fe , ^{48}Ni and ^{54}Zn .

A summary of these models indicating the observables that can be predicted in each case and the information that can be extracted from them can be found in Table 1.2.

Inconsistencies with experimental measurements and recent theory inputs.

The half-lives calculated using the models mentioned previously are in agreement for the available ^{45}Fe , ^{54}Zn and ^{48}Ni experimental information. Furthermore, the angular distribution prediction for ^{45}Fe by the three-body model is in agreement with the experimental results [52]. More recently, in 2016, an experiment was performed to study the decay of ^{67}Kr (using a similar silicon-based setup as the mentioned ones in section 1.9.1). The half-life was found to be 20 times lower than expected by any of the mentioned theoretical approximations [46].

Model	Observable	Information
Goldansky	$\Gamma, E_p/E_T, \Theta_{pp}$	Di-proton emission hypothesis.
3-body	$\Gamma, E_p/E_T, \Theta_{pp}$	Direct emission hypothesis, structure mixing of WF
Di-proton	$\Gamma, E_p/E_T, \Theta_{pp}$	Di-proton hypothesis, energy of the system.
SMEC	Γ	Coupling constants, direct/sequential hypothesis
D-GCC	Γ, Θ_{pp}	Two body interaction strength V_{pp}
Hybrid model	Γ	Direct emission, structure mixing of WF

Table 1.2: Summary of the models described in the text. The observables that can be predicted by each of them Γ (decay width, $\Gamma = \frac{\hbar \ln 2}{t_{1/2}}$), fraction of energy of a single proton E_p/E_T and angular distributions between protons Θ_{pp} and, in the third column, the information that can be obtained from each model when comparing to experimental values. The grey color in some observables denotes a "quantitative information".

This discrepancy inspired to revisit some of the theoretical models. Two new different hypotheses have been proposed to explain this discrepancy: the first one suggesting the ^{67}Kr emission to be a transition between a real two proton emission and a sequential decay (Semi-analytical R-matrix calculation, L.V.Grigorenko et al., 2017). The second one proposing the deformation of the nucleus to be responsible for the low measured half-life (deformed GCC model (D-GCC) S.M Wang., W. Nazarewicz [67], 2018). The former one predicts energy correlations for the emitted protons of ^{67}Kr and a half-life estimate. The calculations are performed for different two-body resonance energies. The deformed GCC model (D-GCC) predicts partial decay widths and two proton angular distributions as a function of the deformation and the strength of the proton-proton interaction. The calculations of the deformed GCC framework are performed for ^{48}Ni (benchmark of the model due to its spherical structure) and ^{67}Kr .

Both models provide a half-life value for ^{67}Kr that is compatible with the experimental result. However, the predicted angular distributions¹ for ^{48}Ni differ from one model to the other, not being compatible between them, as illustrated in Figures 1.22 and 1.23. In the three body approximation, the angular distribution between the protons is expected to be centered around 60° with a wide range of values (from 10° to 100°) but bigger angles are discarded. The GCC model predicts a first maximum at small angles around 25° , a small one at larger angles (140°). Experimental measurements are needed to validate the assumptions made by the different models in order to understand the disagreement between them.

The available (experimental and theoretical) information from ground state two proton emitters is summarized in table 1.3. This table calls for new experimental measurements and for further theoretical approaches to complete the information of the known two proton emitters. Angular and energy distribution calculations with the D-GCC method for the already measured ^{45}Fe nucleus could be a good start to verify the assumptions made by this model. As mentioned in section 1.9.1, the proton energies and angular distributions have been measured with sufficient statistic only for ^{45}Fe . Further advanced experiments for the proton emitters (^{48}Ni , ^{67}Kr and ^{54}Zn) are required to disentangle the nature of the inconsistencies and to verify the assumptions made in each model intending, at a last stage, for a full comprehension of the two proton radioactivity process.

¹extrapolated from the ^{54}Zn results in the 3-body case

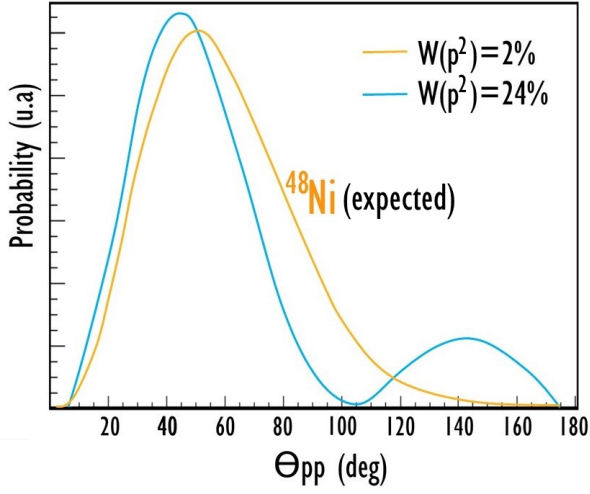


Figure 1.22: Angular distribution predicted for ^{54}Zn by the three-body model [54] for different contributions of the p^2 wave function. In the case of ^{48}Ni , no contribution of the p^2 is expected because of its closed shell. Consequently, the predictions for $W(p^2)=2\%$ (in orange) can be interpreted as the expected angular distribution for ^{48}Ni .

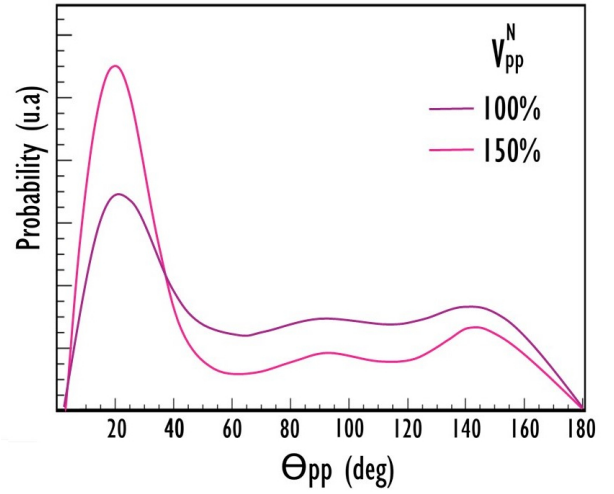


Figure 1.23: Angular distribution predicted for ^{48}Ni by the GCC model [67]. The calculation is made for different percentages of the proton-proton interaction V_{pp}^N . The reference value (100%) in purple corresponds to the finite-range Minnesota force with parameters defined in [68]. The pink curve corresponds to an increased strength of 50% with respect to the standard strength.

Model	$\Gamma, t_{1/2}$	E_p/E_T	Θ_{pp}
R-matrix	$^{45}\text{Fe}, ^{48}\text{Ni}, ^{54}\text{Zn}, ^{67}\text{Kr}$	shared energy	small angles
3-body	$^{45}\text{Fe}, ^{48}\text{Ni}, ^{54}\text{Zn}, ^{67}\text{Kr}$	$^{45}\text{Fe}, ^{48}\text{Ni}, ^{54}\text{Zn}, ^{67}\text{Kr}$	$^{45}\text{Fe}, ^{48}\text{Ni}, ^{54}\text{Zn},$
SMEC	$^{45}\text{Fe}, ^{48}\text{Ni}, ^{54}\text{Zn},$	-	-
D-GCC	$^{48}\text{Ni}, ^{67}\text{Kr},$	-	$^{48}\text{Ni}, ^{67}\text{Kr}$
Hybrid model	$^{45}\text{Fe}, ^{48}\text{Ni}, ^{54}\text{Zn},$	-	-
Experimental value	$^{45}\text{Fe}, ^{48}\text{Ni}, ^{54}\text{Zn}, ^{67}\text{Kr}$	^{45}Fe	^{45}Fe

Table 1.3: Theoretical and experimental available information for the main ground state two proton emitters: decay width or half-life ($\Gamma, t_{1/2}$), fraction of energy of a single proton E_{pp}/E_T and angular distributions between protons Θ_{pp} . In the three-body model, the orange color denotes the possibility of extrapolation for the ^{48}Ni , since no calculation is performed at the moment for this nucleus.

1.10 Motivation of the study of the ^{48}Ni decay products

The double magic ^{48}Ni nuclei, with 28 protons and 20 neutrons, is of special interest for the study of the two proton radioactivity since it is the only nucleus for which theoretical angular distributions are available from two different models at the current stage, as shown in Table 1.3. Besides, they do not predict the same results. The ^{48}Ni structure is probably the easiest case to treat because of its spherical shape. This characteristic makes it a benchmark case for the development of the deformed-GCC calculations made for ^{67}Kr , which is the most recent and the only model taking into account the three different aspects of the two proton emission process: internal structure, coupling with the continuum and three-body decay dynamics. Measurements of the proton angular distribution of ^{48}Ni can thus validate the main hypothesis made within this model.

In addition to the motivation of measurement concerning the two proton emission, the ^{48}Ni nuclei, considered the most proton-rich isotope ever identified, presents interesting characteristics with respect to other nuclei which could help to understand other aspects of nuclear structure: if the shell closure of ^{48}Ni is established, the Ni isotropic chain is by now the only one to host three doubly magic nuclei: ^{48}Ni , ^{56}Ni and ^{78}Ni . Also, ^{48}Ni is the only case of a doubly magic nucleus where the mirror nucleus (^{48}Ca) is stable. The mirror pair ^{48}Ni - ^{48}Ca offers a unique chance to study isovector effects in the $f_{7/2}$ shell.

All these particularities together with the fact that the ^{48}Ni production is accessible in the GANIL facility nowadays, motivated to perform an experiment (see Chapter 3) aiming to produce such a nucleus and study its decay products using ACTAR TPC, a time projection chamber detector (TPC). This device, described in the following section, is suitable for experiments aiming to study multiple particle decays. Individual proton energies and angles of emission between the emitted particles can be obtained.

Chapter 2: ACTAR TPC



Contents

2.1	Gaseous detectors in nuclear physics	52
2.2	Recent TPC developments in nuclear physics	54
2.3	ACTAR TPC	56
2.3.1	ACTAR TPC chamber	58
2.3.2	Effective volume: drift region, detection plane	58
2.3.3	Extraction of the signal: metallic-core PCB and connection to the electronics (ZAP! boards)	60
2.4	GET electronics	61
2.4.1	AGet chip	62
2.4.2	GET trigger.	64
2.4.3	GET decision logic for E791	64

The current chapter is devoted to the ACTAR TPC detector device. First, a brief review of gaseous detectors, their main operation principles and uses in nuclear physics are described in Section 2.1. The physics motivation for further TPC developments and some highlighted examples are discussed in Section 2.2. Within this context, the description of the ACTAR TPC device will be carried out in two main parts: the characterization of the detector and the description of the GET electronics in Sections 2.3 and 2.4 respectively.

2.1 Gaseous detectors in nuclear physics

Historically, one can say that gaseous detectors have been used since the beginning of nuclear physics. The cloud chamber can be considered as the first example of a gaseous detector. It aimed at visualizing charged particle tracks, and it served to prove the existence of particles such as the positron [69], the muon [70] and the kaon [71] in 1932, 1936 and 1947 respectively. Since then, multiple gaseous detection devices have been developed with well-awarded results receiving multiple Nobel Prizes: In 1927 (Arthur H.Compton) for the discovery of the Compton effect by using a cloud chamber [72], later in 1960 for the invention of the Bubble Chamber by Donald A.Glaser [73] and in 1992 for the development of the Multi-Wire-Proportional Chamber by Georges Charpak [74].

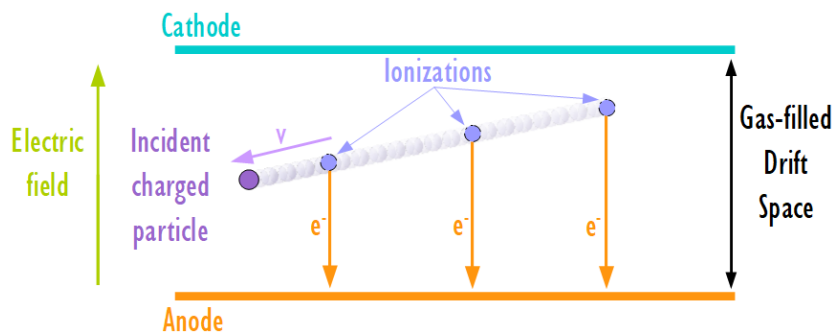


Figure 2.1: Gas detector operation principle. The charged particle travelling in the gas volume (violet dot) ionizes the gas along its trajectory, creating electron-ion pairs. The electrons drift in the inverse direction of the applied electric field (orange arrows) until reaching the anode, where their signal is collected.

The operation principle of any gas detector is based on the ionization of the gas molecules when a charged particle crosses a detection volume. During this process, electron-ion pairs are created. By applying an electric field, the produced electrons and ions drift toward the electrodes on which their signal is collected. This process is illustrated in Figure 2.1. A gaseous detector can operate in different regimes depending on the applied electric field as shown in Figure 2.2: ionization mode, proportional mode, limited proportional mode and Geiger mode. In ionization mode, all primary ionization electrons are collected on the electrode, the measured charge thus corresponds to the induced signal. In proportional mode, the electrons accelerate under the influence of an electric field and eventually get enough kinetic energy to further ionize gas molecules, creating electron avalanches. The measured signal is proportional to the initially generated signal and depends exponentially on the applied electric field. In limited proportional and Geiger modes, the measured signal does not correspond anymore to the particle energy deposit. These two last regimes are used for counting particle purposes. In the other extreme, if a very low electric field is applied, the drifting electrons can be captured by gas molecules, resulting in a loss of signal compared to the energy deposited. This process is called attachment.

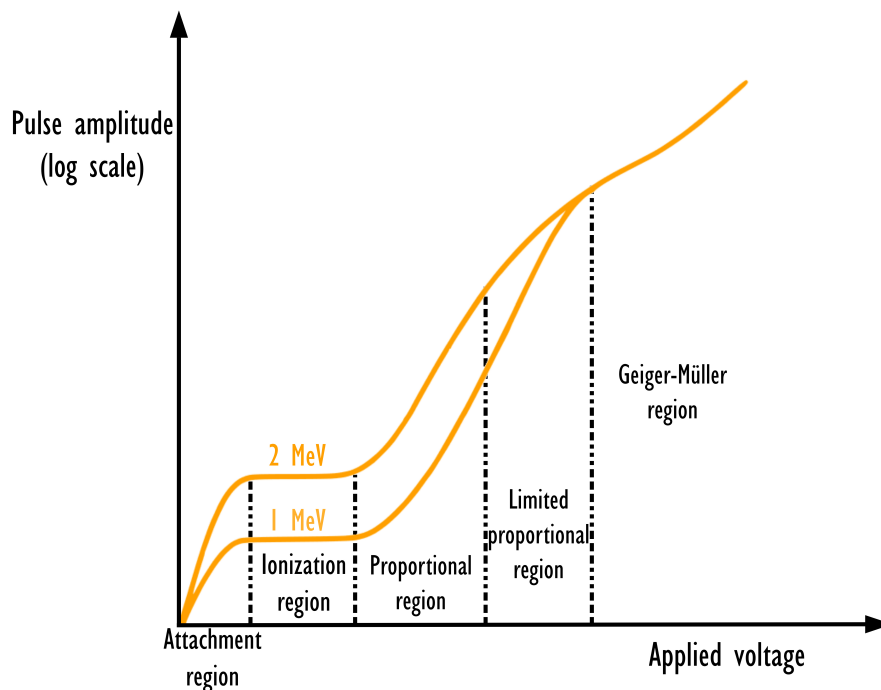


Figure 2.2: Different working regimes of gaseous detectors. The pulse amplitude depending on the applied voltage is plotted for particles depositing energies of 1 MeV and 2 MeV (Image inspired from G.F. Knoll. [76]).

In 1968, a revolutionary gaseous detector, the Multiwire Proportional Counter (MWPC) in which the position of the track could be reconstructed for the first time, was conceived by Georges Charpak. The MWPC is a gaseous detector working in proportional mode in which multiple wires are located in a detection plane. These wires are polarized, resulting in a high electric field in their vicinity, therefore creating an avalanche effect. The charge is further collected on these wires and used to reconstruct the trajectory of the traversing particle. Almost at the same time, the idea of measuring the electron's drift time to get spatial information lead to the first studies made with a Drift Chamber (DC) by Bressani, Charpak, Rahm and Zupancic in 1969 [77]. The next obvious step, the invention of the Time Projection Chamber (TPC) came in 1975 by David Nygren [78], as a combination of a DC and an MWPC detector, consisting of a large gaseous drift space terminated by one or several Multi Wire Proportional Chambers.

The gaseous detectors have been widely used in nuclear and particle physics. In general, they present high detection efficiency, relatively good time resolution and limited radiation damage effects. On the other hand, due to the fact that an avalanche is a statistical process, fluctuations on the collected charge are induced, limiting the energy resolution. Gaseous detectors are versatile devices since their effective thickness can be easily adjusted by changing the pressure of the gas. By modifying the applied voltage, the detector can also become transparent to low energy particles (i.e. β particles). Depending on the goal of the measurements, apart from the general characteristics mentioned above, the choice of the use of a gaseous detector can be justified in different ways. Some examples are listed below for the main nuclear physics uses of gaseous detectors.

Particle counting and position: simple gaseous detectors consisting of a gas-filled volume between two parallel plates with a differential of potential are used for these purposes. They present good rate handling capacities due to fast signal collection and good time resolution because of their reduced thickness. Due to the lower material density, they are more transparent than solid state detectors. If some strips are added to these detectors, the information about the traversing position can be obtained as well. Furthermore, these detectors are usually thin and easy to install.

Energy loss measurements and particle identification: when the deposited energy is measured, because of the generally large gas thickness, the specific energy loss $\frac{dE}{dx}$ of the ionizing particles in the gas along the track can be measured, adding particle identification capabilities. This is the main use of ionization chambers.

Tracking: the main advantage of gaseous detectors against solid ones for tracking purposes is the 4π solid angle detection. It becomes particularly interesting for the study of reactions with the gas (Active Target Mode). By doing so, the reaction vertexes can be determined, which is not possible with solid detectors. Furthermore, in the case of TPCs, by recovering the third dimension from the drift time of the electrons, a full 3D reconstruction of the trajectories can be achieved resulting into a more performant tracking of the particle.

2.2 Recent TPC developments in nuclear physics

A time projection chamber (TPC) is a device that allows for a 3D track reconstruction. It consists of a (large) gaseous drift space in a uniform electric field (ionization regime) and a narrow amplification region (proportional regime) close to the detection plane, as illustrated in Figure 2.3. When the particle traverses the volume, it ionises the gas, and the electrons drift towards the amplification region and the detection plane. From the drift time information, the third dimension is reconstructed. The TPC is a powerful tool for particle identification and tracking in the detection volume. It allows determining vertexes in reactions and emission angles that are not easy (and sometimes even impossible) to determine with solid detectors.

A TPC can work in the "Active target mode" when the gas is employed as a target to produce specific reactions. In nuclear physics, this working mode of the TPCs was developed to study reactions involving unstable nuclei, as reviewed in [79] and [80]. When studying these exotic nuclei, the beam intensities that can be reached are reduced. Active Target detectors compensate this relatively low intensity beams: they do not present major losses of resolution by using thicker targets than solid detectors, and they have a high detection efficiency. These two characteristics make them powerful tools for both direct and inverse kinematics experiments, becoming sometimes the only feasible way of measurement.

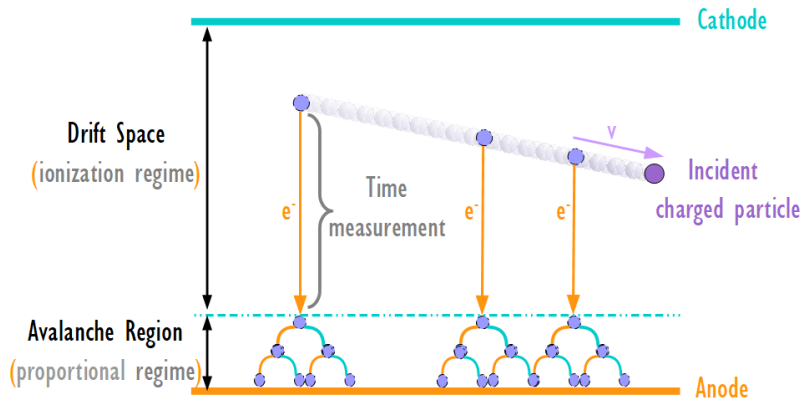


Figure 2.3: TPC detector operation principle. The large drift space is used to measure the drift time of the electrons, from which the third dimension can be reconstructed. The drifted electrons will create discrete avalanches in the proportional region close to the detection plane where the signal is measured.

In nuclear physics, there are mainly two motivations that boosted the development of more performant time projection chambers: the measurement of short half life nuclei decay products (protons) from exotic nuclei and the study of nuclear reactions in inverse kinematics for nuclei far from stability (active target mode experiments).

Depending on the origin of the motivation, some more recently developed TPCs can be highlighted such as MAYA, built at GANIL (2003) [81] and AT-TPC built at NSCL for active target measurements purposes [82]. Within the decay measurements, the CENBG TPC (2005) [83] and the Optical TPC (O-TPC) built in Warsaw (2007) [84] can be pointed out. Both aimed to measure the individual proton energies and the angular distribution for two proton radioactivity and other multi-proton decays. Astrophysical interest of measuring β delayed proton emitter decays with no β background also lead to the construction of TPCs in this field, such as AstroBox (2013)[85]. While in general, the time projection chambers, built to measure in

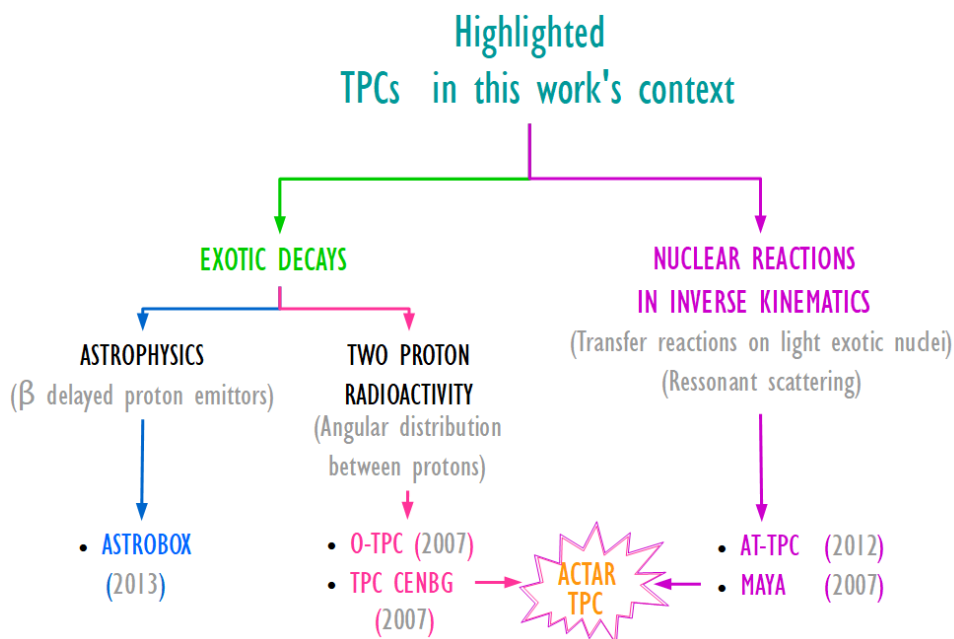


Figure 2.4: Scheme of highlighted recent TPCs designed depending on their goals.

active target mode (MAYA, AT-TPC) are not optimized to work in decay mode and the ones built to measure decay products (CENBG TPC, O-TPC, AstroBox) are not adapted to perform measurements in active target mode, ACTAR TPC is a more versatile tool: it is suitable to perform experiments in both modes.

2.3 ACTAR TPC

The Active TARget and Time Projection Chamber (ACTAR TPC) consists of a large drift volume in which the detector works in ionization mode followed by an **amplification micromegas** system of $128\ \mu\text{m}$ [103] (proportional regime) close to the anode and the detection plane. The detection plane ($256 \times 256\ \text{mm}^2$) is segmented in $2 \times 2\ \text{mm}^2$ pads. Consequently, the produced avalanches create significant signal only on the closest pads. The collected signals are sampled in time for a full 3D reconstruction. In the **active target mode**, the gas in the chamber is used as a target to produce a desired reaction with the beam. In the **decay mode**, the gas is simply used as a thick stopper of the radioactive beam to then measure the following decays. In the present work, ACTAR TPC is used in decay mode, the ions of interest are stopped and detected in the gas volume together with the decay products.

The ACTAR TPC device was born as the fusion between two different projects that developed two different time projection chambers: MAYA, built at GANIL [81] aiming to study direct and transfer reactions of exotic beams on light particles targets (Active Target Mode experiments [86] – [90]) and the CENBG TPC [91] developed at the LP2iB (Laboratoire de Physique de 2 Infinits Bordeaux) to study exotic decays in the neutron deficient region such as two proton or beta delayed proton emission (Decay mode experiments [54], [92]). ACTAR TPC was built at GANIL in collaboration with LP2iB, KUL (Katholieke Universiteit Leuven), USC (Universidad de Santiago de Compostela) and IPNO (Institut de Physique Nucléaire d'Orsay). The main progress with respect to MAYA and CENBG TPC is the fact that each pad from the segmented 2D detection plane is equipped with digital electronics for time sampling. The high number of involved channels resulted into a specific electronics development (General Electronics for TPCs (GET)) [105]. The first front-end electronics board became available in 2014 for signal processing tests [93]. Some years after (2015 and 2016) two different 8-times smaller demonstrators (32×64 pads) of the device were built in GANIL [94], [95] and LP2iB [96] respectively to validate the correct operation of the ensemble. The first ACTAR TPC full size (128×128 pads) experiment in Active Target Mode "Commissioning of the Active TARget and Time Projection Chamber (ACTAR TPC)" [97] was performed at GANIL in 2017. It aimed to study the $^1\text{H}(^{18}\text{O}, ^{18}\text{O})^1\text{H}$ resonant reaction. In 2019, the first decay mode experiment (study of proton emissions from $^{54\text{m}}\text{Ni}$ and $^{53\text{m}}\text{Co}$ [98]) took place at GANIL.

The experiment of the present work, **^{48}Ni two proton emission**, was performed at GANIL in 2021, after being cancelled in 2020 due to COVID-19 pandemic. Other experiments have been performed in 2022 in Active Target mode: the study of the $^{20}\text{O}(d, ^3\text{He})^{19}\text{N}$ transfer reaction, and together with other detectors (PARIS-EXOGRAM, ZDD) ACTAR TPC has been used to perform other experiment aiming to study the loss of magicity in the neutron rich Silicon isotopic chain through the measurements of $^{34,36,38}\text{Si}(p,p')$ reactions. Other experiments (both in Active Target mode and decay mode) have been already accepted at TRIUMF (Measurement of states of ^{21}Al [99] and ^{17}F proton elastic scattering experiments [100]) and RIKEN: two proton emission from ^{67}Kr [101] and proton emission from ^{68}Br , ^{72}Rb , ^{89}Rh , and ^{93}Ag [102].

ACTAR TPC Timeline

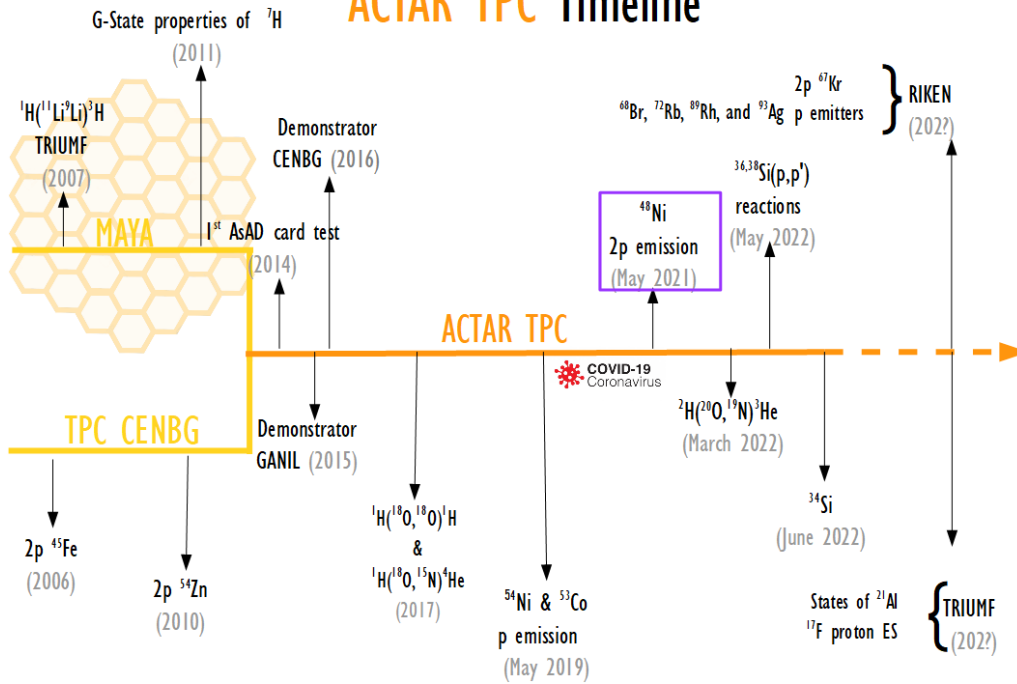


Figure 2.5: ACTAR TPC timeline. In the left yellow part, the main experiments from both MAYA [87], [89], and CENBG TPC [91], [54] together with their dates are shown. In the continuous orange line, the main ACTAR TPC tests for the electronics, both of the demonstrators, and all the experiments that have been performed can be found. Finally, on the dashed part of the timeline, some already accepted future experiments are shown.

The ACTAR TPC detector will be described in the three following subsections: the first one (2.3.1) consists of a general description of the chamber structure. The second one (2.3.2) contains the characterization of the main elements in the effective volume: the drift region and the detection plane. Finally, the last subsection (2.3.3) is dedicated to explain the extraction of the signal and the connection to the electronics.

2.3.1 ACTAR TPC chamber

The ACTAR TPC chamber consists of a stainless steel structure of $606 \times 606 \times 360 \text{ mm}^3$ with two gas inlet and outlet located at opposite corners in the bottom and top of the structure respectively and some feed-through for voltage power supplies (bottom), pulser input signal and signal extraction (top). The flanges are made of 1.5 cm thick aluminum. They minimize the possible deformation due to the internal and external pressure differences. The bottom flange has different holes: to introduce a source in the chamber if needed for tests and to connect a turbo pump, useful for vacuum cleaning before the gas filling process. In the front flange, on the incoming beam side, there is also a hole of 100 mm of diameter in which a "nose" holding an entrance window of 45 mm diameter is mounted. The full chamber rests on a metallic structure that allows to change and fix the horizontal and vertical positions of the detector to better perform the alignment with respect to the beam line. The readout electronics is separated from the detection plane because of geometrical constraints. A large arched steel structure holds it on the top part of the chamber. The sides of this structure are equipped with small ventilators meant to cool the electronic boards.

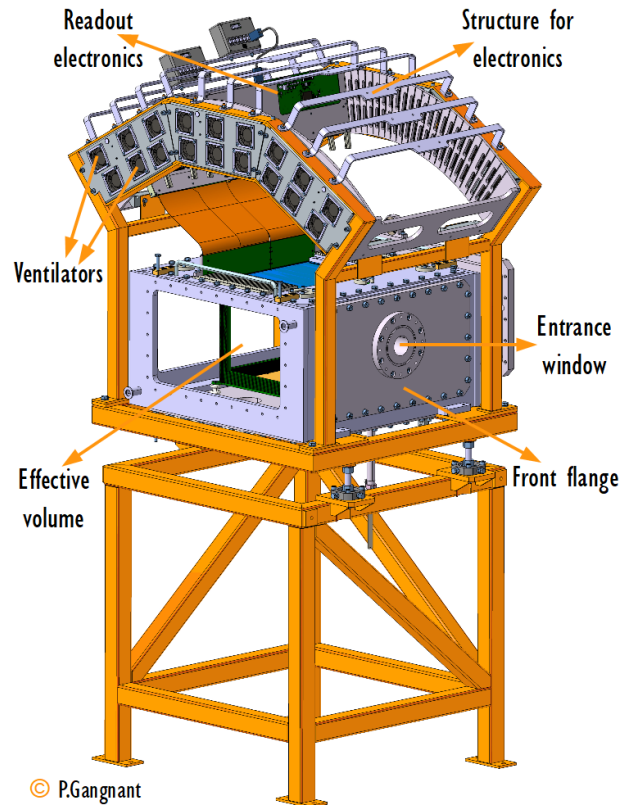


Figure 2.6: Drawing of the ACTAR TPC chamber and main components of the structure.

2.3.2 Effective volume: drift region, detection plane

The main elements of ACTAR TPC for the ionization and detection processes are located inside the effective volume. The ionization volume ($295 \times 295 \times 255 \text{ mm}^3$) is surrounded by a double-wire field cage and the cathode and anode. The signal collection is performed in the detection plane (pad plane), located on the top part of the chamber.

The double-wire field cage and the cathode are placed on the bottom plate, held by four ceramic insulating pillars as shown in Figure 2.7. The field cage ($295 \times 295 \times 255 \text{ mm}^3$) consists of a first internal cage made of copper wires of $20 \mu\text{m}$ diameter with 1 mm pitch and an external one with 2 mm wires pitch, connected through $4.7 \text{ M}\Omega$ resistors, ensuring a constant degradation of the potential to produce an uniform vertical electric field. The field cage is transparent to particles escaping the volume. This allows for the installation of additional detectors around the volume. The choice of a double-wire field cage was done in order to minimize field deformations inside the effective drift region, as explained in [95].

The detection plane (pad plane) and the anode are placed on the top flange. The pad plane consists of 128×128 pads of $2 \times 2 \text{ mm}^2$ (a total of 16384 pixels). It is equipped by a micromegas amplification system of $128 \mu\text{m}$ gap manufactured by the CERN PCB Workshop [103]. The Micromegas (MICRO-MESH Gaseous Structure) is a proportional counting-type amplification system. It consists of a thin metallic grid lying

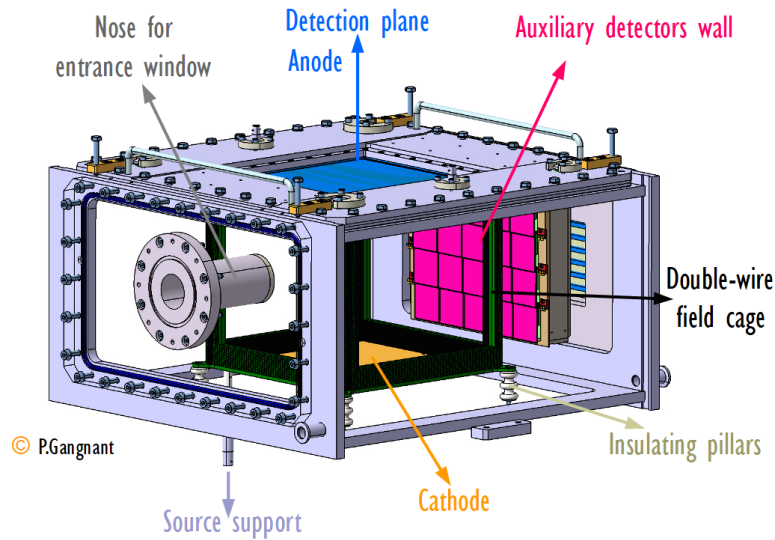


Figure 2.7: Illustration of the effective volume of ACTAR TPC and its main elements described in the text.

above the detection plane. This grid is called micromesh. It is made of stainless steel wires of $18\ \mu\text{m}$ diameter and $45\ \mu\text{m}$ pitch. The micromesh is held by insulating pillars to the anode (pad plane), creating the amplification gap and separating the low field drift region from the amplification region. An illustration of the micromegas is shown in Figure 2.8.

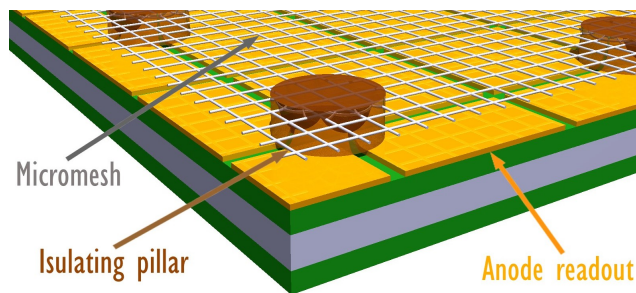


Figure 2.8: Illustration of the micromegas components. The micromesh in grey held by the pillars (dark red) to the pad plane.

The applied voltage between the micromesh and the anode produces a few tenths of kV/cm electric field. Each electron will gain enough kinetic energy between collisions to be able to further ionize the gas, creating an avalanche that generates the signal in the anode. Since the amplification gap is small, the image of the avalanche on the anode is small. This translates into a good spatial resolution. The amplification gap in the case of ACTAR TPC ($128\ \mu\text{m}$) is bigger than the ones used in standard micromegas detectors ($50\ \mu\text{m}$). Since ACTAR TPC involves measurements at low pressure, a larger amplification gap is needed to compensate for the longer ionization mean free path of the electrons in the gas (a higher gain needed). The amplification or gain depends on the gas characteristics and the applied electric field.

When using ACTAR TPC it is possible to adjust the gain independently in different regions of the pad plane by applying a voltage on the pixels. For some experiments in which the central part is used to measure the beam energy and the rest of the particles are expected to be outside this region, the local gain customization can be crucial. In these cases the pads are negatively polarized, the electric field in the amplification gap results to be locally weaker so that the amplification becomes smaller, avoiding saturation

in regions with huge energy deposit and assuring enough amplification in the rest of the detection plane.

Apart from the main elements described above, the effective volume of ACTAR TPC has some space left so that auxiliary detectors such as silicon detectors can be installed around four of the sides of the drift region. Additionally, in the front flange of the volume, there is a cylindrical nose that minimizes the distance of the incoming beam to the drift region, hence minimizing reactions occurring before the active volume when working in active target mode. All the elements mentioned above are also illustrated in Figure 2.7.

2.3.3 Extraction of the signal: metallic-core PCB and connection to the electronics (ZAP! boards)

The extraction of the signal collected on the pads is done with a specific PCB (Printed Circuit Board), built to overcome two main challenges: to assure a high density of individual connections spaced only by 2 mm and the capability of holding pressure differences (about 1 bar) between the outside and the inside of the chamber. Two different prototypes were studied: a normal multilayer PCB glued on top of a metallic plate [95] and the construction of a metallic-core PCB [96], developed at GANIL and at CENBG respectively. The first prototype required the use of intermediate boards to adapt the pitch to a 2 mm (pad size) one. In order to avoid that, the second solution was preferred.

The outside part of the metallic core PCB plate is made of male connectors spaced by 2 mm, each of them taking the signal of one single pad. This external part of the PCB is called FAKIR (in reference to a bed of nails). An illustration of a part of the PCB is shown in Figure 2.9.

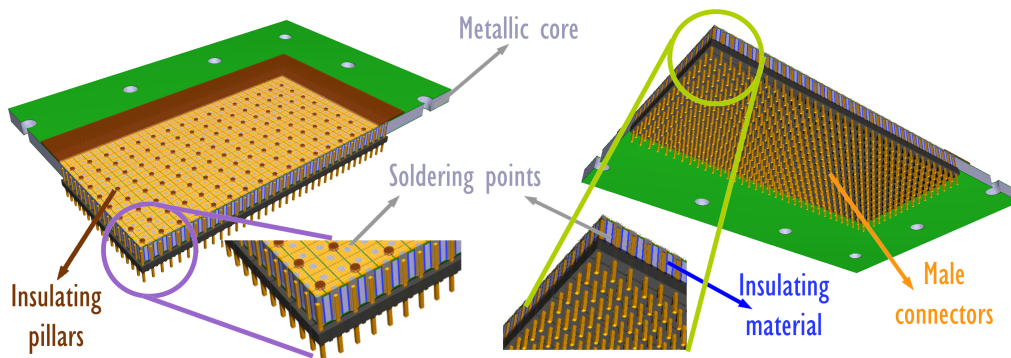


Figure 2.9: View of a part of the pad plane from both sides: internal (left) and external (right) with an indication of its main features.

The connection to the electronics is made by using the ZAP! boards. Apart from being used for signal extraction, they protect the electronics from possible sparks on the pad plane. Both the metal-core-PCB plate and the ZAPs were developed at CENBG [96] and built at CERN and FEDD [104] respectively. They are connected with a Kapton flex cable to the AsAd (ASIC and Analog to Digital Converter) boards as illustrated in Figure 2.10 where the signal is processed and digitized. The full electronics elements and processes are further explained in subsection 2.4.

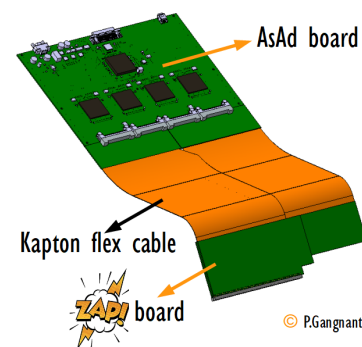


Figure 2.10: Illustration of the elements connecting the pads to the electronics.

2.4 GET electronics

The General Electronics for TPCs (GET) [105], designed for the current generation of time projection chambers and active targets, is a generic acquisition system that can control up to 30000 channels. The first element in the GET electronic system is the AGET chip (Application Specific Integrated Circuit (ASIC) for GET) that will be described in detail in subsection 2.4.1. An AGET chip processes the information of 64 signal channels. Four of them are put together on an AsAd board (ASIC and Analog to Digital Converter (ADC)) where the signal is digitized. The data flux of four AsAd boards is collected in the Concentration Boards (CoBos) that are placed, powered and read in two different Micro-TCA (Micro Telecommunications Computing Architecture) shelves [106] (master and slave) together with a MuTanT (Multi Trigger and Time) module. The trigger and clock from the GET system are given by the master MuTanT module. The shelves are connected at high speed (10 Gb/s) to the data acquisition system. An illustration of the different elements of the GET architecture is shown in Figure 2.11.

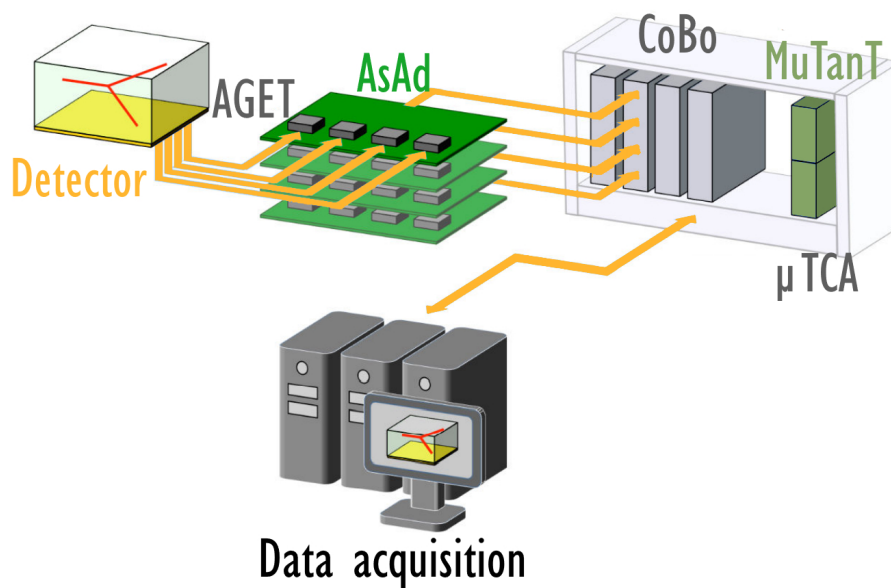


Figure 2.11: GET electronics scheme, including an example of the main elements mentioned in the text. Each of the CoBo boards, located in a μ -TCA shelf, together with the MuTanT module, is connected to four AsAd carts (green), each of them with four AGET chips (grey) that process and record the signal from 1024 pads.

2.4.1 AGet chip

The AGET chip contains the electronics circuits for the processing of the input signals from 64 channels of the detection setup constituting the front end electronics. The signal on each channel is preamplified, shaped and discriminated by selecting some parameter values, which usually can change from one experiment to another. All important electronics parameters described along the subsection and their values in the context of this work are summarized in Table 2.1. A functional scheme for a single channel of the chip is shown in Figure 2.12.

In each AGET chip, in addition to the 64 signal channels, there are four FPN (Fix pattern noise) channels that can be used to suppress the coherent noise of the AGET in an event-by-event basis, as further explained in 4.1.2.

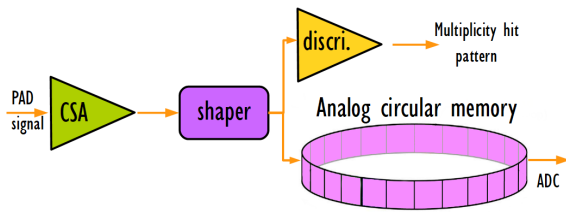


Figure 2.12: One channel signal processing example illustration (see text for details).

The preamplification made with a CSA (Charge Sensitive preAmplifier) can be adjusted fixing the input capacitors C_g so that the full charge range becomes 120 fC, 240 fC, 1 pC or 10 pC. The gain is selected to be 240 fC in the context of this work, a value selected after tests to optimize the proton charge resolution.

The shaping is performed using an analog filter with a peaking time τ that can be modulated from values between 70 ns to 1014 ns.

A large peaking time translates into an improved signal over noise ratio but a worse separation in time in the case of multiple signals within a short time window, (i.e. multiple tracks in the vertical plane). When selecting the peaking time, a compromise between these two effects is pursued. The peaking time τ is set to 334 ns for the current experiment.

The output signal of the shaper (amplified by a gain -2 amplifier) is used to determine whether the channel is hit or not by sending it to a tunable threshold discriminator. Individual thresholds R_{Thr} can be selected by software to determine whether the channel is hit. This value is set to 2.2 % of the full signal range in the current experiment. In "full readout" mode, all the pad signals are read. The readout dead time and the size of the stored data can be reduced if only the channels having a signal over the threshold are stored: the "partial readout" mode. The hit pattern is read by the CoBo board in order to decide whether storing the channel data or not.

The output of the shaper is also sampled in time and stored in a circular analog memory (SCA, Switched Capacitor Array) to be further digitized by an ADC.

Each of the channels is equipped with one of these SCA composed by 512 capacitors (memory spots) in which the signal is written continuously with a tunable frequency W_f from 1 MHz to 100 MHz.

When starting the acquisition, the charge begins to be written cell by cell. While no trigger is received, the charge is overwritten after each complete loop. If a stop signal is received by the SCA, the writing process ends, leading to the reading of the memory content (for one full loop, 512 memory spots). These three stages (writing, overwriting and reading) are illustrated in Figure 2.13. The signal in the SCA is further digitized by the AsAd (ASIC and ADC) boards. As a result, the output data consists of (up to) 512 time samples with a 12 bits amplitude information. After the event reading, the full process starts again.

The stopping signal of the SCA corresponds to the event trigger signal (issued by MUTANT) with an added delay δt , assuring in this way that the full signal is written before the reading takes place, as further illustrated in Figure 2.17.

It is possible to reduce the number of cells to read in the memory (readout depth N) to minimize the readout time and the amount of data. The trigger delay δt , the writing frequency W_f and the readout depth N are adjustable parameters that need to be selected for each experiment conditions, according to the drift velocity of the electrons in the gas. Their values within the context of this work are set to $16 \mu s$, 25 MHz and 256 samples respectively. Consequently, the output data of a channel consists of 256 time samples covering a total range of $10.2 \mu s$.

Due to the channel signal processing described in this subsection by the CSA and the shaper, the output samples are not a direct digitization of the input current distribution. It is possible to reconstruct this information by deconvoluting the data from the response function of the channel electronics, as further explained in section 4.1.5.

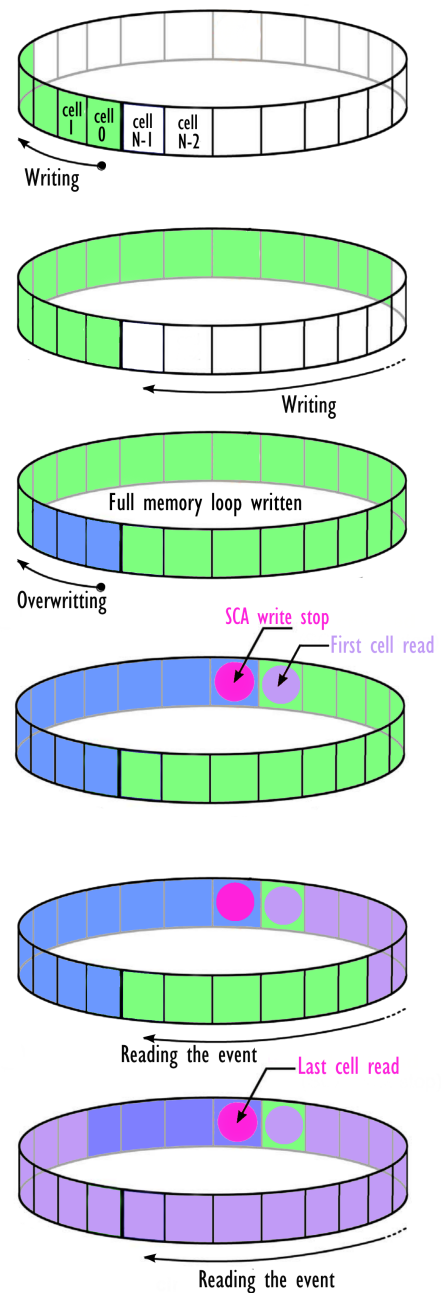


Figure 2.13: Circular memory time evolution. The memory starts to be filled (green) and overwritten (blue) until receiving a write stop signal (pink dot). Then the reading process of the full memory (purple) starts. This process repeats for each event.

2.4.2 GET trigger.

The ACTAR TPC trigger is handled by the MuTanT module. There are three different levels that can be used for the triggering of the GET system: level 0 trigger (L0), consisting of an external trigger, level 1 trigger (L1), an internal trigger taking into account the full multiplicity in the detection plane and the level 2 trigger (L2), delivered after a hit pattern analysis by a dedicated programmed function. In the current experiment, only the two first trigger signals are employed, the L2 level being out of the scope of this work.

During the E791 experiment, the GET system is set in "L0 mode" (triggering made by an external signal). Nevertheless, the L1 signal is used externally, (as further explained in Subsection 2.4.3 and Chapter 3). Therefore, the L1 signal construction process by the MuTanT module is introduced in the following lines.

The individual pad signals after the discriminator are summed, digitized with a 25 MHz frequency ADC and sent to the CoBo modules, where this signal is divided by an average of the observed signal amplitude. A multiplicity signal, result of the sum of these values for all the CoBos (x16) is sent to the MuTanT module, as illustrated in Figure 2.14.

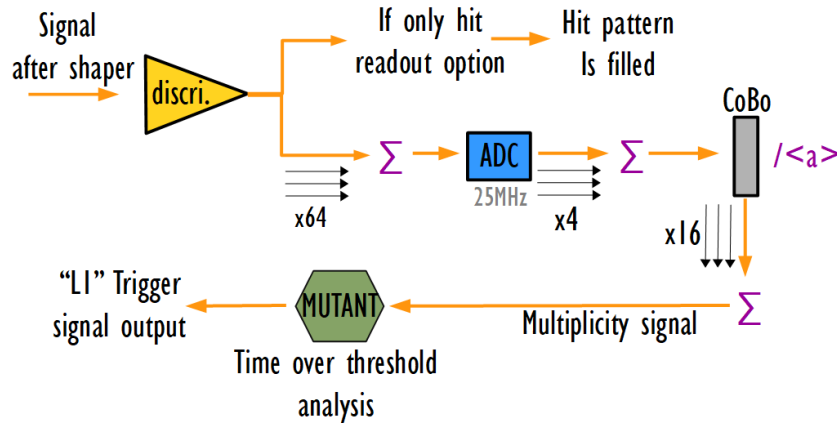


Figure 2.14: Scheme of the L1 trigger signal construction by MuTanT from the single channel signals.

The treatment of this multiplicity signal is based on a time over threshold analysis: in order to generate a trigger, the multiplicity signal has to be above a threshold value M_{Thr} during some time (or equivalently: during a number of time buckets nt_{Thr}). Both parameters are predefined by software. Regarding this experiment, the multiplicity signal is required to be above 15 channel hits during 3 time buckets. This time over threshold analysis is important due to the differences in time and multiplicity for tracks with different vertical angles (i.e. horizontal and vertical tracks with respect to the detection plane). Vertical tracks hit less pads during a longer time compared to horizontal ones, as illustrated in Figure 2.15.

2.4.3 GET decision logic for E791

The events of the current experiment have two different natures, whose characteristics will be further detailed in 5.1: the implantations (nuclei entering the ACTAR TPC volume) and their detected particles emissions. In the case of a "decay event", originated inside the detection volume, the only triggering possibility comes from the GET system. For this reason, the L1 signal, described above, is used externally as an input of a GMT (General Master Trigger) module to trigger the full experiment acquisition ($Trig_{E791}$), as schematized in Figure 2.16.

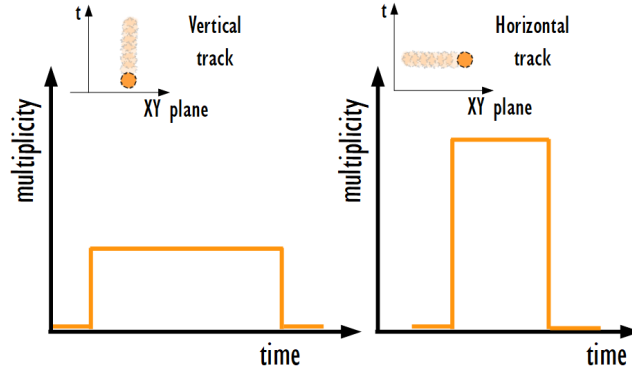


Figure 2.15: Illustration of the multiplicity time over threshold analysis made by the MuTanT module for vertical (left) and horizontal (right) tracks to generate a level 1 trigger.

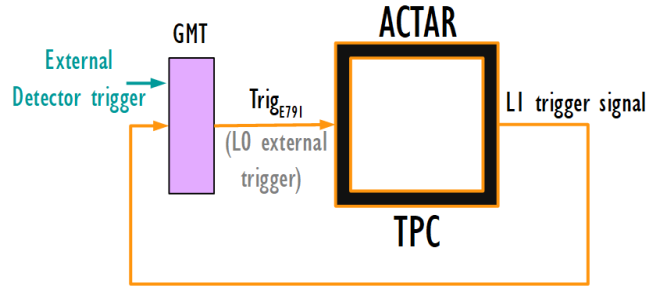


Figure 2.16: Scheme of the trigger logic in the experiment and its different inputs: external detector trigger for implantation events, further discussed in 3.6 and L1 signal for decay events. The GET system is triggered in L0 (external trigger mode).

This signal is taken using one of the available inspection lines of the MuTanT module. A second inspection line of the MuTanT module is used to output a dead time signal starting from the trigger signal as illustrated also in Figure 2.17.

GET parameter	Value
Gain capacitance C_g	240 fC
Peaking time τ	334 ns
Readout threshold R_{Thr}	2.2 % signal range
Trigger delay δt	16 μs
SCA readout depth N	256
SCA writing frequency W_f	25 MHz
Multiplicity threshold M_{Thr}	15
Time buckets over threshold nt_{Thr}	3

Table 2.1: GET electronics parameters in E791 experiment.

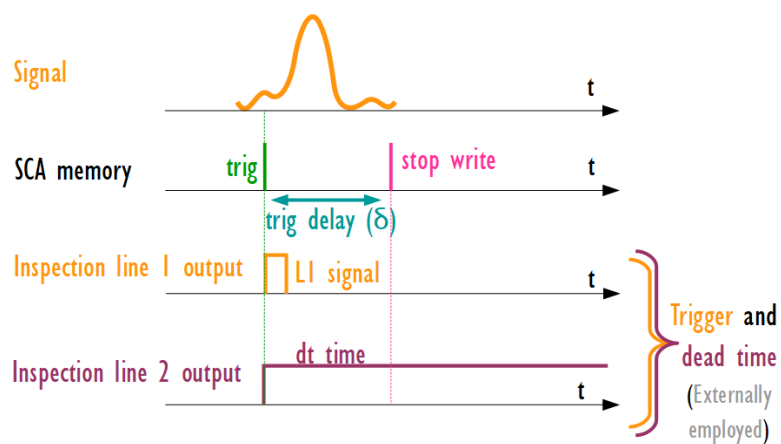


Figure 2.17: Illustration of the internal GET trigger. A trigger signal induces a write stop on the analog memory shifted by a defined trigger delay in order to register the full signal. The inspection line 1 of the module is used to send externally this trigger to the experiment main trigger module (GMT, see Section 3.6). The inspection line 2 output is used to send the dead time corrected from the trigger signal (dark red signal). These two signals are sent into the inspection lines and are externally employed for the experiment trigger and dead time logic.

Chapter 3: E791 Experiment



Contents

3.1	Introduction	68
3.2	Primary and radioactive beam	69
3.3	Selection process (LISE spectrometer)	69
3.4	Additional detectors for identification purposes	71
3.5	ACTAR-TPC: gas and pressure choice	73
3.6	Trigger and time logic	74
3.7	Towards the final settings	76
3.7.1	Online Identification	76
3.7.2	ACTAR TPC "online" measurements	77

This chapter is dedicated to the E791 Experiment performed at GANIL (Grand Accélérateur National d'Ions Lourds) France (May 2021) aiming to measure the ^{48}Ni two proton radioactivity. The main elements and setting choices of the experiment for its three main stages: production, selection and implantation of the exotic nuclei in the ACTAR TPC device will be discussed. The last two sections are devoted to explain the E791 acquisition decision logic and online basic analysis performed to optimize the production and implantation of the nuclei during the experiment.

3.1 Introduction

The E791 experiment was performed at GANIL (Grand Accélérateur National d'Ions Lourds) France aiming to produce ^{48}Ni nuclei, implant them in the ACTAR TPC device and measure their decay products.

The exotic beam is produced by fragmentation of a ^{58}Ni primary beam sent on a natural Ni target, as further discussed in Section 3.2. The exotic fragments are selected using the LISE3 spectrometer [107] in several selection stages, as detailed in Section 3.3. This selection, not being perfect, results into a secondary beam composed by several nuclei. The choice of the gas and pressure in the Active Target Time Projection Chamber is further discussed in Section 3.5. These three main elements of the experiment: initial beam production, fragmentation beam selection and implantation in ACTAR TPC are illustrated in Figure 3.1.

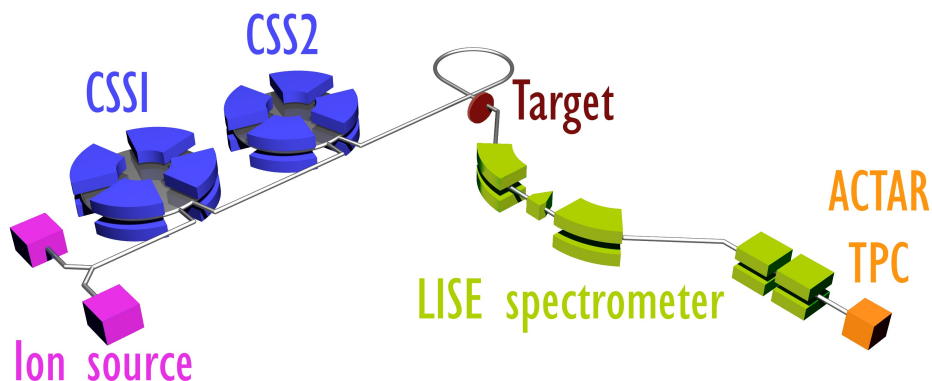


Figure 3.1: Illustration of the main elements composing the experiment: ion source and cyclotrons accelerating system (primary beam production), target and spectrometer (radioactive beam production and selection) and ACTAR TPC device (implantation of the exotic nuclei).

Some position and timing (for time of flight measurements) detectors are located along the spectrometer line. Silicon detectors (for energy loss measurements) are placed in the final Section of the beam line. A description of their main characteristics and location in the beam line can be found in subsection 3.4.

The trigger and time logic of the experiment is built in such a way that the different nature events in this work (implanted ions and decay products) are registered, as explained in Section 3.6.

Due to the fragmentation process, large velocity and angle dispersion are introduced within the produced nuclei. A restrictive selection made with the spectrometer leads to a reduction of the transmitted nuclei. The spectrometer settings are thus chosen as a compromise between a good selection and optimized transmission rates. As a result, the secondary beam, even after the spectrometer selection, results to be a mixture of several nuclei, (a so-called cocktail beam). The experiment was performed during three weeks with a total effective beamtime of 277 hours, in which only 191 hours of measurements were performed using the final optimized settings for the spectrometer. One should notice that the optimization process was not easy and took time. The Section 3.7 is dedicated to the description of such a process.

3.2 Primary and radioactive beam

The primary beam is produced by the acceleration of $^{58}\text{Ni}^{11+}$ ions extracted from an ion source. The acceleration process occurs in three stages, a first cyclotron is used to accelerate the ions up to 1A MeV (C0). They are further injected into the CSS1 cyclotron, where they gain up to 10A MeV. The ions then get stripped in a thin carbon foil ($^{58}\text{Ni}^{26+}$) before entering into the last cyclotron (CSS2), where they get accelerated up to 75A MeV with an average intensity of 5 μA . To produce the secondary radioactive beam, these accelerated ions are sent to a 210 μm $^{\text{nat}}\text{Ni}$ target where their fragmentation occurs, producing essentially nuclei with masses smaller than the one of the beam.

The primary beam is chosen to have the closest Z with respect to the desired nuclei to be produced. This choice minimizes the dispersion in energy and angles in the fragmentation process, as discussed in [108] resulting in a better selectivity in the spectrometer. The target choice $^{\text{nat}}\text{Ni}$ is preferred to a lighter one (for example beryllium) because of the intermediate energy primary beam regime at GANIL. Around these energies (Fermi Energy), the incident beam can pick-up protons from the target before the fragmentation occurs, as discussed in [109]. The probability of removing N neutrons and some (picked-up) protons is higher than the probability of just removing N neutrons. By choosing a proton-rich target instead of a light one, this picking-up is favored and the production of very exotic neutron deficient nuclei increases with respect to the production achieved with a lighter target.

3.3 Selection process (LISE spectrometer)

The fragment selection is achieved using the LISE (Ligne d'Ions Super Epluchés) spectrometer [107]. It is mainly composed of two dipoles with adjustable slits in their focal plane, some quadrupoles to refocus the beam, an achromatic degrader and a Wien filter as shown in Figure 3.2. The purification of the radioactive beam proceeds in three stages when going through all the elements described hereafter.

Magnetic Rigidity selection: when the ion goes through a dipole since the applied magnetic field is perpendicular to the velocity of the incident particle, it will follow a curved path with a radius ρ given by:

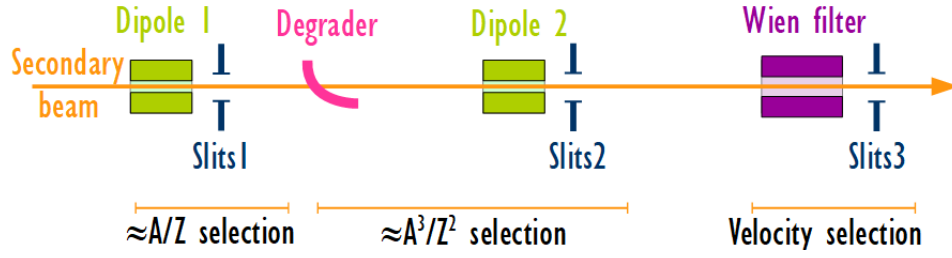


Figure 3.2: Main elements in the selection process of the LISE spectrometer: first dipole ($\approx Av/Z$ selection), achromatic degrader and a second dipole ($\approx A^3/Z^2$ selection) and a Wien filter for the velocity selection. Adjustable slits are placed after each selection stage.

$$\rho = \frac{Av}{QB}. \quad (3.1)$$

Where ρ is the radius of curvature of the path of a charged particle with mass A and charge Q , moving at a speed v that is perpendicular to a magnetic field B . Since the incoming ions are fully stripped, the charge is equal to the number of protons so that $Q=Z$. By defining the magnetic rigidity as the product of the applied magnetic field and the curvature radius of the ion trajectory ($B\rho$), the equation 3.1 can be written as:

$$B\rho = \frac{Av}{Z}. \quad (3.2)$$

By adjusting the applied current in the magnet, ions of interest with a characteristic $B\rho_0$ will continue straight and those with different values will be deviated by the magnetic field. A $(B\rho + \delta)$ window, compromise of purity and intensity, is then selected using adjustable horizontal slits located in the focal plane of the first dipole. After this first stage, the selected ions are dispersed in energy. The second $B\rho$ selection is generally a symmetric process to the first one that compensates the dispersion of the first selection and allows refocusing the beam.

Energy Loss in an achromatic degrader: the insertion of a foil degrader between the two dipoles in the intermediate focal plane enables to make a further selection of the ions depending on their number of protons Z . The traversed thickness (ΔS) in the foil makes the isotopes losing energy as:

$$E_{loss} \propto \frac{Z^2}{A} \Delta S. \quad (3.3)$$

Thus, isotopes before the degrader may have the same ($B\rho \approx \frac{A}{Z}v$) but if they do not have the same Z , the degrader will induce a shift in the $B\rho$ between species before entering the second dipole. The foil degrader is shaped in such a way that the relative difference of $B\rho$ of a species before and after the degrader is conserved, fulfilling the achromatic condition. The effect of this degrader together with the second dipole results in a selection according to A^3/Z^2 .

Selection in velocity: finally the nuclei are selected with a Wien filter or velocity selector which is a device consisting of perpendicular electric and magnetic fields. The module of the total magnetic and electric force for an incident ion with perpendicular trajectory with respect to B , is given by

$$F = q(|E| - |v||B|). \quad (3.4)$$

For beam particles with a velocity $v = \frac{E}{B}$ the Wien filter does not induce any force on them. Selecting then the electric and magnetic fields such as their coefficient is equal to a given reference velocity v_{ref} (for

the desired isotope) $\frac{|E|}{|B|} = v_{ref}$, the Wien filter induces a curvature radius for the contaminants. The slits installed after the Wien filter as shown in Figure 3.3 complete the velocity selection by stopping the ions that go out the filter with a certain radius.

3.4 Additional detectors for identification purposes

Some additional detectors are placed along the beamline for identification purposes, as shown in Figure 3.3. Their working principle, positions along the beamline and uses during the experiment will be discussed.

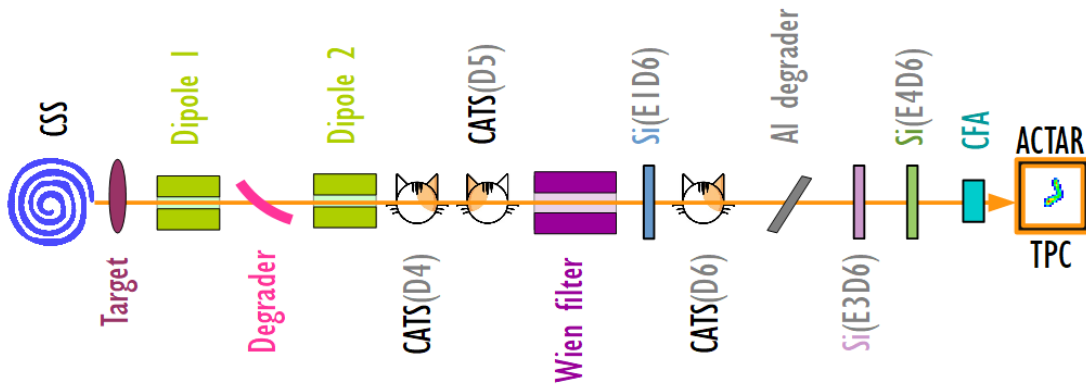


Figure 3.3: Simplified beamline schematic view showing the position of the identification detectors along the beamline. Two CATS detectors (CATSD4) and (CATSD5) are located between the second dipole and the Wien Filter. In the final part of the beamline, a first silicon detector (Si(E1D6)) and another CATS detector (CATSD6). After an aluminum degrader, there are two other silicon detectors Si(E3D6) and Si(E4D6) and a gaseous detector (CFA) right before the ACTAR TPC detection volume.

The **CATS detector** (*Chambre A Trajectoires de Saclay*) is a low pressure multi-wire proportional chamber (MWPC) developed by the CEA/DAPNIA, Saclay [110] to provide event-by-event particle tracking and time information in experiments with radioactive beams. It consists of two cells that share a common anode. The CATS detector has a double stage amplification, in contrast to high pressure chambers where the charge multiplication occurs only at the vicinity of the wires. The electric field is considered to be constant between the cathodes and the anode up to some small distance of the wires, where the second charge multiplication occurs. This property is advantageous for beam tracking as discussed in [110]: significant signals obtained with small thickness of gas, good time resolution and high counting rate capabilities.

The anode is composed of 10 μm gold-plated tungsten wires with 1 mm pitch. The cathodes are placed in parallel with the anode on each side at the same distance from it. Each cathode consists of 28 aluminium oxide strips disposed horizontally and vertically respectively, evaporated on a Mylar foil of 1.5 μm thickness. Each strip signal, induced by the traversing particle, is registered individually for a position reconstruction. The total active area of 70x70 mm^2 is delimited with two extra self-supporting 1.5 μm Mylar windows, one in each of the sides of the detector. They isolate the detector from external pressure conditions, avoiding any deformation of the cathode and preserving the uniformity of the electric field [110]. The low thickness of the Mylar foils ensures the transparency of the detector.

The CATS detectors are placed perpendicular to the beam axis. All the data coming from these detectors

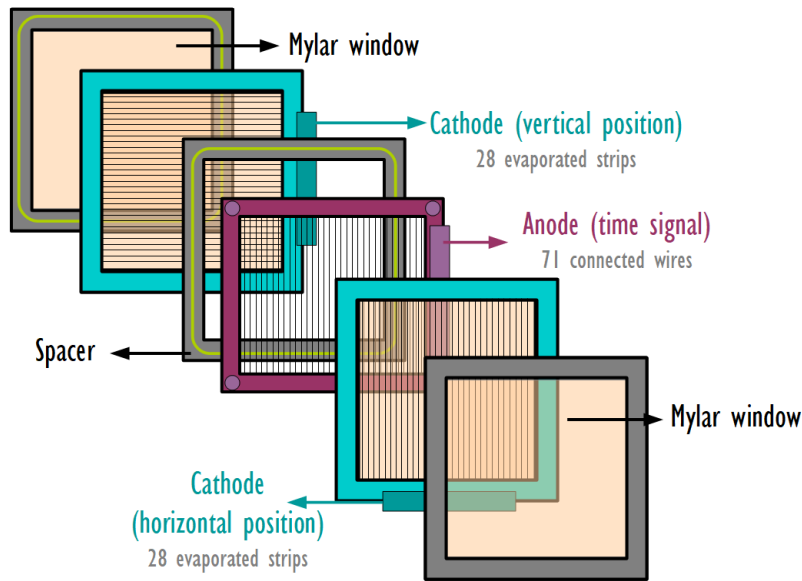


Figure 3.4: Exploded view of a CATS detector and its main components described in the text: Mylar (transparent orange) supporting windows in the extremes, two cathodes (blue) for horizontal and vertical position reconstruction, spacer and anode for time signal (dark red).

aim to identify the ions by their time of flight measurements (timing information) and their different positions along the detector (positions in the X and Y planes, perpendicular to the beam direction). Three different CATS detectors are placed along the beamline as illustrated in Figure 3.3. The first one is located after the second dipole of the LISE spectrometer (CATSD4). This detector is used only for time of flight measurements. The second one (CATSD5), is installed after it (following the direction of the beam). Apart from the timing signals, this CATS is used for particle position reconstruction in the X (dispersion) plane. Finally, a third CATS detector (CATSD6) is located after the Wien filter. It provides, besides from a timing signal, position measurements, in both X and Y planes.

The CFA is a circular, thin multi-wire proportional gas counter of 30 mm diameter. It is similar to the CATS detector but with non stripped cathodes. It is placed inside the ACTAR volume, installed in the "nose" right before the drift region as shown in Figure 3.5. This detector provides timing information for time of flight measurements and allows for a more precise counting of the incoming ions that are really implanted in the chamber because of its proximity to the active volume. It was originally installed to be used as a trigger for the implantation events, but as it is discussed in the following Section 3.6, it was finally removed for the final settings because of its reduced entrance window.

Silicon detectors: Semiconductor detectors in which the incident particles energy deposit is obtained by measuring the number of electron-hole pairs created by the traversing charged particle. There are three silicon detectors installed along the beam line, as shown in Figure 3.3. The first one, (E1D6), 143 μm thick, is located after the Wien filter and before the CATSD6 detector, the second and third one (E3D6 and E4D6) with thicknesses of 143 μm and 300 μm respectively, are installed after the aluminium degrader and before the detection chamber. These three detectors provide energy loss measurements of the incident ions and are used for identification purposes.

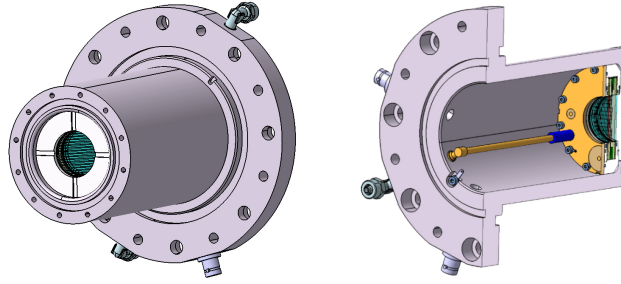


Figure 3.5: Scheme of the placement of the CFA detector inside the nose. Left and right images correspond to a different view of the nose installed inside the ACTAR volume (Views from the inside of the detection volume and from the outside, respectively). In the right one, the structure for the installation of the detector (yellow components) are visible.

3.5 ACTAR-TPC: gas and pressure choice

In this experiment, the ACTAR TPC detector, previously described in Chapter 2, is filled with $Ar(90\%) + iC_4H_{10}(10\%)$. The pressure is set to 300 mbar or 450 mbar depending on the experiment settings as explained in Section 3.7.

The use of a noble gas as the main component of the gas mixture is recommended in gaseous detectors, as discussed in [76]. The ionization in these gases is simpler in comparison to complex molecules, in which many non-ionizing energy dissipation modes are available. Argon is a good compromise between high specific ionization properties and its low cost. The drawback of using only a noble gas (Ar in this case) appears at some gains from 10^3 to 10^4 , as discussed in [111]. In these cases, two different processes can occur during the ionization: some of the atoms of the noble gas can be excited, emitting a photon with a high enough energy (11.6 eV for Argon) to produce photo-electrons in the cathode. Secondly, Ar positively charged atoms can drift to the cathode and neutralize by extracting an electron from it. In both of the processes, new electrons that do not come from the original charged particle ionization can drift towards the detection plane. To avoid spurious signals coming from these electrons, a more complex molecular structure is included in the gas mixture, the quencher component. First, this component absorbs the Ar photons in an efficient way due to its large amount of available excitation modes. Secondly, it also neutralizes the Ar ions before they can reach the cathode. The quencher can also drift to the cathode, but secondary emissions in its neutralization are very unlikely (the radicals of the polyatomic molecule will most likely recombine instead). The efficiency of a quencher gas depends on the number of atoms. Isobutane iC_4H_{10} is commonly used for these purposes.

The pressure of the gaseous detector enables to adjust the density of the material used to stop the ions. Since the energy lost at each collision is a statistical process, the distribution of the stopping points of the nuclei are large. By increasing the pressure in the detector, the number of implanted ions of interest can be maximized. On the other hand, the range of the decay particles becomes smaller when increasing the pressure. For the determination of the angles between the emitted particles, a minimum length is required (greater than the transverse multiplicity) in order to determine the direction of emission of the particles. The pressure is then selected as a compromise between maximizing the number of implantations in the detector and obtaining long enough particle tracks. During the experiment, the pressure value was changed after the analysis of few 2-proton decay events, as it will be discussed in Section 3.7.2.

3.6 Trigger and time logic

In this work, the events of interest have two different natures: the implanted ions and the decay products of these ions. They are triggered in a different way.

Implantation events can be triggered by a signal from any of the detectors in the beamline. Ideally, the CFA detector, placed just before the detection volume (as explained in previous Section 3.4) is used for this purpose. Its position, close to the detection volume, ensures to trigger the events that really enter the chamber. During the experiment, it was confirmed that the CFA detector was reducing the acceptance in ACTAR since the diameter of its entrance window is smaller (30 mm) than the ACTAR TPC one (45 mm). After removing this detector, the E1D6 Silicon detector signal was taken as the implantation trigger instead of the CFA one. As a result, some of the triggered implantation events may have no signal in ACTAR TPC (nuclei that did not reach the chamber) but more implantation events are available for identification purposes.

Decay events occur inside the ACTAR TPC gas volume. These events can thus only be triggered by a signal coming from the pad plane. For this purpose, the MuTanT L1 signal is used. This trigger is built from predefined pad thresholds and a time over threshold multiplicity analysis, as explained in Section 2.4.2.

Other signals are available for both triggers: silicon detectors E1D6 and E3D6 for implantations, and mesh signal for decay events. During the experiment, they were all connected to different inputs of a GMT (Ganil Master Trigger) in order to verify the response of the different elements and easily change the final trigger if needed. The final trigger can be selected by software combining the different GMT inputs. In the E791 experiment, for the final settings, only two triggers were used: silicon E1D6 signal for implantations and L1 ACTAR TPC signal for decays. These signals are also sent and registered as scalers using a Universal Marker Module (U2M), as shown in Figure 3.6. The scaler values allow keeping a trace of possible event losses due to dead time of the acquisition (i.e. if an increment higher than 1 is observed between two registered events).

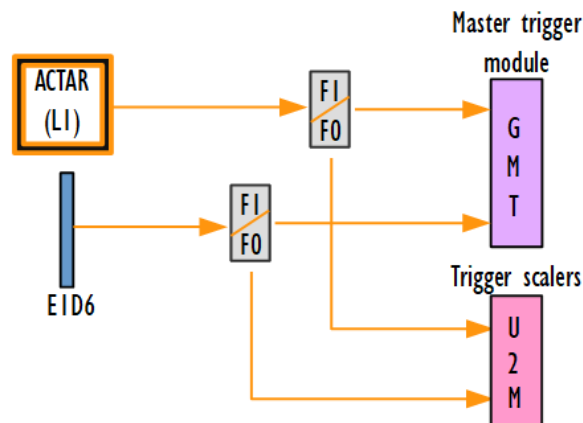


Figure 3.6: Trigger logic during the E791 experiment. More entries were connected to the GMT, but only the ones used for the final settings of the E791 experiment are shown for simplicity. Only E1D6 and L1OK finally contributed to the final trigger in the final settings.

There are four different acquisition branches in the experiment, triggered in a synchronized way by one of them (the master acquisition (VXI)) when none of the others are in dead time.

The master acquisition (VXI) handles the silicon detectors (E1D6, E3D6, E4D6) signals and the scaler registration (U2M). Its main elements are the master trigger module (GMT) and the CENTRUM (Clock and Event Number Transmitter Receiver Universal Module). The GMT module provides the master trigger signal to the slave acquisitions, and the CENTRUM module delivers a time-stamp and an event number to each of the acquisition branches. The master acquisition is inhibited if any of the other branches are in dead time. This common dead time logic ensures that none of the acquisitions is triggered more than the others, leading to a unique time-stamp and event number for the same physical event.

Two acquisition branches (VXI2 and VXI3) are used for CATSD5 and CATSD6 position signals, respectively. The dead time signals are provided by two GAMER (Ganil Acquisition Module for Electronic Resources) modules. They are sent to a Fan-In Fan-Out (FIFO) (or logic) to build a common dead time (DT_{VXI2}) signal) if any of these acquisitions is in dead time.

The GET system composes the last acquisition branch. The dead time signal DT_{GET} is provided by one of the two MuTanT modules (the master one).

The DT_{GET} signal is sent together with the DT_{VXI2} one to a logic or (FIFO) and the output signal is used as inhibit of the GMT. The common dead time logic is illustrated in the top part of the Figure 3.7. All the acquisition dead times are measured by sending the dead time signals to a coincidence module in "OR" mode with a 1 MHz clock, as illustrated in the bottom part of Figure 3.7. This coincidence increments a scaler in U2M. The dead time can thus be obtained in an event-by-event basis from the difference in time between a given event and the previous one: $dt_{event} = dt_{event} - dt_{event-1}$. The dead time of the full acquisition, of the order of $200\mu s$ is dominated by the VXI dead time values.

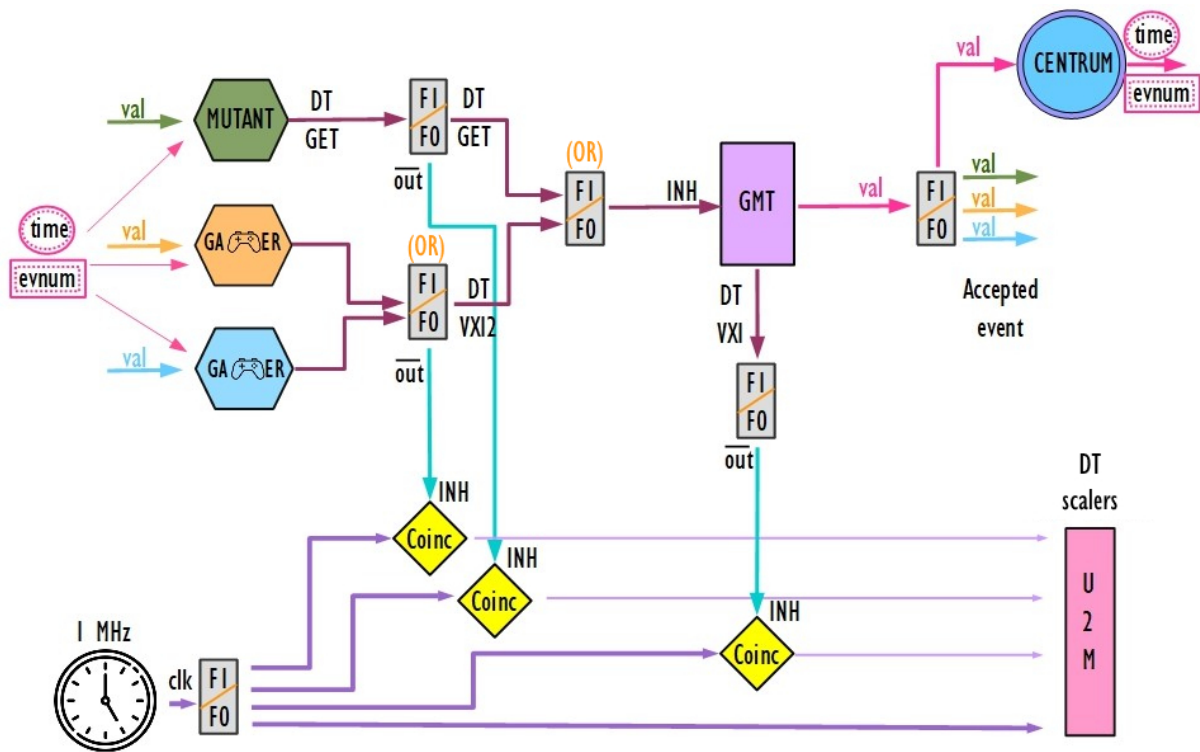


Figure 3.7: In the upper part of the figure, the inhibition of the trigger if any of the systems (GAMERs or MuTanT) is in dead time is shown (dark red arrows). If the event is validated (pink signal) the validation signal is sent to trigger the slave modules (green, orange and blue signals). The time-stamp and event number information are sent to the slave acquisition branches by the CENTRUM module when receiving the validation signal of the master trigger. The bottom part of the figure shows the registration of the different dead times into a U2M (scaler) module by sending the inverted dead time signals (blue) as an inhibition to a coincidence module in "OR" mode with a 1 MHz clock.

3.7 Towards the final settings

The optimization process consists of two main ingredients: an adequate selection of the region of measurement around the nuclei of interest and the maximization of the number of interesting implantations in ACTAR TPC. For both processes, the online identification of the nuclei is a key step. This is typically done by using the available information taken from the identification detectors placed along the beamline (see Figure 3.4) as further described in subsection 3.7.1. In the specific case of the E791 experiment, additional online helpful information can be extracted from ACTAR TPC by measuring both, the distribution of the implantation depth of each of the nuclei and their decay products. The last part of this Section 3.7.2 is dedicated to explain how these measurements are used for identification purposes. When producing such exotic nuclei, the optimization of the settings is particularly difficult and a significant part of the beam time during the experiment was dedicated to it. As a result, the total production, transmission and implantation of the most exotic nuclei are lower than initially expected.

3.7.1 Online Identification

The most basic identification of the ions is made by plotting the energy deposit information given by a silicon detector as a function of the time of flight, measured from the difference of two time signals. In this

identification plot, the different isotopes appear to be separated, since their energy deposit is approximately a function of Z^2 and their time of flight is a function of about $\frac{A}{Z}$. An example of an identification plot is shown in Figure 3.8.

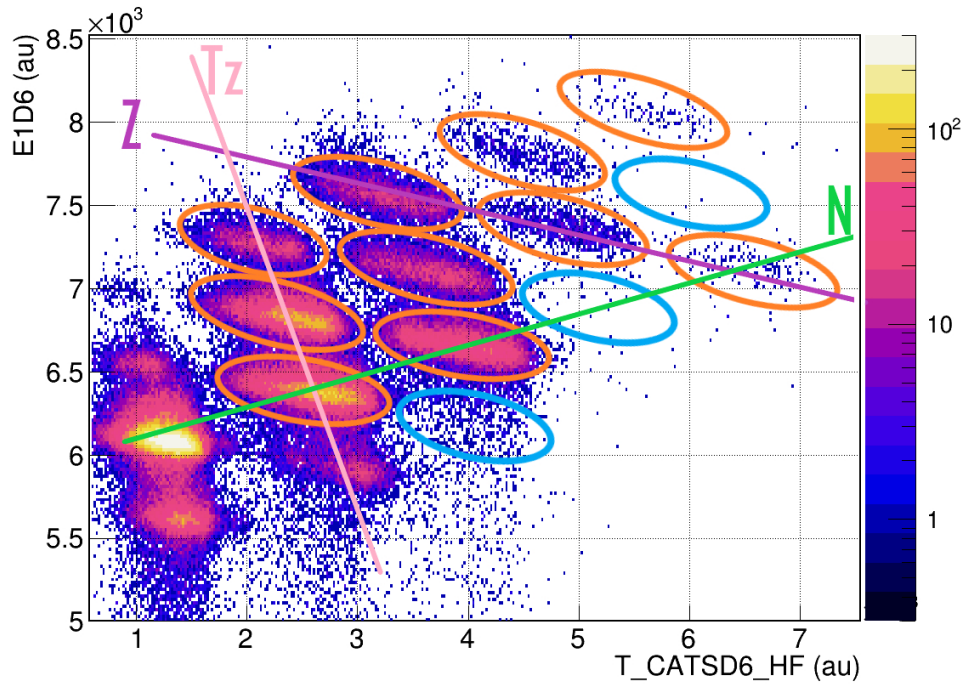


Figure 3.8: Measured time of flight between the cyclotron radiofrequency (HF) and the CATSD6 detector against the energy deposit in a silicon detector (E1D6) for four small runs in the final configuration. Different nuclei can be distinguished in the identification plot (orange ellipses). Also, some holes (blue ellipses) corresponding to unbound nuclei are observed. The Z , T_z and N lines are drawn in purple, pink and green respectively.

During the E791 experiment, in order to increase the number of transmitted exotic nuclei along the spectrometer, the momentum slits after the first selection dipole were opened. The consequence of this choice is a large momentum acceptance of the spectrometer. The effect in the identification plot ΔE -ToF is an overlap of the nuclei with the same Z . The basic identification process is thus not suitable for the final analysis to recognize the different isotopes, as it will be explained in Section 5.2.

The time of flight versus the energy deposit identification plot was nevertheless used online. First to verify the production of the different fragments: the accumulated identification plot during a certain time gives, just by looking at it, first information of the region of measurement: the non-observation of unbound nuclei (holes) helps to identify the rest of the nuclei around. Second information is extracted by comparing the production rates with the ones predicted by LISE++ [131] simulations.

3.7.2 ACTAR TPC "online" measurements

When dealing with a cocktail beam, the identification of the species is a key point for the interpretation of the measurements made with ACTAR TPC. The identification process allows separating the decay information associated to each ion. This is performed (in the analysis stage) creating contours in the identification plot and requesting the time of flight and the energy deposit values of each event to be inside

each of them. Under a specific contour condition, distributions of implantation depth and information about the associated decays can be obtained individually for each species.

In order to cross-check the identification of the different isotopes during the experiment, the decay products (protons) of the implanted nuclei were analyzed semi-online. After an implantation, the associated decay events are searched within a time window. The distribution of the time difference between decay and implantations events $N(t)$ follows the decay law:

$$N(t) = N_0 e^{\frac{\ln 2}{T_{1/2}} t}. \quad (3.5)$$

where N_0 is the value of nuclei at a time $t=0$ and $T_{1/2}$ the half life, characteristic for each nucleus. A first estimation of the half-life can thus be obtained by fitting the curves with the previous equation 3.5. Taking into account that N_0 depends also on the half life as: $N_0 = N_A \frac{\ln 2}{T_{1/2}}$ (where N_A is the number of measured decays) and incorporating a background factor N_{bg} to take into account fake coincidences, the equation 3.5 can be rewritten:

$$N(t) = N_{bg} + N_A \frac{\ln 2}{T_{1/2}} e^{\frac{\ln 2}{T_{1/2}} t}. \quad (3.6)$$

The N_{bg} term is calculated in a first step by fitting the decay events correlated at negative times (fake coincidences). This parameter is further fixed when performing the fit for the half life estimate with equation 3.6. An example of the described fit process is shown in Figure 3.9. Since the half-lives are well-known

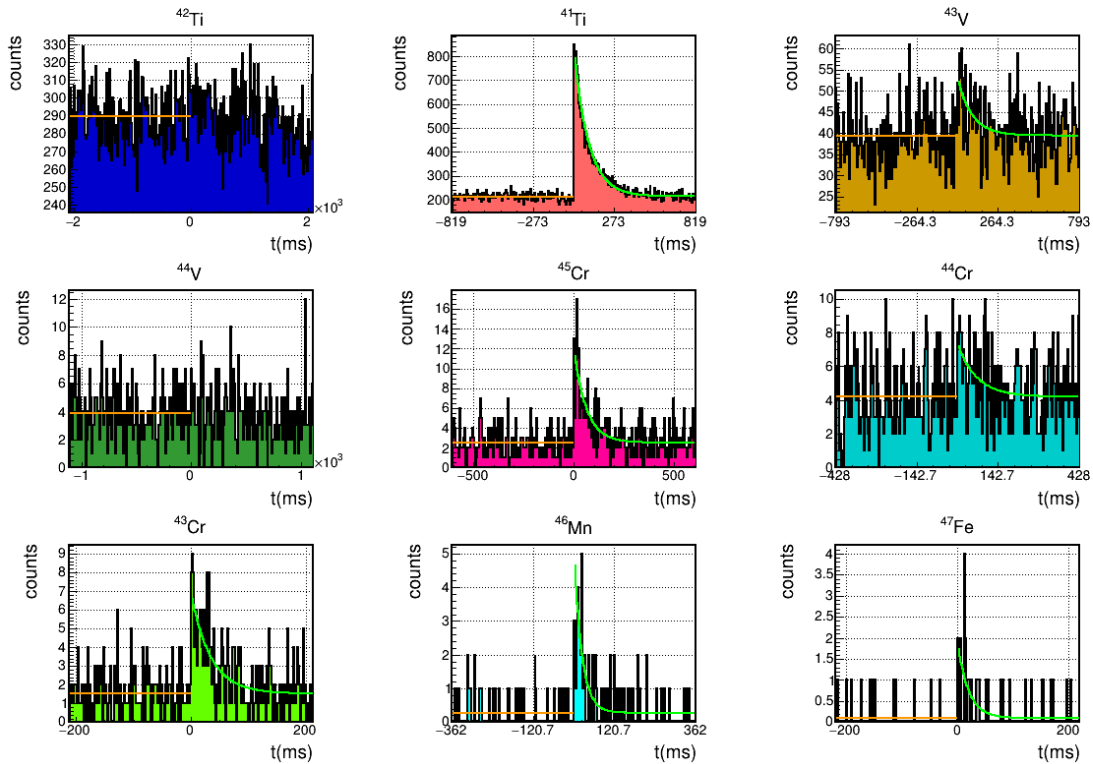


Figure 3.9: Time difference between implantation events and associated decays for a group of measured nuclei (same data set as the one used in Figure 3.8). Just by a first look, the non-proton emitters (or low branching ratio proton emitters) can be identified: (^{42}Ti , $^{43,44}\text{V}$, ^{44}Cr). The background fit is shown at negative times (orange line). The green line corresponds to the half-life fit. These plots aimed, in a first stage, to verify identification hypothesis during the experiment.

for the nuclei in the region, by comparing them to the experimental fitted values, the different nuclei can

be identified. The non-observation of proton emissions from some of the species also helped to identify those nuclei known to decay exclusively by β or EC processes. Both experimental observables were used to adjust the spectrometer settings to allow the transmission of the desired nuclei through the beamline.

Once the settings of the spectrometer are optimized for the transmission of the nuclei of interest, the optimization of the implantation depths in ACTAR takes place. For that, experimental distributions of implantation depths were obtained by measuring the stopping point of the implantation tracks in ACTAR TPC, as illustrated in Figure 3.10. This information was used to verify and adjust the LISE++ simulated

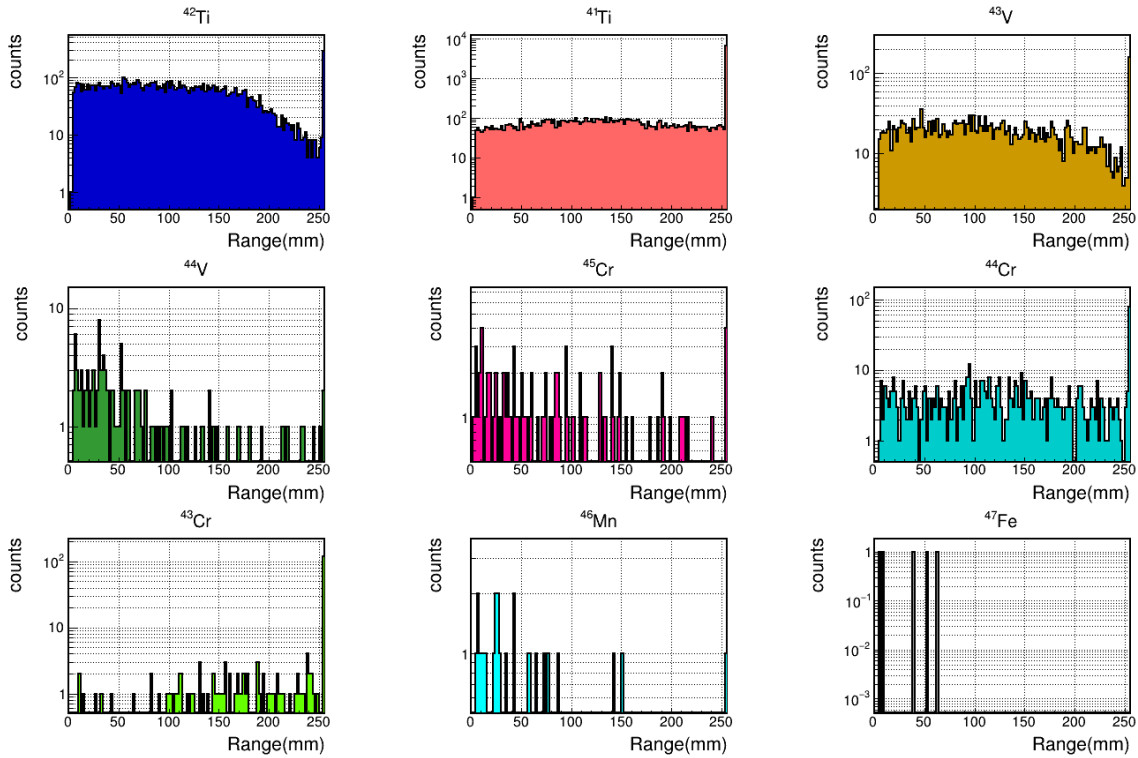


Figure 3.10: Stopping point of the implanted ions in ACTAR TPC for a group of measured nuclei using the same set of data as in Figures 3.8 and 3.9.

values for the implantation distributions and to modify several aspects of different elements in the beamline such as the wedge thickness or the angle of the degrader. Such an analysis helped to get optimal conditions for the implantation of ^{48}Ni , meaning that its implantation profile is centered in the detection volume.

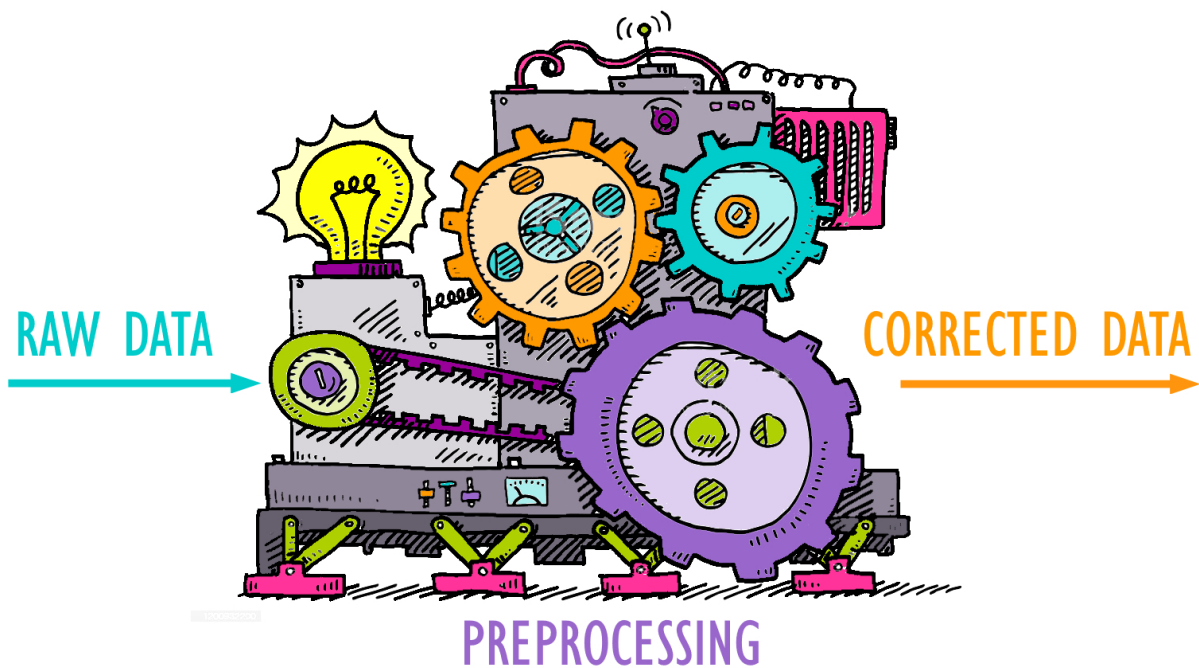
Unfortunately, even within the optimized settings, the distribution is larger than the detection volume. Apart from optimizing the implantation ranges, the only way of covering more of the implantation range with ACTAR TPC is an increase of the gas pressure, as already mentioned in previous Section 3.5.

The initial pressure was set to 300 mbar. The first measurement of a two proton emission from ^{48}Ni during the experiment allowed to optimize experimentally the pressure value in ACTAR TPC. These protons have predicted energies of about 650 KeV [113], [114], [115]. The measured lengths were large enough (around 30 mm) so that an increase of the pressure in the detector by a factor of 1.5 (450 mbar) could be performed during the experiment without any critical loss in angular resolving power. This major change in the settings divides the full set of data into two groups, (first and second pressure configuration) as further discussed in the analysis chapter 5. The characteristics of these two settings are summarized in Table 3.1

	Configuration 1	Configuration 2
Pressure (mbar)	300	450
Mesh voltage (V)	250	270
Cathode voltage (V)	4000	4900

Table 3.1: Different pressure configurations during the experiment and associated voltages in ACTAR TPC.

Chapter 4: Pre-treatment of signals and drift velocity measurements



Contents

4.1	ACTAR TPC signal corrections and calibrations	82
4.1.1	Baseline Correction	82
4.1.2	Fixed Pattern Noise (FPN) Correction	83
4.1.3	Pad signal amplitude gain-matching	84
4.1.4	Pad time signal alignment	86
4.1.5	Input signal reconstruction	87
4.2	CATS detector calibrations (CATibrations)	89
4.3	Drift velocity measurements	90
4.3.1	Procedure	91
4.3.2	Alpha source tests	92
4.3.3	Drift velocity from proton tracks	94
4.3.4	Discussion and comparison of drift velocity results.	95

This chapter is dedicated to the first procedures to be applied on raw data to correct for systematic effects, for ACTAR TPC (Section 4.1) and for the CATS detectors (Section 4.2). The last section is dedicated to explain drift velocity experimental measurements performed using ACTAR TPC. The characterization of this value is important for the analysis of the tracks and the choice of experimental conditions.

4.1 ACTAR TPC signal corrections and calibrations

When treating an event in ACTAR TPC, the samples need to be analysed on a channel-by-channel basis to retrieve global information of the event, such as the total deposited charge or the charge distribution in time. The main systematic effects (observed and studied on previous test measurements [93], [96], [116]–[118]) are discussed in this section. In order to improve the accuracy of the measurements, some first corrections need to be performed in an individual-channel basis: baseline and coherent noise corrections, explained in Sections 4.1.1 and 4.1.2 respectively. The pads having independent electronic chains for the processing of the signal may not generate exactly the same digital output data for a given charge deposit. When analysing an event (readout of the samples for all pads), the gain-matching of the different channel responses in amplitude and time are needed. These two processes are explained in Sections 4.1.3 and 4.1.4 respectively.

As mentioned in Section 2.4.1, the output samples measured in ACTAR TPC are not a direct digitization of the input current distribution, but it can be reconstructed, as explained in the last Section 4.1.5.

4.1.1 Baseline Correction

There exist some systematic distortions of the measured signal at a "pad level" [93] that can be corrected by analysing the baselines (collected data with no signal), by subtracting them from the measured signals. To perform such a correction, an external (random) trigger is sent to MuTanT while no signal is sent to the pads. The registered signal in full readout mode is averaged for about 1000 events to reduce the contribution of the measured intrinsic noise. This correction is performed independently for each pad since the position and the shape of the baseline may differ from one channel to another, as shown in Figure 4.1.

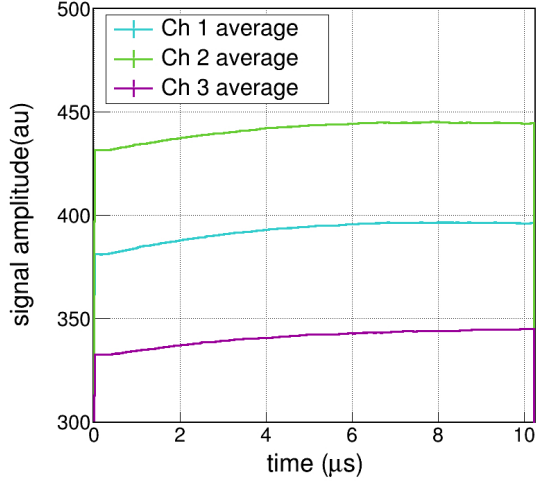


Figure 4.1: Different channel baseline measurements from the averaging of 1000 events. The position of the baselines vary between them.

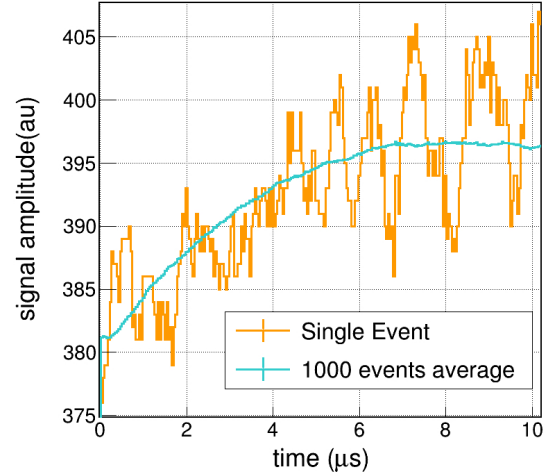


Figure 4.2: Single Event baseline measurement for a given channel and average of the signals of 1000 events for the same pad. The baseline is not constant with the sampling time.

As discussed in Section 2.4, a pad signal consists of 256 time samples covering a total range of $10.2 \mu\text{s}$. In an ideal case, a constant offset of the baseline for the measured signal is expected. This is not the case as it can be seen in Figure 4.2 in which a single event and the average of 1000 events of a single channel signal is shown. The baseline has a shape as a function of the time sample. Furthermore, the data for the first sample and the last one exhibit a systematic effect (lower values). The former distortion is due to readout of the buffer memory and the latter one is related to the position at which the write stop occurs in the SCA analogue memory, as discussed in [93]. These two systematic effects are present also when a measurement (with amplitude different from zero) is performed. Thus, by subtracting the baseline (calculated from 1000 events for each channel), the two effects are considered to be corrected. The correction for a given channel i measuring an induced charge q is given by:

$$s_i(q) = s_i(q) - \langle s(0) \rangle_{1000}. \quad (4.1)$$

4.1.2 Fixed Pattern Noise (FPN) Correction

Each AGET chip contains four extra (fix patter noise, FPN) channels (as mentioned in 2.4.1) located regularly between the 64 signal channels at channels 11, 22, 45 and 56. The FPN have been designed to measure the coherent noise of the electronics on an event-by-event basis. Apart from correcting for electronic effects, they are used to correcting for possible cross talk signals coming from the neighbouring channels (occurring at the chip level). This effect can be observed in figure 4.3, where a small peak in amplitude can be noticed. In Figure 4.4 an event signal from a single channel is plotted together with the four measurements of the AGET FPNs.

The "FPN correction" consists of a subtraction of the corresponding FPN signal from the sample signal:

$$s_i(q) = s_i(q) - \langle s_{FPN}(q) \rangle_4 \quad (4.2)$$

The correction s_{FPN} can be done with respect to the closest FPN channel or with respect to the average value from the four channels in the chip. The two possibilities have been studied in [93]. The latter one being the best method to reduce the coherent noise, requires the registration of all the FPN values (1024 channels in total for each event) which turns out to be bigger than the total number of registered amplitude channels (above a defined threshold) in a standard event (from 100 to 500 pads in the context of this work). To minimize the size of the registered data, it is possible to reduce the number of FPN channels read within an event. In the current experiment, only two FPNs per AGET were stored, the ones located in the intermediate positions of the chip (22 and 56) and the correction is performed by subtracting their average signal.

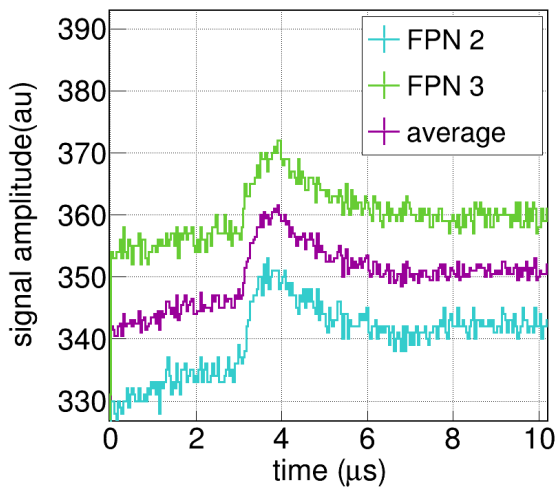


Figure 4.3: FPN signals and average value between them, used to correct the channel signal.

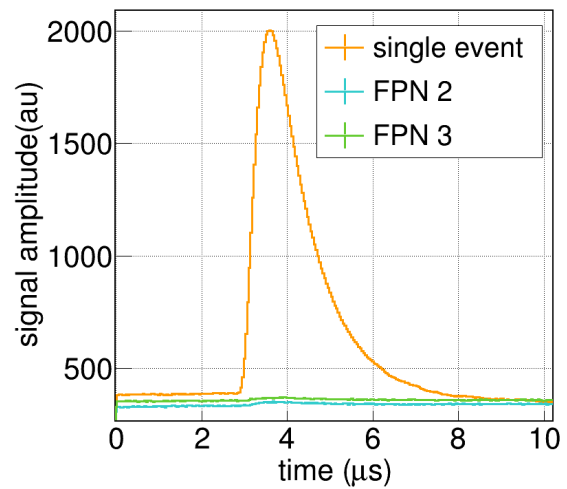


Figure 4.4: For a single event: Pulser signal of a channel (orange) and signals from the four FPN channel of the AGET.

4.1.3 Pad signal amplitude gain-matching

In order to correctly analyse a track event, it is necessary to take into account the signal amplitudes from all the pads together. The amplitude response to a given collected charge varies for each channel. First, due to the electronics itself and secondly, due to small pad-micromesh distance variations, as mentioned in [96]. The latest one having a small effect and requiring advanced tests (scan with ^{55}Fe X-ray source and MAGBOLTZ calculations [116]) is out of the scope of this work. The effect of the variation of the amplitude responses is shown in Figure 4.5 in which the response of all channels for 6 different charges (sent using an external pulser) are plotted together.

The correction of the electronic gain effect requires to gain match the whole amplification of all channels. This is performed by sending pulse signals (with values covering the full amplitude range) on the mesh. For each input of the pulser V_{pulser} a channel-by-channel average amplitude response is calculated from about 1000 events:

$$Ampl_i(V_{pulser}) = \langle Ampl_i(V_{pulser}) \rangle_{1000} \quad (4.3)$$

The response of a given channel can be characterized by the curve of these averaged amplitude values as a function of the pulser input value, as shown in Figure 4.7. By performing a linear fit, the coefficients a_i and b_i characterizing the channel response can be obtained.

In order to gain-match the response from an individual channel i , the $Ampl_i(V_{pulser})$ curves need to be shifted towards the reference one. The calibration coefficients (c_i^0 and c_i^1) are obtained by fitting the channel response $Ampl_i(V_{pulser})$ against the reference values $Ampl_{ref}(V_{pulser})$. The correction for a given channel is then given by:

$$Ampl_i(q) = c_i^0 + c_i^1 Ampl_i(q) \quad (4.4)$$

The result of applying this correction can be seen in Figure 4.6.

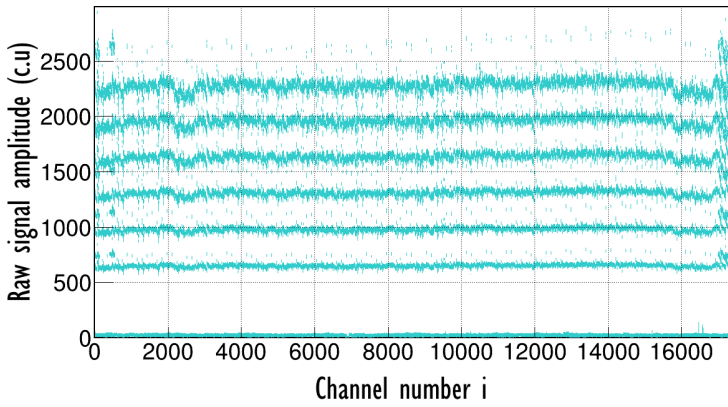


Figure 4.5: Baseline corrected amplitudes of the signal for all channels (128x128) with six different values for the amplitude of the pulse injected on the micromesh (~ 1000 events per pulser value). Variations of the amplitude response between the different channels can be observed.

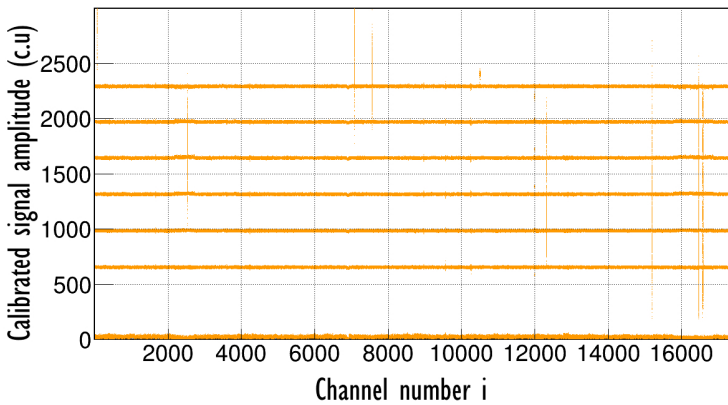
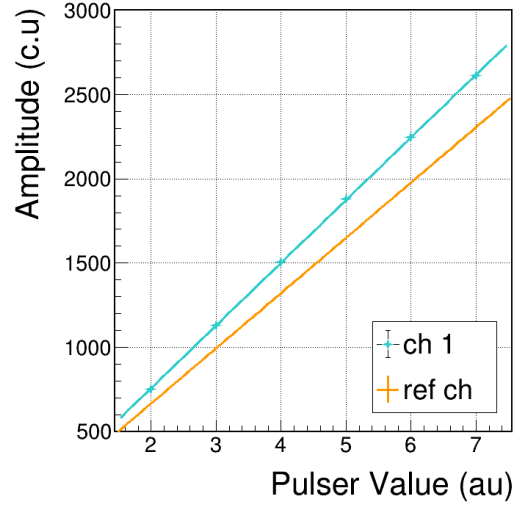


Figure 4.6: Corrected amplitudes of the signal for all channels (128x128) using the same data set of Figure 4.5 (~ 1000 events per pulser value). The vertical lines correspond to non-working channels (10 pads), representing 0.06% of the total number of pads.

Figure 4.7: Average response of a single channel (blue) as a function of the injected charge from an external pulse. The reference channel response shown in orange is chosen averaging 16 different channels.



4.1.4 Pad time signal alignment

Due to a clock distribution problem of the CoBo boards, there exist small variations of the time signal peak positions between the pads, as illustrated in Figure 4.8 where the time peak position (time bucket with the maximum amplitude) is plotted for a group of events given an input external pulse value. Since the position of the time bucket with the maximum amplitude is voltage-independent, the time correction is performed for a single pulse value input V_p by averaging the measured time over about 1000 events $t_i(V_p) = \langle t_i(V_p) \rangle_{1000}$. By selecting a reference channel time t_{ref} , the channel time signals are shifted as:

$$t_i = t_{ref} + t_{shift} \quad (4.5)$$

This results in an alignment of the time signal for all the pads, as shown in Figure 4.9

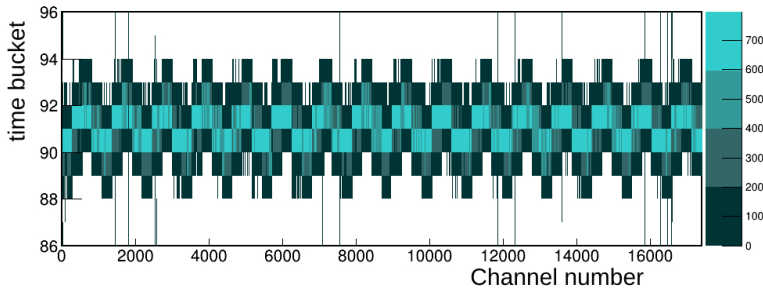


Figure 4.8: Raw time peak values for all channels (128x128) using a given pulse value (~ 1000 events).

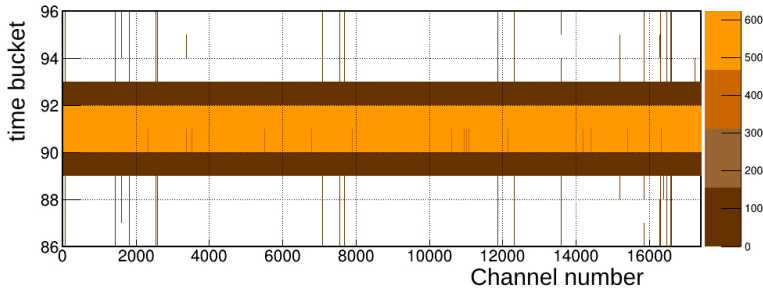


Figure 4.9: Corrected time values for the same data set of Figure 4.8 (~ 1000 events per pulser value).

4.1.5 Input signal reconstruction

As mentioned in Section 2.4, the output samples are not a direct digitization of the input current distribution. Although the treatment of the output samples is possible and sufficient in most of the cases, a more performant analysis can be achieved using the reconstructed input charge distribution. This can be important in the case of too vertical tracks, as evidenced in Section 6.10. The process of the signal input reconstruction is described in this section, and its use is later discussed in Chapter 5 when talking about the track fitting process. The use of the reconstructed signal requires a specific gain-matching correction (See Section 4.1.3 using reconstructed signal pulser responses).

The output measured signal $s_{out}(t)$ is the result of the pre-amplification and shaping of the input signal i_{int} in the AGET chips. All these processes (illustrated in Figure 4.10) compose the electronic response function $h(t)$ defined:

$$h(t) = \frac{1}{C_g} \cdot r_{shaper}(t) \cdot 2k \quad (4.6)$$

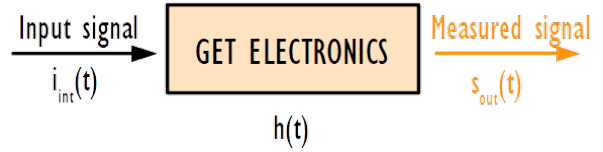


Figure 4.10: Scheme of input signal, response function and measured signal of the electronics.

The response function has mainly four terms: the $\frac{1}{C_g}$ term comes from the preamplification being C_g the gain capacitor. $r_{shaper}(t)$ represents the response due to the shaping. The factor 2 comes from the gain -2 amplifier located after the shaper. Finally, the k term corresponds to the conversion from amplitude to coder units.

Mathematically, the output charge distribution $s_{out}(t)$ is defined from the convolution of the input signal and the electronic response function:

$$s_{out}(t) = i_{int}(t) * h(t) \quad (4.7)$$

If the response function is known, then the input signal can be reconstructed by deconvoluting $s_{out}(t)$ from the response function.

To build an estimate response function $h(t)$ of the GET electronics, an output charge distribution $s_{out}(t)$ and the corresponding input signal $i_{int}(t)$ need to be determined. For this purpose, two different known signals $s_{pulser}(V = -600mV)$ and low voltage one¹ $s_{base}(V = +20mV)$ are sent to the different channels using the AsAd pulse generator². The output charge distribution $s_{out}(t)$ produced from the induced charge for a given channel i is calculated from the difference of these two signals (averaged for about 1000 events) as:

$$s_{out}^i(t) = \langle s_{pulser}^i(t) \rangle_{1000} - \langle s_{base}^i(t) \rangle_{1000} \quad (4.8)$$

Furthermore, by using the FPN channels in "functional test mode", the input signal i_{int} (from the sent pulse voltage) is recorded bypassing the amplification and shaping processes of the electronics. A single value, average of the two FPN channels signals from 1000 pulser events, is used for all the channels within the same AGET:

$$FPN_{out}^i(t) = i_{int}^i(t) = \langle FPN_{pulser}^i(t) \rangle_{1000} - \langle FPN_{base}^i(t) \rangle_{1000} \quad (4.9)$$

¹The use of the low voltage signal corrects for systematic effects as discussed in [93].

²Electronics internal pulser able to send individual signals to each channel.

Once s_{out} and s_{int} are determined, the response function can be extracted as the deconvolution of the output sample from the input signal. This is performed in the frequency space by using a FFT (Fast Fourier Transform) algorithm. Due to the imperfections in the response function, the deconvolution process induces an increase of high frequency noise in the reconstructed signal. To smooth the signal, a numerical low-pass filter $\Phi(f)$ is needed. The final reconstructed Fourier transform of the signal is then:

$$I_{rec}(f) = \frac{S_{out}(f)}{H(f)} \cdot \Phi(f) \quad (4.10)$$

where the capital letters stand for the $I_{rec}(f) = \mathcal{F}(i_{rec}(t))$. Some different filters have been applied to real signals from proton events in order to select a reasonable filter order and cutoff frequency in the context of the current work. Results with orders of 2, 4 and 8 (cutoff frequency fixed to 3 MHz) and cutoff frequencies of 5, 3, 1 MHz (filter order fixed to 8) are shown in Figures 4.11 and 4.12 respectively. The higher order filters result in a sharper attenuation of high frequencies. A lower filter cut frequency results in a more accurate time precision but a larger broadening of the reconstructed signal, as discussed in [93]. The chosen values (filter of order 8 and frequency 3) result from a balance between the signal-to-noise ratio and the reconstructed distribution precision.

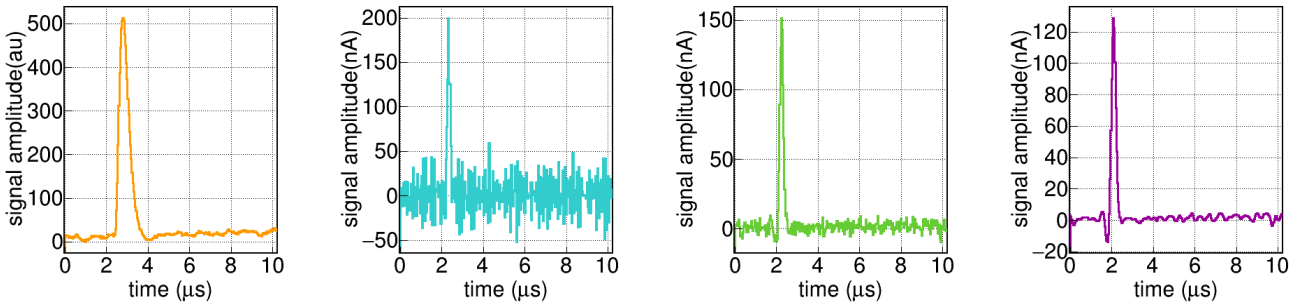


Figure 4.11: One pad signal example. In orange, the output signal, in blue, green and purple the reconstructed signal with filters of order 2, 4 and 8 respectively with a fixed cutoff frequency of 3. The latest one is chosen as a good compromise between time precision and low distortion of the signal.

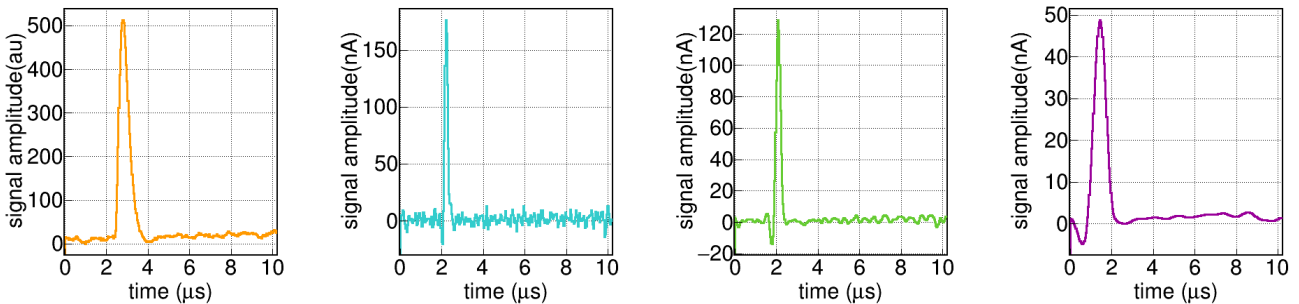


Figure 4.12: One pad signal example. In orange, the output signal, in blue, green and purple the reconstructed signal with filters of cutoff frequency 5, 3 and 1 respectively with a fixed filter order of 8. The cutoff frequency of 3 (green) is selected for the filter since it minimizes the fluctuations of the signal and preserves a good time precision.

4.2 CATS detector calibrations (CATibrations)

The analysis of the position signal provided by the CATS detector, described in Chapter 3 requires the use of the different 27 independent strip charge signals. For each charged particle traversing the detector, there are some fired strips in the cathodes around a central one (detecting a maximum deposited charge). The value for the positions (in the x and y plane) can be estimated using different approximations. In this work, a Gaussian fit is performed for each event to obtain the center of the position distribution. This value is further multiplied by the strip pitch (2.35 mm) to obtain the relative position in length units.

For a detection plane d (x or y), the position is calculated:

$$position(d) = N_c(d) * 2.35 \quad (4.11)$$

with c being the position of the center of the Gaussian peak and $N_c(d)$ the number of the CATS strip corresponding to the center of the Gaussian fit for a given detection plane d .

The charge response of each of the 27 channels to an induced charge may be different between them, as shown in the left of Figure 4.13. A gain matching, similar to the process described in Section 4.1.3 for the ACTAR TPC device, needs to be performed for the channels of the CATS detectors.

By sending different signal pulses on the wires, the gain matching coefficients (c_0^i , c_1^i) adjusting the individual channel responses to a reference channel are obtained³.

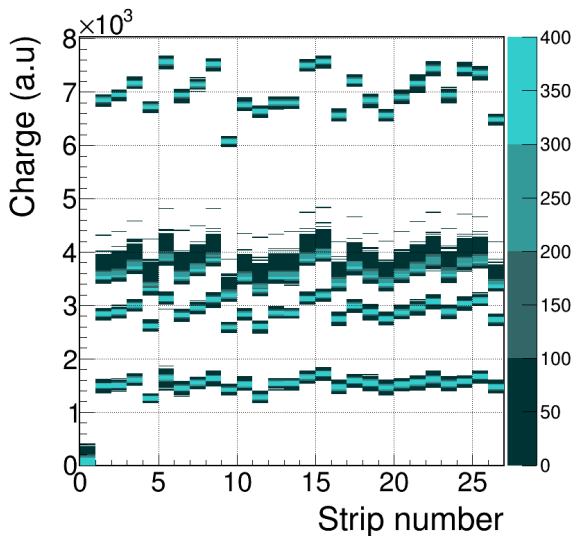


Figure 4.13: CATSD6 charge response of one of the positions (Y) for different pulser values without applying any gain matching.

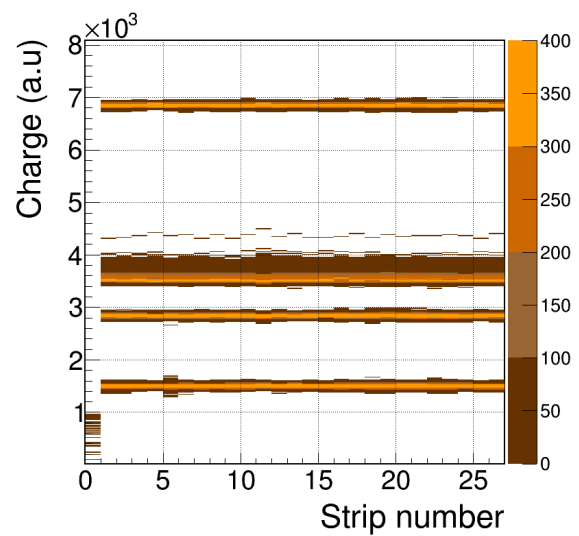


Figure 4.14: CATSD6 charge response of one of the positions (Y) for different pulser values after the gain matching process.

Ideally, for a good position reconstruction of a charged particle traversing the detector, only few channels, corresponding to the maximum charge response ones, need to be taken into account. This is achieved considering the charges above a defined pedestal ($Qd[i] > Qd_{ped}[i]$), defined from a measurement with no signal.

³More detailed in previous Section 4.1.3

The CATS charge deposit signal is calibrated as follows:

$$Qd_{cal}[i] = \begin{cases} Qd_{cal}[i] = 0 & (Qd[i] < Q_{ped}) \\ Qd_{cal}[i] = Qd[i] * c_0^i + c_1^i & (Qd[i] > Q_{ped}) \end{cases} \quad (4.12)$$

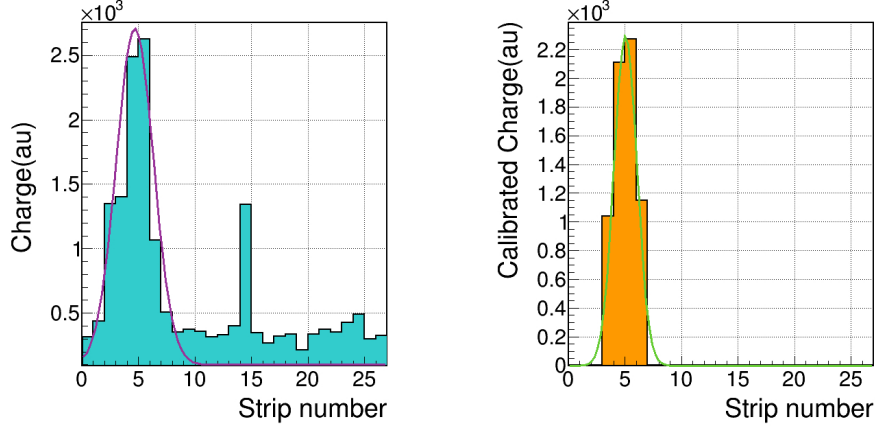


Figure 4.15: Comparison of CATSD6 (y position) signal for a single event for non-calibrated charge and calibrated one (left and right, respectively). The fit used to reconstruct the position is shown in purple and green lines.

4.3 Drift velocity measurements

When using a TPC detector, the third dimension information (z coordinate) is taken from the drift time of the electrons in the gas, as mentioned in Section 2.2 and expressed in equation 4.13. The length of the tracks (one of the most important analysed quantities in the detector) is thus sensitive to the drift velocity value, that converts the time information into length units. Consequently, a precise value of the drift velocity needs to be calculated to be further employed for the analysis of the tracks.

$$z = v_{drift} \cdot t \quad (4.13)$$

The electrons in the gas acquire a drift velocity proportional to the acceleration $\frac{eE}{m_{e^-}}$ due to the applied electric field strength E and the average time between collisions (τ) which depends on the gas characteristics and pressure. The drift velocity can be predicted from the relation [119]:

$$v = \frac{eE}{m_{e^-}} \tau \quad (4.14)$$

Usually written in terms of the mobility factor $\mu = \frac{e}{m_{e^-}} \tau$ as

$$v = \mu E \quad (4.15)$$

The drift velocity can be calculated using MAGBOLTZ simulations [120] knowing the gas characteristics, pressure and applied voltage. The drift velocity obtained for the gas mixture of the current experiment

(Ar(90%) + iC_4H_{10} (10%)) at different E/P (electric field strength divided by the pressure) values are shown in Figure 4.16

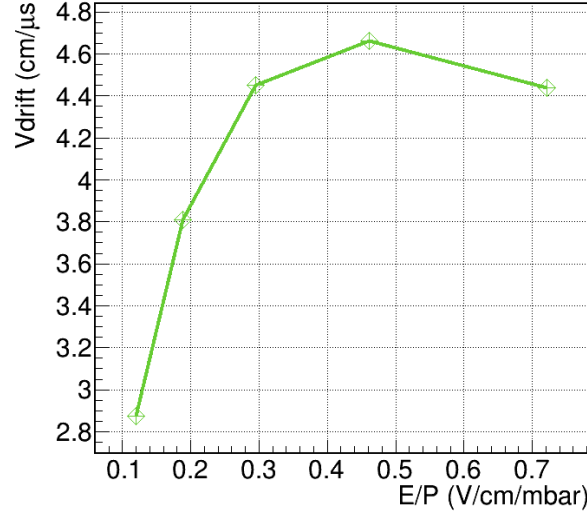


Figure 4.16: Calculated drift velocity using MAGBOLTZ simulations [120] for different values of E/P and a gas mixture of Ar(90%) + iC_4H_{10} (10%). From E/P=0.3 (V/cm/mbar) a saturation of the drift velocity value can be observed.

In some gases like argon-hydrocarbon mixtures, there exists a saturation effect in the drift velocity with respect to the applied voltage [76], as can be seen from the simulation result in Figure 4.16 for values of E/P above 0.3 V/cm/mbar. When performing an experiment with a TPC detector, working in this saturation region is desired. This prevents from critical changes on the drift velocity in the case of small electric field or pressure variations.

Experimental measurements of the drift velocity value were carried out before the experiment with an alpha source, aiming to select a convenient E/P value within the saturation region and to obtain an experimental value of the drift velocity. The general experimental procedure is introduced in Section 4.3.1. In the next two sections 4.3.2 and 4.3.3, drift velocity results from alpha-particle source tests and from the experiment (using protons) are discussed. In the last Section 4.3.4, these results are compared to simulated data using MAGBOLTZ/GARFIELD [120] [121].

4.3.1 Procedure

The experimental measurement of the drift velocity is possible by sending charged particles into the detector and analysing their trajectories. The energy of the incident particles need to be chosen within a correct energy interval: small enough so that they do not escape the detector and large enough to allow for an analysis of their trajectories in the gas. The range of a particle in the gas can be approximated by the distance between the final point and the initial point of the track⁴ ($\Delta p = p_f - p_i$) :

$$l_{xyz}(v_d) = \sqrt{\Delta x^2 + \Delta y^2 + \Delta z^2} = \sqrt{\Delta x^2 + \Delta y^2 + v_d^2 \Delta t^2} \quad (4.16)$$

This equation can be written in terms of the two-dimensional measured length (drift velocity indepen-

⁴The determination of p_i and p_f is further discussed in 5

dent) and the time difference:

$$l_{xyz}(v_d) = \sqrt{l_{xy}^2 + v_d^2 \Delta t^2}. \quad (4.17)$$

and further linearized as:

$$(l_{xyz}(v_d))^2 = l_{xy}^2 + v_d^2 \Delta t^2 \quad (4.18)$$

where l_{xy} and Δt can be measured experimentally.

Fitting the squared measured length in the (X,Y) plane (l_{xy}^2) against the squared time difference between the stopping and starting point (Δt^2) allows obtaining the squared drift velocity value (v_d)² denoted as V_D .

The incertitude in the drift velocity calculation is given by:

$$\Delta v_d = \frac{\Delta V_D}{\sqrt{4V_D}} \quad (4.19)$$

where ΔV_D is the error obtained from the linear fit.

4.3.2 Alpha source tests

Tests with an alpha source (²³⁹Pu + ²⁴¹Am + ²⁴⁴Cm) were performed before the experiment in order to optimize the settings and have an accurate experimental information about the drift velocity. The source main emissions are alpha particles with energies of 5.16 MeV, 5.49 MeV and 5.81 MeV. The process described in the previous section is performed for the three alpha particles by selecting the events with elliptical cuts in the l_{xy} against Δt plots, as shown in Figure 4.17. The linear fit is performed in (l_{xy}^2) against (Δt^2) for the three different group of events, as illustrated in Figure 4.18.

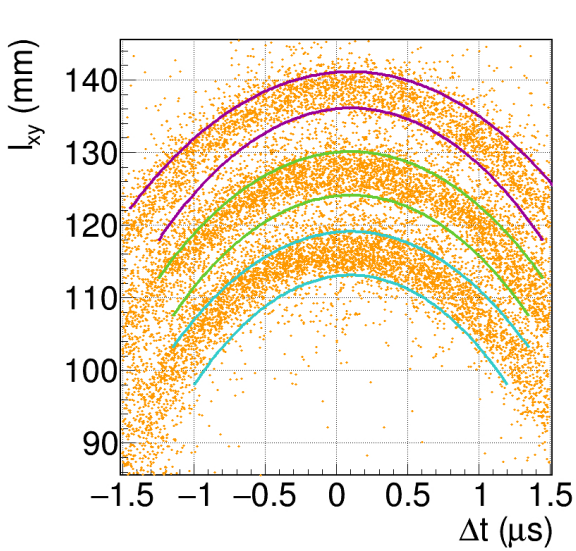


Figure 4.17: Time difference and length in xy dimensions and elliptical cuts.

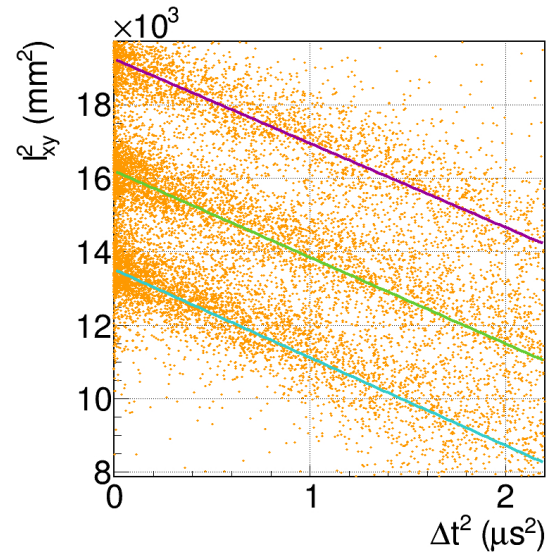


Figure 4.18: Linearization of length and Δt and performed fit from which the v_d^2 value is extracted.

The result of the measured drift velocity is taken from the average of the three different drift velocities obtained for each alpha particle (See Equation 4.20).

$$v_{drift} = \langle \text{sqr}t(v_{drift}^2) \rangle_{3\alpha} \quad (4.20)$$

This measurement, performed with $Ar(90\%) + iC_4H_{10}(10\%)$ at a pressure of 200 mbar, is repeated for different applied electric field values (E_{drift}). The electric field created in the ACTAR TPC detector depends on the applied voltages in the cathode ($V_{cathode}$) and the anode (V_{mesh}). This value is given by:

$$E_{drift} = \frac{V_{cathode} - V_{mesh}}{d_{drift}} \quad (4.21)$$

where d_{drift} is the distance between the cathode and the anode (256 mm). In the present work, E_{drift} was modified by changing the cathode voltage. The results of the measured drift velocities as a function of the E/P factor are shown in Figure 4.19. Alpha-source drift velocity measurements were carried out in experimental conditions for the two different pressure configurations. The result of the former one is also included in Figure 4.19, at $E/P=0.488$ (V/cm/mbar). Unfortunately, for the second configuration, the pressure is too high to be able to reconstruct the alpha tracks.

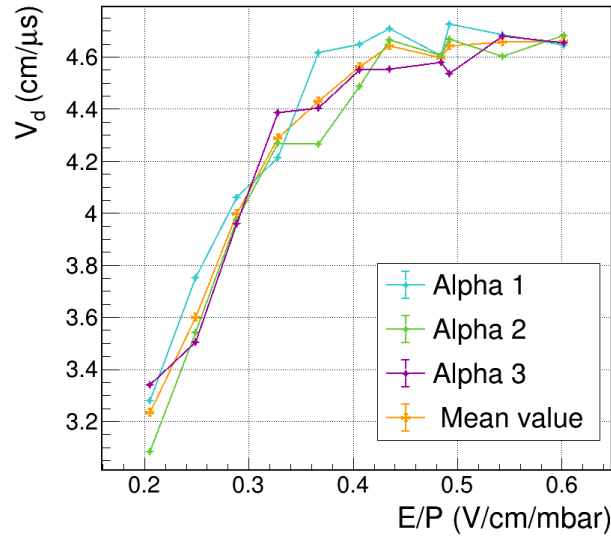


Figure 4.19: Drift velocity measurements as a function of the applied voltage on the cathode. The errors are omitted for an easier visualisation of the different components. (They are further included in Figure 4.22). The blue, green and purple lines correspond to the results obtained individually for the three energetically different alpha particles emitted by the $^{239}\text{Pu} + ^{241}\text{Am} + ^{244}\text{Cm}$ source. The orange one is an average of the three values.

This curve indicates the behaviour of the drift velocity with respect to the electric field. It is more convenient to select values of E/P over 0.4 V/cm/mbar from which the variation of the drift velocity with respect to the electric field and the pressure is smaller.

4.3.3 Drift velocity from proton tracks

The same process explained before can be carried out for proton tracks. ^{41}Ti , one of the isotopes studied in this work, is a well-known β -proton emitter with proton peaks at 988 keV and 1542 keV. These protons are slow enough to stay confined in the detector in most of the cases⁵ and energetic enough to have a few centimeters track to perform the drift velocity measurements. The drift velocity calculation corresponds to the average of the two different values of v_{drift} (obtained for each proton) since no energy dependence is expected, as in the case of alpha measurements.

$$v_{drift} = \langle \text{sqr}t(v_{drift}^2) \rangle_{2p} \quad (4.22)$$

The two different energy proton tracks can be selected in the same way as in the α tests (elliptical cuts in Δt against l_{xy} plot) but a second selection technique made in further steps of the analysis is performed instead. This technique consists in a pre-selecting of the ^{41}Ti protons in energy with a provisional value of the drift velocity. Details about the method to associate the protons to the ^{41}Ti emitter, the calculation of the proton lengths from a fitting of the track and the selection in energy are the focus of the analysis chapter 5. The l_{xy} against Δt and $(l_{xy})^2$ against $(\Delta t)^2$ proton distributions are shown in Figure 4.20 and 4.21 respectively.

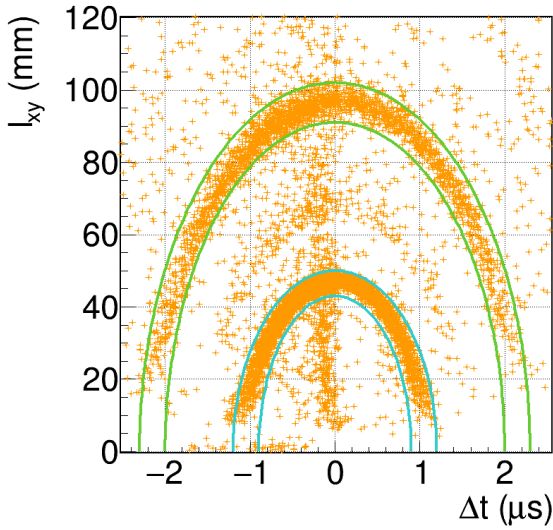


Figure 4.20: ^{41}Ti protons 2D lengths l_{xy} against time differences Δt between the beginning and the end of the tracks. Two main components can be observed, corresponding to 988 keV and 1542 keV protons. The measurements are made for the second configuration (pressure=450 mbar). The ellipses are plotted for comparison with the alpha results. The two components are selected by their energy value, instead using a preliminary value of the drift velocity (see Chapter 5).

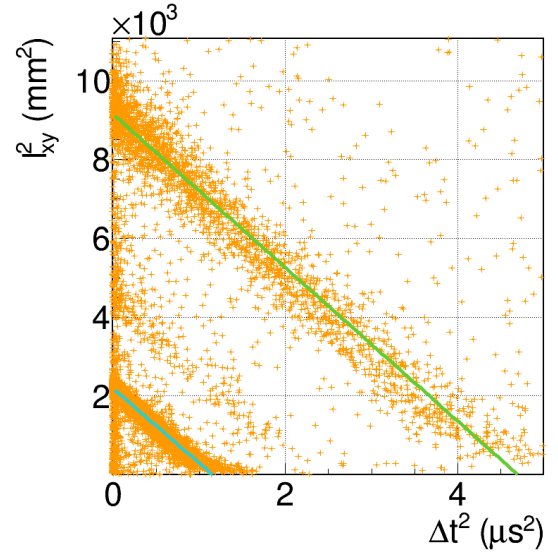


Figure 4.21: Linearization of both parameters and the corresponding fit performed to obtain the squared drift velocity value v_D^2 , denoted as V_D . An intermediate energy proton line with lower branching ratio is observed. This proton is not used for the average of the drift velocity because of its low statistics.

⁵Depending on the implantation position of ^{41}Ti

Measuring the drift velocity with proton tracks (for high enough statistics) is a more precise method for the calculation of this value than the alpha measurements, in which the tracks are not fully inside the detector due to the positioning of the alpha source outside the active volume. Furthermore, it becomes the only way to measure the drift velocity for the second pressure configuration (pressure set to 450 mbar). The final values of the drift velocity for both of the ^{41}Ti proton peaks are shown in Table 4.1 and plotted together with the alpha drift velocity measurements in Figure 4.22. The difference in precision comes from statistical effects. There are considerably fewer events in the first configuration than in the second one and more low energy protons (988 keV) than high energy (1542 keV) ones. The drift velocity value, used for further analysis steps, is the average value of the two different peaks for each of the pressure configurations.

	Configuration 1	Configuration 2
Peak 1	44 ± 1 (mm/us)	43.5 ± 0.4 (mm/us)
Peak 2	45 ± 2 (mm/us)	44 ± 1 (mm/us)
Mean	44 ± 1 (mm/us)	43.8 ± 0.5 (mm/us)

Table 4.1: Drift velocity results from the analysis of ^{41}Ti proton tracks for both configurations of the experiment, with pressures set to 300 and 450 mbar respectively.

4.3.4 Discussion and comparison of drift velocity results.

The comparison of these values with GARFIELD/MAGBOLTZ [121], [120] calculations present systematic differences, the predicted drift velocity being notably bigger. This could imply that the simulation does not reproduce well the experimental results at low pressure. These calculations, performed for particle physics, are mainly compared to higher pressure data sets [122]. Further studies with a high number of measurements, different gas mixtures and pressures, could be an interesting test of validity of these calculations at low pressure.

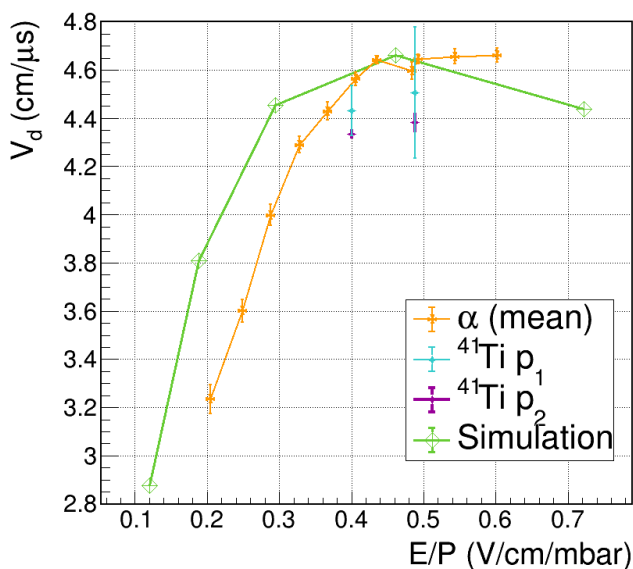
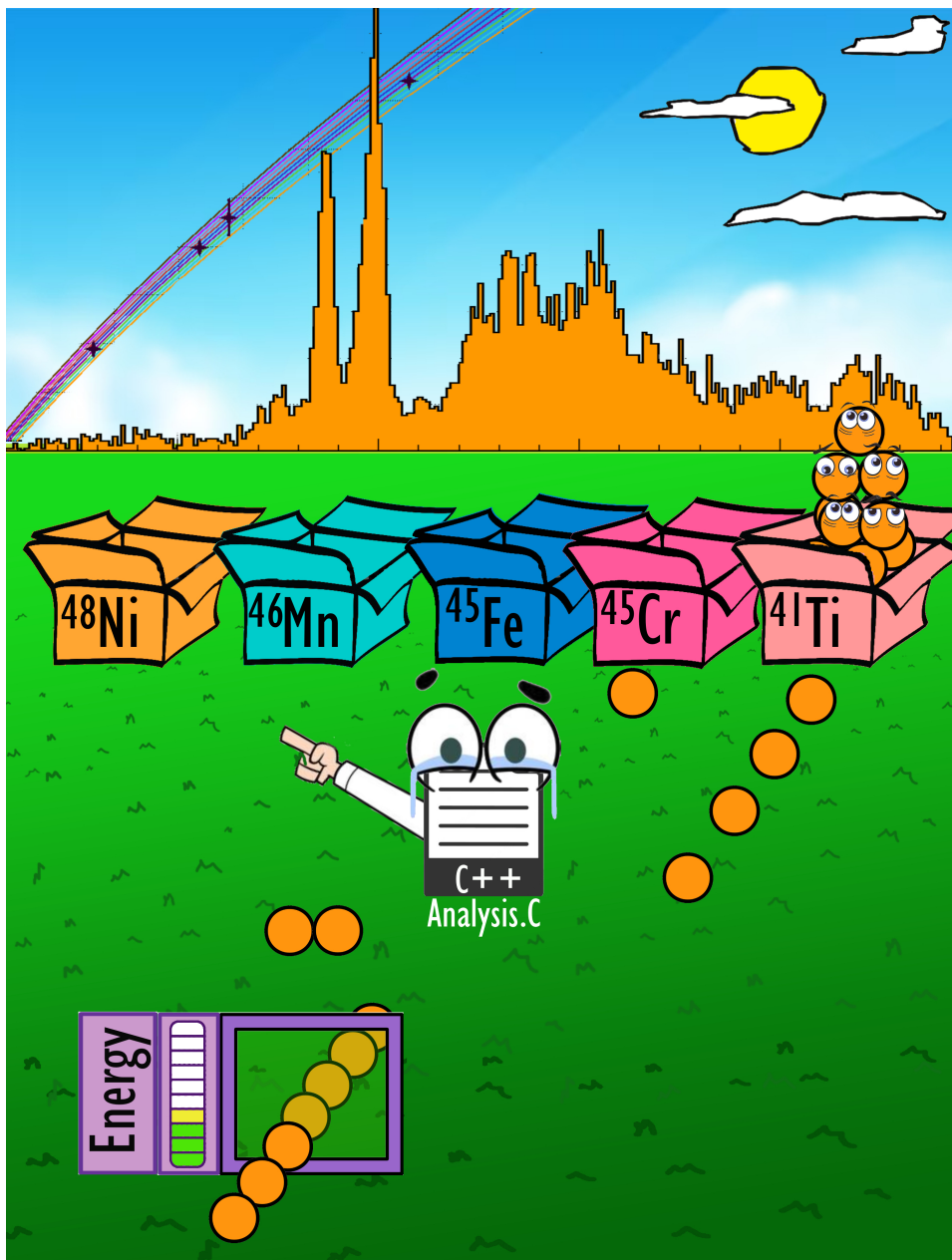


Figure 4.22: Drift velocities obtained using alpha source, from the proton track analysis compared with the simulation values. The orange points represent the average drift velocity value from the three different alpha particles. The blue and purple points are the v_{drift} obtained from the proton track analysis for the first and the second configuration respectively (300 and 400 mbar). Finally, the green curve are the values obtained with simulations using GARFIELD/MAGBOLTZ [121], [120].

Chapter 5: Analysis



Contents

5.1	Implantation and decay events, observables	98
5.2	Identification of the nuclei	100
5.2.1	Experimental parameters for identification.	102
5.2.2	Extrapolation of parameter values for exotic nuclei	103
5.2.3	Identification radius	103
5.2.4	Probabilities	104
5.2.5	Limitations and use of the 4D identification analysis	105
5.3	Proton track analysis	106
5.3.1	Number of tracks and initial fit values	106
5.3.2	Signal fitting	109
5.3.3	Proton energy determination	116
5.3.4	Interpretation and cleaning of the energy proton distributions: escaping protons	122
5.4	Implantation–Decay correlations	124
5.4.1	Time condition	124
5.4.2	Spatial condition	125
5.5	Non-neutralization of the ions, track dispersion parameter.	127
5.5.1	Fraction of emissions from the cathode	128
5.5.2	Drifting time of ions	132
5.6	Observables: half-life, proton energies, branching ratio	133
5.6.1	Half-life measurements	133
5.6.2	Proton Energies	135
5.6.3	Branching Ratio	142

The analysis of the E791 Experiment is presented in this chapter. The different nature of the events in the data set, implantations and decays described in Section (5.1), divide the analysis into three main parts: the identification of the produced nuclei (Section 5.2), the decay events (protons) analysis (Section 5.3) and finally, the correlation between both (Section 5.4).

An important effect encountered during the analysis, the non-neutralization of the ions in the gas, is reported in Section 5.5. Finally, the impact of this effect and the different strategies to obtain the results of the main observables: half-life, proton energies and branching ratios are addressed in the last section of this chapter (5.6).

5.1 Implantation and decay events, observables

In the experiment, due to the relatively long half-life of the studied nuclei (in the order of tens of milliseconds), compared to the drifting time of the electrons (order of micro seconds), the implanted ions and their decay products are triggered and registered as different events: implantations and decays, as already mentioned in the E791 experiment chapter 3.

An **implantation**, in the framework of this experiment, is an exotic nucleus, part of the secondary beam, that successfully reaches the ACTAR TPC detector and stops inside it, as illustrated on the left of Figure 5.1. Due to the large acceptance of the spectrometer during the experiment, several species fulfill these two criteria. The identification of each species (using the information available from the different detectors along the beamline) constitutes the first part of the data analysis, discussed in detail in the Section 5.2 of

this chapter.

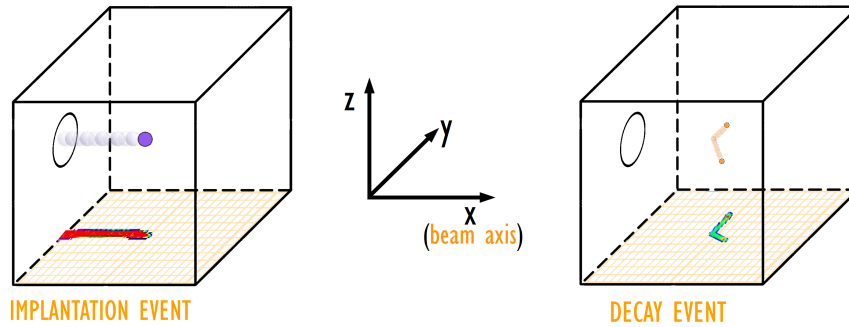


Figure 5.1: Illustration of the two main different events occurring in ACTAR TPC. An implantation (left) consists of an exotic nucleus entering the detector’s active volume and stopping inside. A decay event (right) registers the signals from particles (protons) emitted during the decay of an implanted ion. The X and Y axis correspond to the pad plane coordinates. The X axis goes along the beam direction and the Y axis, perpendicular to it. The vertical axis (Z) is perpendicular to the detection plane.

From the signal of the implantation event recorded in ACTAR TPC, the stopping point of the incoming nucleus P_{impl} in the volume can be determined. This information is used on an event-by-event basis to associate the decay events to the implantation by imposing a spatial condition. This process constitutes the third stage of the analysis, detailed in section 5.4. By measuring the stopping points of the incoming nuclei, the implantation depth distributions for each species can be determined. This information (already used for settings optimization during the experiment as discussed in Section 3.7) is needed to determine the detection efficiency of the detector, an important parameter to take into account when determining the branching ratios, as it will be detailed in Section 5.6.3.

A **decay** event consists of a charged decay product (proton(s)) from an implanted exotic nucleus in ACTAR TPC. These events only leave a signal in the ACTAR TPC device. An example of a two proton emission decay is illustrated in Figure 5.1. The analysis of the decay events (Section 5.3) provides information about the number of emitted protons, the length of each of the track signals from which the energy is determined and the relative emission angles for multi-proton emission cases. The decay point is also employed for the correlation between implantation and decay events, explained in Section 5.4.

From the analysis of both implantations and decays events, different observables can be measured, such as the half-life and the branching ratios of the proton emission decay branches. If the event consists of more than one particle emission, further details can be determined such as the number of emitted particles, the angular distribution and the individual proton energies, as schematically illustrated in Figure 5.2. The capability of measuring such details when multiple proton emission occurs is a characteristic of TPC detectors, being impossible to measure with silicon detectors.

The **half-life** information is determined from the time difference between the implantation event and the decay one from the time-stamp value, as already mentioned in Section 3.7. The determination of the half-life is further detailed in Section 5.6.1.

The **branching ratio** of decay modes involving different numbers of emitted protons is estimated from the number of decay events with different numbers of tracks. The determination of the number of tracks in a single event is further explained in Section 5.3.1.

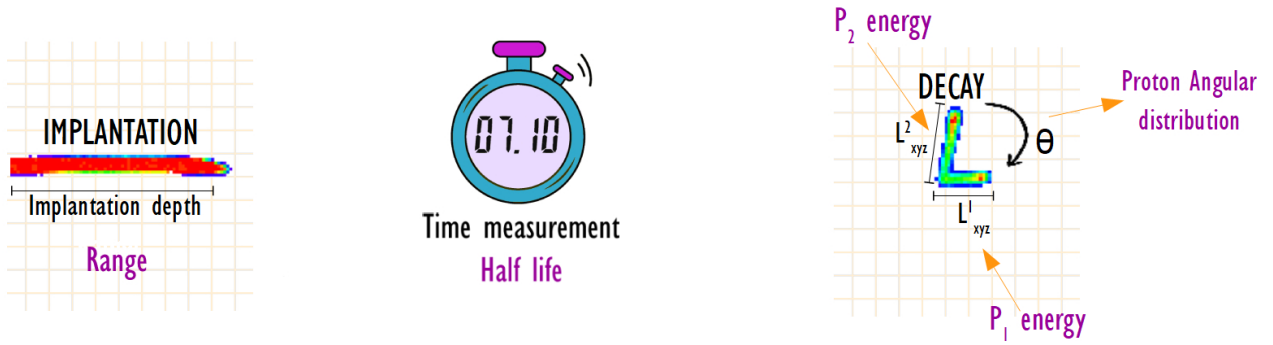


Figure 5.2: Pad plane projection schematic view of two different measured events (implantation and decay) in ACTAR TPC. In black, the quantities that can be directly measured (Implantation depth, time between the implantation and the decay, lengths of the proton tracks, angle between the protons). In purple, the main observables that can be obtained from them: half-life, proton energy and angular distributions.

To get the **individual proton energies** for both single and multiple track events, the length of the track(s) needs to be measured. This is performed by fitting the signal from these tracks, as further explained in Section 5.3. The energy of the protons can be estimated from their lengths using range to energy conversion tables as detailed in Section 5.3.3. For a given nucleus, we can estimate the branching ratio of the transitions by identifying and quantifying the different components in the decay proton energy distribution, as discussed in Section 5.6.3.

The **angular distribution information**, for multi-proton events, is obtained by computing the angle between the tracks. This is performed ideally after the fit process.

5.2 Identification of the nuclei

The fragmentation beam, even after the spectrometer selection, is composed by several nuclei (so-called cocktail beam). As introduced in Section 3.7, a first identification of the different components during the experiment allowed to select the correct mass region for the measurements and to tune the spectrometer for an optimization of the implantation of the desired nuclei in the ACTAR TPC detector. Besides, for the study of decay products associated to a specific nucleus, the identification process becomes one of the most important tasks in the analysis. The identification of the ions can be done by measuring the time of flight (between two time measurements) and the energy deposit in a silicon detector (2D identification matrix), as explained in Section 3.7.1.

In the current experiment, due to the very small number of events in the most exotic cases, the identification contours need to be extrapolated from the less exotic nuclei (see dashed pink contours in Figure 5.3). Furthermore, due to the specific conditions of the experiment (large momentum acceptance of the spectrometer), the nuclei overlap in the 2D identification matrix, as can be clearly seen in the blue dashed circles of Figure 5.3. This overlapping is much more relevant in the time of flight parameter for nuclei with same Z and $\Delta N = \pm 1$. When projecting this parameter on a Z line for a group of nuclei with equal Z (see Figure 5.4), a tail towards the lower N nucleus time of flight distribution is observed.

A first set of contours is created on a run-by-run basis for all nuclei in this 2D identification matrix (corresponding approximately to the ellipses shown in Figure 5.3) for a first basic identification of the nuclei

and the starting point of the more complex identification process described below. The result of these cuts for the $N=20$ line (^{41}Ti , ^{42}Ti in the projection on the Z line are also shown in Figure 5.4).

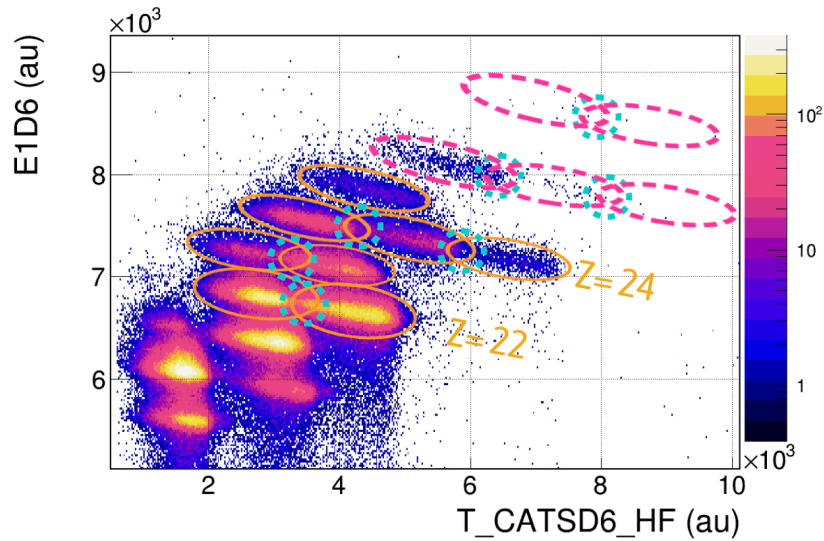


Figure 5.3: Measured time of flight between the cyclotron radiofrequency (HF) and the CATSD6 detector versus the energy deposit in a silicon detector (E1D6) for about 12 h of measurement in the final configuration. The different nuclei are delimited by the ellipses. The orange ones represent well-produced nuclei from which the contours can be defined. The dashed pink ellipses, represent the most exotic nuclei for which an extrapolation of the contours is needed. The blue dashed circles show the overlap in Z of the different isotopes.

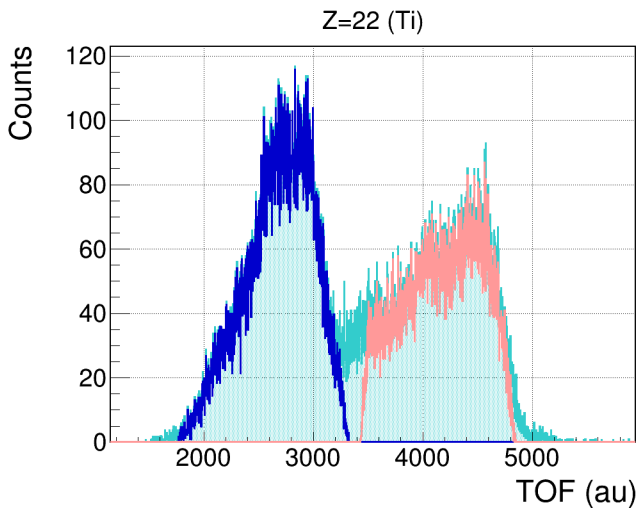


Figure 5.4: Projection of the time of flight for the $Z=22$ line (see Figure 5.3). The histogram in light blue corresponds to the projection of a global Z contour. In pink and blue, the projected time of flight values fulfilling initial contour conditions of ^{41}Ti and ^{42}Ti respectively (reduced with respect to those plotted in Figure 5.3). The tail of the ^{41}Ti ($N=19$) distribution contaminates the neighbour nuclei ^{42}Ti ($N=20$).

A common way of reducing the contamination between the nuclei (high-rate experiments) is simply to decrease the size of the contours, meaning rejecting some of the events. In the current work, this may lead to significant losses, especially for the most exotic nuclei. A more complex (4-dimensional) identification analysis is performed instead aiming to obtain an associated error of the (predicted) identification on an event-by-event basis, avoiding in this way to discard the events.

5.2.1 Experimental parameters for identification.

By including other parameters in the identification process, a better separation of the nuclei can be achieved. Within this work, four different experimental parameters are used for this purpose: the energy deposit in two of the silicon detectors E1D6 (located right after the Wien filter) and E3D6 (placed after the aluminium degrader), the time of flight T_CATSD6_HF (measurement between the cyclotron radiofrequency HF and the CATS detector placed after the Wien filter CATSD6) and the position (y-axis) given by the CATSD6_Y detector (see beamline scheme 3.3).

By approximating these parameters to be Gaussian-distributed, for a given nucleus Y , the expected values of the parameters $P_i(Y)$ are centered around a mean value $P_i^0(Y)$ with a width $\sigma_i(Y)$. For the less exotic isotopes, these values are obtained experimentally performing a Gaussian fit for events fulfilling the contour conditions in the 2D identification matrix, as shown in Figure 5.5 for the E1D6 value of one of the Z-lines ($Z = 24$, Cr).

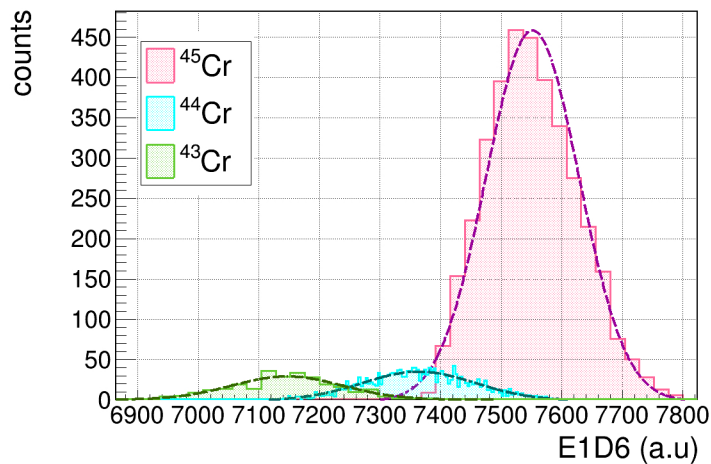


Figure 5.5: E1D6 energy values for a given run fulfilling the contour conditions in the 2D identification matrix for three different nuclei with same Z (^{45}Cr , ^{44}Cr , ^{43}Cr). The expected values for the centroid and the sigma for these three well-produced nuclei are obtained from the Gaussian fit, shown by the dashed lines.

5.2.2 Extrapolation of parameter values for exotic nuclei

The expected values of the parameters P_i^0 for the most exotic nuclei are obtained by extrapolation from the less exotic ones. This is carried out by fitting, for the different parameters, the expression predicting the mean values P_i^0 as a function of the number of protons Z and the isospin T_z of the nucleus:

$$P_i^0(Z, T_z) = [p_0] + [p_1] * Z + [p_2] * T_z + [p_3] * Z * T_z + [p_4] * Z^2 + [p_5] * T_z^2 \quad (5.1)$$

An example of this surface fit for the extrapolation of the E1D6 average value parameter is shown in Figure 5.6.

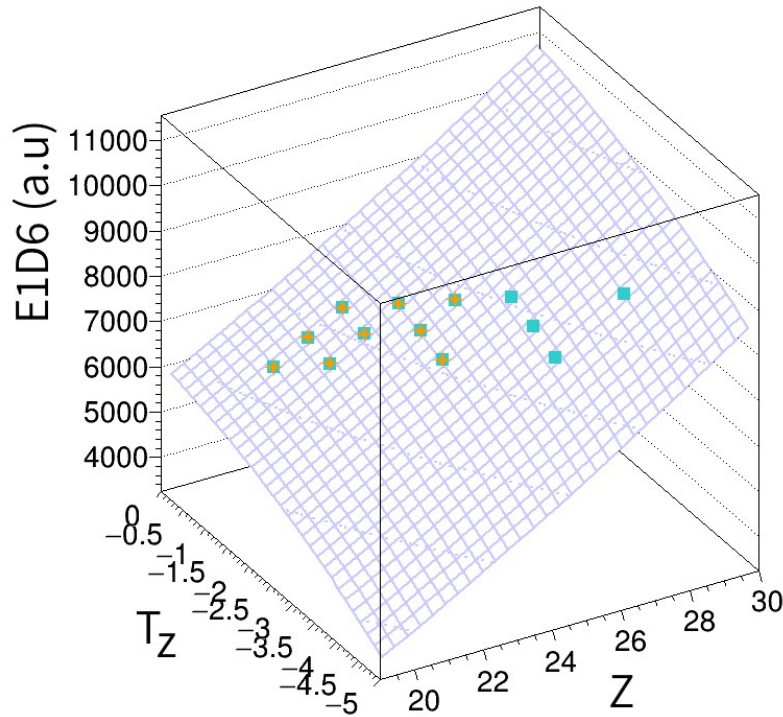


Figure 5.6: Centroid position of the E1D6 parameter as a function of Z and T_z . The experimental points (in orange) of the central values of E1D6 for the less exotic nuclei (obtained from a Gaussian fit) are used to fit the surface with Equation 5.1 to get the extrapolated values (blue points at higher Z) for the nuclei for which the statistics is insufficient.

The same process is repeated for all the parameters: centroids P_i^0 and widths (σ) for E1D6, E3D6, T_CATS6_HF, CATSD6_Y. In the case of the σ extrapolation for higher Z , the quadratic terms in Equation 5.1 are neglected.

5.2.3 Identification radius

In order to identify a given event A , a comparison between the experimental values of the identification parameters \vec{P}^A with the expected values for each nucleus group Y $\vec{P}_i^0(Y)$ needs to be performed. Assuming the parameters to be independent, the criteria of identification is defined as the distance between \vec{P}^A and $\vec{P}_i^0(Y)$ (i.e. measured energy value in E1D6 and the predicted values for the different candidates Y).

Taking all parameters into account at once, since they are not directly comparable between them, requires a change of basis. This is performed by using the reduced parameter values $p_i^r(Y)$, renormalized by the dispersion value $\sigma_i(Y)$:

$$p_i^r(Y) = \frac{P_i^A - P_i^0(Y)}{\sigma_i(Y)} \quad (5.2)$$

The identification radius of a measured event A with respect to a candidate nucleus Y is defined:

$$R(\vec{P}^A, Y) = \|\vec{p}^r(Y)\| = \sqrt{\sum_{i=1}^n (p_i^r(Y))^2} \quad (5.3)$$

where n is the number of identification parameters (4 in the current work).

The event A is identified to be a nucleus X within the candidate nuclei for which $R(\vec{P}^A, Y)$ is minimum.

If the correlation between the parameters is taken into account, the identification radius with respect to a nucleus X is defined:

$$R(\vec{P}^A, Y) = \sqrt{\sum_{i=1}^n \frac{1}{\lambda_i(Y)} (p_i^r(Y) \cdot \vec{v}_i(Y))^2} \quad (5.4)$$

where $\vec{v}_i(Y)$ and $\lambda_i(Y)$ are the eigenvectors and eigenvalues of the correlation matrix between the parameters, result of a change of basis of the initial parameters space $\vec{u}_1, \dots, \vec{u}_n$ (correlated) to a second space of parameters (non correlated) $\vec{v}_1, \dots, \vec{v}_n$.

The correlation factor is obtained performing a two-dimensional gaussian fit defined as:

$$G(P_i, P_j, Y) = \frac{N}{2\pi \cdot \sqrt{1 - \rho_{ij}^2} \cdot \sigma_i \cdot \sigma_j} \cdot \exp \left(-\frac{1}{2 \cdot (1 - \rho_{ij}^2)} \left[\frac{\Delta P_i^2}{\sigma_i^2} + \frac{\Delta P_j^2}{\sigma_j^2} - \frac{2 \cdot \rho_{ij} \cdot \Delta P_i \cdot \Delta P_j}{\sigma_i \cdot \sigma_j} \right] \right) \quad (5.5)$$

where P_i and P_j are two different identification parameters, σ_i , σ_j their respective widths, ΔP_i , ΔP_j the distance of the experimental values to their respective expected values P_i^0 , P_j^0 and ρ_{ij} the correlation coefficient.

Within this work, the correlation between the parameters of identification is approximated to be the same for each group of nuclei with the same number of neutrons (N). The correlation coefficients are obtained for the most produced of the nuclei in each N line fulfilling the 2D identification matrix contours conditions (^{41}Ti for the N=19 line, ^{43}V for N=20 and ^{45}Cr for N=21).

5.2.4 Probabilities

In order to estimate the error when identifying an event A with measured identification values P^A , the probability of identification as a nucleus of type Y_i ($P(Y_i|P^A)$) needs to be calculated. This is obtained using the Bayes theorem as:

$$P(Y_i|P^A) = \frac{P(P^A|P(Y_i)) \cdot P(Y_i)}{\sum_j P(P^A|Y_j) \cdot P(Y_j)} \quad (5.6)$$

where $P(P^A|P(Y_i))$ are the relative probabilities and $P(Y_i)$, the intrinsic probabilities (a priori) for each nucleus type Y_i . The intrinsic probability takes into account the experimental production rates of the different groups of nuclei. It is calculated by comparing the number of events N_i fulfilling a given contour condition (defined in the 2D-ID matrix) to the total number of nuclei.

$$P(Y_i) = \frac{N_i}{\sum_j N_j} \quad (5.7)$$

An event A is identified as a nucleus Y_i if the absolute probability $P(Y_i|P^A)$ is bigger than the one obtained for the rest of the candidates. The associated identification error is calculated from the absolute probability value:

$$\epsilon(X_i|P^A) = 1 - P(Y_i|P^A) \quad (5.8)$$

5.2.5 Limitations and use of the 4D identification analysis

Two different type of events are used for the analysis described in the previous subsections: non-implanted events and implanted events in the detection volume. For the former group, the available information measured in ACTAR TPC is useless, and no associated decay events can be studied. On the other hand, the events that correctly stop in the detector are used in the identification process in a special way, not only by using the identification detector signals but also by studying their decay products. This information became a key step when optimizing the settings during the experiment, as explained in Section 3.7, and it is further employed to estimate the limits and performance of the identification process (i.e. the observation of two-protons events associated to a nucleus not emitting two protons indicates a wrong identification of the event). As later reported in Section 5.6.2, identification issues are found for the most exotic nuclei. A more suitable modeling of the parameter distributions may be required to reproduce the mixing of the different species, as further discussed in Chapter 7, especially for the time of flight parameter.

The 4-D identification method having, at the current date, some limitations, it is used in the following way: the initial contour conditions defined in the 2D identification matrix are kept as a first identification guidance. The identification is performed on an event-by-event basis within three different categories, as schematized in Figure 5.7: The identification of "type 1", obtained when the parameters (energy E1D6 and time of flight T_CATSD6_HF) belong to a candidate nucleus contour defined in the 2D identification matrix and the identification analysis predicts the same identity for the event. The identification of type 2, obtained when the contour identification and the 4-D identification analysis are not in agreement. Finally, the identification of type 3 concerns events that do not fulfill any contour condition in the 2D-ID matrix and are thus classified only by the 4-D identification analysis.

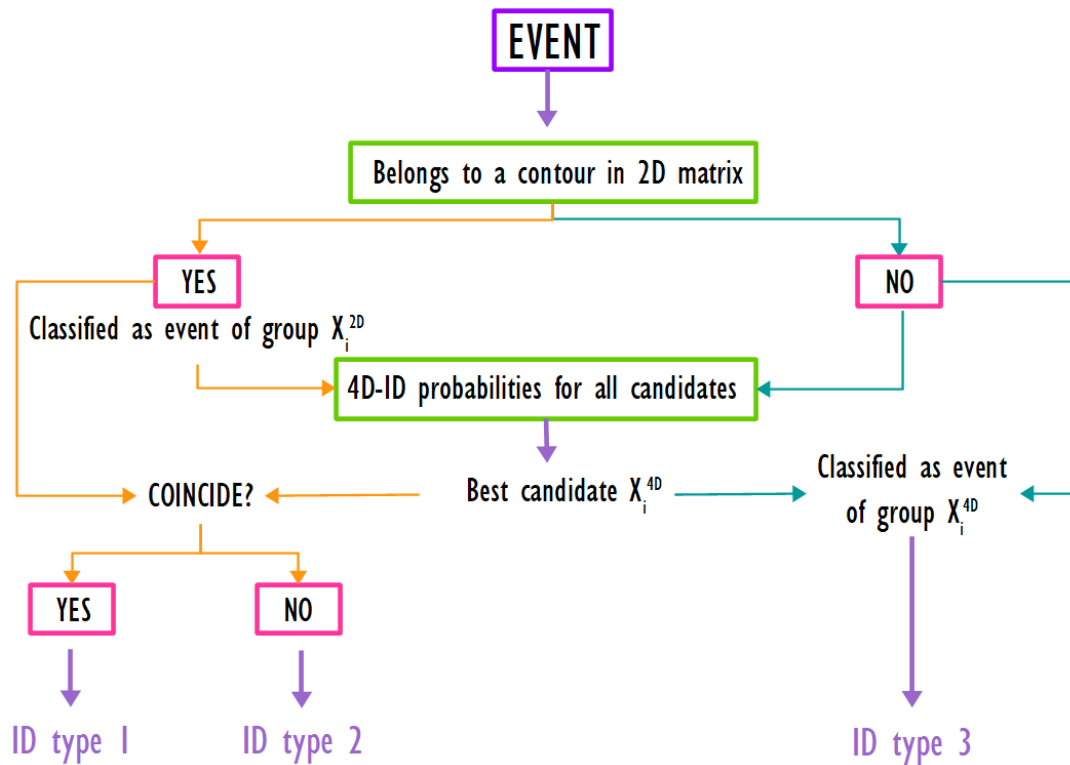


Figure 5.7: Scheme of the use of both 2D contour-based classification of the nuclei using the identification matrix (see Figure 5.3) and the 4-dimensional identification analysis. Note that all events are classified and more or less strict identification conditions can be further applied.

In the present work, an identification of type 1 will be required for most of the nuclei except for the most exotic ones (^{45}Fe , ^{49}Ni and ^{48}Ni) where the events with identification of type 2 will be taken into account as well. In both cases, the energy deposit and time of flight are requested to lead to one of the defined contours in the 2D identification matrix. Under this requirement, the remaining contamination in the present results (See Chapter 6) may always happen from lower N values, and it is considered negligible otherwise (i.e.: ^{41}Ti cannot be contaminated from its higher N neighbour ^{42}Ti) because of the definition of the cuts in the identification matrix, as shown in Figure 5.4.

5.3 Proton track analysis

The analysis of the proton tracks is carried out in several steps: first, the number of protons in each event and a first estimate of the emission and stopping point(s) of the track(s) in the detector need to be determined (subsection 5.3.1). A fit of the proton tracks is performed using the information of the previous step as initial values (subsection 5.3.2). Once the tracks are fitted, the range of the particles in the gas are determined and converted into energy units as described in subsection 5.3.3. Further considerations concerning the resulting proton energy distribution and background are further studied in Section 5.3.4.

5.3.1 Number of tracks and initial fit values

First of all, a linear 3D fit is performed to divide the decay data set into two groups: one track events and more than one track events. For the second group, the number of tracks n_T is determined using a 3D

adaptation of the Hough algorithm [124]. In both cases, a pre-calculation of the emission point P_0 and the stopping point(s) P_1^n is performed. These three steps are discussed in the following subsections 5.3.1, 5.3.1 and 5.3.1 respectively.

Linear fit (single track and multiple track)

In order to divide the data set into single and multiple track cases, a first linear 3D fit of the particle track is performed, using the linear least squares fitting technique (adapted code from [123]).

In the context of this analysis, most of the tracks are indeed one-particle emissions. By selecting fits with unsatisfactory regression coefficient¹, multiple particle emissions, scattered tracks or events with extraneous traces are separated from the one-particle emission case. Performing this first linear fit is fast, and it reduces significantly the number of calls to a more complex function (Hough 3D) to determine the number of tracks in an event.

Hough 3D algorithm (determination of n-track events)

When the linear fit is not satisfying, the Hough 3D algorithm [124] is employed to determine the number of tracks in the event.

The Hough algorithm, originally proposed for line detection in a 2D space by Hough in 1962, is a voting scheme for locating geometric objects in point clouds. The idea behind this algorithm is to discretize the infinite space, converting it into an accumulator space (Hough space), a finite number of parameter cells.

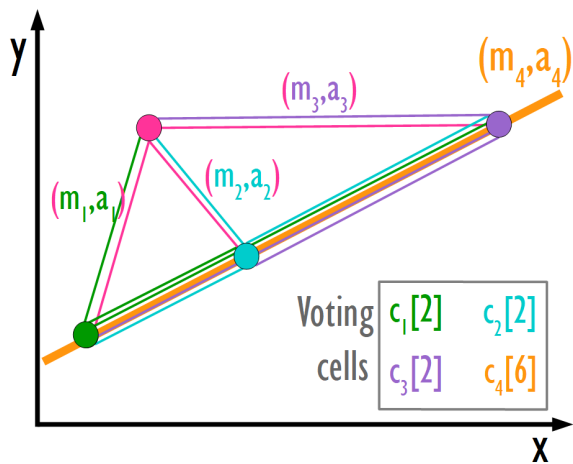


Figure 5.8: Group of four points in two dimensions. The lines connecting them correspond to the number of line candidates $N=4$. The three aligned points will vote for the same cell c_4 corresponding to the line with coordinates (m_4, a_4) which correspond to the orange line.

In a basic 2D case, for a measured point in a point cloud, there are infinite lines that can pass through it. Determining the common line to which a group of points belong to, in this way, results into an infinite comparison of the possibilities. The Hough "discretization" of the infinite space is made by the construction of the lines between the measured points (not infinite), with line coordinates (m_i, a_i) . The space is then discretized with a number of N lines (corresponding to all the lines built between the measured points) and the parameter voting cells, c_i for each line. An individual point belonging to this parameter space "votes" for all lines to which it may belong to by adding a vote in the correspondent parameter cell. A parameter cell with many votes then corresponds to a line with many points. An illustration of this space discretization in a simple case containing few points is shown in Figure (5.8).

¹selected to be the average distance between the cluster and the projection over the fit (4 pads), which takes into account the width of the proton track.

The voting process is done in an iterative way by selecting the line with the maximum number of votes and removing the corresponding points that are close to it. Then, following lines are found in an iterative way until very few points are left or a specified number of lines is found. The line coordinates for the discretization of the space are usually not the Cartesian ones. In particular, when using the adaptation of the Hough 3d algorithm [124], this is performed based on the Roberts's minimal and optimal line representation [125] and the discretization of the line orientations based on the tessellation of Platonic solids method [126].

As an input for the algorithm, a point cloud data in the format (x, y, z) is required. This is provided by selecting the pads that received an amplitude signal over a defined threshold in one event. Other parameters need to be specified as the maximum number of lines (nl), the minimum vote count (minvotes) and the step width (dx). The maximum number of lines in this work is selected to be three, since no more than three particle emissions are expected. The minvote is the minimum count that one line needs to be chosen and it is set to 9 in this work. This value is chosen by testing the algorithm on the smallest tracks. The step width corresponds to the spread of the points around the lines, and it is important to avoid a two lines output corresponding to a wide track. To adapt this parameter to the current analysis, first information about individual track widths in an event-by-event basis is required, since their values within the data set can be quite different from one event to another (energetic protons escaping the volume have much more thinner tracks than lower energy protons not escaping the detector). Instead of adapting this parameter for each event, which will require a previous fit of the track, the output lines are compared in a second step such that they do not have the same direction by computing their cross product. This allows to discard two parallel lines corresponding to the same wide track. Then, the default value proposed in [124] for the Hough space cell width, defined in Equation 5.9 is chosen.

$$dx = \frac{\sqrt{(x_{max} - x_{min})^2 + (y_{max} - y_{min})^2 + (z_{max} - z_{min})^2}}{64} \quad (5.9)$$

Track extreme points determination

The decay point P_0 and the stopping point(s) of the different proton(s) P_1^n are obtained by the determination (in 3D) of the extreme points of the tracks, the "Good Extreme Candidates (GEC)".

The points corresponding to the maximum and minimum values of the track in the three coordinates X,Y,Z compose the first six points of the GEC group, as illustrated in Figure 5.9. A seventh candidate can be found, taking the 3D point coordinates containing the maximum collected charge a_{max} on the detection plane.

One track case: If the event consists of a single proton, there are only two different extreme points in the track, meaning that only two of the 7 GEC points are different from each other. In this simple case, the maximum and minimum values of one of the coordinates (i.e. P_{xmin} and P_{xmax}) allow determining the extreme points of the track. To avoid a wrong result in the case of parallel tracks with respect to the axes, the distances $\Delta_x = P(x_{max}) - P(x_{min})$ and $\Delta_y = P(y_{max}) - P(y_{min})$ are computed, and the extreme points are taken from the coordinate with the larger distance between the points. To determine which of the extremes is the emission point and which is the stopping one, the distance to the center of mass of the track is computed. Due to the shape of the energy deposit (Bragg Peak curve), the extreme point closer to the center of mass is assigned to be the stopping point of the track.

Multiple-track case: For an event with n identified tracks, the GEC points are compared between them to determine the $(n+1)$ extreme points. Three of them out of 7 are different in a two-proton decay,

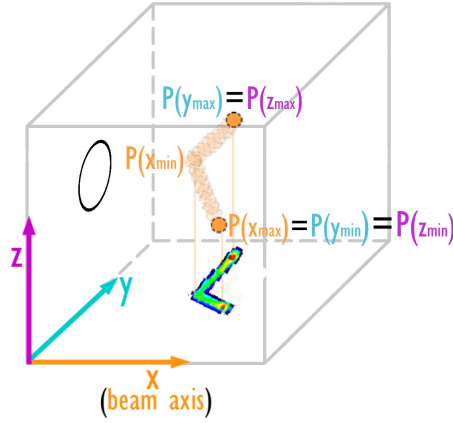


Figure 5.9: Scheme of a two-proton track and the corresponding extreme points in 3D. In the two-tracks case, only 3 points from the 6 extremes candidates are different from each other.

as illustrated in Figure 5.9 and four out of 7 in a three-proton decay. This simple method is fast and satisfactory within this framework in which the maximum of particles in an event is three. In the case of inconsistencies between the number of tracks given by the Hough 3D algorithm and the number of (different) extreme values found, the event is treated manually using a fitting interface. Once the $n+1$ extreme points are obtained from the GEC group, the emission point can be identified from the rest of the extreme track points by computing their distances to the intersection of the previously defined lines.

The number of tracks in an event n , the emission points P_0 and the stopping points of the tracks P_1^n , constitute the initial values for the next step of the analysis, the track fit. Examples of events with different numbers of protons and the pre-fit obtained values as explained below are shown in Figure 5.10.

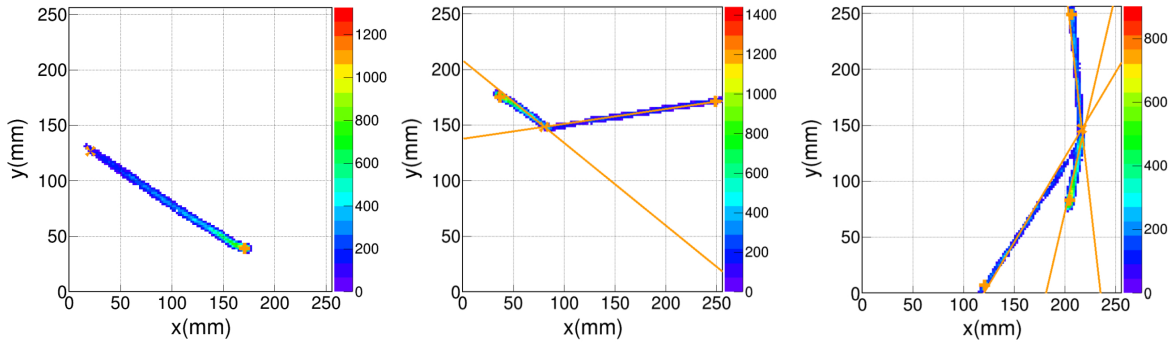


Figure 5.10: Examples of single proton emission (left), β -two proton emission (center) and β -three proton emission (right) in the pad plane projection. The lines are the output of the Hough algorithm as explained in the text. The decay points and the stopping point(s) (or limits in the pad plane) of the different tracks, are represented in orange.

5.3.2 Signal fitting

The fit of the tracks is performed by minimizing the difference between the experimental measured amplitudes (S^{exp}) for each pad (n) and the expected value given by a model function S^{fct} defined by a set

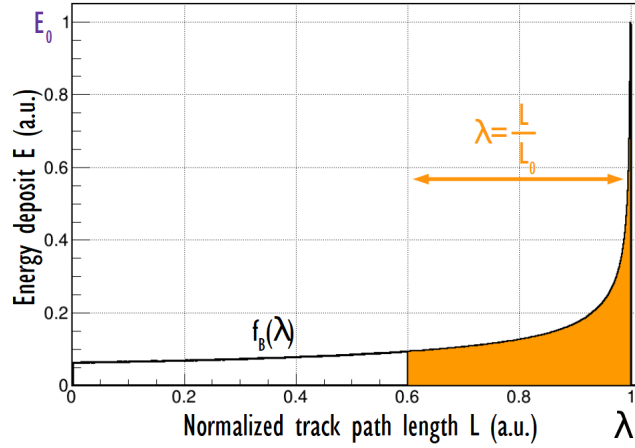


Figure 5.11: Normalized energy loss function f_B of a 10 MeV proton simulated with GEANT4. The energy deposit $E(\lambda)$ for a particle with reduced length λ is shown in orange.

of parameters Θ as defined in Equation 5.10.

$$D^2(\Theta) = \sum_n (S^{exp}(n) - S^{fct}(n)). \quad (5.10)$$

The model function may reproduce the energy loss along the track, taking into account the dispersion due to the drift of the electrons until reaching the detection plane. This is achieved by its convolution with a normalized Gaussian distribution.

Energy loss function

The energy deposit of a proton in a gas has a well known shape (Bragg Peak curve), easily reproduced from energy loss tables or simulation. Since the signal amplitude recorded in each pad is proportional to the initial energy deposit of the ionizing particle, the energy loss function f_E can be built using a Bragg Peak curve. This function is composed of two main ingredients: the track curve, defined as the segment between the initial P_0 and final P_1 points of the track, and the Bragg peak energy loss model.

The coordinates of a point in the trajectory axis can be defined with a coordinate $\epsilon \in [0, 1]$ along the path where the extreme values of ϵ : 0 and 1 correspond to the initial and final points in the trajectory axis (P_0 and P_1 respectively), as written in Equation 5.11.

$$P(\epsilon) = P_0 + \epsilon(P_1 - P_0). \quad (5.11)$$

The vertical information $z(\epsilon)$, since it is measured from the drift time, has no absolute value and needs to be converted into length units by multiplying by the drift velocity v_{drift} , a concept introduced and calculated in the previous chapter 4. $z(\epsilon)$ is defined as:

$$z(\epsilon) = z_w + [\epsilon(t_1 - t_0)] \cdot v_{drift}. \quad (5.12)$$

where z_w is the vertical position of the detector entrance window (centered at 110 mm) equal to the Z value at the initial point of a proton ideally emitted in the center of the entrance window.

The Bragg Peak model used in the context of this work consists of an energy-loss function f_B for a proton of maximum energy E_0 and associated length L_0 , both normalized to 1. The function, built from the Bragg peak curve obtained for a reference proton of 10 MeV using a GEANT4 [127],[128] simulation, is shown in Figure 5.11.

For a measured particle with energy $E < E_0$ and thus a length $L < L_0$, the reduced length parameter can be defined as $\lambda = \frac{L}{L_0}$. The energy deposit $E(\lambda)$ for a particle with reduced length λ is given by Equation 5.13. It corresponds to a fraction of the full Bragg peak model, as illustrated in orange in Figure 5.11.

$$E(\lambda) = E_0 \frac{\int_{1-\lambda}^1 f_B(\lambda) d\lambda}{\int_0^1 f_B(\lambda) d\lambda} \quad (5.13)$$

The energy loss along the track f_E can thus be described using the reduced length parameter λ , an amplitude scale factor A and the previously defined coordinate along the path, $\epsilon \in [0, 1]$, as shown in Equation 5.14.

$$f_E(\epsilon|\lambda, A) = Af_B(\lambda + (1 - \lambda)\epsilon) \quad (5.14)$$

The amplitude scale factor will adjust for the proton energy value with respect to the normalized maximum amplitude (reference proton amplitude value at $\lambda \approx 1$). The length parameter λ takes values from 0 to 1 depending on the energy of the proton to be fitted.

Dispersion of the charge deposit due to the drift of the electrons

The charge deposit can be defined in two dimension (XY plane) by convolution of the energy loss function $f_E(\epsilon|\lambda, A)$ in the trajectory axis with a Gaussian of width σ (5.15).

$$f_{XY} = f_E(\epsilon|\lambda, A) \cdot G_{2D}(\epsilon, \sigma_{XY}) \quad (5.15)$$

The width parameter σ_{XY} corresponds to the dispersion of the signal due to the drift towards the pad plane. This dispersion depends on the vertical coordinate as $\sqrt{z(\epsilon)}$: a charge created further from the pad plane produces a more dispersed signal with respect to an ionization that takes place close to the pad plane. Since the electric field is uniform in the gas volume, the dispersion is the same for the whole pad plane $\sigma_{XY}(z(\epsilon))$. It is defined from two parameters (σ_{XY}^0 and σ_{XY}^1) by Equation 5.16:

$$\sigma_{xy}(z(\epsilon)) = \sigma_{XY}^0 + \sigma_{XY}^1 \sqrt{z(\epsilon)} \quad (5.16)$$

The distribution function can also be defined in three dimensions in order to take into account the full time distribution measured on each pad. This is carried out by the use of a three dimensions normalized Gauss distributions for the convolution. The dispersion factor along the Z axis $\sigma_z(z(\epsilon))$ is defined from two extra fit parameters (σ_z^0 and σ_z^1) as shown in Equation 5.17:

$$\sigma_z(z(\epsilon)) = \sigma_z^0 + \sigma_z^1 \sqrt{z(\epsilon)} \quad (5.17)$$

The dispersion factors are the same for all proton tracks within the same detector and gas settings (drift voltage, pressure). Ideally, once a large number of fits are performed, the functions $\sigma_{xy}(z(\epsilon))$ and $\sigma_z(z(\epsilon))$ can be determined and fixed, as further discussed in Section 7.2.

Contribution of all pads and set of parameters

The amplitude signal of a single pad is built as the sum of the contributions of all points along the trajectory as defined in Equation 5.18

$$S_{ampl}^{fct} = \frac{1}{\sqrt{2\pi} \cdot \sigma_{XY}} \cdot \int_{\epsilon=0}^{\epsilon=1} f_E(\epsilon|\lambda, A) \cdot G_{2D}(\epsilon, \sigma_{XY}) \cdot d\epsilon \quad (5.18)$$

If the time information is taken into account (full 3D fit) this Equation is written:

$$S_{3D}^{fct} = \frac{1}{\sqrt{2\pi} \cdot \sigma_{xy} \sigma_z} \cdot \int_{\epsilon=0}^{\epsilon=1} f_E(\epsilon|\lambda, A) \cdot G_{3D}(\epsilon, \sigma_{XY}, \sigma_Z) \cdot d\epsilon \quad (5.19)$$

The functions defined in Equations 5.18 and 5.19 are two different models that can be used for the minimization (Equation 5.10).

The set of parameters Θ used to minimize the measured values with respect to the defined distribution function can be divided in three groups: The track curve parameters, Θ_p : composed of the initial and final track points \vec{P}_0 and \vec{P}_1^i , the Bragg peak model parameters Θ_B : λ^i , A^i , and the parameters that define the dispersion of the signal in the XY plane: Θ_d : σ_{xy}^0 , σ_{xy}^1 and σ_z^0 , σ_z^1 for the dispersion in the third dimension. This results (for a single-particle fit) in a total of 12 parameters for a fit taking into account the dispersion in Z and 10 parameters otherwise. In the case of a multiple track event, the number of parameters in the second case, depending on the number of particles, n_t , is given by:

$$n_\Theta = \Theta_p(n_t) + \Theta_B(n_t) + \Theta_d = (3 + 3n_t) + 2n_t + 2 \quad (5.20)$$

Different levels of fit

Two different functions for the minimization process have been described in the previous subsections: the fit taking into account only the dispersion in the XY plane and the one taking into account also the dispersion in the Z dimension (3D).

The 3D fit is performed using, apart from the amplitude signals, the full time signal distribution for each pad. This fitting process requires the use of the reconstructed input signal obtained from the response function, process explained previously in Section 4.1.5. This fit, being the most accurate option (especially for vertical tracks or events with multiple tracks), requires large computing times.

A third intermediate-level fit is defined by including a timing term $S_t^{fct}(n)^2$ as a contribution to the function S_{amp+t}^{fct} to be minimized, as expressed in Equation 5.21. An arbitrary coefficient ζ is included and adjusted to assure similar contributions of both amplitude and time components in the minimization process.

$$S_{amp+t}^{fct}(\Theta) = \sum_n (S_{amp}^{fct}(n))^2 + \zeta (S_t^{fct}(n))^2. \quad (5.21)$$

The time information associated to the pads (S_t^{fct}) is defined considering a time average of the signal contribution along the track, weighted with the corresponding amplitude:

$$S_T^{fct}(x, y) = \frac{\int_{\epsilon=1}^{\epsilon=0} t(\epsilon) \cdot f_E(\epsilon|\lambda, A) \cdot G_{2D}(\epsilon, \sigma_{XY}) \cdot d\epsilon}{\int_{\epsilon=1}^{\epsilon=0} f_E(\epsilon|\lambda, A) \cdot G_{2D}(\epsilon, \sigma_{XY}) \cdot d\epsilon}. \quad (5.22)$$

The intermediate solution (2D amplitude+T) fit being a good compromise between performance and computing time is preferred in this work for single proton fits. For multiple tracks events, a 3D fit from the reconstructed input signal is performed. Examples of single and a two proton fits are shown in Figures 5.12 and 5.13 respectively.

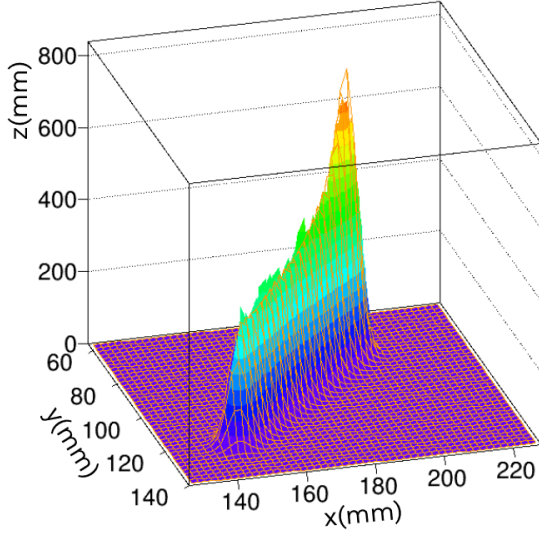


Figure 5.12: Pad plane amplitude distribution of a proton track. The result of an amplitude +T fit, using Equation 5.21 is shown in orange.

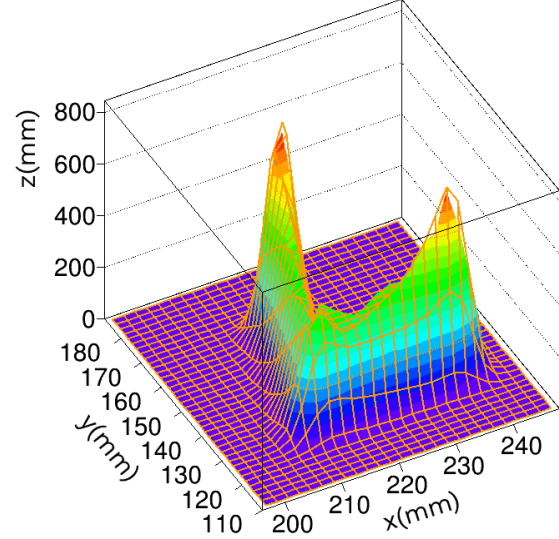


Figure 5.13: Pad plane amplitude distribution of a two proton event. The result of an amplitude +T fit, using Equation 5.21 is shown in orange.

Proton length distribution for single proton emission.

The proton trajectory lengths are calculated using the initial and final points of the tracks obtained after performing the fit of the tracks as expressed in Equation 5.23

$$l_{xyz} = |\overrightarrow{P_0P_1}| = \sqrt{(P_0(x) - P_1(x))^2 + (P_0(y) - P_1(y))^2 + v_d^2 (P_0(t) - P_1(t))^2} \quad (5.23)$$

Representing together all the proton lengths, a first proton distribution can be obtained, as illustrated in Figure 5.14.

Two predominant peaks can be distinguished around $l_{xyz} = 47$ mm and $l_{xyz} = 96$ mm, known proton branches of ^{41}Ti at 988 keV and 1542 keV respectively. This proton distribution is dominated by the most produced and implanted nuclei in ACTAR TPC. By associating the implantations to the decay events (see section 5.4) individual proton length distributions for each species can be obtained.

Length error due to drift velocity uncertainty.

Since the number of interactions of a particle in a gas is a stochastic process, the measured length may not be exactly the same from one event to the other. The widths of the peaks in the proton distribution of Figure 5.14 are explained mainly due to this effect. The error due to the fitting process may contribute as well to a spread of the proton peaks (i.e, determination of a length $l \pm \Delta l$ for the same track). Consequently, the error associated to the fitting process (excluding the error due to the drift velocity value, treated independently in this subsection) is considered to be taken into account in the proton distribution.

As already mentioned in Section 4.3, the calculated length is sensitive to the drift velocity input value. The error associated to the uncertainty of the calculated drift velocity ($\Delta L_i^{v_{drift}}$) depends on the length of the track (so the energy of the protons) and the angle of emission with respect to the detection plane, as

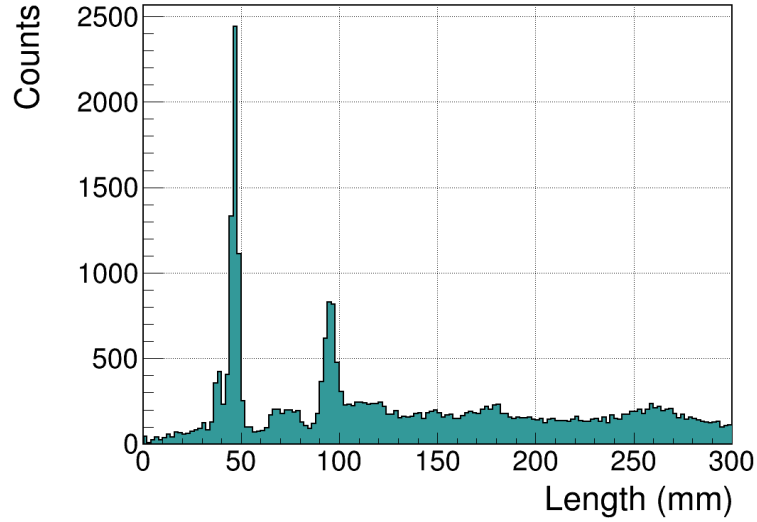


Figure 5.14: Proton lengths obtained for the group of runs of the second experimental configuration (450 mbar pressure setting) after the fitting process. Some peaks can be distinguished at $l_{xyz} = 47$ mm and $l_{xyz} = 96$ mm, corresponding to the well known proton branches of ^{41}Ti at 988 keV and 1542 keV respectively.

illustrated in Figure 5.15. These errors have values between 0 (for horizontal tracks) with respect to the pad plane up to 3 mm for the most energetic protons emitted with vertical angles ($>80^\circ$).

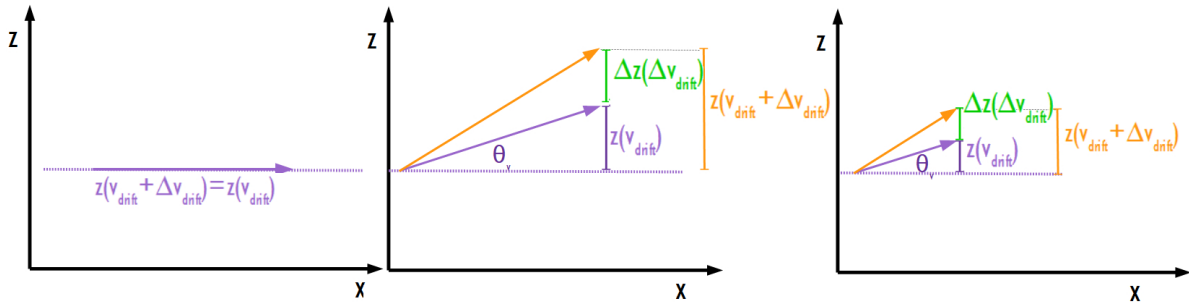


Figure 5.15: Scheme illustrating the (angle and energy) dependencies of the length error associated to the uncertainty of the drift velocity: in the case of a horizontal trajectory (left), there is no dependence with the drift velocity value. When the particle is emitted with a vertical angle θ_v (represented by the purple line in the figure at the center) with respect to the pad plane, the error of the drift velocity results into a shift on the calculated Z value (orange) which is proportional to Θ_p . In the case of a track emitted with the same angle θ_p as the previous case but smaller energy (left figure), this uncertainty due to the drift velocity error becomes smaller.

The length uncertainty is introduced on an event by event basis by converting a single entry (one track length value) into a normalised Gaussian distribution centered on the l_{xyz} value with standard deviation as defined in Equation 5.24. An example of this process is shown for some counts in Figure 5.16.

$$\sigma = l_{xyz}(v_{drift} + \Delta v_{drift}) \quad (5.24)$$

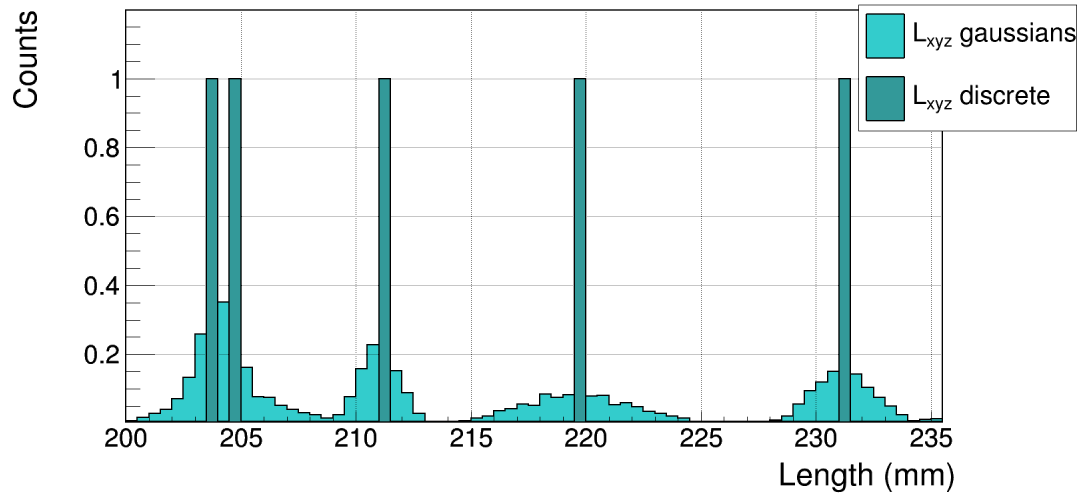


Figure 5.16: Some examples of track lengths obtained after the track fitting (blue counts). A small bin 0.5 mm is chosen to better illustrate the effect of adding the error in an event-by-event basis, as explained in the text (light blue Gaussians centered in the fitted length values (dark blue)). Within similar proton energies (205 -230 mm tracks), a large spread (i.e. $l_{xyz} = 220$ compared to the one at $l_{xyz} = 211$) is observed. This corresponds to a proton track emitted in a more vertical way with respect to the pad plane.

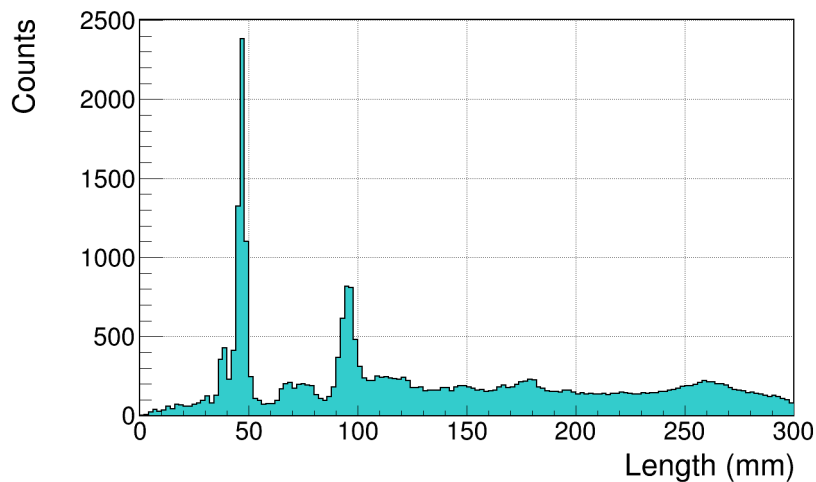


Figure 5.17: Same length distribution as the one on Figure 5.14 including the errors associated to the drift velocity uncertainty. The histogram is filled with Gaussians of centers $l_{xyz}(v_{drift})$ and $\sigma = l_{xyz}(v_{drift} + \Delta v_{drift})$ with integral values of 1.

5.3.3 Proton energy determination

The energy of the protons can be determined using two different methods: using the track length information or measuring the total deposited charge in the detector. Both methods are valid only for protons that deposit the full energy in the detector (not escaping the detection volume). The case of escaping protons will be discussed in subsection 5.3.4.

Length to energy conversion using SRIM

The conversion from the measured length of the proton tracks to energy is performed using SRIM (Stopping and Range of Ions in Matter) [130], a group of programs used to calculate the range of ions into matter. The target characteristics (components and density ρ) and the incident particle need to be defined as the input for this calculation. In the framework of this work, the simulations are performed for an incident proton towards a gaseous target composed by argon $Ar(90\%)$ and isobutane $iC_4H_{10}(10\%)$ at 300 mbar and 450 mbar for the first and the second configurations respectively. The density of the gas is calculated knowing the gas characteristics, pressure and temperature using LISE++ [131].

The output of the simulation includes, among other parameters, a range (R) to energy (E) table. The simulated proton energy E^{sim} for a given proton range (measured track length l_{xyz}) is calculated by interpolation of the two closest SRIM table values

The energy calculation is sensitive to the target density value and therefore to the pressure and the temperature of the gas since the detection volume remains constant. Small changes of any of them can induce changes in the energy–range SRIM output tables. The values of these two parameters are monitored and registered each 10 s during the experiment. The temperature changes during the experiment and oscillates with 1°C amplitude for day and night measurements. The pressure, on the other hand, remains constant, as observed in Figure 5.18 and 5.19 respectively.

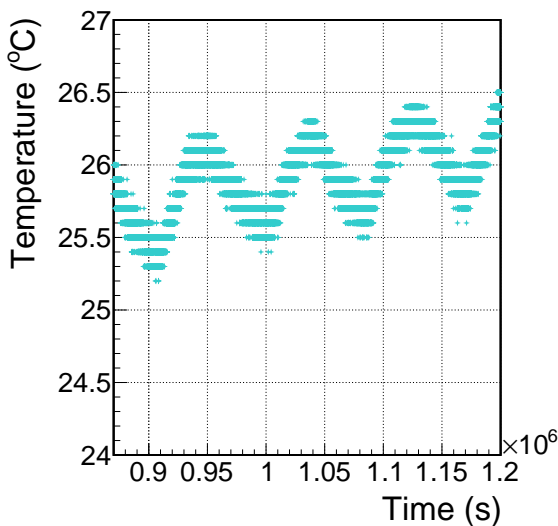


Figure 5.18: Temperature monitoring in which a clear day/night temperature oscillation of 1°C amplitude can be observed.

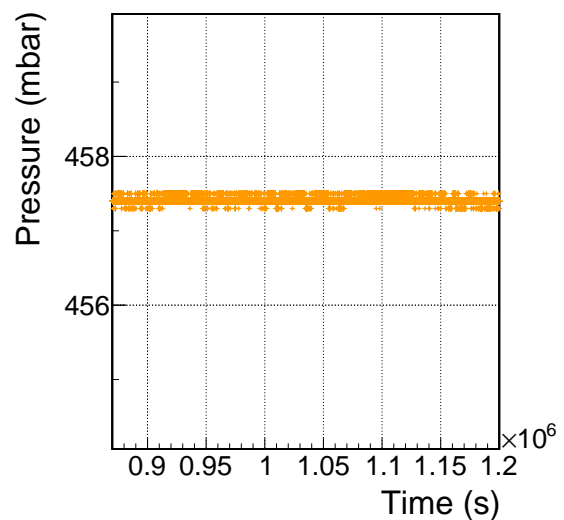


Figure 5.19: Pressure monitoring during the second configuration of the experiment.

Two SRIM calculations are therefore performed with $\pm 1^\circ\text{C}$ for some fixed proton lengths to study the induced energy shift due to the temperature variation. The energy varies by 2 to 3 keV depending on the proton length, as shown in Figure 5.20. An event-by-event temperature correction is not justified in the context of this work since the detector length resolution is about 2.5 mm at $L=70$ mm, that corresponds to an energy shift of about 20 keV.

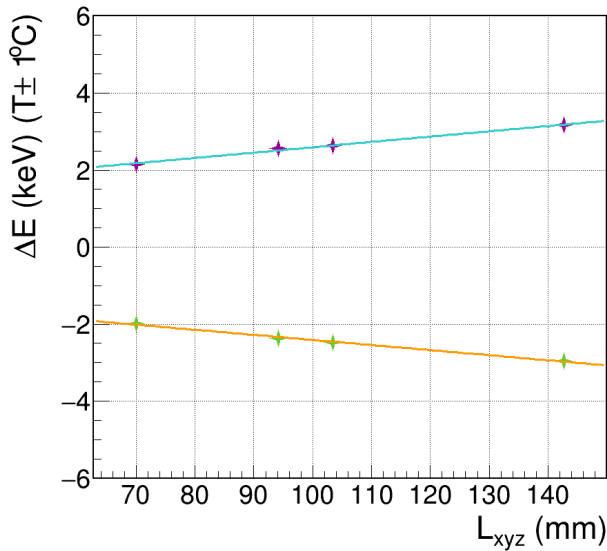


Figure 5.20: Calculated energy shifts between a reference temperature value (25°C) within $\pm 1^\circ\text{C}$ for a given proton length and with a fixed pressure. The orange and purple lines correspond to $+1^\circ\text{C}$ and -1°C variations, respectively. In the ranges of lengths covered in this work, variations by 2 to 3 keV are observed.

Adjustment of simulation input values (known energy proton analysis).

Although no correction in an event-by-event basis for temperature and pressure are performed in the current analysis, the input values for the SRIM simulation are selected to avoid systematic errors in the calculated energies. A study of the input values is performed by comparing measured proton tracks in ACTAR TPC to their known energy values. This study is performed for two group of events corresponding to the two different pressure configurations. By determining the input value over a large number of events, possible temperature effects (day/night), small pressure shifts or gas flux variations are indirectly being averaged.

Only well known energy reference protons with relatively small errors are chosen for this process: the two main proton branches of ^{41}Ti : 988(13) keV and 1542(6) keV, that can be distinguished in Figure 5.14 together with two other reference values² 1260(36) keV (low intensity ^{41}Ti branch) and 1198(12) keV (from ^{46}Mn) constitute the group of protons employed for the optimization of the simulation input values. By performing several (n) SRIM calculations with initial pressure and temperature values slightly shifted from the experimental ones, the values reproducing best the reference energies can be obtained. Considering a perfect gas in which $PV = NRT$ (relationship between pressure (P), volume(V), amount of gas (n), and temperature (T)) the process is simplified by changing just one of the two parameters.

Eight different SRIM tables $T_n^{SRIM}(P_n)$ are obtained using input pressure values P changed by ± 5 , ± 10 , ± 15 and ± 20 mbar from the reference experimental value. The range versus energy plot of these simulations, together with the reference proton values, are shown in Figure 5.21.

A χ^2 test is performed for each of the simulation results T_n^{SRIM} , by calculating the differences between

²These proton peaks are analysed in Chapter 6

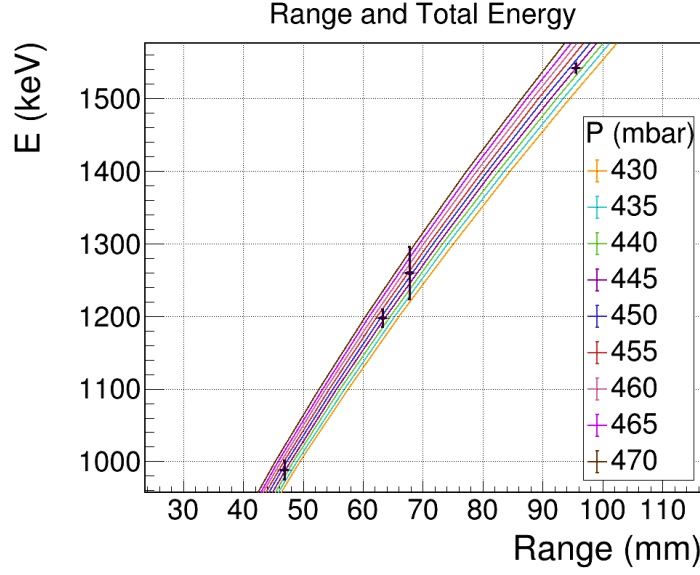


Figure 5.21: Different SRIM simulation Range–Energy curves generated with different pressure values around the experimental pressure setting ($P=450$ mbar in this case). The points correspond to the measured track lengths for well known protons and their reference energy values. Further details of the error components can be found in Equation 5.26 and Figure 5.22.

the predicted energies E_i^{sim} and the reference energy E_i^{ref} value for each of the four reference protons:

$$\chi^2(T_n^{SRIM}) = \sum_{i=1}^{i=N} \frac{E_i^{ref} - E_i^{sim}}{\sqrt{(\Delta E_i^{ref})^2 + (\Delta E_i^{sim})^2}} \quad (5.25)$$

where ΔE_i^{ref} are the uncertainties of the energy values from the literature. The uncertainty of the simulated proton energies ΔE_i^{sim} is approximated:

$$\Delta E_i^{sim} = \sqrt{E^{sim}(L + \Delta L) - E^{sim}(L) + \Delta L^2} \quad (5.26)$$

as schematized in Figure 5.22.

The pressure input value P as a function of $\chi^2(T_n^{SRIM})$ has a parabolic shape, as shown in Figure 5.23 and the vertex $\chi^2(T_n^{SRIM})(P_{min})$ can be easily calculated fitting the points using a parabolic function. The value of the pressure in the vertex, P_{min} corresponds to the pressure that minimizes the differences between the reference energy values and the measured ones, so the optimal pressure value to be used as an input for the SRIM simulation. The final pressure values obtained for each of the configurations are showed in Table 5.3.3.

Configuration	$P_{min} \pm \Delta P_{min}^{eff}$
P=300 mbar	298 ± 2 mbar
P=450 mbar	446 ± 1 mbar

Table 5.1: Pressure input values minimizing the differences between energy values from the literature and simulated ones for both experiment configurations $P=300$ mbar and $P=450$ mbar.

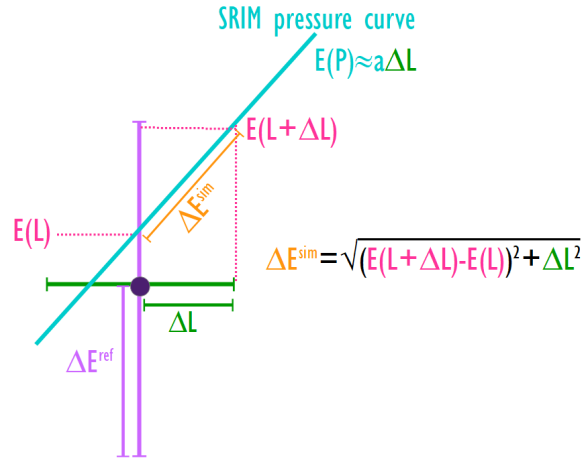


Figure 5.22: Example of one point and its error components, as employed in the χ^2 test. In blue one of the simulation curves at a given pressure P . In purple, the error associated to the reference energy, in green, the error of the length of the proton tracks. The error ΔE^{sim} is shown in orange, and it is calculated as expressed in Equation 5.26, under the approximation of a linear pressure variation between $-\Delta L$ and ΔL .

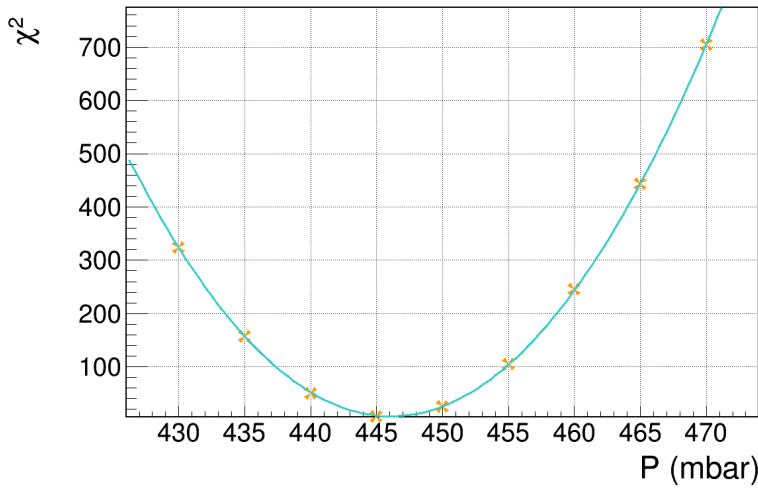


Figure 5.23: χ^2 values obtained (for the second configuration) when transforming the length into energy with different input pressure values, as indicated in Equation 5.25. The blue parabolic fit is used to obtain the pressure value that minimizes the difference between the literature energy values and the simulated ones.

The uncertainty of the pressure is calculated by taking the parabola χ^2 values at +1 unit (one standard deviation, 68% confidence level error [132]) from the vertex value $\chi^2(P_{min})$:

$$\Delta P_{min} = P(\chi^2 + 1) \quad (5.27)$$

The results from the χ^2 being bigger than 1 are corrected as:

$$\Delta P_{min}^{eff} = \Delta P_{min} \sqrt{\chi_{min}^2} \quad (5.28)$$

Energy conversion error in one event

Due to the uncertainty in the pressure input in SRIM, the conversion from track length into energy units induces a systematic uncertainty in the energy value of an event i :

$$\Delta E_i^P = E_i(P) \pm E_i(P + \Delta P). \quad (5.29)$$

Two SRIM calculations are therefore performed with $\pm\Delta P$ to determine the error contribution. The error depends on the pressure uncertainty (different for the two pressure configurations) and on the length of the track (proton energy) due to the shape of the range–energy curves (see Figure 5.21). The energy shift varies from approximately 4 to 6 keV (first configuration) and 1 to 2 keV (second configuration) depending on the proton length, as shown in Figure 5.24. By fitting this dependence, the energy error contribution due to the uncertainty of the pressure as a function of the length can be calculated for each configuration (c) from the linear coefficients a_c and b_c :

$$\Delta E_i^P(L_{xyz}) = a_c L_{xyz} + b_c. \quad (5.30)$$

The values of these coefficients are shown in Table 5.3.3.

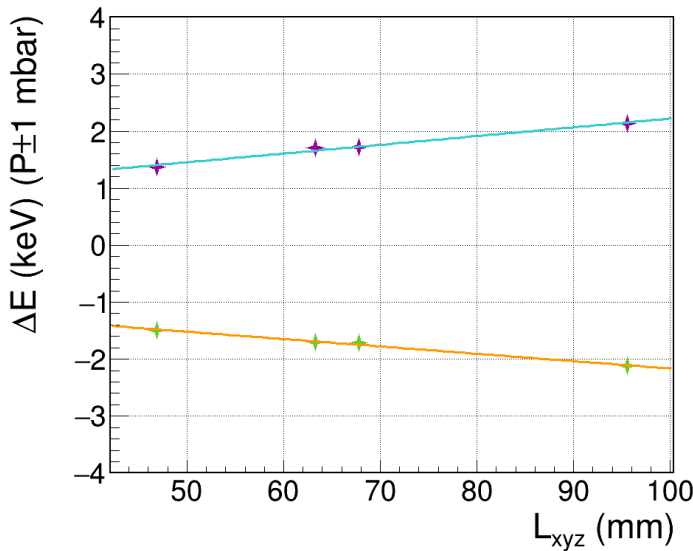


Figure 5.24: Induced energy shift depending on the proton length when taking a pressure value $P \pm \Delta P$. The points correspond to the reference measured proton lengths.

Configuration	a_c	b_c
P=300	2.5 ± 0.2	0.028 ± 0.002
P=450	0.85 ± 0.05	0.012 ± 0.001

Table 5.2: Coefficients for the calculation of the length–dependent error associated to the pressure uncertainty (Equation 5.30). The value is taken conservatively from the P-2 mbar curve fit, since it presents slightly bigger length dependencies.

First energy proton distribution

By transforming the proton fitted length into energy using SRIM energy-length tables as explained in the previous subsection, the two experimental data sets (corresponding to the different pressure configurations during the experiment) can be put together in a single proton energy distribution, as illustrated in Figure 5.25. The main peaks correspond to the two main proton branches of ^{41}Ti as previously mentioned. The lower energy peak around 870 keV corresponds to the main proton branch³ of ^{44}Cr in this energy range.

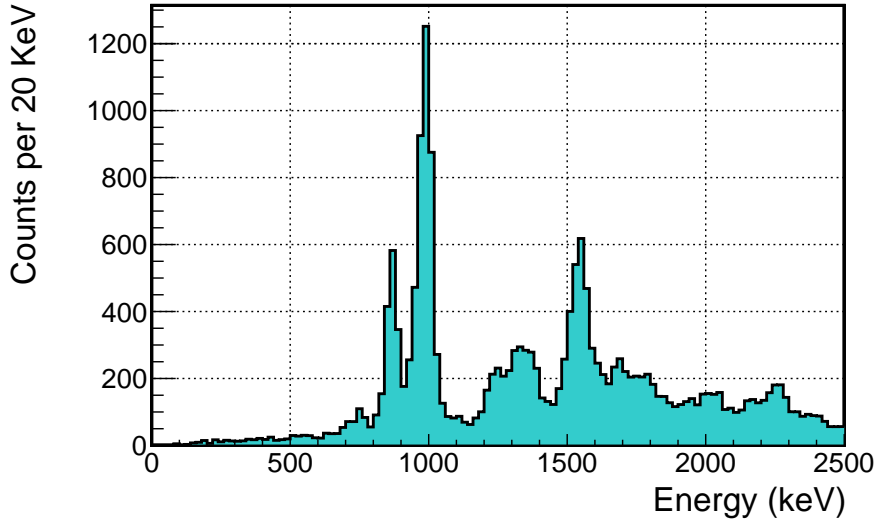


Figure 5.25: Proton energies obtained from the fitted length of the tracks by transforming them into energy units using SRIM energy-length tables. The plot shows all the decay events measured during the experiment.

The contribution of each proton in the energy distribution of Figure 5.25 is a normalized Gauss distribution centered at the proton energy obtained from the length-to-energy conversion using SRIM with a width σ defined as:

$$\sigma = \sqrt{(\Delta E_i^P)^2 + (\Delta E_i^{v_{drift}})^2} \quad (5.31)$$

where ΔE_i^P is the error due to the pressure uncertainty in the length to energy conversion (defined in Equation 5.29) and $\Delta E_i^{v_{drift}}$ is the error due to the drift velocity uncertainty (defined in Equation 5.24) converted into energy units.

Energy from total charge measurements

A second method to obtain the proton energies consists of measuring the total charge deposited in the detector. This is achieved summing the charges of all pads. The total amplitude distribution, built for all single proton events (shown in purple in Figure 5.26) shows a much lower resolution than the energy distribution obtained by transforming the track lengths into energy units. Only the two main peaks (from ^{41}Ti proton emissions) can be distinguished. Although the total amplitude information is not enough by itself to reconstruct in a precise way the energy of the protons, when combined with the calculated energy (from track length), it leads to a useful strategy to reduce the background from the proton energy distribution, as further discussed in Section 5.3.4.

³Further discussed in Section 6.3

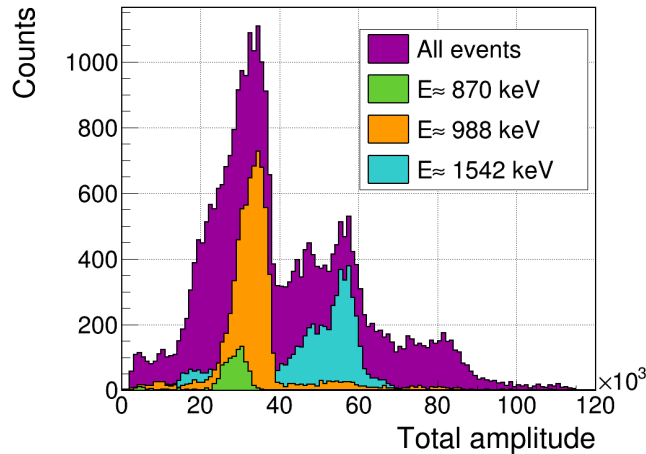


Figure 5.26: The total measured amplitude for proton events is represented in purple, from which only the two main energy peaks of ^{41}Ti can be distinguished with a poor resolution in comparison to the proton energy distribution shown in Figure 5.25. The total amplitude measured for the three main energy peaks (selected by gates on peaks from Figure 5.25) in green, orange and blue are also plotted together.

The total charge deposit for events with a given energy value (obtained from length to energy conversion) are plotted in Figure 5.26 for the main energy peaks in Figure 5.25. A trend towards smaller total charge values is observed for all the peaks (calculated energies too big with respect to the total energy deposit in the detector). This effect is better observed at high energies, for which the probability of a proton escaping the volume is higher. The identification of these events and the process carried out to remove them from the proton energy distribution are discussed in the next section 5.3.4.

5.3.4 Interpretation and cleaning of the energy proton distributions: escaping protons

The escaping proton events can be used for the determination of half-lives, branching ratios between different number of proton emissions and also for angle determination. Unfortunately, their energy cannot be reconstructed by any of the methods mentioned in subsections 5.3.3 and 5.3.3: an incomplete proton track results in wrong length–energy and total charge–energy conversions.

Due to the size of the detector and the pressure settings, optimal for a low energy proton detection, protons with energies above 2.5 MeV may always escape the volume. Lower energy protons can also go out of the detection volume, depending on their decay point.

Protons escaping from the detection plane

A decay is considered to be fully confined in the XY plane if the track is away from the borders of the pad-plane by 4 pads (threshold set to a single pad fired in this region). The proton distributions shown in previous sections are built under this condition.

Protons escaping through the anode or cathode

The particles can also escape through the anode or the cathode. The identification of such events is not as trivial as on the sides of the detection plane, and it is performed by comparing the energy values obtained using the two different methods explained in previous Sections 5.3.3 and 5.3.3: length–energy

and total charge–energy conversions, since they must be proportional. For an escaping–proton measured length–energy, the total collected charge in the detector is lower than expected, since the maximum deposit of charge (Bragg Peak) is not measured. By selecting the events with non–proportional total charge and calculated proton energy, these escaping proton events can be identified, as shown in Figure 5.27.

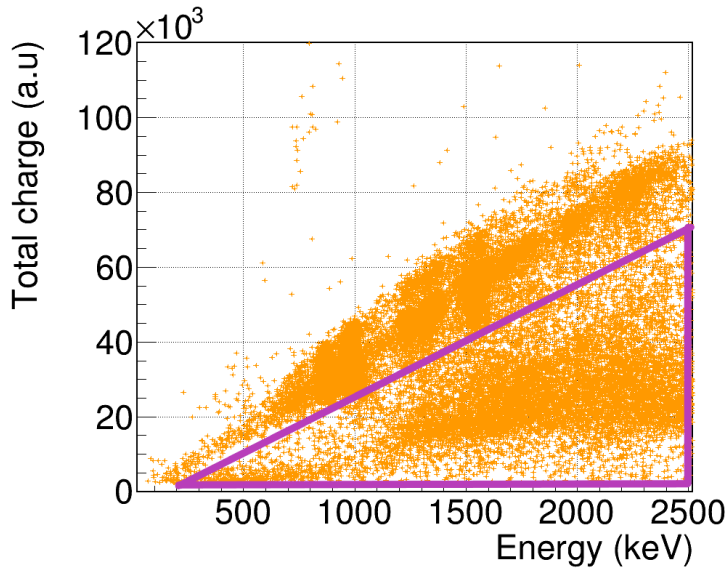


Figure 5.27: Total charge measured in the pad plane as a function of the measured energy (converted from track lengths). All the events within the purple contour are considered to have non-proportional total charge and proton energy, corresponding to escaping protons from the cathode and anode planes and are subtracted from the proton energy distribution.

In some cases, for the protons escaping through the anode, the large energy deposit when traversing the detection plane can lead to compatible total measured charge–energy values. The tracks whose maximum charge is close to the saturating values of the electronics (3500a.u for a maximum value of 4096 a.u) are considered to traverse the pad plane and are consequently removed from the proton energy distribution.

Three different examples of XY–confined proton events are shown in Figure 5.28 to illustrate the two different ways of escaping through the cathode and anode and an example of a fully confined proton.

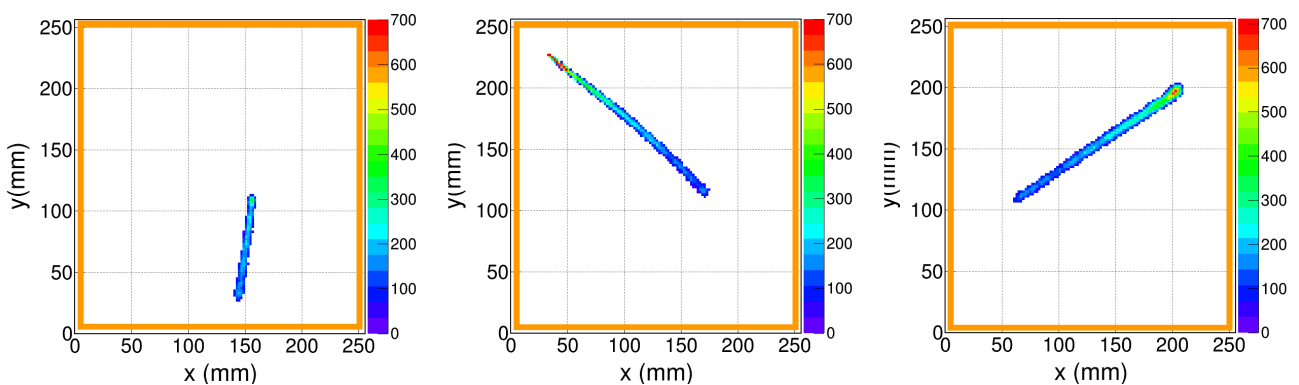


Figure 5.28: Example of three XY–confined proton tracks. The left case corresponds to an event escaping through the cathode (low energy deposit and no Bragg peak). The track in the center corresponds to a proton going out through the detection plane, characterized by a large energy deposit in few pads at the end of the track. The narrow dispersion indicates the close position to the pad plane. The track represented on the right corresponds to a proton fully confined in the detector.

Energy proton distribution from fully measured proton decay events

The result of removing the escaping protons in the energy proton distribution (as explained in the previous subsection) is shown in Figure 5.29. This selection not being perfect (conditions are taken in a conservative way) leads to a reduction of around 36% of the number of events with respect to the first energy proton distribution in 5.25 with no relevant loss in the main proton energy peaks, as can be seen in Figure 5.29.

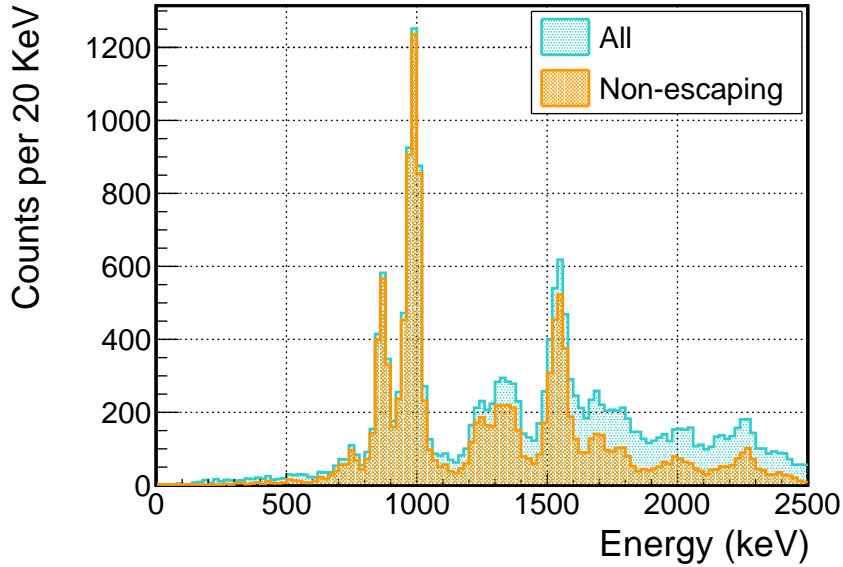


Figure 5.29: The proton energy distribution obtained for all proton tracks is shown in blue. The distribution built for events not fulfilling the contour condition defined in Figure 5.27 and with non saturating pads, corresponding to escaping proton tracks, is plotted in orange. The reduction of background events is more important at higher energies, since the probability of high energy protons escaping the volume is larger.

5.4 Implantation–Decay correlations

The recorded events in the experiment are classified as implantations or decays using the GMT (Ganil Master Trigger) module. As mentioned in Section 3.6, the acquisition parameter value registered for each event by this module has different fixed values depending on the signal that triggered the acquisition (L10K (ACTAR) or E1D6 (beamline)). A condition on this parameter allows for a classification of the events into the two different groups. Following this first step, the decay products have to be associated to their corresponding implantation. The correlations are made requiring time and spatial conditions between both as it is further discussed in Subsection 5.4.1 and Subsection 5.4.2 respectively.

5.4.1 Time condition

The time values associated to each event are given by the time-stamp provided by the CENTRUM module, as explained in Section 3.6. The time condition is defined by requesting the time difference Δt between the implantations t_{imp} and the decay events t_{dec} to be smaller than a defined time window value

W_t^Y for each species Y .

$$\Delta t = t_{imp} - t_{dec} < W_t^Y. \quad (5.32)$$

The width of this time window is chosen depending on the nucleus half-life $T_{1/2}(Y)$, selected to be n times bigger than this value: $W_t^Y = nT_{1/2}(Y)$. The n factor value is selected by comparing the events from wrong correlations $E_{\Delta t^-}$ (same time condition defined in Equation 5.32 at negative times) with respect to the positive coincidences $E_{\Delta t^+}$. As it can be seen in Figure 5.30, the number of real correlations $E_C = E_{\Delta t^+} - E_{\Delta t^-}$ of a well produced nucleus depending on this multiplying factor saturates around $n=8$. The time condition for a given nucleus Y applied in this work is thus fixed to:

$$\Delta t(Y) < 8T_{1/2}(Y) \quad (5.33)$$

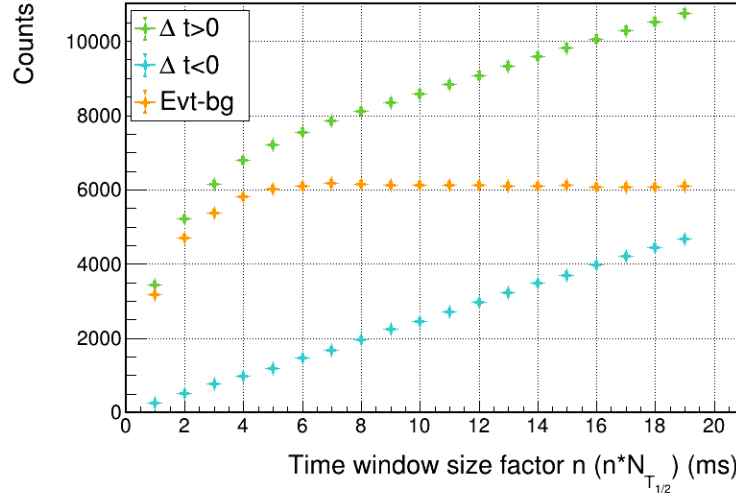


Figure 5.30: Number of events fulfilling the time condition depending on the n factor as $n \cdot N_{T_{1/2}}$ (green points). The same condition is applied at negative times (blue points). The number of real correlations, resulting from the difference between the two previous values, is shown in orange. The different curves are obtained as an example for ^{41}Ti and the first configuration of the experiment.

5.4.2 Spatial condition

When measuring with ACTAR TPC, information about the stopping point P_{imp} of the incoming ion and the decay points P_0 are available if the implantation occurred inside the detection volume, as discussed in previous sections. The spatial condition is defined by requesting a maximum distance d between these two points. Since the third dimension measurement is not absolute, especially in the case of the decay events, this condition is applied in two dimensions (on the detection plane XY), as illustrated in Figure 5.31.

$$|P_{imp} - P_0| < d \quad (5.34)$$

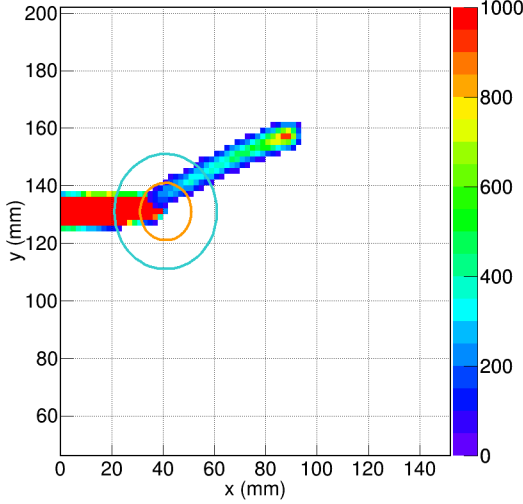
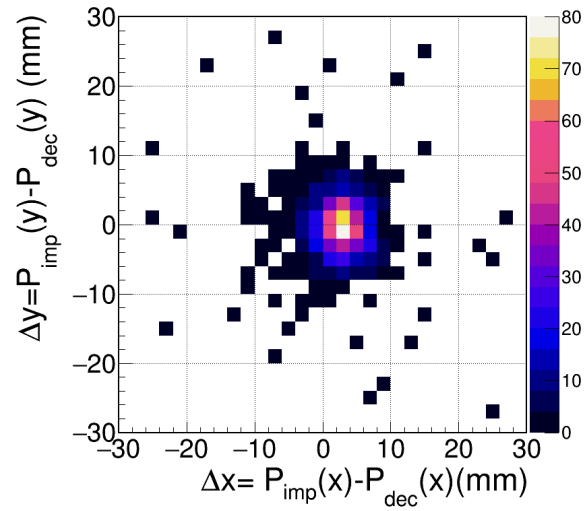


Figure 5.31: Example of an implantation and decay "match". The implantation and decay events histograms in 2D are superimposed in the same plot. The orange and blue circles correspond to distances conditions $d(x,y)$ of 10 and 20 mm respectively.

The spatial condition needs to be larger than the inaccuracies in the determination of the implantation stopping points and the emission points of the decay. The former one is determined by searching the coordinates of the last hit pad in the x plane $P_{imp} = x(x_{max}, y(x_{max}))$. For the determination of the decay point (P_0) a fit of the track is performed as previously explained in Section 5.3.2. Ideally, a two-dimensional plot of their differences $\Delta P(x, y) = P_{imp}(x, y) - P_0(x, y)$ should correspond to a circle centered on 0,0. A shift is observed in both axis as shown in Figure 5.32. This shift is quantified ($\Delta x \approx 2.4$, $\Delta y \approx -1.4$) by performing a two-dimensional Gaussian fit. A correction of this effect could be performed in the future, as further discussed in Chapter 7. In the context of this work, these values are considered to be the minimum required distances in both axes.

Figure 5.32: Differences of calculated stopping point of the implantation event P_{imp} and the determined point of emission of the decay event P_0 in both axis. This distribution is obtained as an example for a group of events of ^{41}Ti in the first pressure configuration.



To find an optimal maximum value for the spatial condition, similarly to the previous analysis of the time window size, a comparison between random coincidence events, happening at negative implantation-decay times and those at positive times is performed changing the spatial condition value d . As it can be observed in Figure 5.33, the number of real coincidences $E_C = E_{\Delta t^+} - E_{\Delta t^-}$ starts saturating around 12 mm within the statistical fluctuations. The spatial 2-dimensional condition for the association of implantation and decay events is thus fixed to:

$$\Delta d < 12(\text{mm}) \quad (5.35)$$

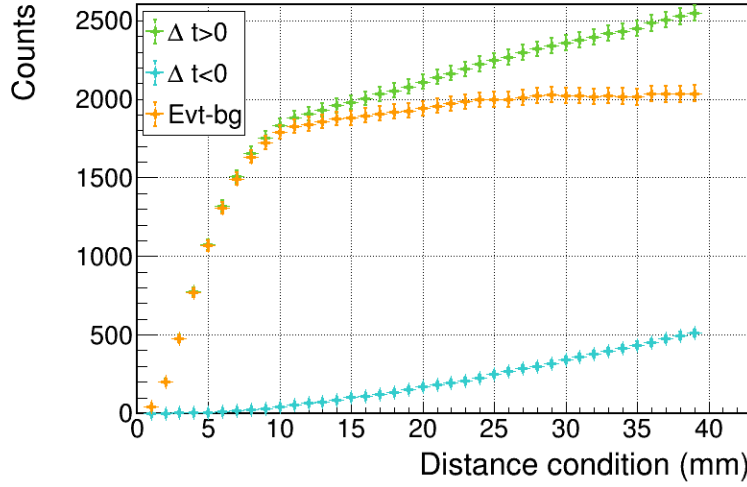


Figure 5.33: Number of events fulfilling the time condition $\Delta t < 8T_{1/2}$ and the two-dimensional distance condition d between the implantation stopping point and the decay point as a function of the value of d . The same conditions are applied at negative correlation times (blue points). The number of real coincidences, result of subtracting the two previous values, is shown in orange. The different curves are obtained as an example for ^{41}Ti and the first configuration ($P=300$ mbar) of the experiment.

5.5 Non-neutralization of the ions, track dispersion parameter.

The dispersion parameter, defined in Section 5.3.2 depends on the vertical coordinate z as $\sqrt{z(\epsilon)}$ (with $\epsilon \in [0, 1]$ as defined in Section 5.3.2). A charge created further from the pad plane produces a more dispersed signal with respect to an ionization that takes place close to the pad plane. When representing the dispersion value at the end of the track versus the vertical angle θ_v of emission (with respect to the pad plane) for a given proton length, two different components are observed, as shown in Figure 5.34.

If the emission of the protons occurs around the entrance window height (where the ions enter the detection volume), only a dependence of the angle of emission in the dispersion and a small variation due to the size of the entrance window is expected (low-dispersion component in Figure 5.34). The component with higher dispersion values indicates that the emission of the proton occurs, in some of the cases, higher in z , meaning that some of the nuclei are not neutralised in the gas of ACTAR TPC and are drifted towards the cathode. If the decay of these ions is occurring at the cathode, the emitted protons may escape the volume at positive angles of emission with respect to the pad plane, which explains the lack of events in the second component at angles above zero and confirms the hypothesis of the drifting of the ions in the gas. This effect was already reported in [98].

This non-neutralization and drifting of the ions affects the measured observables in ACTAR TPC, especially the half-life and branching ratio, as further discussed in Sections 5.6.1 and 5.6.3. The quantification of the number of drifting ions and the possibility of the identification of their decay points on an event-by-event basis (discussed in Subsection 5.5.1) together with the estimation of the drift time of the nuclei (Subsection 5.5.2), are important parameters of study for further corrections in the measured observables.

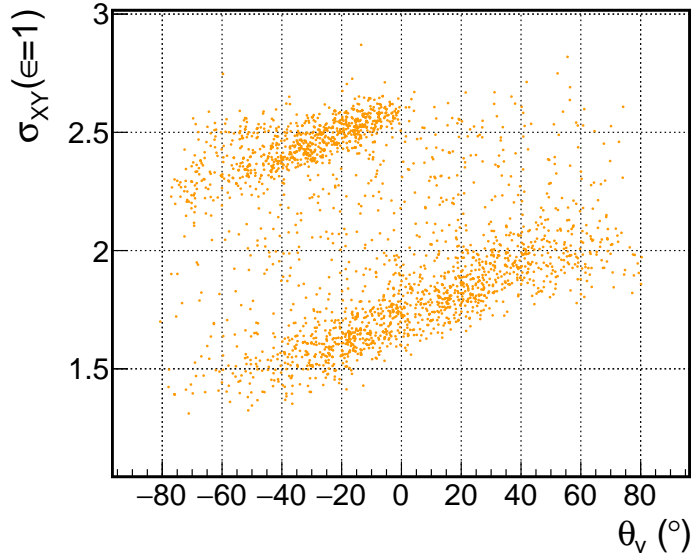


Figure 5.34: Dispersion parameter at the final point of the proton tracks as a function of the vertical angle of emission with respect to the pad plane. The graph is built for the second pressure configuration in the experiment (P=450 mbar) and for a selected proton length, from the ^{41}Ti predominant peak at low energy.

5.5.1 Fraction of emissions from the cathode

Two different methods are proposed to estimate the fraction of ions emitted from the cathode in the detection volume:

Method 1: Counting of the number of events in each of the dispersion regions, taking into account only emissions towards the pad plane. The different dispersion regions are selected using the one dimension dispersion distribution at the decay point ($\epsilon = 1$), shown in Figure 5.35. The different region fractions N_r (with r standing for the three different regions: entrance window N_w , cathode N_{cath} and on flight decays N_f) are calculated by comparing the measured events in each of the dispersion regions with respect to the total number of measured events N_T :

$$N_r(\%) = \frac{N_r}{N_T} \times 100 \quad (5.36)$$

The uncertainty of the number of protons measured in a given region r (N_r) is obtained (assuming a correct selection in the regions) from the variance of a binomial distribution:

$$\Delta N_r = \sqrt{N_T \frac{N_r}{N_T} \left(1 - \frac{N_r}{N_T}\right)} \quad (5.37)$$

Method 2: The fraction of drifting nuclei can also be approximated using the information about the asymmetry of the measured number of protons going towards the pad plane $N_{\rightarrow padplane}$ and those going towards the cathode $N_{\rightarrow cathode}$. Presuming an isotropic emission of the decay products, in the former case:

$$N_{\rightarrow padplane} = \frac{N_{non-drift}}{2} + \frac{N_{drift}}{2} \quad (5.38)$$

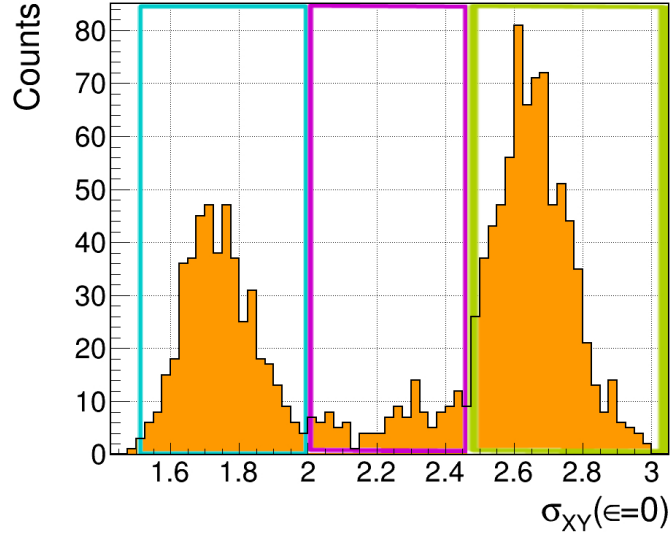


Figure 5.35: Dispersion at the decay point ($\epsilon = 0$) for all protons going towards the pad plane for the second pressure configuration of the experiment and a selected proton length (47mm). Three regions can be distinguished: The low dispersion region in blue (protons emitted from a vertical position corresponding to the entrance window), the high dispersion region in green (decay products emitted from the cathode) and the region in purple (on-drift decays).

In the second case, under the assumption of no proton emission during the drift, half of the protons will escape the detection volume and are consequently not measured:

$$N_{\rightarrow cathode} = \frac{N_{non-drift}}{2} \quad (5.39)$$

When comparing both, the percentage of drifting ions is obtained as:

$$\frac{N_{\rightarrow cathode}}{N_{\rightarrow padplane}} = \frac{N_{non-drift}/2}{N_{non-drift}/2 + N_{drift}/2} = \frac{N_{non-drift}}{N_T} (x100) = N_{drift}(\%) \quad (5.40)$$

Where N_T is the total number of measured events, sum of the drifting and non-drifting ones:

$$N_T = N_{non-drift} + N_{drift} \quad (5.41)$$

The drifting factor obtained using this method, due to the assumption of no emission during the drift, includes a percentage a of the on-flight emissions (N_f):

$$N_{non-drift} = N_w + [a \cdot (N_f)] \quad (5.42)$$

Similarly, a fraction of the on-flight events (b) (proton emitted close enough to the cathode to escape the volume) may be counted in the drifting cases:

$$N_{drift}(\%) = N_{cath} + [b \cdot (N_f)] \quad (5.43)$$

The error of the drifting factor is obtained by error propagation of $\Delta N_{\rightarrow cathode}$ and $\Delta N_{\rightarrow padplane}$:

$$\Delta N_{non-drift} = \sqrt{\left(\frac{N_{\rightarrow cathode}}{(N_{\rightarrow padplane})^2}\right)^2 \cdot (\Delta N_{\rightarrow cathode})^2 + \left(\frac{1}{N_{\rightarrow padplane}}\right)^2 \cdot (\Delta N_{\rightarrow padplane})^2} \quad (5.44)$$

Where both errors $\Delta N_{\rightarrow cathode}$ and $\Delta N_{\rightarrow padplane}$ are defined considering a binomial distribution for positive and negative angles with respect to the total number of measured events N_T .

An illustration of the use of the two methods in a few-events case is shown in Figure 5.36. The percentages of events emitted from the entrance window, cathode and during the drift, calculated using the two different methods, are shown in Table 5.3.

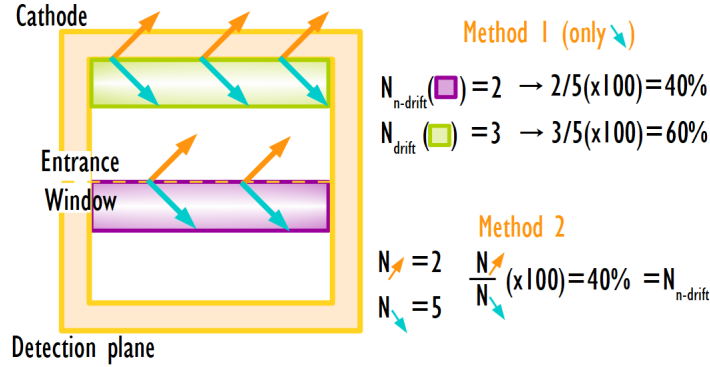


Figure 5.36: Use of the two different methods, as explained in the text (simplified by assuming no emissions on-drift). The emissions are considered to be isotropic (equal number of events going towards the detection plane (blue) and the ones going towards the cathode (orange)). Using the first method, the two regions (green and purple) are identified and the events (towards the pad plane) are counted and compared to the total number of measured events (5) to obtain the fraction of drifting nuclei. When using the second method, the events going towards the cathode (orange) and those going towards the pad plane (blue) are compared, obtaining the drifting fraction.

Method	Entrance window	On flight	Cathode
Dispersion factor	$41 \pm 1\%$	$10 \pm 1\%$	$49 \pm 1\%$
Asymmetry of emission angles	$+[a \cdot (N_f)] = 54 \pm 2\%$	$(N_f)\%$	$+[b \cdot (N_f)] = 46 \pm 2\%$

Table 5.3: Estimated fractions of emissions from the entrance window, the cathode and during the drift of the ions using two different methods explained in the text. When using the second method, the obtained drifting fraction contains some percentage of the events decaying while drifting to the cathode. In all cases the angles are taken in the $[5, 60]$ range, avoiding for a wrong vertical angle calculation in the case of small angles and reducing the possibility of the proton escaping the volume in the case of an emission from the window in the case of large vertical angles.

As it can be seen in Table 5.3, the different estimates of the drifting ratio are in agreement within the errors if the on-flight decays are summed up to the entrance window ones for the first method. This is justified if an isotropic emission of the protons is found for this intermediate region (meaning no protons escaping through the cathode), which is the case when analysing the positive and negative angles with respect to the pad plane in the three different dispersion regions (see Table 5.4). In the high dispersion region, no emissions towards the cathode are found, which assures the correct selection of the events emitted from the cathode by the dispersion value. The errors are calculated considering binomial distributions for positive and negative angles with respect to the total number of measured events in each region N_T .

Region	Towards pad plane	Towards cathode
$\sigma_{XY}(\epsilon = 0) \in \{1.4, 2\}$	$51 \pm 2\%$	$49 \pm 2\%$
$\sigma_{XY}(\epsilon = 0) \in \{2, 2.4\}$	$50 \pm 3\%$	$50 \pm 3\%$
$\sigma_{XY}(\epsilon = 0) \in \{2.4, 3\}$	$1.8 \pm 0.5\%$	$98.2 \pm 0.5\%$

Table 5.4: Angles measured towards the pad plane and the cathode for the different regions defined by the dispersion value in Figure 5.35.

By the use of the dispersion measured value, a characterization on an event-by-event-basis concerning the origin of the proton emissions can be achieved⁴. The use of this information allows for a study of the effect of the non neutralization of the isotopes on the measured observables, as further discussed in 5.6.

The fraction of drifting nuclei, which is needed to estimate the number of decay losses, is calculated for all single proton events (no proton energy conditions) using the second method. The results for each nucleus are shown in Table 5.5. In Figure 5.37, the relation between the half-life and the drifting factor can be observed: for long half-live nuclei, the drifting percentage seems to saturate at around 50%. For smaller half-lives, this value decreases and reaching drifting rates compatibles with 0 within the uncertainty. (⁴⁶Fe with $T_{1/2} = 13\text{ms}$). For those nuclei with very short half-lives (from $T_{1/2} = 13\text{ms}$, included the ⁴⁶Fe) the loss of events due to the drift of the ions is considered to be zero.

⁴¹ Ti	⁴⁵ Cr	⁴⁴ Cr	⁴³ Cr	⁴⁶ Mn	⁴⁷ Fe	⁴⁶ Fe
52.2(0.8)	62(3)	42(2)	32(5)	53(6)	25(9)	13(13)

Table 5.5: Drifting percentage for nuclei with a half-life longer than 13 ms obtained using the second method (See 5.5.1). These values will be used to estimate the loss of events in each case.

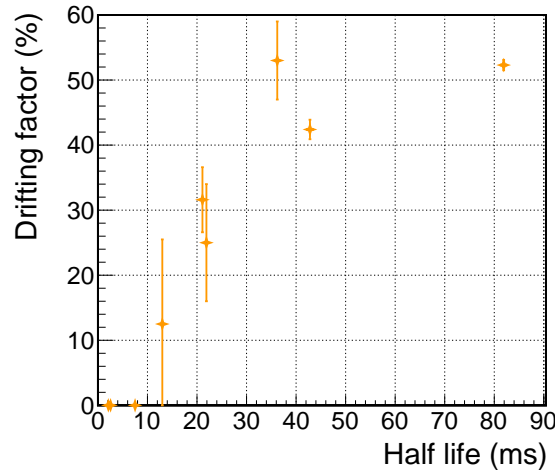


Figure 5.37: Obtained drifting percentage as a function of the half-life of each of the nucleus.

⁴The definition of each of the dispersion regions is made independently for both pressure configurations.

5.5.2 Drifting time of ions

The dispersion value at the initial point of the track (for a given proton length, the second pressure configuration of the experiment and only for negative angles) obtained for different decay time intervals is shown in Figure 5.38.

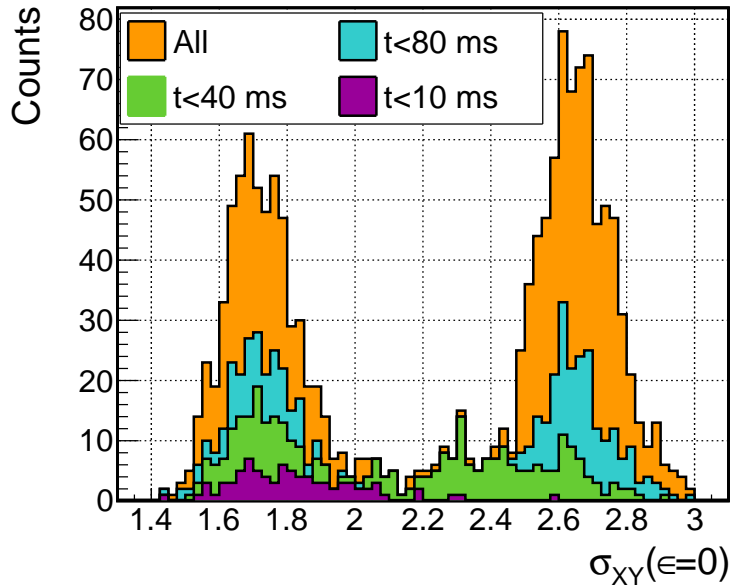


Figure 5.38: Signal dispersion at the start point of the proton track, fulfilling different time conditions between the implantation and the decay events. The orange distribution is built without any time condition. The green and blue distributions are built for conditions $t < 40\text{ms}$ and $t < 80\text{ms}$ respectively. For small times (purple distribution) no events with high dispersion values are found. The intermediate time region $t < 40\text{ms}$ is characterized by contributing the most in the "on flight" region with respect to the $t < 10\text{ms}$ and the $t < 80\text{ms}$ distributions. Also, some dispersion values $\sigma_{XY}(P_0) > 2.4$, corresponding to emissions from the cathode, start to be observed.

The distributions reveal a drifting time of the nuclei of around 40 ms. The distributions for $t > 40\text{ms}$ and $t < 40\text{ms}$ are plotted together for a better comparison in Figure 5.39. The distribution at times above 40 ms has a low number of counts at intermediate dispersion values, indicating that most of the drifting nuclei reach the cathode within 40 ms. The possibility of neutralisation during the drifting may not be excluded due to the existence of some events in the "on-drift emission" region at times above 40 ms. The drifting time is a crucial parameter when determining the half-life of the nuclei with ACTAR TPC, as further discussed in a dedicated subsection of this chapter (5.6.1).

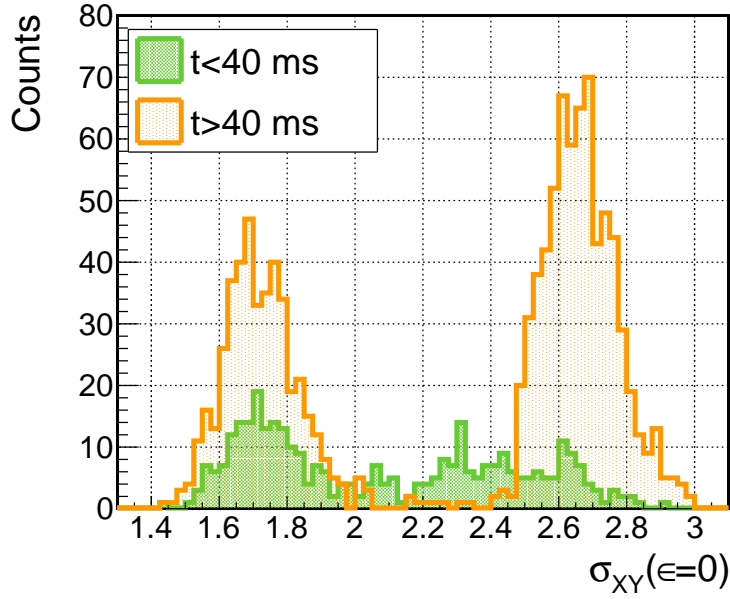


Figure 5.39: Signal dispersion at the starting point of the proton tracks for times between implantation and decay events below 40 ms and above 40 ms. The lack of counts in the intermediate (on-drift decay) region indicates that in most of the cases, the drifting ions reach the cathode within approximately 40 ms.

5.6 Observables: half-life, proton energies, branching ratio

Following the analysis steps described in the previous sections of the chapter, the observables of interest: half-lives, proton energy peaks and branching ratios, can be calculated for each nucleus. This section is dedicated to explain how the different observables are determined and to describe some encountered effects due to the non-neutralization of the ions. Specific sections will address the final results for each of the nuclei in Chapter 6.

5.6.1 Half-life measurements

As already introduced in Section 3.7.2, the half-life of the nuclei can be obtained by fitting the distribution of the time difference between implantation and decay events using the decay law Equation 5.45 adding a background term to take into account random correlations:

$$N(t) = N_{bg} + N_A \frac{\ln 2}{T_{1/2}} e^{-\frac{\ln 2}{T_{1/2}} t}. \quad (5.45)$$

The time differences between the implantation of ^{41}Ti nuclei and the decay products, fulfilling the space and time conditions defined in the previous subsection 5.31 are represented in orange in Figure 5.40 as an example. This distribution presents an excess of counts at small half-lives with respect to the (well-known) half-life, represented by the green line. In order to study the nature of this effect, two other time distributions, one obtained for protons going towards the cathode and the other for decay events going towards the pad plane, are plotted together in green and blue respectively in the same Figure 5.40. The former one explains the excess of counts at short times when taking into account all the protons together.

The inverse situation (lack of events at short times) is observed when taking into account only tracks going towards the pad plane.

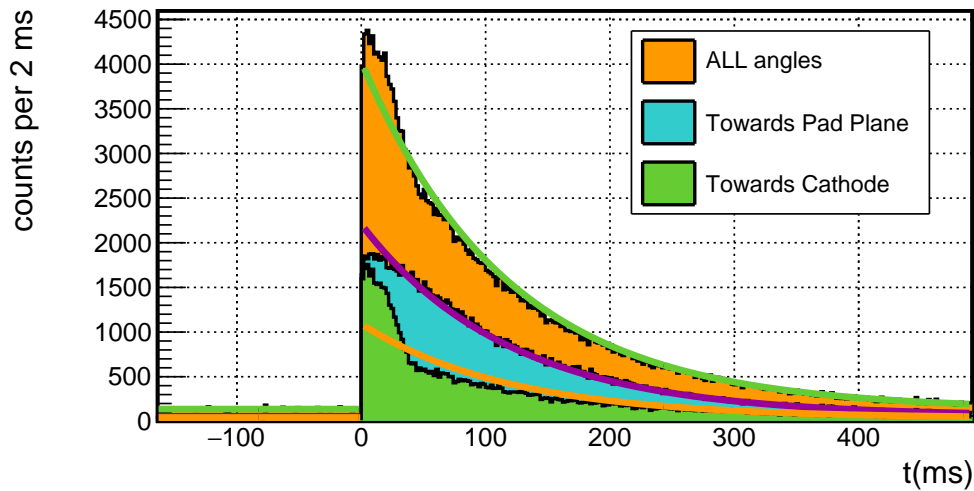


Figure 5.40: Time differences between implantations of ^{41}Ti and their (correlated) decay events. In orange, for all decay events, in blue and green, for proton tracks going towards the pad plane and the cathode respectively. The exponential lines (result of the fit using Equation 5.45 with the half-life fixed to the known value in each of the cases) give a hint of how the time distribution should look like.

The first situation can be explained due to the non neutralization of the nuclei in the chamber, effect mentioned in previous section 5.5. The non-neutralized nuclei drift towards the cathode due to their positive charge. In the case of reaching it, half of the proton decays emitted will not be measured. For short times, as discussed in subsection 5.5.2, the nuclei may not have enough time to reach the cathode, so all the decay products are measured. This phenomenon explains the excess of counts at small times when taking all events into account (orange distribution).

Following this reasoning, fitting the half-life using only proton events going towards the pad plane should fix this problem. As shown in Figure 5.40, this is not the case due to a lack of counts at small-time differences values.

Since this effect is not fully understood at the current stage, the fitting of the half-life is performed using the time distribution of all events but starting from a given time t , ignoring events with small-time differences where the two effects are observed.

The value from which the fit is performed is selected by studying the convergence of the fits performed for the three different time distributions by changing the starting time point for the fit, as shown in Figure 5.41.

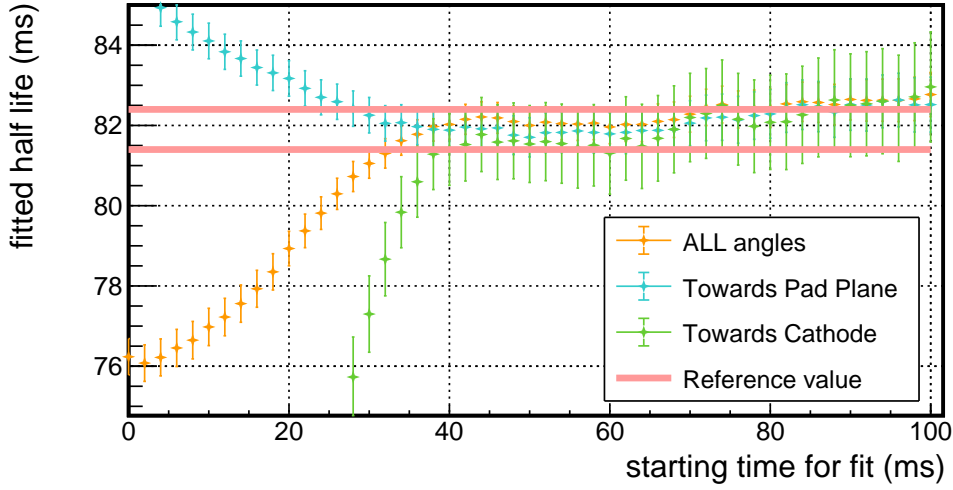


Figure 5.41: Fit results for the three different time distributions of ^{41}Ti (all decays in orange, protons towards the pad plane in blue and to the cathode in green) performed from different starting points. The known value of the half-life is drawn in pink. A convergence of the three fits is observed from $t=40$ ms within the error bars, as already found in Section 5.5.2.

The value from which the fit is performed is studied independently for each of the measured nuclei.

5.6.2 Proton Energies

Correlating implantations with decays as explained in previous Section 5.4 allows obtaining individual proton energy distributions for each of the measured species, as shown for ^{41}Ti as an example in Figure 5.42.

In order to take into account wrong implantation–decay correlations, a second proton distribution is built under exactly the same conditions explained along the chapter (identification of the nuclei, selection of escaping protons, spatial coincidence between implantation and decay) but fulfilling the time condition at negative decay times:

$$-8T_{1/2}(Y) < t_{impl} - t_{dec} < 0 \quad (5.46)$$

The number of wrong correlations for a species Y depends directly on its implantation rate N_Y^{impl} , the total implantation rate N_T^{impl} and on its half-life, which defines the (shorter or longer) time condition imposed for the correlation of events. The number of wrong proton coincidences becomes important for well-produced nuclei as ^{41}Ti , as can be seen in Figure 5.42 and is negligible or even null in the case of nuclei with lower implantation rates and shorter half-lives. The final proton energy distribution for each nucleus is obtained by subtracting the proton distribution for negative times from the positive one, as shown in Figure 5.42 in orange.

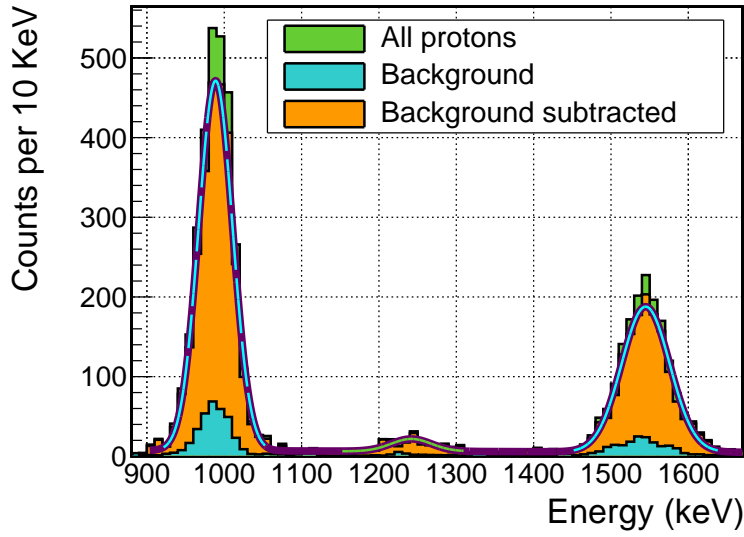


Figure 5.42: A part of the ^{41}Ti proton distribution built by associating the decay events to the implantations is shown in green. The distribution used to further extract the energy values of the proton peaks (represented in orange) is built by subtracting the wrong correlations (shown in blue), estimated by correlating the events at negative times as explained in the text.

The energies of the different proton peaks are obtained from the proton distribution by using a multi-Gaussian fit, performed using the maximum likelihood method with a function ($f_{N_g}(E_p)$) consisting of a sum of N_g Gaussians ($\sum f_g^i(E_p)$) and a common background of type $f_{bck}(E_p) = a + bE_p$. This background term is included to take into account the escaping proton cases (from the cathode or anode) not correctly removed when applying the length, total deposited charge and maximum charge deposited conditions explained in subsection 5.3.4 or real proton events emitted from other energy states of the precursor with low branching ratios. In the former case, the "background" is more important at larger energies than at lower ones (more probability of escaping protons at larger energies). The energy dependent term bE_p is included in the background equation to take this into account.

The standard deviation of the different Gaussians $\sigma_i(E_p)$ is fixed to the resolution of the detector at a given proton energy, (calculation further detailed in Subsection 5.6.2), under the assumption of negligible energy states widths in comparison to the resolution of the detector.

$$f_{N_g}(E_p) = \sum_{i=1}^{n=N_g} [f_g^i(E_p)] + f_{bck}(E_p) = \sum_{i=1}^{n=N_g} \left[A_i * \exp \left(-0.5 \left(\frac{E_p - \mu_i}{\sigma_i(E_p)} \right)^2 \right) \right] + a + b(E_p) \quad (5.47)$$

Since the proton distributions are built taking into account the main errors in the process on an event-by-event basis (length error due to the uncertainty on the drift velocity and error in the energy conversion due to the pressure uncertainty, as explained in 5.3.3), the proton energy error is the one obtained for the parameter μ_i in Equation 5.47 when performing the fit. In the case of a χ^2 value bigger than 1 this value is corrected as:

$$\Delta E = \Delta\mu_i \cdot \sqrt{\frac{\chi^2}{NDF}} \quad (5.48)$$

The different proton distributions and the obtained energy values for the proton peaks will be presented for each nucleus in the next Chapter 6.

The next two subsections are dedicated to the estimation of the resolution of the detector as a function of the proton energy (Subsection 5.6.2) and the study of the energy dependence on the decay point of the proton, consequence of the non-neutralization of some of the nuclei, (Subsection 5.6.2) which will justify the addition of a systematic uncertainty to the energy results obtained for short half-life nuclei or individual measurements.

As mentioned in the first stage of the analysis in Section 5.2, proton emitter nuclei correctly implanted in ACTAR TPC can be used in a special way for identification purposes. The last subsection addresses the comparison of different proton distributions between neighbouring nuclei, aiming to evaluate the possible contamination between species.

Energy resolution

The energy resolution of the detector is estimated by performing a first Gaussian fit to different (high statistic and well-separated) proton peaks selected along the full energy range⁵. The results of these fits (width σ corresponding to one standard deviation and proton energy E_p) are shown in Figure 5.43. The energy resolution can be written in a general way [134] as:

$$\sigma(E_p) = p_0 + p_1 E_p + p_2 \sqrt{E_p} \quad (5.49)$$

The obtained parameters when performing a fit using Equation 5.49 are shown in Table 5.6. The error sizes and χ^2 values indicate an excess of parameters with respect to the number of points. A second fit ignoring the second term (compatible with 0) in Equation 5.49 is performed instead. The results are also shown in Table 5.6. The dominating error in p_0 is used to evaluate the function 5.49 and estimate the (energy dependent) error of the energy resolution, as represented by the shadow region in Figure 5.43.

Parameter	Value fit 1	Value fit 2
p_0	34.5 ± 36	-15 ± 3
p_1	0.04 ± 0.03	0
p_2	-1.6 ± 2	1.2 ± 0.1
χ^2	0.55	1.01

Table 5.6: Resolution results, obtained performing a fit using Equation 5.49 and those obtained neglecting the second term of Equation 5.49.

The resolution estimate for ACTAR TPC is further employed as the uncertainty when determining a single proton energy. In this way, all the errors, including the error when performing the fit and the statistical fluctuations, are considered to be taken into account.

⁵Proton peaks: ⁴⁴Cr (867 keV), (1686 keV), ⁴⁵Cr (2015 keV) and ⁴¹Ti (989 keV) , (1546 keV). The different proton peaks are further shown in 6.

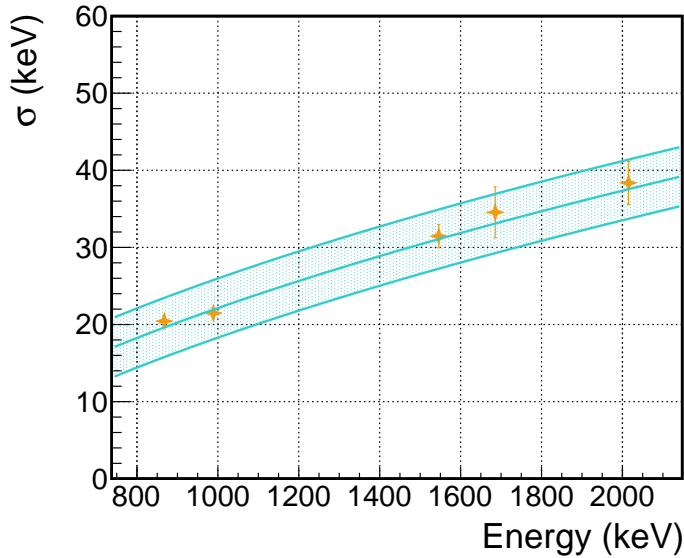


Figure 5.43: Peak widths corresponding to one standard deviation as a function of the measured proton energy E_p for high statistic and well separated proton peaks selected along the energy range (orange points). The blue line is the result of fitting these points with Equation 5.49 with the second term equal to zero. The shadowed region corresponds to the evaluation of the equation in the extreme values of the (dominating) error obtained for the parameter p_0 , represented by the upper and lower blue lines.

Energy dependence on the decay point

When calculating the energies for protons emitted from the entrance window and those from the cathode⁶ a shift with respect to the values obtained when all events are taken into account is observed, as represented in Figure 5.44.

This effect is not fully understood at the current stage. Two different hypothesis (besides from the possibility of a systematic error when performing the track fits) are considered: For protons emitted from the cathode, the (low-energy) beginning of the track can be highly-dispersed in the XY plane so that the signal deposit may not be higher than the defined threshold in the pads, translating into a lost of the beginning of the track. The second hypothesis is the loss of energy due to the recombination of electrons while drifting in the gas. The probability of recombination is bigger in the case of a proton emitted from the cathode, since the created electrons travel systematically more distance.

The length to energy conversion, explained in Section 5.3.3, is adjusted comparing different proton lengths to their well-known energies without any condition on their decay point. By selecting the energy calibration in this way, the two effects in Figure 5.44 are being averaged. This energy shift effect, not yet being fully understood and requiring a dedicated analysis, will be (preliminarily) handled in the following way in this work:

For nuclei with similar half-lives and drifting factors than the ones employed for the "energy calibration" process (mainly protons from ^{41}Ti), this effect is neglected if the energy values are determined from the distribution containing all proton events.

⁶Selection made as explained in 5.5.1

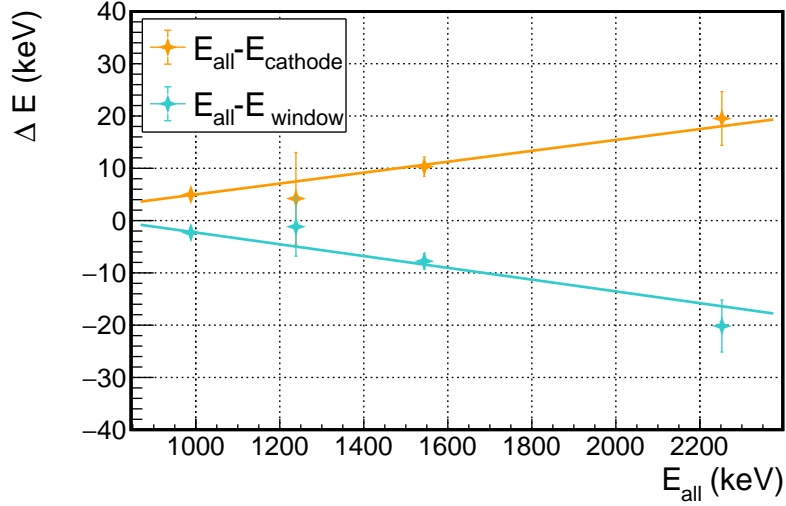


Figure 5.44: Energy differences obtained when taking into account only protons emitted from the cathode or anode (orange and blue points respectively) with respect to the energy value obtained when taking into account all protons (E_{all}). The lines represent a first order polynomial fit, performed to estimate the variations as a function of the energy. The represented values correspond to the main proton peaks of ^{41}Ti measured at the second pressure configuration of the experiment.

If only one group of proton events is taken into account for the calculation of the proton energies (i.e. very short half-life nuclei where no emissions from the cathode are possible or an individual measured energy) a systematic error needs to be included in the energy results. As shown in Figure 5.44, the energy differences depend on the proton energy and can be approximated to a polynomial of first order. The results of both fits are presented in Table 5.7.

Parameter	$E_{all} - E_{cathode}$	$E_{all} - E_{window}$
p_0	-5 ± 3	9 ± 3
p_1	0.010 ± 0.003	-0.011 ± 0.002

Table 5.7: Results of the first order polynomial fit performed for the different energy shifts represented in Figure 5.44.

For completely neutralized or short half-lives nuclei, or, on the other extreme, for nuclei with small neutralization factor a systematic error in the measured energy is included as:

$$\Delta E_{syst}(keV) = \begin{cases} 9 - 0.011 \cdot E_{all} & \text{Cathode} \\ -5 + 0.010 \cdot E_{all} & \text{Entrance Window} \end{cases} \quad (5.50)$$

Evaluation of contamination between nuclei

When associating the decay events to each of the nuclei groups as explained in Section 5.4 and even selecting only the events of "Identification of type 1"⁷, some events have been identified to be wrongly classified. This is noticed when observing the proton distribution of ⁴⁶Mn in which the two main intensity protons of the (high produced) ⁴⁴Cr are reproduced, as shown in Figure 5.45.

In order to account for wrong identifications and to associate the protons to the correct nucleus, the different neighbouring nuclei energy distributions are plotted together, and the intensities are compared. If a nucleus N_A is identified as another one N_B , in terms of probability, the proton distribution of the former one may be contaminated by the highest intensity energy peaks of the second. This effect may be detectable and of influence in the cases of low production/implantation rates or proton branching ratio of the first nucleus N_A , as it is the case for ⁴⁶Mn. Furthermore, since an identification of type 1 or 2 (See Section 5.2.5) was required for all the events (meaning the energy deposit and time of flight leading to one of the defined contours in the 2D identification matrix) the contamination in the present results happens most likely from lower N values as discussed in Section 5.2 (i.e.: ⁴⁵Fe cannot be contaminated from its higher N neighbour ⁴⁶Fe).

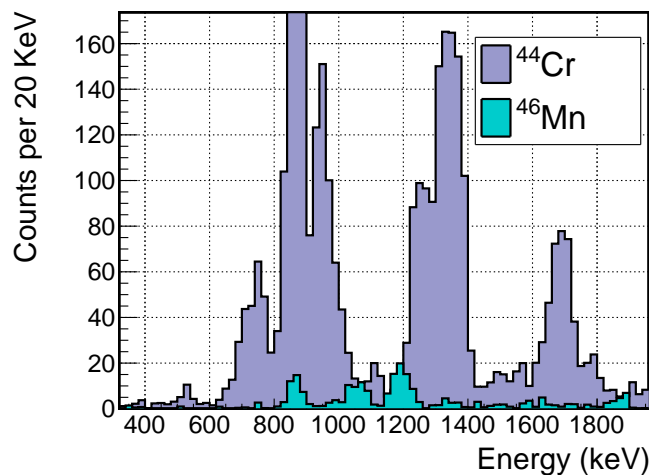


Figure 5.45: ⁴⁴Cr emitted proton energy distribution (purple) and ⁴⁶Mn one (blue). The two highest intensity peaks of the former one are present in the ⁴⁶Mn distribution. The ⁴⁴Cr distribution has been cut for a better comparison. The distribution and the values of the calculated proton energies are further presented in sections 6.3 and 6.5.

For the $Z=24$ (Cr) group, no relevant contamination has been detected. The distributions are shown in Figure 5.46.

By comparing the ⁴⁷Fe proton distribution to the one of its closer neighbour ⁴⁶Fe, as shown in Figure 5.47, two similar proton energy peaks are found around 1000 keV. Following the same reasoning as for the $Z = 24$ line, if there exists a contamination, the highest intensity proton energy of the contaminant should be present, which is not the case as can be seen in Figure 5.47 between the different Fe isotopes.

⁷See 5.2.5 for details

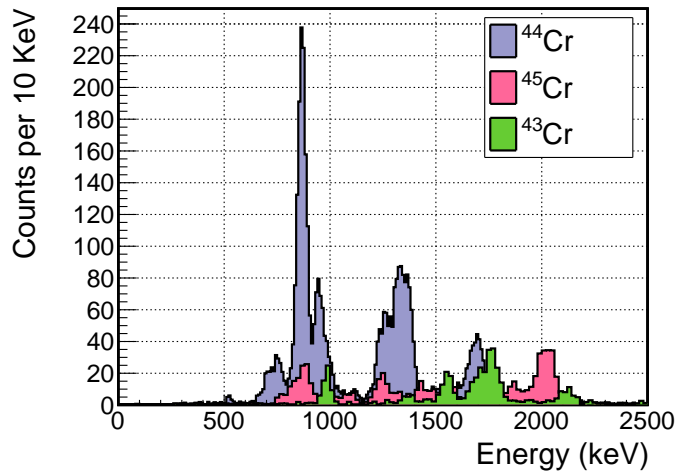


Figure 5.46: ^{44}Cr , ^{45}Cr and ^{43}Cr emitted proton energy distributions plotted together in purple, pink and green respectively. The two highest intensity peaks of the most produced and implanted nucleus ^{44}Cr are not observed in any of the neighbouring nuclei proton distributions. Visually it could seem the case for ^{45}Cr and the first intensity peak of ^{44}Cr , but the obtained values when fitting the different distributions (see sections 6.3 and 6.2.) confirm that they correspond to different proton peaks.

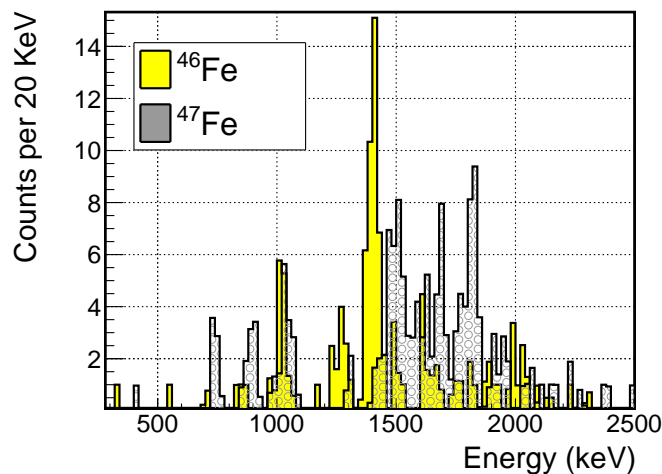


Figure 5.47: ^{47}Fe , ^{46}Fe proton distributions plotted together in grey and yellow respectively. The main peak of ^{46}Fe is not reproduced in the ^{47}Fe distribution. (See sections 6.6 and 6.7 for individual plots.)

5.6.3 Branching Ratio

The number of detected protons with energy E_i for a given nucleus Y $N_p^{(Y)}(E_i)$ can be calculated by integrating the individual Gaussian peaks $f_g^i(E_i)$, obtained when performing the multi-Gaussian fit defined in Equation 5.47:

$$N_p^{(Y)}(E_i) = \int_{-\infty}^{+\infty} f_g^i(E) \cdot dE = \frac{\sqrt{2\pi}\sigma_i A_i}{s_b} \quad (5.51)$$

where s_b is the size of the bin in the proton energy distribution, included to normalize the peak amplitude parameter A_i . The error of $N_p^{(Y)}(E_i)$ is calculated:

$$\Delta N_p^{(Y)}(E_i) = \frac{\sqrt{2\pi}}{s_b} \sqrt{\sigma_i^2 (\Delta A_i)^2 + A_i^2 (\Delta \sigma_i)^2} \quad (5.52)$$

where ΔA_i are the fit errors associated to this parameter and $\Delta \sigma_i$ the energy-dependent error calculated when fitting the resolution of the detector (see Section 5.6.2). The comparison of this value $N_p^{(Y)}(E_i)$ with the total number of implantations $N_T^{(Y)}$, in the hypothetical case of an infinite volume (no escaping protons and all nuclei correctly implanted) and a perfect detection system, this corresponds to the absolute branching ratio:

$$BR_i^{(Y)} = \frac{N_p^{(Y)}(E_i)}{N_T^{(Y)}} \quad (5.53)$$

This is obviously not the case in the current experiment. The $N_p^{(Y)}(E)$ values need to be corrected for the detection efficiency of the protons in the detection volume. Furthermore, due to the drifting of the ions in the gas, the total number of implantations needs to be corrected by the fraction of losses $\epsilon_L^{(Y)}$, calculated for each species considering a loss of a 50%⁸ of the drifting nuclei (drifting factors previously calculated in Section 5.5.1). The dead time correction of 1% (estimated from averaging all the runs) is for the moment neglected in the calculation.

$$BR_i^{(Y)} = \frac{N_p^{(Y)}(E)}{N_T^{(Y)} \cdot \epsilon_0^{(Y)}(E) \cdot (1 - \epsilon_L^{(Y)})} \quad (5.54)$$

A simulation, developed for previous works [133] and [135], has been adapted for the current experiment in order to calculate the intrinsic efficiency value $\epsilon_0(x, E, P_{set})$, function of the implantation point x , the proton energy E and the pressure of the different experimental settings P_{set} . The last part of this section (subsection 5.6.3) is dedicated to explain the main features of the simulation. One of the simulated efficiency distribution, is shown in Figure 5.48 as an example. The efficiency distributions for each pressure configuration have been obtained from the simulation of a finite number of points in the (x, E) space (see Section 5.6.3) and the interpolation between these points.

The effective detection efficiency that needs to be used for the analysis of the proton energy distributions is built from the intrinsic efficiency $\epsilon_0(x, E, P_{set})$ convoluted with the implantation probability distribution of an ion Y in the detector $P_Y[i_x, P_{set}]$. The implantation points for each nucleus $N_Y[i_x, P_{set}]$ are obtained experimentally, as already mentioned in Section 5.1, by measuring the last hit pad i_x in the beam axis for events confined in the detection volume in the two different pressure configurations (P_{300}, P_{450}). The

⁸Under assumption of proton isotropic emission, half of the protons emitted from the cathode are not detected

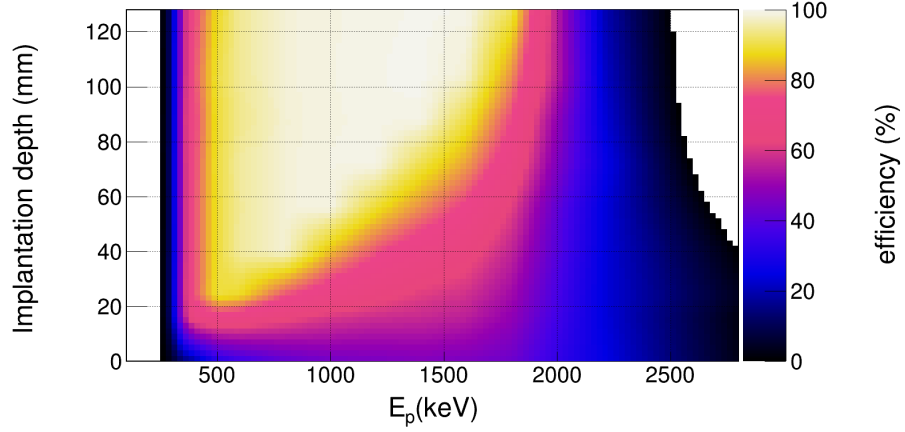


Figure 5.48: Simulated detection efficiency for different proton energies and implantation depths for the second pressure configuration of the experiment (450 mbar). Since the volume of the detector is symmetric, only half of the implantation values are simulated.

probability of an implantation in an experiment pressure configuration P_{set} at a pad position i_x over all settings can be calculated:

$$P_Y[i_x, P_{set}] = \frac{N_Y[i_x, P_{set}]}{N_Y^{tot}[P_{300}] + N_Y^{tot}[P_{450}]} \quad (5.55)$$

where $N_Y^{tot}[P_{set}]$ corresponds to the total number of implanted ions in one setting:

$$N_Y^{tot}[P_{set}] = \sum_{i_x} N_Y[i_x, P_{set}] \quad (5.56)$$

The energy dependent efficiency for a given nucleus Y is calculated using the simulated efficiency and the experimental implantation depths:

$$\epsilon_0^{(Y)}(E) = \sum_{set} \left\{ \sum_{i_x} [P_Y[i_x, P_{set}] \cdot \epsilon_0(x[i_x], E, P_{set} | \vec{a}_0)] \right\} \quad (5.57)$$

The statistical uncertainty on this energy dependent efficiency is computed from the uncertainty on the individual simulation results ϵ_0 . The lower and upper uncertainties for an individual simulation are calculated from the confidence intervals obtained from the number of detected protons out of the number of simulated emissions (confidence interval of a binomial probability).

$$\Delta\epsilon_{\pm}^{(Y)}(E) = \sqrt{\frac{\sum_{set} \left\{ \sum_{i_x} \left[\left(P_Y[i_x, P_{set}] \right)^2 \cdot \left(\Delta\epsilon_{\pm}(x[i_x], E, P_{set} | \vec{a}_0) \right)^2 \right] \right\}}{\sum_{set} \left\{ \sum_{i_x} \left(P_Y[i_x, P_{set}] \right)^2 \right\}}} \quad (5.58)$$

where $\Delta\epsilon_+$ and $\Delta\epsilon_-$ are the differences with respect to the efficiency value ϵ_0 . The implantation profiles for both configurations and the energy dependent efficiency obtained from Equation 5.57 are shown for ^{41}Ti as an example in Figure 5.49 and 5.50 respectively.

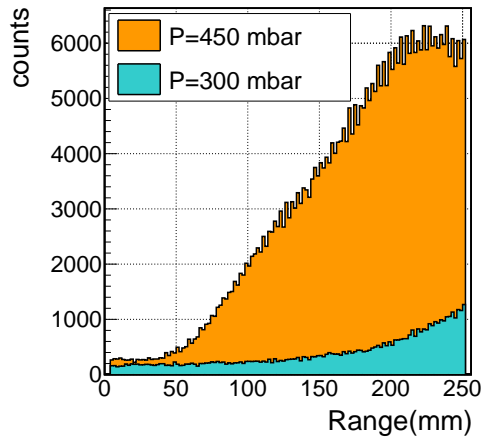


Figure 5.49: Experimental implantation distributions for ^{41}Ti in both experimental pressure configurations.

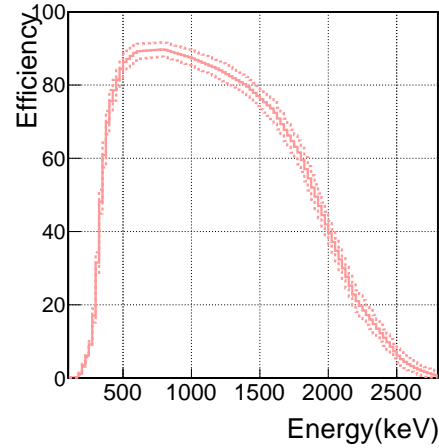


Figure 5.50: Energy dependent detection efficiency for protons emitted in ^{41}Ti decays, calculated using Equation 5.57 from the experimental implantation distributions and the simulated efficiency.

Simulation description

The simulation, developed for previous works [133] and [135], is composed of four different steps concerning the generation of the events, the tracking of the proton and the collection and electronic processing of the signal.

Event generator

Protons with different energies (16 values within the range of interest from 200 keV to 2500 keV) are randomly generated in the YZ plane distributed in a disc of diameter $d_W = 45\text{mm}$ (size of the entrance window) centered at (x_i, y_W, z_W) where $y_W = 128\text{ mm}$ and $z_W = 110\text{ mm}$ are the entrance window positions in the YZ plane respectively and x_i is the implantation depth. This is repeated for different positions in the beam axis $x_i (\pm 1\text{ mm})$. Since the detection volume is symmetric, only half of the detector is simulated (9 values from 8 mm to 120 mm).

Proton tracking

The proton tracks and their energy loss along their paths are generated using GEANT4 simulation toolkit [127], [128]. The pressure in the simulation (second parameter of the simulation) is adjusted to reproduce the SRIM pressure curves used to transform track lengths into energy values, as explained in Section 5.3.3 for each pressure configuration during the experiment, as shown in Figure 5.51.

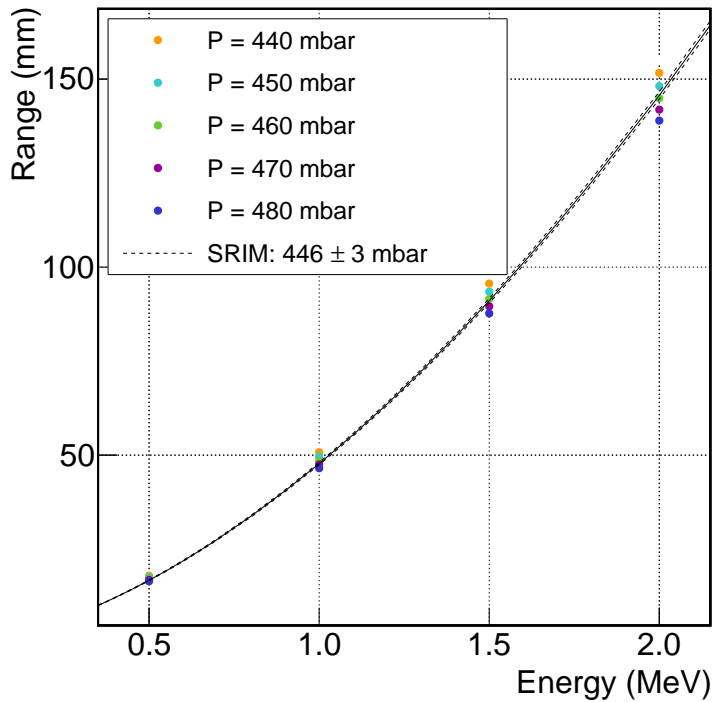
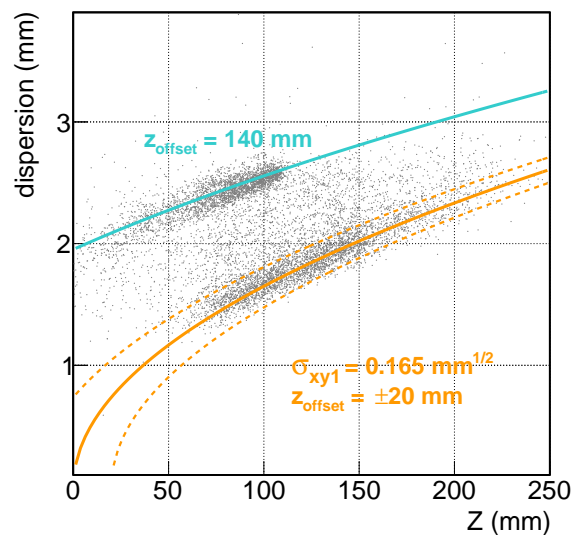


Figure 5.51: Pressure simulated values to adjust the SRIM curve selected as explained in Section 5.3.3 for the length to energy conversion second pressure configuration of the experiment.

Signal collection

For each of the track points, electrons are created and drifted towards the detection plane with a dispersion of a 3D Gaussian shape. The dispersion parameters are adjusted to reproduce the experimental results⁹ obtained after the fitting of the proton tracks as illustrated in Figure 5.52.

Figure 5.52: Dispersion values as a function of the Z parameter. The orange curve represents the dispersion parameters reproducing the emissions from the entrance window of the detector, used for the simulation (solid orange line). The blue curve represents dispersion values characteristics of an emission from the cathode. The experimental results are plotted in grey.



⁹The original experimental plot as a function of the vertical angle of emission with respect to the pad plane can be seen in Figure 5.34

The signal collection and amplification due to the micromegas on the pad plane is taken into account with a gain parameter G_c that includes two different processes: the ionization and the amplification of the signal. The reference value G_c is adjusted to reproduce the total charge deposit curve¹⁰ as a function of the proton energy, shown in Figure 5.53.

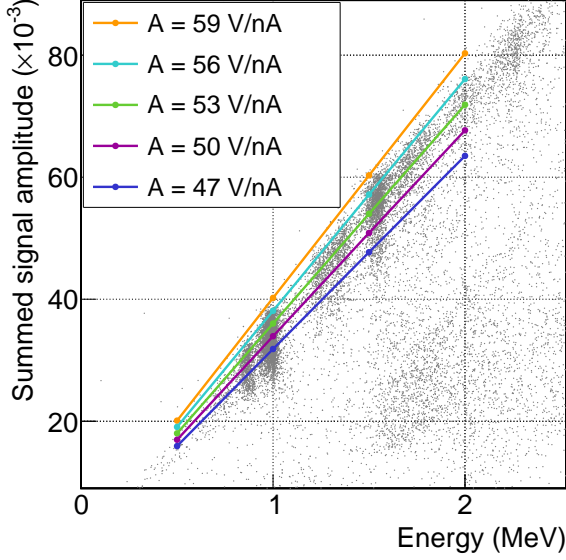


Figure 5.53: Total energy deposit as a function of the proton energy. The color lines represent different amplification values chosen to adjust the experimental values results (gray points)

Processing of the signal

The processing of the signal is simulated by the use of the theoretical response function $h(t)$ of the electronics, adjusted to empirical response functions of the electronic channels from calibration measurements, as presented in Section 4.1.5. To account for the intrinsic fluctuations in the signal processing, two sources of noise are included: an input noise n_i related to the collection of the charge and an output noise n_o of the electronics channels. These two parameters are fixed to reproduce experimental data of pads in *read always* mode¹¹ for events with no signal in ACTAR TPC (selection of implantation events not reaching the active volume).

Once the parameters $\vec{a}_0(\text{window}_{shape}, P_{set}, \sigma_{XY0}, \sigma_{XY1}, G_c, h(t), \tau, n_i, n_o)$ are defined, the analysis of the tracks is performed by counting the detected events $N_i^{(det)}$ (confined in the detector and fulfilling a pad multiplicity threshold) with respect to the simulated ones $N_i^{(sim)}$.

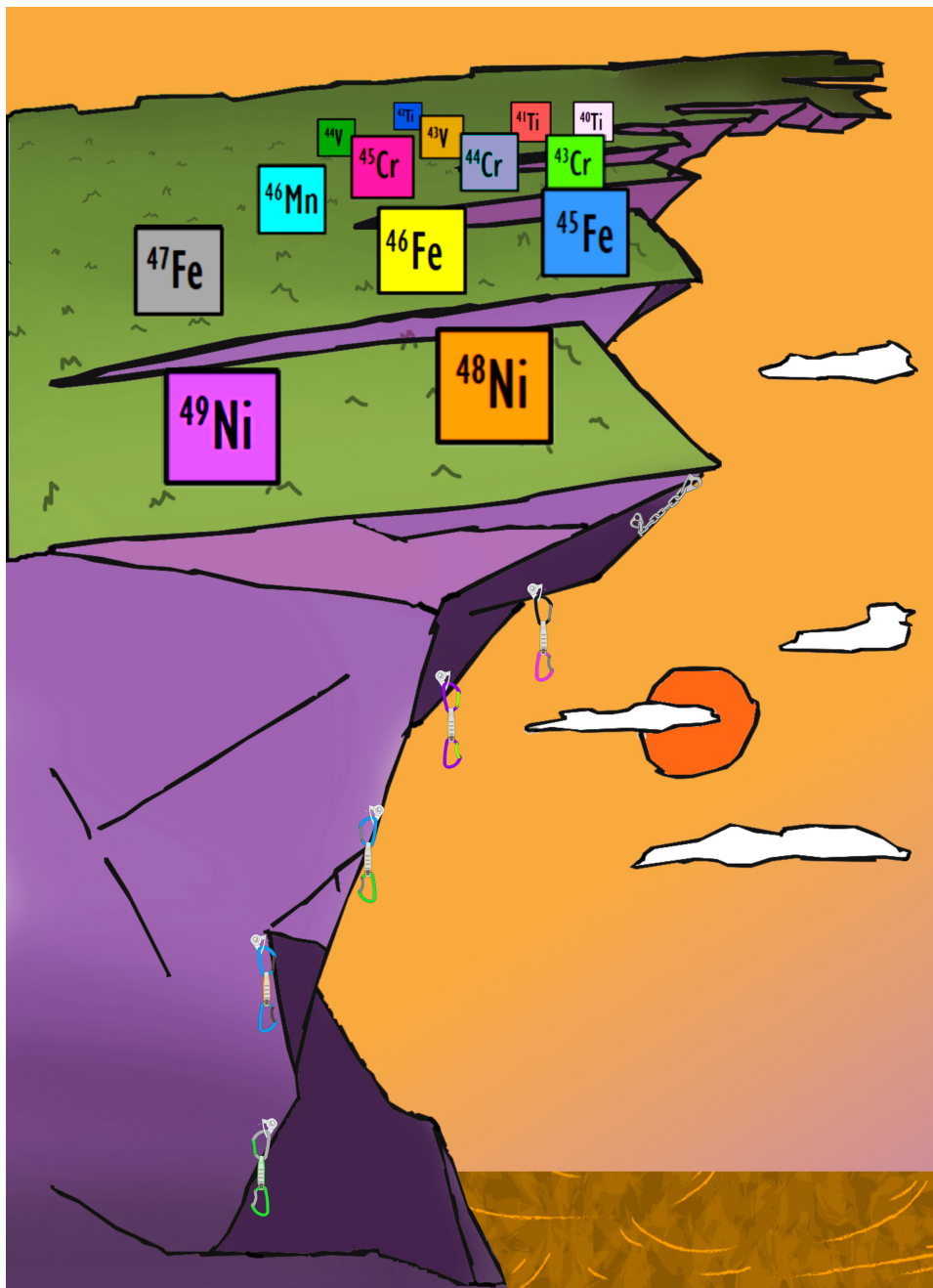
$$\epsilon_i = \frac{N_i^{(det)}}{N_i^{(sim)}} \quad (5.59)$$

The error of ϵ_i is calculated by the quadratic sum of the statistical uncertainty (calculated from the binomial distribution) and the error result of varying the most relevant parameters: pressure, amplitude and shape of the beam profile.

¹⁰Original experimental plot in Figure 5.27 (for both configurations)

¹¹The values of these pads are saved without further conditions for any trigger input

Chapter 6: Results



Contents

6.1	^{41}Ti	150
6.2	^{45}Cr	154
6.3	^{44}Cr	158
6.4	^{43}Cr	165
6.5	^{46}Mn	172
6.6	^{47}Fe	177
6.7	^{46}Fe	182
6.8	^{45}Fe	186
6.9	^{49}Ni	189
6.10	^{48}Ni	193
6.11	Summary of main results	197

In this chapter, the analysis results are presented nucleus per nucleus. Some common considerations can be done concerning the notation and the different analysis stages.

In the measured mass region, the main decay modes are β^+ emission or electron capture (often followed by single or multiple proton emissions from the daughter(s)). In the chapter, since these two decay modes are analogous processes, they will be both denoted as β .

The values obtained in the current work are denoted "*E791*" when a comparison with the literature value "*L*" is performed. The literature values are taken from averaging the available experimental data, as recommended by J.C.Batchelder [29]. The values from a previous work by Dossat *et al.* [140] are often the only experimental reference and are denoted "*D*" in the case of a comparison with them.

The events that have been taken into account for each of the nuclei groups have been selected with an identification of type 1 (see Section 5.2.5) except in the most exotic cases (^{45}Fe , ^{49}Ni and ^{48}Ni) where the events with identification of type 2 have been taken into account as well. This choice reduces the number of wrong identification of the different isotopes, but evidences of contamination are found for some nuclei, as in the ^{46}Fe case, discussed in Section 6.7. Due to the shape of the original contours created in the 2D identification matrix, as explained in Section 5.2, the contamination happens mainly from lower *N* nuclei (i.e: the contamination of ^{46}Fe within the identified ^{45}Fe nuclei is considered negligible).

Despite some improvements are already foreseen for the identification (see Chapter 7), they have not been implemented at the current stage. Consequently, the results presented in this work are still preliminary.

The total proton branching ratio (number of observed decays with respect to the total number of correctly implanted nuclei) needs to be corrected from the effect of losses of events due to the drifting of the ions towards the cathode. This is performed by considering a loss of a 50% of the drifting nuclei, under the assumption of an isotropic emission. The estimation of the drifting ratio is made individually for each nucleus by comparing positive and negative numbers of (single proton) emissions, as previously explained in Section 5.5.1. The uncertainty of the total branching ratio is obtained from the drifting factor error values, under the assumption of the drifting factor uncertainty being the main contribution of the total branching ratio error. In the particular case of very short half-life isotopes, the drifting factor is neglected.

The branching ratios of the different emissions (β -1p, β -2p ...) are calculated with respect to the total number of observed decays and the error is estimated considering binomial distributions for each of the

different decay modes. The results for all nuclei are summarized at the end of the chapter in Section 6.11.

The half-lives have been obtained following the procedure discussed in Section 5.6.1, fitting the implantation-decay time distributions with the decay law from a given time t to avoid the effect of the drifting of the ions in the measured half-life. This time is selected from the convergence of two fits: the one taking into account all protons and the one taking into account protons going towards the pad plane. The former one is taken as the final half-life value because the time distribution to fit has a higher number of events. In the particular case of very short half-life nuclei, the half-life is estimated performing a fit from $t=0$ ms to $t=20$ ms to assure the non-drifting of the ions (inverse logic). Also in the case of very short half-life nuclei, the daughter decays (second event associated to the same implantation event in the time window) are removed for a better estimation of the half-life of the parent nucleus.

The different proton energies, from the β -p decays, are obtained by fitting the proton energy distributions associated to each of the nucleus. This is performed by using the weighted maximum likelihood method and the multi-Gaussian function, as discussed in Section 5.6.2. The error of these energy values correspond to the error of the fit of the energy distribution, since it is built taking into account the length to energy conversion and the drift velocity errors in an event-by-event basis, as discussed in Section 5.3.3. In the case of a measurement of a single energy value from a proton track, the uncertainty is estimated as one standard deviation from the resolution of the detector, calculated in Section 5.6.2. In this way, the statistical and fit uncertainties are also taken into account. In the case of very exotic nuclei, a systematic uncertainty in the energy results needs to be taken into account, as explained in Section 5.6.2. A decay-point dependent length to energy conversion will be performed in the future in order to correct this effect, as discussed in Chapter 7.

The intensities from the different identified proton emissions (from β -single proton cases) are estimated using Equation 5.54 as explained in Section 5.6.3. This is performed comparing the total number of implanted nuclei (corrected from the drifting effect) and the number of decays for each proton group (integrals of each individual Gaussian) corrected from the detection efficiency of the protons in the effective volume.

The error associated to the angles between protons (from β -2p and 2-p decays) is estimated performing a simulation in which the original angle of emission of the particles is compared to the "detected" one, under the assumption of a negligible error contribution of the fitting process.

In the further sections, the results obtained for each nucleus are presented following a similar structure:

- Small introduction concerning available information of the nucleus in the literature and values of interest for the current work (energies below 2.5 MeV) used to compare the results.
- Estimation of the number of implantations, total branching ratio and different decay mode intensities
- Half life measurement
- Identified proton transitions from β -1p

Depending on the nucleus, further results are extracted as β -2p energy proton distributions, measured energies or angular distributions. In the case of ^{48}Ni , a detailed description on an event-by-event basis will be carried out.

6.1

 ^{41}Ti

^{41}Ti ($Z = 22$, $N = 19$) is a radioactive nucleus with a 81.9(5) ms half-life. It decays mainly by β -p emission with a branching ratio of 92.4(6)%, as shown in Table 6.1. Its decay products (see Table 6.2) have "well known" energies, some of them with an optimal value (below 2.5 MeV) to be measured with ACTAR TPC in the experiment conditions. Due to these characteristics together with the high production and implantation of this nucleus, its decay products have been used in different stages of the analysis. First, during the "online" analysis (Section 3.7) for the identification of the cocktail beam components. Then, for the estimation of the drift velocity and the adjustment of the pressure input for the SRIM simulations for length to energy conversions (Sections 4.3.3 and 5.3.3). In general, it has been employed to validate the different analysis steps, such as half-life determination or the study of the neutralization of the implantations (Sections 5.6.1 and 5.5).

	$T_{1/2}(\text{ms})$	decay	BR(%)
^{41}Ti	81.9(5) ^{b,d,e,g}	β -p	92.4(6)% ^{b,e,g}

Table 6.1: Half-life, main decay mode and branching ratio

^a A. Honkanen [136]

^d R.G Sextro [139]

^b M.Bhattacharya [137]

^e C. Dossat [140]

^c W.Liu [138]

^f Z.Y. Zhou [141]

^g W.Trinder [142]

E_p (keV)	BR(%)
750(12) ^{a-c}	0.08(2) ^{a-c}
988(13) ^{a-e}	5.6(8) ^{a-e}
1260(36) ^{a,c,d,f}	0.96(21) ^{c,d}
1542(6) ^{a,c,d,f}	5.06(16) ^{a,c,d}
1588(11) ^{a,b}	0.44(9) ^{a,b}
1842(39) ^c	0.76(27) ^c
1977(12) ^{a-d}	0.5(9) ^{a-d}
2079(29) ^{c,d}	0.87(11) ^{c,d}
2270(9) ^{a,c,d,f}	1.31(18) ^{a-d}

Table 6.2: ^{41}Ti reference proton energies in the laboratory frame and branching ratios below 2.5 MeV.

A total of 43×10^4 ^{41}Ti events have been correctly implanted in ACTAR TPC. From those, 30×10^4 decay events have been detected. For ^{41}Ti , the calculated drifting ratio is $52.2 \pm 0.8\%$ ¹. This corresponds to a total of 26.0(5)% of decay losses. The total number of implanted events is thus corrected by this factor, as shown in Table 6.3. The recalculated total proton branching ratio with respect to this value is 88.0(4)%, much closer to the literature value. The estimated branching ratios of the different kinds of emissions with respect to the observed number of decays can be seen in Table 6.3. Two β delayed two proton emission events have been found associated to ^{41}Ti . Although this emission is not impossible from this nucleus,

¹All nuclei values are shown in Table 5.5

it has never been observed in previous experiments. These two events need a further analysis, since a contamination from the more exotic neighbour ^{40}Ti cannot be excluded.

Implanted	Implanted _{corr}	Decays	β -1p (rel %)	β -2p (rel %)
43×10^4	30×10^4	28×10^4 (88.0(4)%)	28×10^4 (100.0(4)%)	2 (7×10^{-4} %)

Table 6.3: ^{41}Ti number of implantations in ACTAR TPC, total number of detected decay events and their classification into β delayed one or two proton emissions.

Half-life

The time difference between the identified ^{41}Ti events and their associated decay events is shown in Figure 6.1. The obtained half-life, result of the fitting of this distribution, is in agreement with previous works results (see Table 6.4).

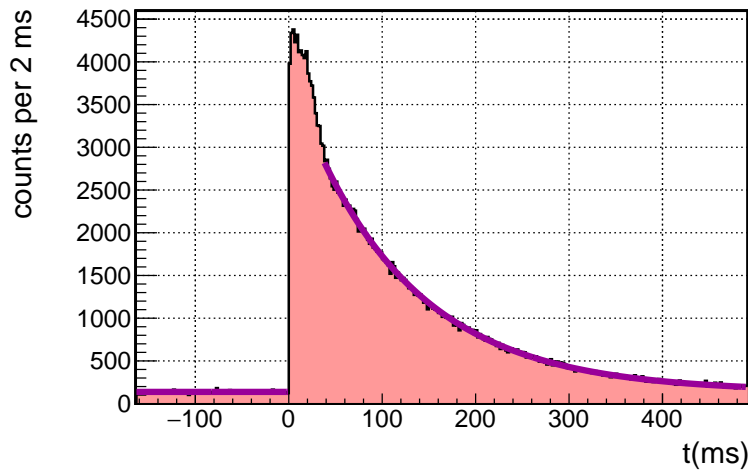


Figure 6.1: Time difference between the identified ^{41}Ti nuclei and their associated proton decays. The purple line corresponds to the performed fit from $t=36$ ms.

	E791	Literature
$T_{1/2}(\text{ms})$	81.79(36)	81.9(5)

Table 6.4: Obtained half-life and literature reference values.

Proton energies

The proton energy distribution for ^{41}Ti , is shown in Figure 6.2. The different peaks are fitted using a sum of seven Gaussians.

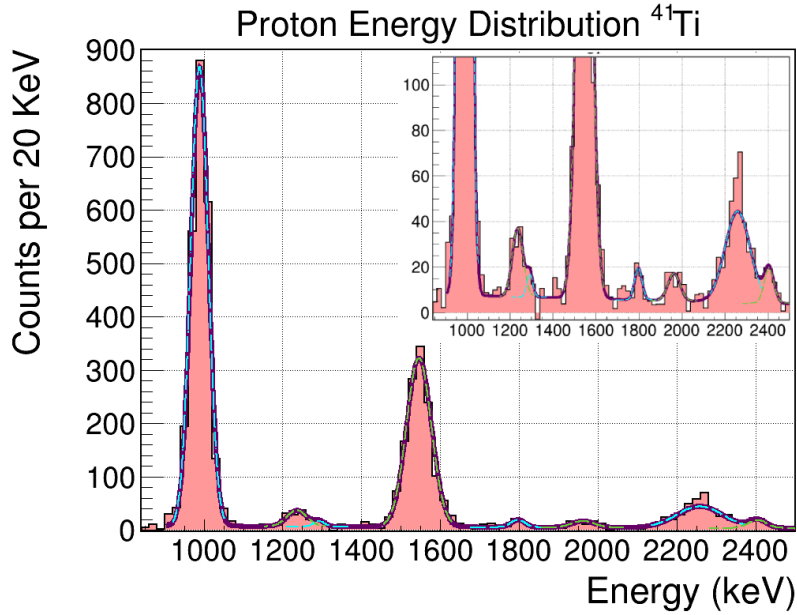


Figure 6.2: ^{41}Ti single-proton energy distribution. The purple line is the result of fitting a group of 7 peaks that are drawn in blue and green lines. A zoom of the lower statistic region is shown on the top right of the figure.

Peak	E(keV)	BR(%)
1	988.4(0.4)	1(0.2)
2	1241(4)	0.04(0.008)
3	1544.2(0.9)	0.66(0.08)
4	1780(10)	0.014(0.006)
5	1960(10)	0.028(0.01)
6	2257(3)	0.54(0.08)
7	2390(10)	0.15(0.04)

Table 6.5: Proton peak energies (from left to right in Figure 6.2)

The energies of the main peaks (with higher branching ratios) reported in the literature (see Table 6.2) at $E_L=988(13)$ keV, $E_L=1260(36)$ keV, $E_L=1542(6)$ keV and $E_L=2270(9)$ keV are reproduced in the current work within one standard deviation uncertainty. The peak at $E_L=1842(39)$ keV, only reported in one of the experiments [138] is in agreement within 2σ from the result in the current experiment $E_{E791}=1780(10)$. There are three proton energies reported in the literature (see Table 6.2) that are not measured in the current experiment: The low energy peak at $E_L=750(12)$ keV and the high energy one at $E_L=2079(29)$ are

missing, most likely due to their low branching ratio which is an order of magnitude lower than the rest of them in the first case (0.08) and probably too low for the ACTAR TPC efficiency at high energies in the second case (0.87(11)) at 2079 MeV. Nevertheless, a small proton group can be distinguished around 2079 keV in the proton energy distribution of Figure 6.2 but compatible with the background estimate. Higher statistics or a cleaner spectra will be needed to confirm its observation. The proton peak at $E_p=1588(11)$ keV reported in [136] and [137] is also not found in the current experiment. This can be explained due to the proximity of another proton group (with a higher branching ratio) emitted at a very similar energy $E_{E791}=1544(1)$ keV and taking into account the resolution of ACTAR TPC (around 32 keV in this energy range).

A new proton peak is reported in the current work, the highest energy one (peak 7) with $E_{E791}=2390(10)$ keV that has most likely been measured together as a proton group with the (higher branching ratio) proton group at $E_L=2270(9)$ keV in previous experiments. The energy values from Table 6.5 are plotted together with the literature values from Table 6.2 in Figure 6.3.

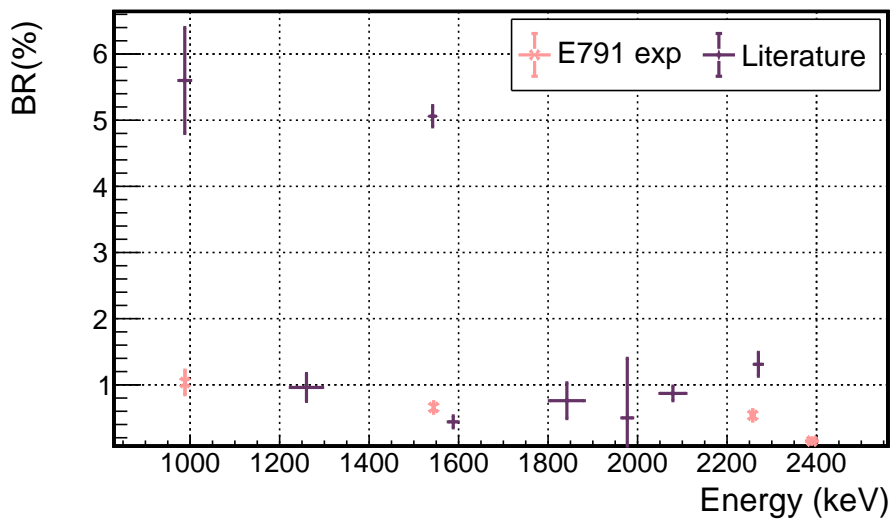


Figure 6.3: ^{41}Ti proton peak energies and intensities obtained in the current work (pink) and literature energy values of Table 6.2 (purple).

Despite the good agreement with the literature values for the proton energies, the associated proton intensities or branching ratios (BR) obtained at the current stage, shown in Table 6.5 are much smaller than expected by a factor of 5 and 7 respectively for the main two proton peaks. This huge inconsistency, not found for the rest of the nuclei as discussed along the Chapter, needs to be further studied. The fit of a partial number of the associated protons of ^{41}Ti could be a possible explanation.

6.2

 ^{45}Cr

^{45}Cr ($Z = 24$, $N = 21$) with a 60.9(4) ms half-life is the least exotic of the $Z = 24$ measured group during the experiment. It decays mainly by β but also by β -p with a branching ratio of 34.4(8)%, as shown in Table 6.6. Some of the decay protons, in the energy region of interest (up to 2.5 MeV), have already been measured and reported in previous works (see Table 6.7).

	$T_{1/2}(\text{ms})$	decay	BR(%)
^{45}Cr	60.9(4)	β -p	34.4(8)%

Table 6.6: Half-life, main decay mode and branching ratio^a

E_p (keV)	BR(%)
924(30)	0.4(3)
1275(24)	0.5(2)
1436(26)	0.4(2)
1574(27)	0.4(2)
2041(9)	19.6(15)

Table 6.7: ^{45}Cr reference proton energies^a in the laboratory frame and branching ratios

^a All values from C. Dossat [140]

A total of 16480 identified ^{45}Cr nuclei are correctly implanted in the detection volume. From those, 3794 decay events have been registered. By correcting from the losses due to the drift of the ions (drifting rate of $62 \pm 3\%$), this leads to a total proton branching ratio of $31 \pm 1\%$, close to the value reported by Dossat *et al.* [140] (34.8(8)%). All the events have been identified as β delayed single proton emissions. These values are summarized in Table 6.8.

Implanted	Implanted _{corr}	Decays (β -1p)
16480	11371	3794 (31(1)%)

Table 6.8: ^{45}Cr events reaching ACTAR TPC, the total number of detected β delayed one proton decay events

Half-life

The time distribution between the ^{45}Cr implantations and the associated decay events is shown in Figure 6.4. The half-life result, which is compatible with the literature value of Table 6.6, can be found in Table 6.9.

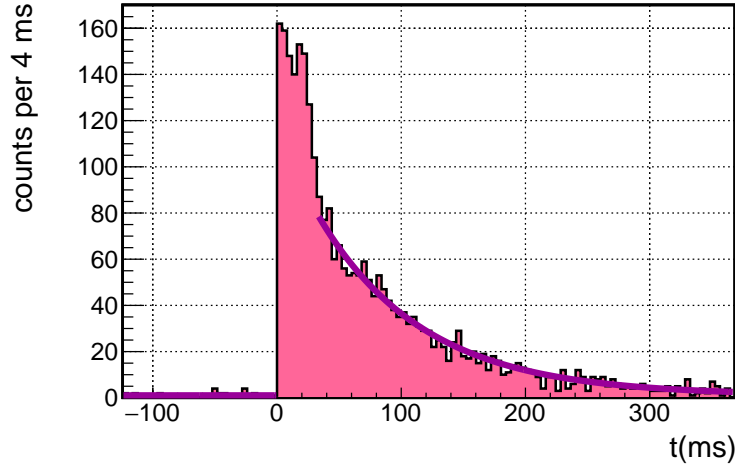


Figure 6.4: Time difference between the identified ^{45}Cr nuclei and their associated proton decays. The purple line shows the result of the fit, performed from $t=32$ ms.

	E791	Dossat
$T_{1/2}(\text{ms})$	59(2)	60.9(4)

Table 6.9: Obtained half-life for ^{45}Cr and previous work value.

Proton energies

The ^{45}Cr proton distribution is fitted using twelve peaks and Equation 5.47. The distribution together with the result of the fit are shown in Figure 6.5. The obtained energy values can be found in Table 6.10 and are compared to previous results in Figure 6.7.

The proton energy measurements performed in a previous work by Dossat *et al* [140] are carried out using silicon detectors. When measuring in such a low energy region, there is a high β background. From the comparison of the energies and given the resolution of the measurements (see Figure 6.6) it is not surprising that some of the reported proton peaks are actually a group of them.

For ^{45}Cr , it may be the case for the first proton group reported in [140] $E_D = 924(30)$, equivalent to the three first proton peaks ($E_{E791} = 773(10), 831(7), 886(4)$) measured in ACTAR TPC. For the second literature proton energy $E_D = 1275(24)$, two different peaks are discerned: $E_{E791} = 1244(5)$ and $E_{E791} = 1330(10)$ (peak number 6 and 7 respectively). The other proton values obtained in previous works are in agreement with the measured ones within the one standard deviation uncertainty except the last one that it is found at a smaller energy $E_{E791} = 2018(3)$ with respect to the value in Dossat $E_D = 2041(9)$, compatible only within two σ uncertainty. Some proton groups are measured for the first time in this experiment (peaks 4,5,10,11).

The intensities of the proton peaks, shown in Table 6.10 are in agreement within one standard deviation uncertainty with respect to the measured ones in Dossat.

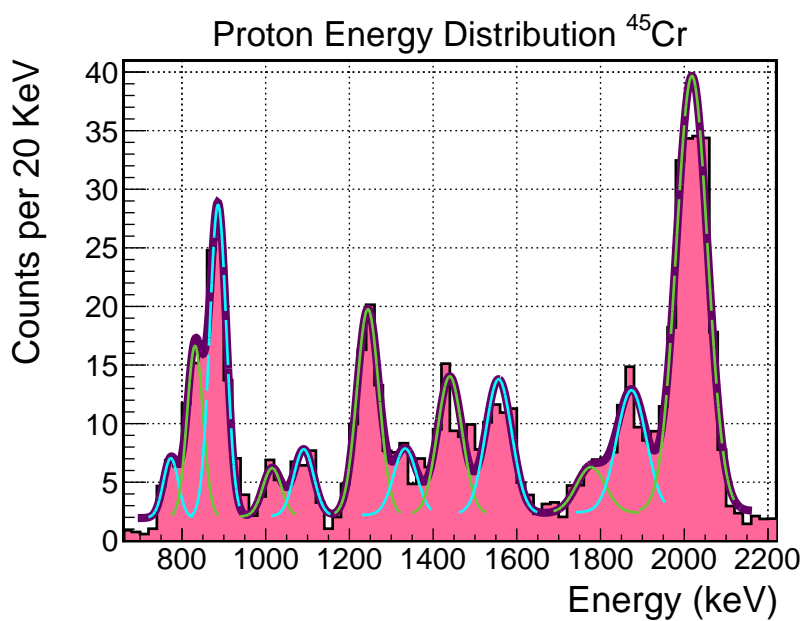


Figure 6.5: ^{45}Cr single-proton energy distribution. The purple line is the result of fitting a group of 12 peaks that are drawn in blue and green lines.

Peak	E(keV)	BR(%)
1	773(10)	0.12(0.06)
2	831(7)	0.4(0.1)
3	886(4)	0.7(0.2)
4	1020(10)	0.13(0.07)
5	1091(9)	0.19(0.08)
6	1244(5)	0.7(0.2)
7	1330(10)	0.25(0.09)
8	1440(8)	0.6(0.1)
9	1557(8)	0.7(0.2)
10	1780(20)	0.4(0.2)
11	1870(10)	1.5(0.4)
12	2018(3)	8(1)

Table 6.10: ^{45}Cr energy values for each proton peak (from left to right in Figure 6.5).

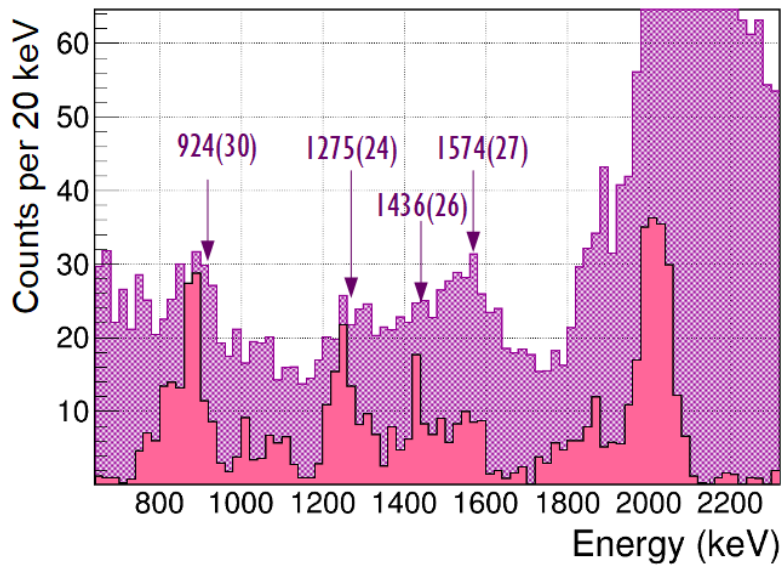


Figure 6.6: ^{45}Cr proton distribution obtained in the current experiment (pink) and the one from Dossat *et al.* for the same energy range. The latter one has been multiplied by a factor of 0.06 for a better comparison of the peaks.

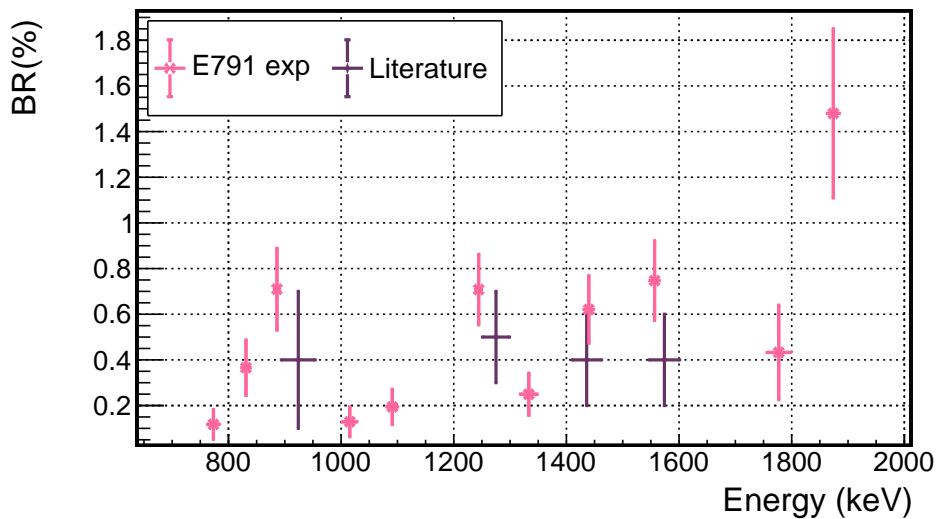


Figure 6.7: Obtained ^{45}Cr proton energies and intensities (pink) and those from the literature (purple).

6.3

 ^{44}Cr

^{44}Cr ($Z=24$, $N=20$) with a 42.8(6) ms half-life decays mainly by β but also by β -p with a branching ratio of 12.2(9)%, as shown in Table 6.11. Some of the decay proton energies below 2.5 MeV have already been measured and reported (see Table 6.12).

	$T_{1/2}(\text{ms})$	decay	BR(%)
^{44}Cr	42.8(6) ^a	β -p	12.2(9) ^a %

Table 6.11: Half-life, main decay mode and branching ratio

E_p (keV)	BR(%)
742(25) ^b	0.6(2) ^b
890(11) ^a	1.7(3) ^{a,b}
1353(12) ^a	1.1(3) ^{a,b}
1702(15) ^a	0.6(3) ^{a, b}
840(19) ^c	1.7(7) ^c
971(19) ^c	0.35(6) ^c
917(19) ^c	1.39(7) ^c
1266(19) ^c	0.69(5) ^c
1337(17) ^c	1.10(5) ^c
1645(13) ^c	0.70(4) ^c
1735(19) ^c	0.39(4) ^c

Table 6.12: ^{44}Cr proton energies in the literature below 2.5 MeV. The published results are shown in a first group (delimited by the horizontal line). More recent but preliminary results by P. Ascher *et al.* [146] are shown in the second group on the table.

^a C. Dossat [140]

^b M.Pomorski [145]

^c P. Ascher [146]

A total of 65×10^3 ^{44}Cr events have been correctly implanted in the detection volume. 9×10^3 decay events have been associated to these implantations. The proton emission branching ratio of 17.4(2) % (calculated taking into account the drifting factor of $(42 \pm 2\%)$) is higher than the values in previous works. This may indicate the measurement of the daughter decay and possibly a contamination from ^{43}Cr , which is the closest neighbour and a β -p emitter with a branching ratio of 100%. The branching ratios between the different kinds of emissions (with respect to the observed decays) are estimated (see Table 6.13). β delayed two proton emission and alpha emissions have been associated to ^{44}Cr . The former events may be the result of the contamination of ^{43}Cr , result of a wrong identification of some of the nuclei. The alpha

emissions are most likely decay events from the daughter nucleus, as it will be discussed in a dedicated subsection (6).

Implanted	Implanted _{corr}	Decays	β -1p (rel %)	β -2p (rel %)	α (rel %)
65×10^3	51×10^3	8.9×10^3 (17.4(2)%)	8.8×10^3 (99(1)%)	60 ($0.67^{+0.10}_{-0.09}$ %)	27 ($0.3^{+0.07}_{-0.06}$ %)

Table 6.13: ^{44}Cr events implanted in the detection volume, the total number of detected decay events measured after the implantations and their classification into β delayed proton emissions and alpha emissions.

Half-life

The time distribution between the ^{44}Cr identified nuclei and their associated decay events is shown in Figure 6.8. The half-life result, compatible with the reported values in previous works, can be found in Table 6.14.

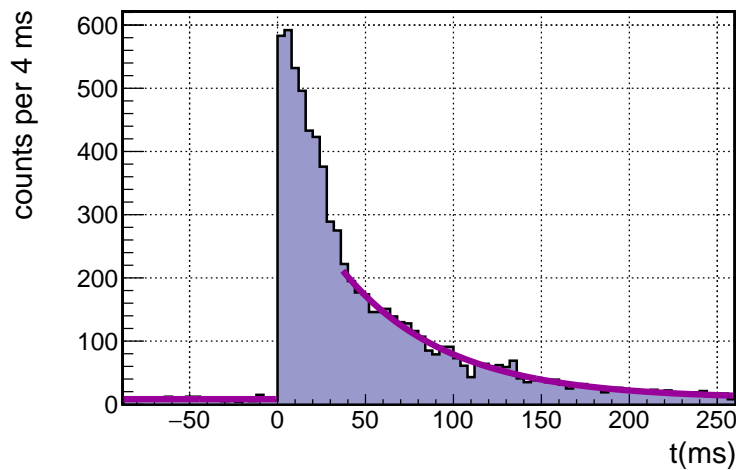


Figure 6.8: Time difference between the identified ^{44}Cr nuclei and their associated proton decays. The purple line shows the result of the fit performed from $t=36$ ms.

	E791	Dossat
$T_{1/2}(\text{ms})$	41(2)	42.8(6)

Table 6.14: Half-life measured for ^{44}Cr and value from Dossat.

Proton energies (β -1p)

The proton distribution for ^{44}Cr is shown in Figure 6.9. The different energies are obtained by fitting a function composed by ten peaks. The obtained energies are shown in Table 6.15.

For the first peak reported in [145] ($E_L=742(25)$ keV), two different components can be distinguished in the current work (peaks 2 and 3) with energies of $E_{E791}=709(3)$ keV and $E_{E791}=760(2)$ keV. Similarly, two different components ($E_{E791}=866.4(6)$ keV and $E_{E791}=945(2)$ keV) are found for the peak $E_D=890(11)$ keV, reported in [140] as the proton linking the IAS of ^{44}V to the ground state of ^{43}Ti . When measuring both together as it may be the case in [140], the obtained energy may be shifted from the most predominant peak towards the value of the second proton group, as it seems to be the case. The higher energy protons ($E_D=1353(12)$ keV and $E_L=1702(15)$ keV) also measured in [140] are in agreement with the result of this work within one standard deviation uncertainty. New proton peaks are reported at $E_{E791}=524(9)$ keV, $E_{E791}=993(6)$ keV, $E_{E791}=1100(10)$ keV and $E_{E791}=1259(2)$ keV. The latest one is most likely fitted together in the work by Dossat *et al.* [140] with the higher energy peak at $E_{E791} = 1347(2)$. The proton energies are also in good agreement with preliminary results of ^{44}Cr proton distributions obtained from energies above 800 keV [146]. These results are plotted together with the proton energies obtained from previous works (Table 6.15) in Figure 6.10 for an easier comparison.

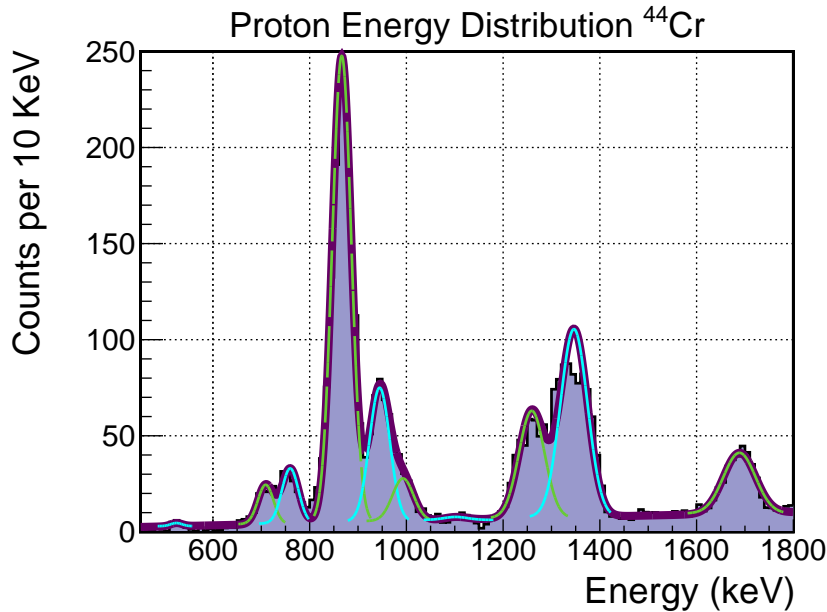


Figure 6.9: ^{44}Cr single-proton energy distribution. The purple line is the result of fitting a group of 10 peaks, represented individually by the pink and green lines.

The proton intensities associated to each of these peaks are systematically higher than the reported values in the literature but in agreement within one standard deviation uncertainty. In the case of the first proton peak $E_L = 742$ KeV, the intensity of 0.6(2) can be reproduced if the intensities of the two components found (at $E_{E791}=709$ and $E_{E791}=760$) are summed up: 0.44(0.09). The intensities are, in general, also in agreement with preliminary results from P. Ascher *et al* [146].

Peak	E(keV)	BR(%)
1	524(9)	0.01(0.01)
2	709(3)	0.18(0.05)
3	760(2)	0.26(0.07)
4	866.4(0.6)	2.6(0.5)
5	945(2)	0.8(0.2)
6	993(6)	0.26(0.07)
7	1100(10)	0.02(0.01)
8	1259(2)	0.9(0.1)
9	1346(2)	1.6(0.2)
10	1689(3)	0.9(0.1)

Table 6.15: ^{44}Cr energy values for each proton peak (from left to right in Figure 6.9).

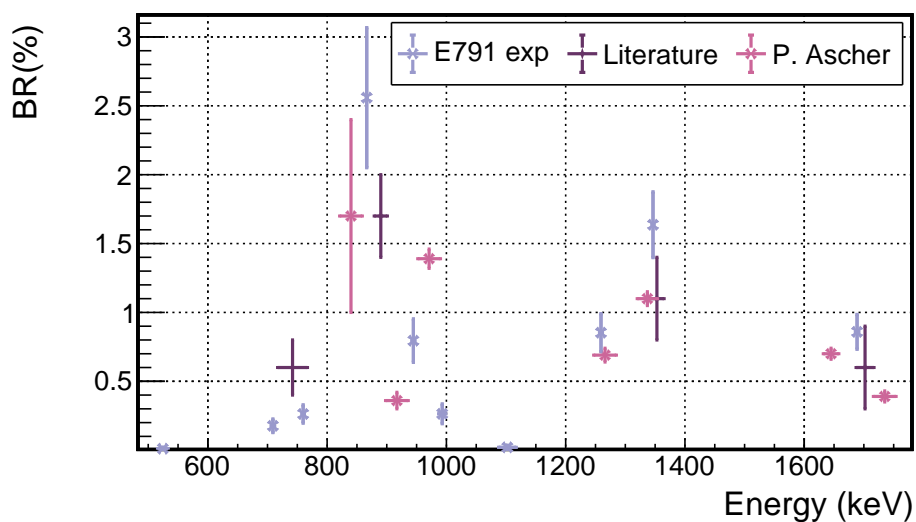


Figure 6.10: The obtained ^{44}Cr proton energies are plotted in light purple. The already published energy values of Table 6.7 are plotted in purple. Preliminary results from P. Ascher *et al.* [146] are represented by the pink points.

Mass and decay energy of ^{44}Cr

The proton energies (from β -p emissions) obtained for ^{44}Cr in this work together with γ information of the same nucleus from a preliminary work by P. Ascher *et al.* [146] and the known masses for the quintet of mass $A=44$ (^{44}Ca , ^{44}Sc , ^{44}Ti , ^{44}V , and ^{44}Cr) allow for a further interpretation of the results, explained in the following paragraphs.

The IMME for mass $A=44$

As explained in Section 1.5.3, the isobaric multiplet mass equation (IMME) links states of a given isospin multiplet (see Equation 1.7[23]). For the quintet of mass $A=44$ of interest in the current work, characterised by $T = 2$, $I^\pi = 0^+$ and T_z values ranging from $T_z = -2$ to $+2$ composed of ^{44}Ca , ^{44}Sc , ^{44}Ti , ^{44}V , and ^{44}Cr , all masses are known with a precision ranging from 0.3 keV to 51 keV. The experimental ground-state masses (GS Δm_{EXP}), the excitation energies (E^*) of the $T = 2$ states in the $T_z = -1, 0, +1$ nuclei, and the mass excess of the multiplet members are shown in Table 6.16. The ground-state masses are taken from the 2020 Atomic Mass Evaluation [149] and the excitation energies are taken from the ENSDF web pages [150] accessed on August 22, 2023, except for the excitation energy of ^{44}V (private communication of P. Ascher).

nucleus	^{44}Ca	^{44}Sc	^{44}Ti	^{44}V	^{44}Cr
(GS Δm_{EXP})(keV)	-41468.7(3)	-37816.0(18)	-37548.6(7)	-23808.1(73)	-13421.9(512)
E^* (keV)	0.0	2780(4)	9338(2)	2807.6(4)	0.0
$T=2$ IAS Δm (keV)	-41468.7(3)	-35036.0(44)	-28210.6(21)	-21000.5(73)	-13421.9(512)

Table 6.16: Ground-state masses, excitation energies and mass excess of the IAS for $A = 44$ nuclei.

With these mass excess values of the multiplet members, the coefficients of the IMME are fitted. The results are shown in Table 6.17.

a(keV)	b(keV)	c(keV)	χ^2
194.1(21)	7017.1(40)	-28211.0(19)	0.15

Table 6.17: IMME calculated coefficients

The difference of the experimental mass excess and the result of the predicted one by the IMME formula with coefficient values of Table 6.17 is shown in Figure 6.11. The experimental data are in agreement with the expectation of the IMME, proving its validity for the mass $A=44$ quintet, for which unexpectedly large IMME d and e coefficients were found in a previous work from C.Y. Fu *et al.* [151].

Proton-emission energy from the IAS

With the data presented in the previous paragraph, the total decay energy of the proton emitted in the β decay of ^{44}Cr from the IAS in ^{44}V can be determined to be 1026(9) keV, using the ground-state mass excess of -29315.6(57) keV and 7289.0 keV for ^{43}Ti and ^1H respectively. This yields a proton energy of 1003(9) keV. From the experimental data obtained for ^{44}Cr in the current work, a proton peak is found

at 993(6) keV, that could be associated with the decay from the IAS. However, its branching ratio is less than 1%. Since the decay is a $0^+ - 0^+$ transition, the feeding of the IAS can be precisely calculated.

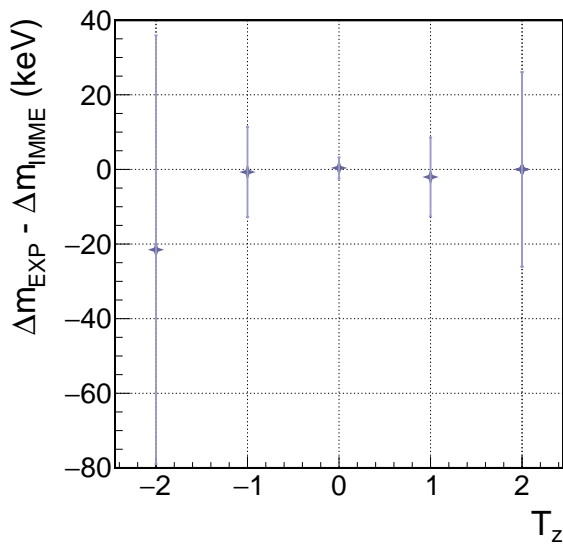


Figure 6.11: Difference between the experimental mass excesses and the result from a fit of the IMME for the five states of the $A=44$ $T=2$ multiplet. All the values are in agreement with zero which demonstrates that the experimental data are in agreement with the expectations of the IMME.

Using a half-life value of 42.8(6) ms² and a Q value for the decay to the IAS of 7579(52) keV, the obtained branching ratio for the super-allowed decay to the IAS is 29.9(14)%. This means that the decays from the IAS state are mainly γ emissions, since the obtained proton branching ratio (lower than 0.5%) is extremely weak. This may indicate that the IAS in ^{44}V is a quite pure state with basically no $T = 1$ component, which prevents this state to emit protons.

Alpha emissions

Some alpha emissions have been identified by plotting the length versus the total collected charge in the pad plane, as shown in Figure 6.12, where a group of tracks with much higher total deposited charge/length ratio than the expected value for proton events are distinguished.

The tracks of a proton and an alpha particle with the same length (103 mm) are shown in Figures 6.13 and 6.14. In the former case, the total deposited charge value is 70% lower than in the alpha event. The analysis of these alpha events requires a different length to energy conversion and changes in the track fitting process (i.e: the Bragg Peak model should be taken from an alpha particle), out of the scope of this work. The average half-life of these events (168.4 ms) indicates that they have been emitted most likely from the daughter nucleus ^{44}V with 111 ms half-life from a β - α decay to the double magic ^{40}Ca . β - α emissions have been already reported for this nucleus (^{44}V) in a previous work [143]. The study of decay events associated to ^{44}V during the experiment may help to understand if this emission is occurring from the ground state or from the isomeric state of ^{44}V , first reported in [144].

²average of present value and literature half-life from Dossat et al. [140] and Borrel et al. [148]

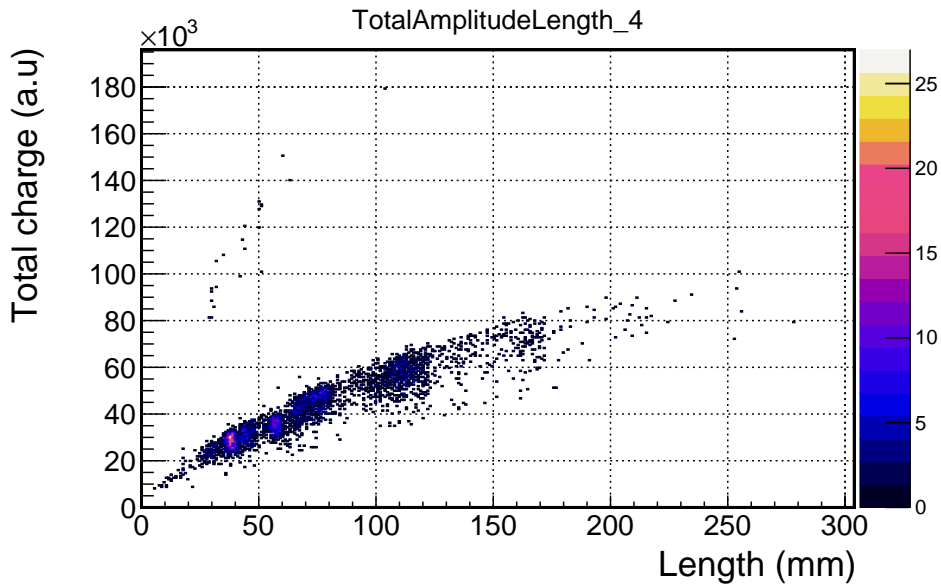


Figure 6.12: Particle track length versus total deposited charge in the pad plane for ^{44}Cr decays. A group with a charge much larger than expected compared to the track length can be observed. These events are the identified alpha emissions.

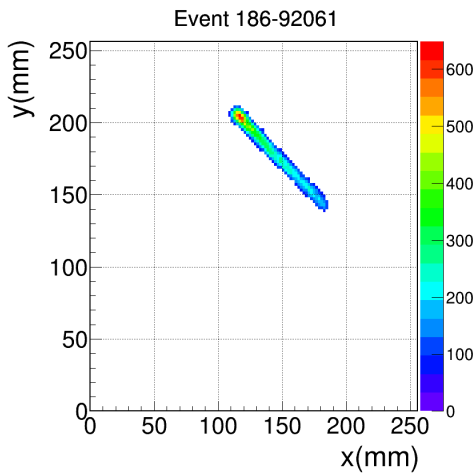


Figure 6.13: Pad plane signal of a 103 mm proton track, selected from a run with no changes in the settings with respect to the alpha event in the right.

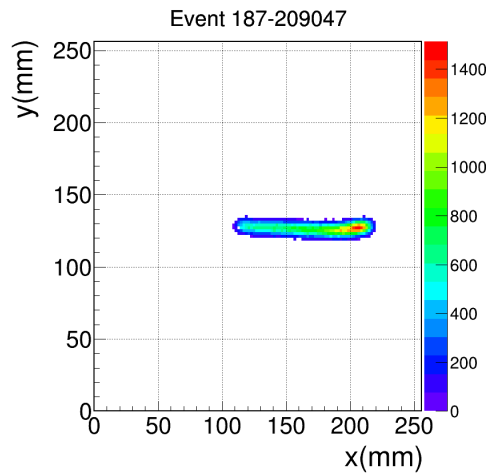


Figure 6.14: Pad plane signal of a 103 mm alpha track. Note the difference of scale of both plots, indicating a much higher energy deposit in the alpha example.

6.4 ^{43}Cr

^{43}Cr ($Z=24$, $N=19$) with a 21.1(4) ms half-life is the most exotic of the $Z=24$ group measured during the experiment. It decays mainly by $\beta p(s)$ (91%) with a branching ratio of 79.3%, 11.6% and 0.13% for the delayed one, two and three proton emission respectively, as shown in Table 6.18. Some of the decay products energies in the region of interest (up to 2.5 MeV) have already been measured in previous works (see Table 6.19).

	$T_{1/2}(\text{ms})$	decay	BR
^{43}Cr	21.1(4) ^{a,b}	β -p	79.3(30)% ^{a,b}
		β -2p	11.6(10)% ^b
		β -3p	0.13($^{+18}_{-8}$)% ^b

Table 6.18: Half-life, main decay mode and branching ratio

E_p (keV)	BR(%)
991(17) ^{a,c}	0.6(1) ^a
1568(16) ^{a,c}	2.1(11) ^a
1776(11) ^{a,c,d}	7.1(12) ^a
2181(49) ^{a,c}	4.7(7) ^a
4263(19) ^{a,c,d}	5.6(7) ^a (b-2p)

Table 6.19: ^{43}Cr reference proton energies and branching ratios

^a C. Dossat [140]

^c J. Giovinazzo [147]

^b L. Audirac [92]

^d V. Borrel [148]

A total of 4367 ^{43}Cr events have been correctly implanted in the detection volume. From those, 3764 decay events have been detected, which corresponds to a proton branching ratio of 102(3)% when taking into account the drifting factor for this nucleus ($32\pm 5\%$). This value is higher than the expected total proton branching ratio (92.5(3)%). This inconsistency it is probably due to a wrong estimate of the drifting factor due to the small number of single proton events staying in the volume taken into account to calculate it. Nevertheless, the estimated branching ratios of the different kinds of emission with respect to the observed number of decays are calculated (see Table 6.20).

Implanted	Implanted _{corr}	Decays	β -1p (rel %)	β -2p (rel %)	β -3p (rel %)
4367	3668	3764 (102(3)%)	3543 (94.1(4)%)	215 (5.7(4)%)	6 (0.16 $^{+0.1}_{-0.06}$ %)

Table 6.20: ^{43}Cr events reaching ACTAR TPC, the total number of detected decay events and their classification into β delayed one, two or three proton emissions with respect to the number of observed decays.

Half-life

The time distribution between the identified ^{43}Cr events and their decay products is shown in Figure 6.15. The obtained half-life value, in agreement with previous values, is shown in Table 6.21.

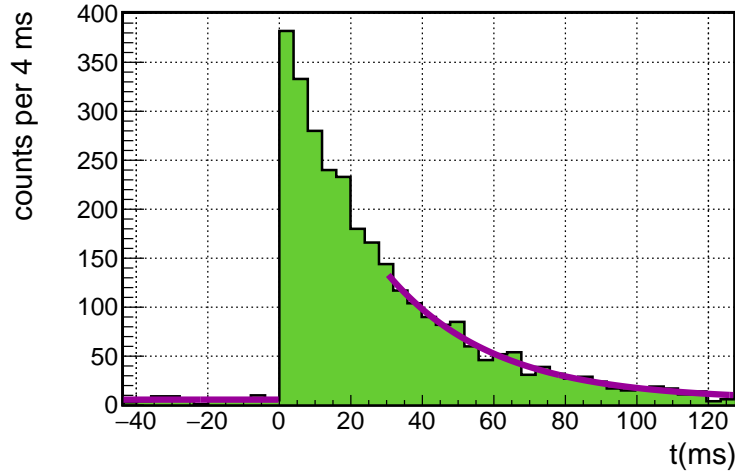


Figure 6.15: Time difference between the identified ^{43}Cr and their associated detected protons. The fit result, performed from $t=30$ ms, is drawn in purple.

	E791	Literature
$T_{1/2}(\text{ms})$	21(2)	21.1(4)

Table 6.21: Obtained half-life of ^{43}Cr and literature value.

Proton energies (β -1p)

The proton distribution for ^{43}Cr is shown in Figure 6.16. The energy values of each proton group are obtained fitting a function defined as a sum of six Gaussians. The obtained energy values and intensities are shown in Table 6.22 and are plotted together with the previous reported energy values of Table 6.19 in Figure 6.17.

A good agreement is found for the reported proton energy values in [140], [147] and [148] in Table 6.19 except for the highest energy one $E_L = 2181(49)$, compatible only within two standard deviations to the obtained result $E_{E791} = 2116(9)$. Two new proton peaks are found in this work at $E_{E791}=1370(10)$ keV and $E_{E791}=1690(9)$ keV. The latest one is most likely measured as a part of the highest intensity proton at $E_{E791}=1764(5)$ keV in previous experiments performed with silicon detectors.

The obtained intensities associated to each proton peak present higher discrepancies. Only the branching ratio corresponding to the third peak at $E_{791}=1553(5)$ is in agreement within one standard deviation uncertainty. In the case of the most intense peak, the total branching ratio 7.1(12) reported in the literature can be reproduced within 2σ error if the two energy components identified in this work (2.4(0.5), 2.3(0.6)) are summed up, under the hypothesis that they have been measured together in previous experiments. The disagreements at high energy values (lower than expected) are most likely the result of

an overestimation of the background in this energy region. On the other hand, at small energy values, for the first peak at $E_{791} = 984$ keV, the proton intensity is found to be higher by a factor of 3.

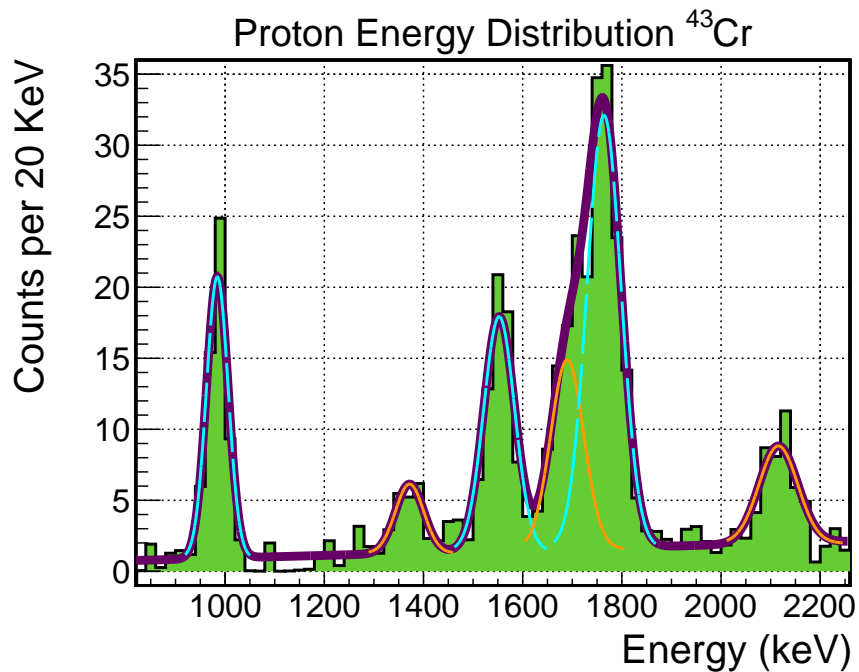


Figure 6.16: ^{43}Cr single-proton energy distribution. The result of the fit (group of 6 peaks) is represented in purple. The individual components are represented by the blue and orange lines.

Peak	E(keV)	BR(%)
1	984(3)	1.7(0.4)
2	1370(10)	0.6(0.2)
3	1553(5)	2.4(0.5)
4	1690(9)	2.3(0.6)
5	1764(5)	5.8(1)
6	2116(9)	3.1(0.8)

Table 6.22: ^{43}Cr single proton energies for the different proton peaks in Figure 6.16 labeled from left to right.

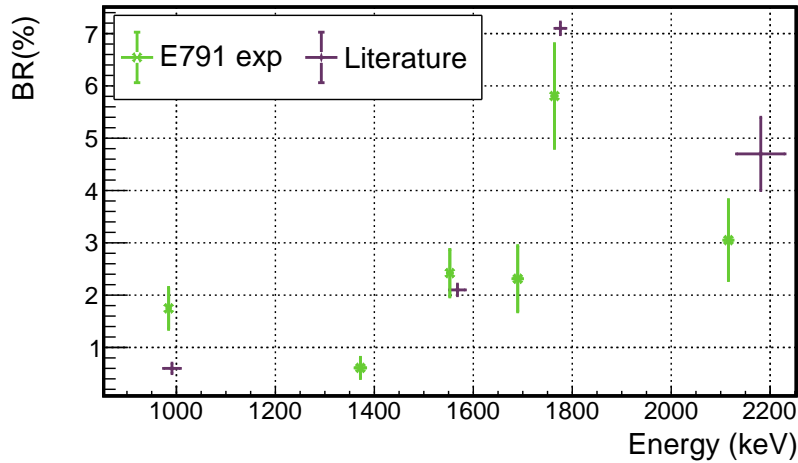


Figure 6.17: ^{43}Cr proton peak energies obtained in this work (green) and literature energy values (purple).

β -2p emissions

For the events identified as β -2p emissions, the angles between the protons and the energies of the ones confined in the volume can be estimated. The angular distribution is built for ^{43}Cr taking all 2-proton events. The result, shown in Figure 6.18, is compatible with an isotropic emission, as expected for β delayed two proton emission decay.

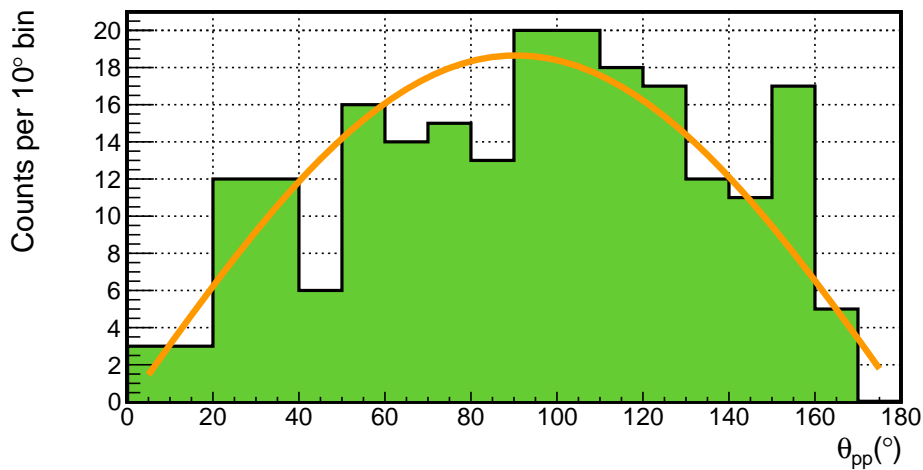


Figure 6.18: ^{43}Cr β -2p angular distribution for all identified events and sine function normalized to the number of entries of the histogram.

For some of the β delayed two proton emissions, the energy of (at least) one of the protons could be measured. The proton energy distribution built from those events, shown in Figure 6.19, does not present any conclusive structure, so it is not possible to identify any transition.

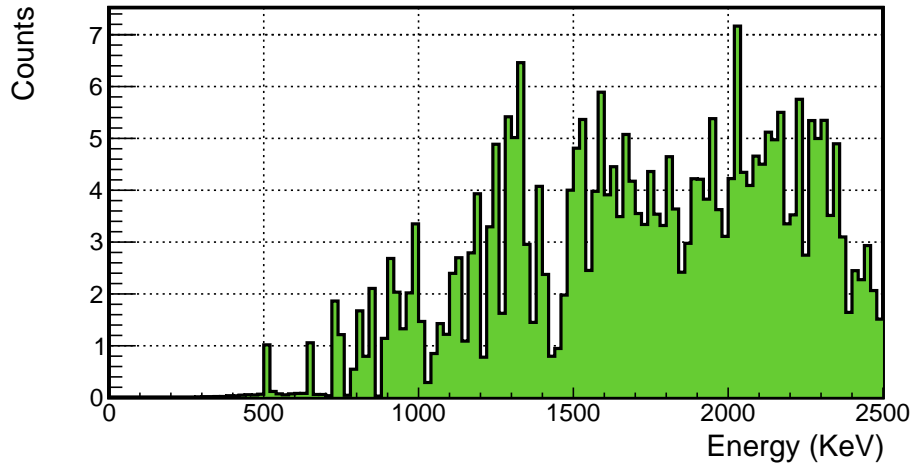


Figure 6.19: Proton energies reconstructed from (at least) one of the protons emitted in the β delayed two proton emission.

In some special cases (10 events), the two protons are fully stopped in the active volume of ACTAR TPC. The energy values of the two independent protons are plotted in Figure 6.20. Four different events are found with a close energy value (E_{p_2}) around 1600 keV, which may indicate the existence of a transition of this energy from an excited state of any of the daughters. In four of the cases, the two protons have a very similar energy between them $E_{p_1} \approx E_{p_2} \approx 2092$ keV (average value). With an average total energy of $E_{pp} = 4185(27)$ keV (see Table 6.23), that could correspond to the one associated to a β -2p decay in the literature $E_L(\beta$ -2p)=4263(19) keV (compatible within two standard deviation uncertainty). Those events could correspond to a β delayed direct two proton emission from an excited state of ^{43}V . One of these two proton events together with the corresponding implantation is shown as an example in Figure 6.21.

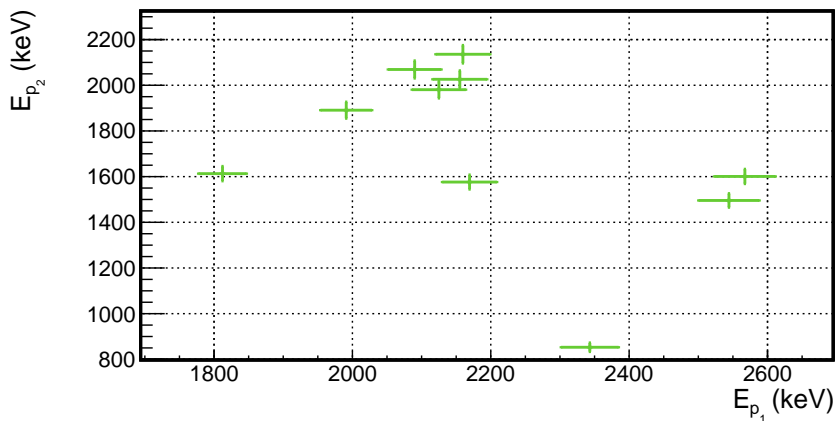


Figure 6.20: Proton energies reconstructed for the two protons emitted in the β delayed two proton emission.

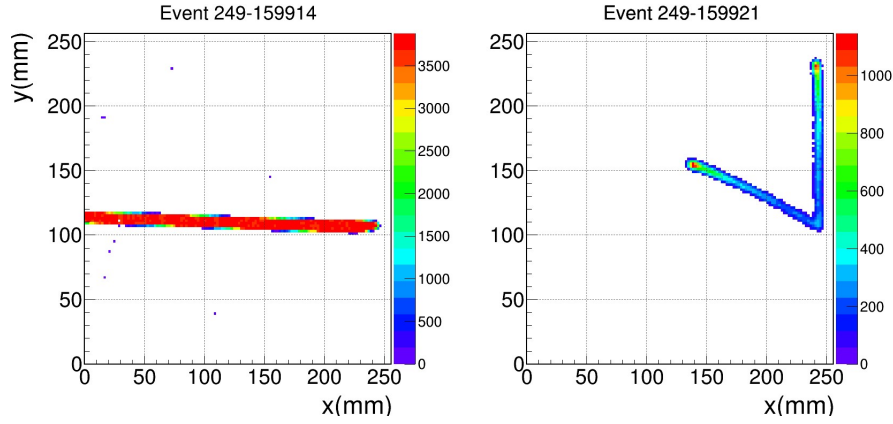


Figure 6.21: The implantation event (pad plane signal) is shown on the left. The two proton emission event, coming 14.5 ms after the implantation one, is shown on the right.

Event	E_{p_1} (keV)	E_{p_2} (keV)	$E_{p_1 p_2}$ (keV)
1	2026(38)	2155(40)	4181(54)
2	1981(37)	2125(39)	4106(54)
3	2069(38)	2090(39)	4159(54)
4	2136(40)	2160(40)	4295(56)

Table 6.23: Reconstructed proton energies from β delayed two proton emissions with similar energy values.

The angle distribution, obtained for this group of events, is shown in Figure 6.22. A simulation for protons around this energy has been performed to study the influence in the angle distribution measurement when requiring the two protons to stay inside the detection volume. Indeed, when measuring "confined protons" a small bias towards smaller angles is introduced: when the angle between the protons becomes larger the probability of one of them escaping the detector is higher, so the probability to measure large angles in this energy range is smaller. However, when comparing the results with the simulated angular distribution, small angles seems to be favoured, as shown in Figure 6.22. When representing the rest of the β -2p events (for which the two protons also remained inside the detector volume but with different energies) the angular distribution seems to be in good agreement with the simulated one, as shown in Figure 6.23. Interesting further studies could be performed in optimal conditions for the measurements of protons on this energy range to study whether these emissions are sequential or they are a direct emission of two protons from an the excited, process that has never been evidenced so far.

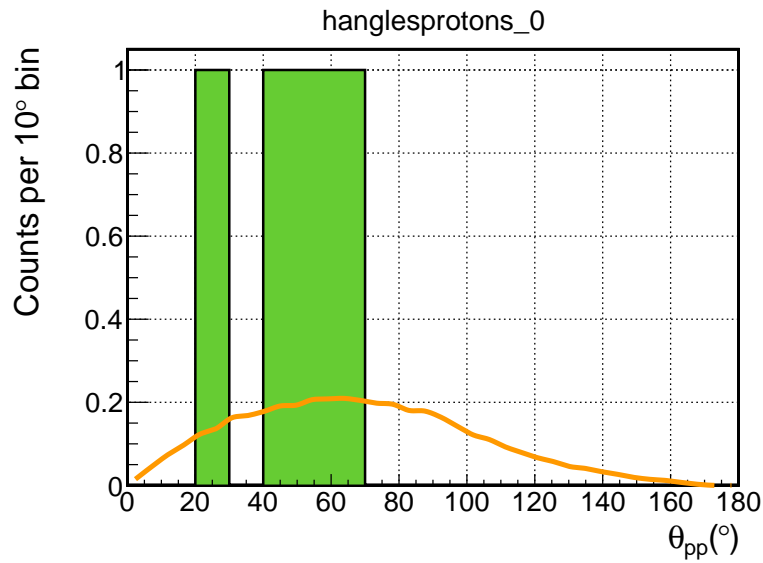


Figure 6.22: Proton angular distribution reconstructed for the four events with similar energies around 2 MeV (green). The orange curve represents the expected angular distribution when requiring the two protons to stay inside the detection volume, obtained by simulation.

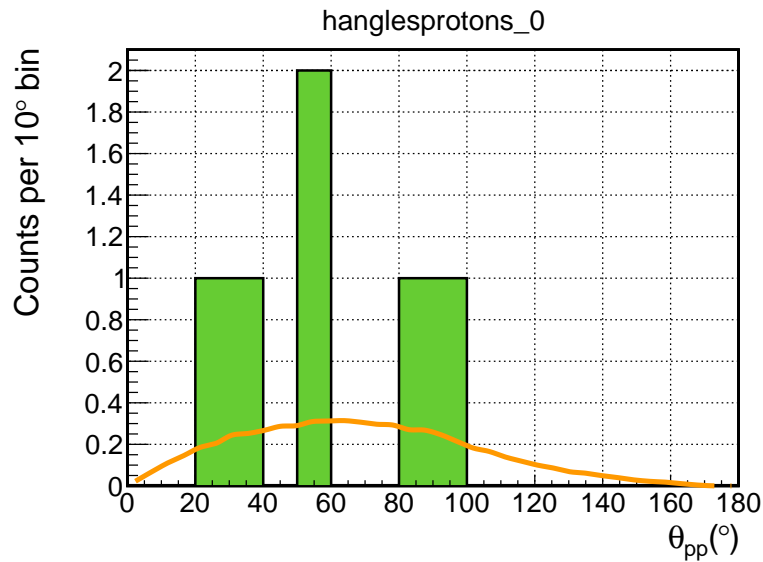


Figure 6.23: Proton angular distribution reconstructed for rest of the β -2p events for which the two proton energies could be measured, excluding the four events for which the protons have similar energies. The orange curve represents the expected angular distribution when requiring the two protons to stay inside the detection volume, obtained by simulation.

6.5 ^{46}Mn

^{46}Mn ($Z = 25$, $N = 21$) with a 36.2(4) ms half-life is the only nucleus with $Z = 25$ measured in the current experiment. It decays by β with a β -p emission with a branching ratio of 57.0(8)%, as shown in Table 6.24. In the energy region of interest (up to 2.5 MeV) two decay energies have been measured and reported in previous experiments (see Table 6.25). This nucleus has a strong astrophysical interest since it provides information about unreachable excited states of ^{46}Cr by measuring the energies of the emitted β -p protons. This enables the study of the inverse reaction:



which consist of an important missing ingredient for Supernova of type II models (nucleosynthesis of ^{44}Ti). A dedicated experiment using ACTAR TPC for this purpose has been already proposed by A.M. Sanchez-Bénitez *et al.* [153].

	$T_{1/2}(\text{ms})$	decay	BR(%)
^{46}Mn	36.2(4) ^a	β -p	57.0(8)% ^a

Table 6.24: Half-life, main decay mode and branching ratio

E_p (keV)	BR(%)
1198(12) ^a	1.8(3) ^a
2307(13) ^a	1.7(4) ^a

Table 6.25: ^{46}Mn reference proton energies in the laboratory frame and branching ratios

^a C. Dossat [140]

A total of 4192 identified ^{46}Mn ions (identification of type 1³) are implanted in ACTAR TPC. From those, 1555 decay events have been registered, which corresponds to a proton branching ratio of 49(2)% when correcting the total number of implantations by the drifting factor (53(6)%). This value is lower than the one measured in previous experiments (57.0(8)%). The branching ratio of the different types of emissions with respect to the measured proton events is shown in Table 6.26. β delayed two proton emission decays have been found for the first time for this nucleus.

Implanted	Implanted _{corr}	Decays	β -1p (rel %)	β -2p (rel %)
4192	2976	1512 (49(2)%)	1501 (99.3 ^{+0.2} _{-0.3} %)	11 (0.7(2) ^{+0.2} _{-0.3} %)

Table 6.26: ^{46}Mn events reaching ACTAR TPC, the total number of detected decay events and their classification into β delayed one or two proton emissions.

³See Section 5.2.5

Half-life

The time distribution between the ^{46}Mn identified nuclei and their associated decay events is shown in Figure 6.24. The half-life result, compatible with the reported values in previous works, can be found in Table 6.27.

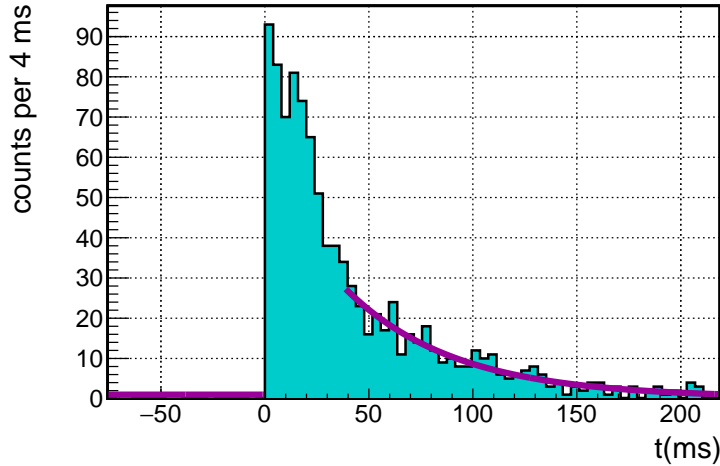


Figure 6.24: Time difference between the identified ^{46}Mn nuclei and their associated detected protons. The result of the fit, performed from $t=38$ ms, is drawn in purple.

	E791	Dossat
$T_{1/2}(\text{ms})$	36(3)	36.2(4)

Table 6.27: Obtained half-life for ^{46}Mn and previous work value.

Proton energies ($\beta-1p$)

The single proton distribution for ^{46}Mn is shown in Figure 6.25. The determined energy and intensity values from the different proton groups, obtained fitting the distribution with a sum of 11 peaks, are shown in Table 6.28 and are plotted together with the literature ones in Figure 6.26 for an easier comparison.

The two proton peak energies and the associated intensities of ^{46}Mn already measured by Dossat et al [140] (see Table 6.25) are well reproduced in the current experiment within one standard deviation uncertainty (Peaks 6 and 11). The peaks 3 and 7 ($E_{E791}=864(4)$ keV and $E_{E791}=1350(10)$ keV) are identified as a contamination from ^{44}Cr , whose main proton emissions have energies of $E_{E791}=866.4(0.6)$ and $E_{E791}=1346(2)$ keV. Because of the high production and implantation rates of this nucleus, and due to an imperfect identification procedure, some of the events have been identified as ^{46}Mn , as explained in Section 5.6.2. Although this contamination problem should be solved in the future with a better identification of the ions, as further discussed in Chapter 7, other proton peaks, not corresponding to any of the neighbouring nuclei main proton values are found in this energy region below 2.5 MeV. The energy proton groups 5 and 10 (from left to right) with measured energies of $E_{E791}=1065(6)$ keV and $E_{E791}=1870(10)$ keV respectively are clearly identified. Despite the reduced statistics, some other proton groups can be distinguished at

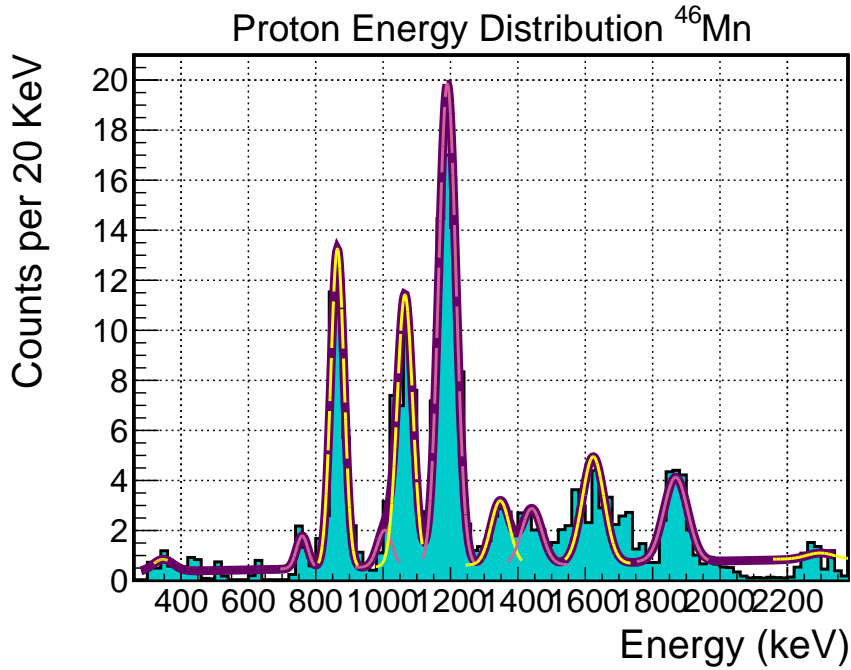


Figure 6.25: ^{46}Mn single-proton energy distribution. The purple line is the result of fitting a group of 11 peaks, represented by the yellow and pink lines. The third and seventh proton peaks have been identified as a contaminant from ^{44}Cr , as explained in the text.

Peak	E(keV)	BR(%)
1	347(12)	0.1(0.1)
2	760(20)	0.1(0.09)
3	864(4)	1.2(0.3)
4	1005(10)	0.2(0.1)
5	1065(6)	1.3(0.3)
6	1191(4)	2.6(0.5)
7	1350(10)	0.4(0.2)
8	1440(20)	0.4(0.2)
9	1620(20)	1.1(0.4)
10	1870(10)	1.7(0.6)
11	2300(22)	0.5(1.0)

Table 6.28: ^{46}Mn energy values for each proton peak (from left to right in Figure 6.25). The peaks in purple (3 and 7) are identified as a contamination from ^{44}Cr as explained in the text.

$E_{E791}=1005(10)$ keV , $E_{E791}=1620(20)$ keV (peak 4 and 9). Finally, two proton peaks at low energies

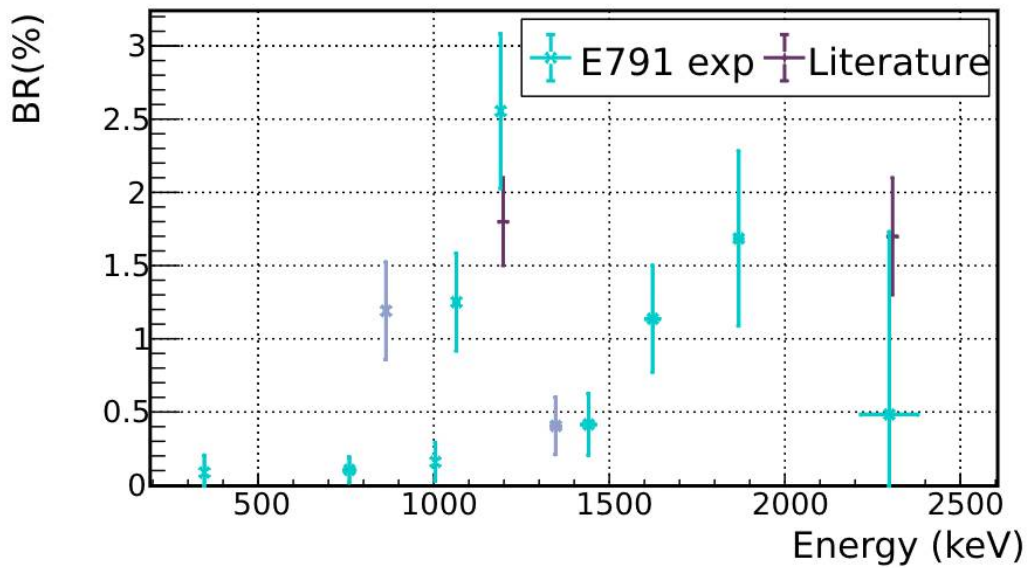


Figure 6.26: The ^{46}Mn proton peak energies obtained in this work are plot in blue. The energy values of previous work are plotted in purple. The points drawn in light purple correspond to the main proton peaks of the contaminant (^{44}Cr).

($E_{E791}=347(12)$ keV , $E_{E791}=760(20)$ keV) can be discerned, but a higher statistics may be needed to conclude.

The study of proton energies below 1 MeV (the most interesting cases for astrophysical reasons) with ACTAR TPC is a very interesting proposal ([153]) but it may require a change of the settings on the detector. The measurement of the first proton peak at $E_{E791}=347(12)$ may be close to the limits of detection efficiency within the current experiment settings. A change of the pressure of the detector will allow for better track reconstructions at low energies.

β delayed two proton emission

From the identified β -2p events, the angles of emission could be reconstructed. The obtained angular distribution (see Figure 6.27) is compatible with an isotropic emission of the protons, as expected for a sequential two proton emission. For five of these events, the individual proton energy of one of the protons has been measured. Three of them have similar energies and could be part of a proton transition around 850 keV from any of the daughter nucleus ^{46}Cr or ^{45}V .

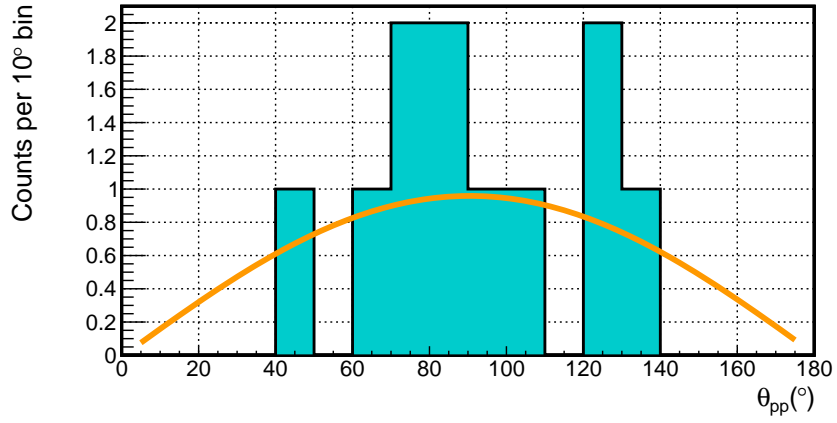


Figure 6.27: ^{46}Mn β two proton angular distribution and sine function normalized to the number of entries of the histogram.

Event	Energy p_1 (keV)
1	1267(27)
2	972(22)
3	806(18)
4	894(20)
5	851(19)
6	1675(33)

Table 6.29: Reconstructed proton energies (when possible) from β delayed two proton emissions from ^{46}Mn events.

6.6 ⁴⁷Fe

⁴⁷Fe ($Z = 26$, $N = 21$) with a 21.9(2) ms half-life is the least exotic of the $Z = 26$ measured group during the experiment. It decays mainly by β -p with a branching ratio of 88.4(9)%, as shown in Table 6.30. Some of the decay protons with energies below 2.5 MeV have been measured in a previous work by Dossat *et al.* [140] (see Table 6.31).

	$T_{1/2}$ (ms)	decay	BR
⁴⁷ Fe	21.9(2)	β -p	88.4(9)%

Table 6.30: Half-life, main decay mode and branching ratio ^a.

E_p (keV)	BR(%)
1516(19)	1.9(7)
1682(20)	4(12)
1825(15)	5.3(7)
2410(28)	1.9(7)

Table 6.31: ⁴⁷Fe reference proton energies in the laboratory frame and branching ratios^a.

^a All values from C. Dossat [136]

A total of 2021 events have been identified as ⁴⁷Fe (identification of type 1⁴) from which 1184 decay events have been registered, which corresponds to a proton branching ratio of 67(4)% when correcting from the drifting factor (25(9)% for ⁴⁷Fe). Although the total proton branching ratio is lower than the one from the literature (88.4(9)%), the branching ratios of the different kinds of emission with respect to the observed proton decays can be obtained (see Table 6.38). Evidences of a small β -2p decay branching ratio for this nucleus are found for the first time⁵.

Implanted	Implanted _{corr}	Decays	β -1p (% _r)	β -2p (% _r)
2021	1768	1184(67(4)%)	1179 (99.6 ^{+0.2%} _{-0.3%})	5 (0.4 ^{+0.3%} _{-0.2%})

Table 6.32: ⁴⁷Fe events reaching ACTAR TPC, the total number of detected decay events and their classification into β delayed one or two proton emissions.

⁴See Section 5.2.5

⁵These events have been identified far enough from the neighbour ⁴⁶Fe group in the identification matrix (see Figure 5.3)

Half-life

The time distribution of the ^{47}Fe isotopes and their decays is shown in Figure 6.28. The obtained half-life value is in agreement with previous work results but presents a high uncertainty due to the lack of statistics, a consequence of the problem of the drifting ions in the detection volume.

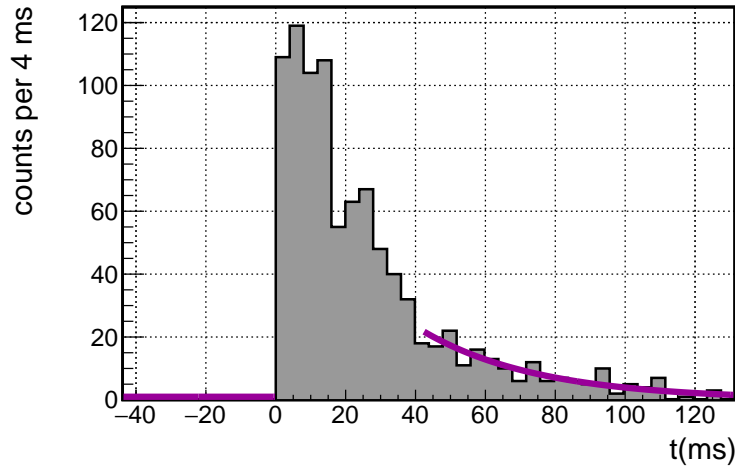


Figure 6.28: Time difference between the identified ^{47}Fe events and their associated decays. The fit, performed from $t = 42\text{ms}$, is shown in purple.

	E791	Dossat
$T_{1/2}(\text{ms})$	23(3)	21.9(2)

Table 6.33: Obtained half-life for ^{47}Fe and previous value by Dossat *et al.*

Proton energies (β -p)

The proton energy distribution for ^{47}Fe is shown in Figure 6.29. In this case, three different fits are performed for a better background estimate due to the reduced number of counts. The first group is composed by the three first peaks, well-separated from the rest. The second group, from the fourth peak until the 10th one, and finally, the lower statistics one (from 11th to 14th). The obtained energy and intensity results are shown in Table 6.34 and compared with previous work values in Figure 6.30.

The proton energy values reported in the literature are well reproduced within one standard deviation uncertainty in the current work (proton groups 6,8,9 and 14). In the region of 1400–1800 keV, three more peaks are found with respect to the literature value. They have been (most likely) measured together with close proton peaks in previous works, as discussed in Section 6.2. Furthermore, low energy peaks at 741(8)keV, 895(9)keV and 1041(9)keV have been clearly identified together with a fourth one with poor statistics at 1310(20)keV. The peaks above 2000 keV, due to the very low number of events and small efficiency of the detector, may need higher statistics to conclude the existence of the different proton groups. The intensities of the proton peaks, shown in Table 6.34, are in agreement within one standard deviation uncertainty with respect to the measured ones by Dossat *et al.*

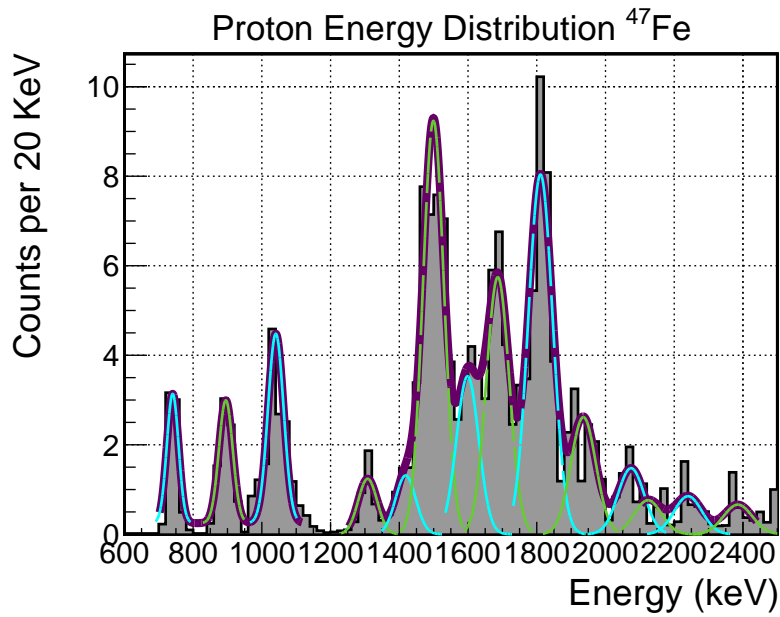


Figure 6.29: ^{47}Fe single-proton energy distribution. The purple line is the result of fitting three different group of peaks as explained in the text. The individual Gaussians are represented by the blue and green lines.

Peak	E(keV)	BR(%)
1	741(8)	0.4(0.2)
2	895(9)	0.4(0.2)
3	1041(9)	0.8(0.3)
4	1310(20)	0.3(0.2)
5	1420(20)	0.4(0.2)
6	1499(6)	3.1(0.7)
7	1599(56)	1.5(0.6)
8	1690(10)	2.8(0.7)
9	1811(8)	6(1)
10	1940(10)	2.5(0.9)
11	2070(20)	2.2(1)
12	2124(40)	1.4(1)
13	2240(30)	2(1)
14	2390(30)	3(2)

Table 6.34: ^{47}Fe proton energies obtained in this work. The different groups for the fit are delimited by the horizontal lines in the table.

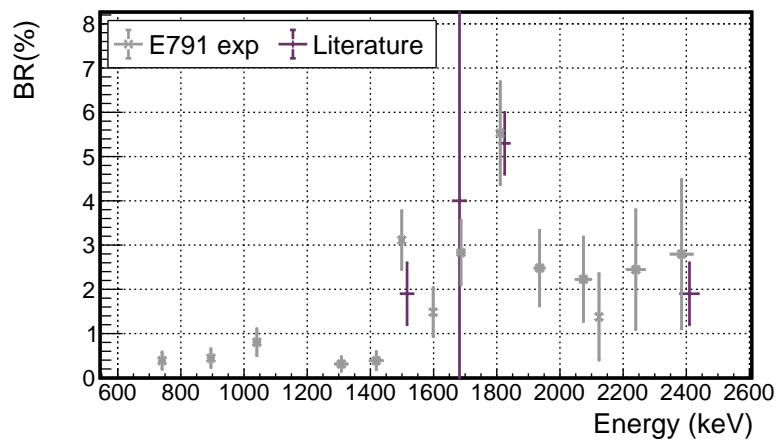


Figure 6.30: The ^{47}Fe proton peak energies obtained in the current work are plotted in grey and those from Dossat *et al.* in purple.

Proton energies ($\beta - 2p$)

From the β delayed two proton emission events, four proton energies (from non escaping cases) have been measured (see Table 6.35). For one of the events, both proton stayed confined, and their energy could be measured, revealing similar values: $E_{p_1} = 1700(33)$ and $E_{p_2} = 1491(30)$ respectively. With a $\approx 12\%$ of energy difference, this event could be compatible with a direct proton emission from an excited state of ^{47}Mn . The signal of the implantation event and the correlated decay one in the XY plane are shown in Figure 6.31.

Event	Energy p_1 (keV)	Energy p_2 (keV)
1	1034(23)	-
2	1700(33)	1491(30)
3	1559(31)	-

Table 6.35: Reconstructed proton energies (when possible) from β delayed two proton emissions from ^{47}Fe events.

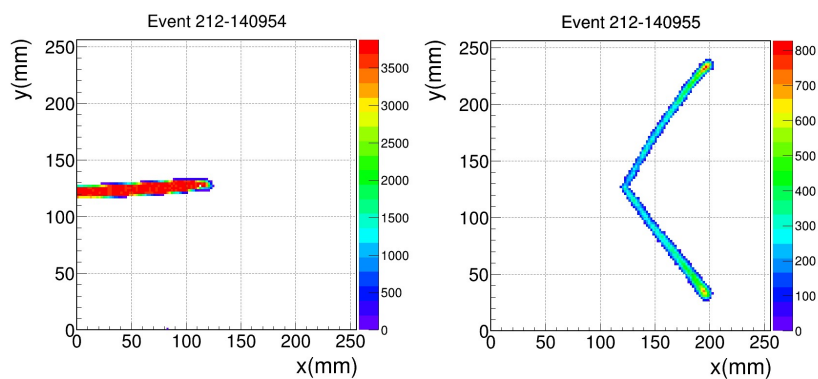


Figure 6.31: The implantation of ^{47}Fe (identification of type 1) is shown on the left and the β delayed two proton emission on the right, emitted 3.65 ms after the implantation.

6.7 ⁴⁶Fe

⁴⁶Fe ($Z = 26$, $N = 20$) with a 13.0(20) ms half-life decays mainly by β delayed one proton emission with a branching ratio of 66(4)%. A small β delayed two proton emission branching ratio has also been established in [145], as shown in Table 6.36. Some of the decay protons with energies below 2.5 MeV have been measured in previous works (see Table 6.37).

	$T_{1/2}$ (ms)	decay	BR(%)
⁴⁶ Fe	13.0(20) ^a	β -p	66(4)% ^{a,b}
		β -2p	0.4(6)% ^b

Table 6.36: Half-life, main decay modes and branching ratio

E_p (keV)	BR(%)
733 ^b	1.2(7) ^a
1028 ^b	1.6(8) ^a
1426(27) ^a	10(3) ^a
1656(23) ^a	4(4) ^a

Table 6.37: ⁴⁶Fe reference proton energies in the laboratory frame and branching ratios

^a C. Dossat [140] ^b M.Pomorski [145]

A total of 467 ⁴⁶Fe nuclei have been correctly implanted in the detection volume, from which 562 decay events have been detected, indicating that the decays of the daughter are also measured within the time window. When selecting only the first decay fulfilling the spatial and time conditions, the total number of decay events decreases to 360, which corresponds to a proton branching ratio of 77.1%, still higher than the literature value. Because of the short half-life of this nucleus, and the calculated drift factor ($11 \pm 12\%$), compatible with 0, the loss of events due to the drifting of the ions is neglected. The estimated relative branching ratios for the different observed emissions with respect to the number of measured decays can be seen in Table 6.38.

Implanted	Decays	β -1p	β -2p
467	360 (77.1%)	357 (99.2 ^{+0.5%} _{-0.8%})	3 (0.8 ^{+0.8%} _{-0.5%})

Table 6.38: ⁴⁶Fe events reaching ACTAR TPC, the total number of detected decay events, (removing the daughter decays) and their classification into β delayed one or two proton emissions.

Half-life

The time distribution between the ^{46}Fe identified nuclei and their associated decay products is shown in Figure 6.32. The half-life result is obtained in this particular case, with the inverse logic than in the previous cases: due to the very short half-life of this nucleus, the fit has been performed for all events and restricting the fit to the short time difference range below 20 ms, to assure the non-drifting of the ions.

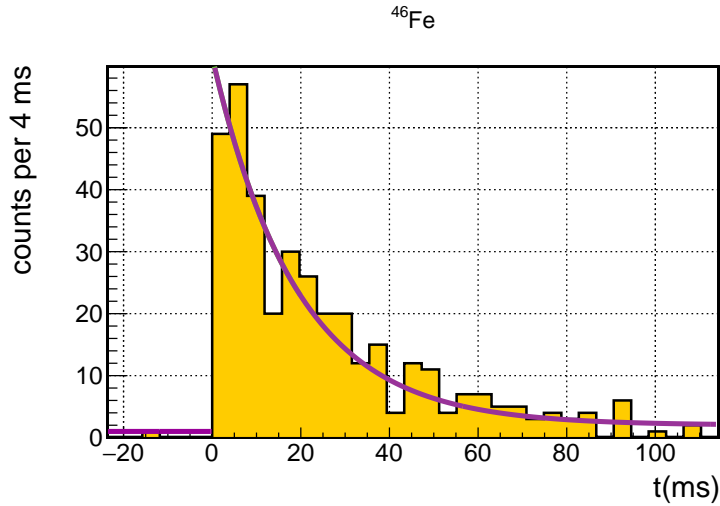


Figure 6.32: Time difference between the identified ^{46}Fe nuclei and their associated proton decays. The purple line shows the result of the fit, performed from $t=0$ up to $t=20$ as explained in the text. The values can be found in Table 6.39

	E791	Literature value
$T_{1/2}(\text{ms})$	11(3)	13.0(20) ^r

Table 6.39: Half-life obtained for ^{46}Fe and literature value.

Proton energies (β -p)

From the β delayed single proton emission cases, 101 protons could be measured. The energy distribution built from these events is shown in Figure 6.33. As in the ^{47}Fe case, the fit of the proton energy distribution of ^{46}Fe is divided into three regions for a better estimate of the background. The two first peaks (first group), the peaks 3 to 5 (second group) and the two last ones (third group) are fitted together. The results are shown in Table 6.40 and plotted together with previous work values in Figure 6.34.

The proton peaks measured in previous works are well reproduced, except for the low energy peak at $E_L=733$ keV [145]. The uncertainty of this value is not determined, and it could be compatible with the proton group found at $E_{791}=850(10)$ keV in this work. The rest of the values from Table 6.37 are in agreement within one standard deviation uncertainty (when calculated). Three other proton groups are found in this work, corresponding to the peaks 3, 5 and 7 with energies of 1260(8) keV, 1500(20) keV and 1885(28) keV respectively. The two first ones have been (most likely) measured together with the

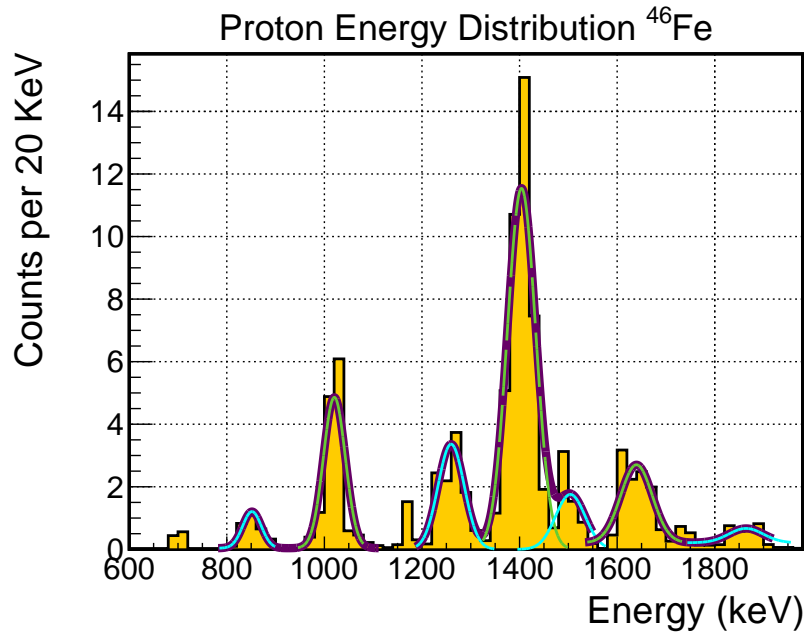


Figure 6.33: ^{46}Fe single-proton energy distribution. The purple line is the result of fitting individually three groups of peaks, whose individual components are drawn in blue and green lines.

higher intensity proton peak at 1404 keV in previous works with silicon detectors due to the β background. The intensities of the proton peaks, shown in Table 6.40, are in agreement within one standard deviation uncertainty with respect to the values of the literature. The intensity associated to the first peak at $E_L=733$ keV is in agreement with the intensity for the peak found at $E_{791}=850$ keV which may be an indication of a systematic energy shift between the two measurements.

Peak	E(keV)	BR(%)
1	850(10)	0.7(0.4)
2	1022(6)	3(1)
3	1260(8)	2.8(0.9)
4	1404(5)	11(2)
5	1500(20)	1.8(0.9)
6	1640(20)	2(1)
7	1885(28)	2(2)

Table 6.40: Obtained ^{46}Fe single proton energies. The horizontal lines indicate the different groups for fitting.

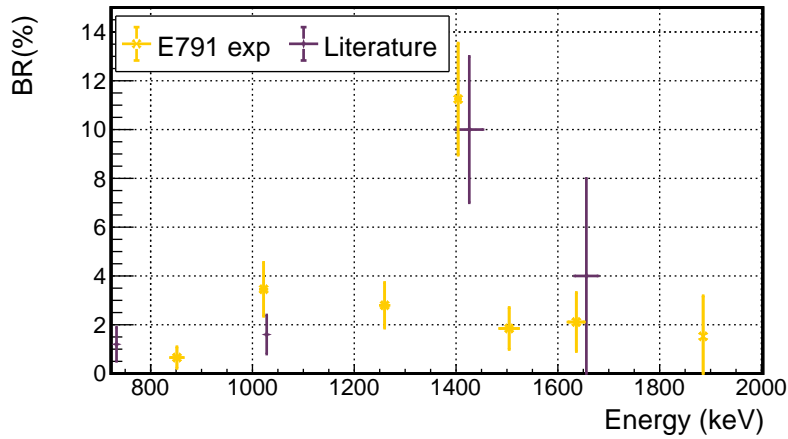


Figure 6.34: ^{46}Fe proton peak energies obtained in the current work (yellow) and those from the literature (purple).

Proton energies (β -2p)

From the β delayed two proton emission events, the energy of one of the emitted protons could be measured in each case. The energy values, shown in Table 6.41, do not constitute any proton group.

Event	Energy (keV)
1	1458(30)
2	1301(27)
3	1659(33)

Table 6.41: Reconstructed proton energies (when possible) from β delayed two proton emissions from ^{46}Fe events.

6.7 ⁴⁵Fe

⁴⁵Fe ($Z = 26$, $N = 19$) with a 2.56(2) ms half-life is the most exotic of the $Z = 26$ measured group during the experiment. It decays mainly by two proton emission, with a branching ratio of 70(4)%. The study of this nucleus, as already mentioned in Chapter 1, established for the first time the ground state two-proton radioactivity in 2002 [16],[42]. The decay of this nucleus was later measured using a time projection chamber with a high number of events by K. Miernik *et al.* [52] and the angular and energy correlations between the two protons emitted from the ground state were determined. Other decay channels were also observed (β delayed one, two and three proton emissions) as shown in Table 6.42. The total energy of the 2-proton decay Q_{2p} , calculated in [45] and the individual proton energy distribution values can be seen in Table 6.43.

	$T_{1/2}$ (ms)	decay	BR(%) ^a
⁴⁵ Fe	2.56(20) ^a	β -p	18.9(35)%
		β -2p	7.8(23)%
		β -3p	3.3(16)%
		2p	70(4)%

Table 6.42: Half-life, main decay mode and branching ratio

^a K. Miernik *et al.* [52]

^b C. Dossat *et al.* [45]

Q_{2p} (keV)	E_p/Q_{2p} (keV)
1150(15) ^b	0.5(1) ^a

Table 6.43: ⁴⁵Fe two proton total energy and individual proton energies (distribution centered at $E_p = 500$ with a standard deviation of 100 keV)

Only a total of 11 identified ⁴⁵Fe ions (5 with identification of type 1 and 6 with type 2 (see Section 5.2.5) are correctly implanted in ACTAR TPC. Ten other events, initially identified as the neighbour nucleus ⁴⁶Fe, have been associated to two proton emission decays and are thus included as part of the ⁴⁵Fe events in this section. This indicates a problem in the identification process that makes difficult the estimation of the branching ratio for the different emissions. The values, taking into account only the events originally identified as ⁴⁵Fe, are shown in Table 6.44. The average half-life value, calculated for all events, is $\langle T_{1/2} \rangle = 1.6_{-1}^{+2}$ ms, where the error has been estimated using the Schmidt method [154].

Implanted	Decays	2p	β -1p (%)
11	8 (73%)	6 (75_{-24}^{+16} %)	2 (25_{-16}^{+24} %)

Table 6.44: Events initially identified as ⁴⁵Fe reaching ACTAR TPC, the total number of detected decay events and their classification into two proton or β delayed one proton emission. The relative intensities are calculated with respect to the total number of observed decays.

Two proton emission events

The angular and energy correlations between the two emitted protons, shown in Figure 6.35 and Figure 6.36, are obtained from the two proton events identified as ^{45}Fe and those wrongly identified as ^{46}Fe . Both results, despite a reduced statistics, are consistent with the previous studies [52]. The average total energy is 1070(5)keV, consistent within the uncertainty with the calculated total energy of the decay 1150(15). The energy distribution of the two proton events (see Figure 6.36 shows a E_p/E_{pp} value is centered at 0.5 (equal energy sharing for the two protons with a standard deviation of 12%). A sequence of measured events after a ^{45}Fe implantation is shown in Figure 6.37 as an example.

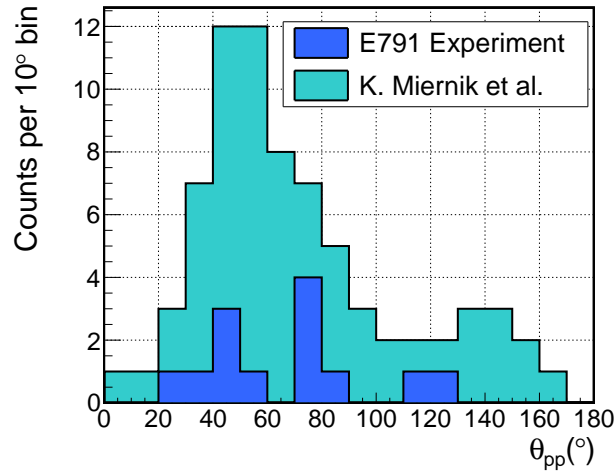


Figure 6.35: ^{45}Fe angular distribution obtained in this work (dark blue) for the events from which the angle could be reconstructed (13 events) together with the results obtained in [52] (light blue). The latest one has been approximated to an integer number of counts.

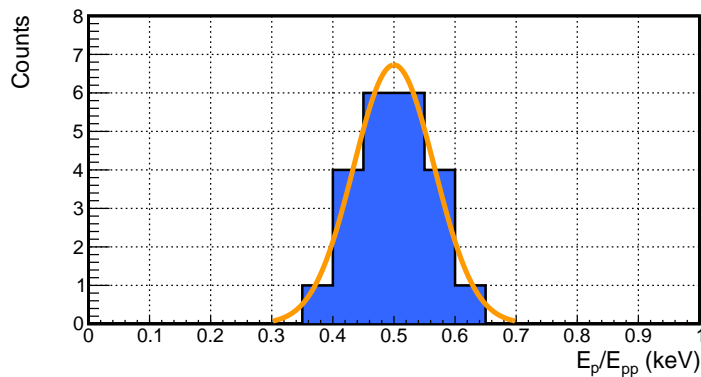


Figure 6.36: ^{45}Fe energy distribution obtained for the events from which the individual proton energies could be reconstructed (total of 22 protons)

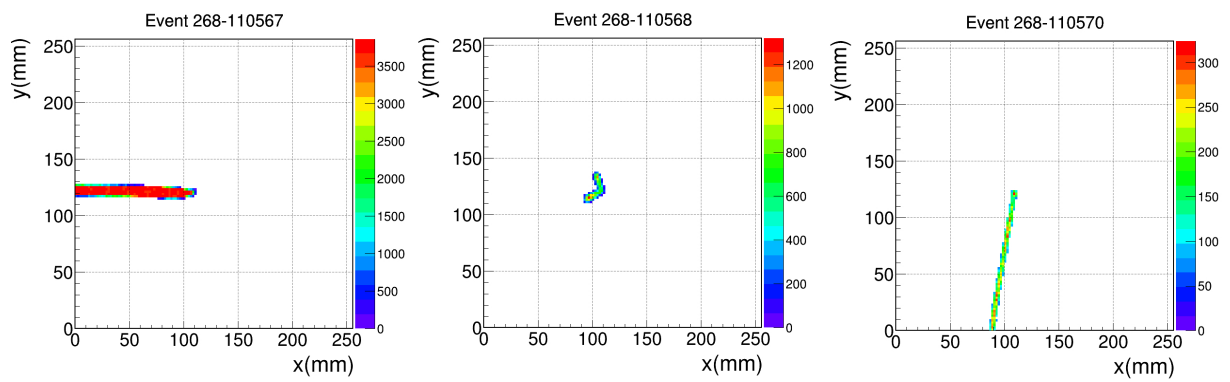


Figure 6.37: Sequence of events measured after the implantation of a ^{45}Fe nucleus (left): two proton decay event (middle) emitted 2.93 ms after the implantation and decay of the daughter nucleus ^{43}Cr (right) emitted 20 ms after the first event.

6.9 ^{49}Ni

^{49}Ni ($Z=28$, $N=21$) with a 7.5(10) ms half-life is a very exotic nucleus that has been measured with very low statistics and no proton transitions have been reported so far. Only the total proton-emission branching ratio has been determined to be 83.4(13.2)% in previous works by Dossat *et al.* as shown in Table 6.45.

	$T_{1/2}(\text{ms})$	decay	BR(%)
^{49}Ni	7.5(10) ^a	β -p	83(13)% ^a

^a C. Dossat [140]

Table 6.45: Half-life, main decay mode and branching ratio

A total of 66 ^{49}Ni events with an identification of type 1 or 2 have been measured during the experiment. The decay events of 53 of them have been measured. This corresponds to a proton branching ratio of 83%, which is in agreement with the estimate by Dossat *et al.* [140]. 36 of the decay events are identified as β -p decays, from which only four proton events are fully recorded in the ACTAR TPC device. 17 decays are identified as β -2p transitions and a last one is identified as a β -3p decay. The estimated branching ratios are shown in Table 6.46.

Implanted	Decays	β -1p	β -2p	β -3p
65	53 (83%)	36 ($67^{+7}_{-8}\%$)	17 ($32^{+8}_{-7}\%$)	1 ($2^{+4}_{-2}\%$)

Table 6.46: ^{49}Ni events reaching ACTAR TPC, the total number of detected decay events and their classification into β delayed one, two or three proton emissions.

Half-life

The time difference between the identified ^{49}Ni and their decay products is shown in Figure 6.38. The half-life, in agreement with the value from Dossat *et al.* [140] (as shown is Table 6.47). The result is obtained from all events (excluding daughter decays and under the assumption of a negligible number of nuclei drifting towards the cathode) and is in agreement with the literature value ($T_{1/2} = 7.5(10)\text{ms}$) [140].

β delayed proton emission

Only three of the decay products of the β delayed single proton emissions are not escaping the detection volume. The energy values are shown in Table 6.48, which can indicate the presence of two different proton groups: $E_1 = 912(20)\text{(keV)}$ and $E_2 = 1541(22)\text{(keV)}$ (average value of the obtained energies).

	E791	Dossat
$T_{1/2}(\text{ms})$	7(2)	7.5(10)

Table 6.47: Half-life obtained for ^{49}Ni and value from Dossat *et al.* [140].

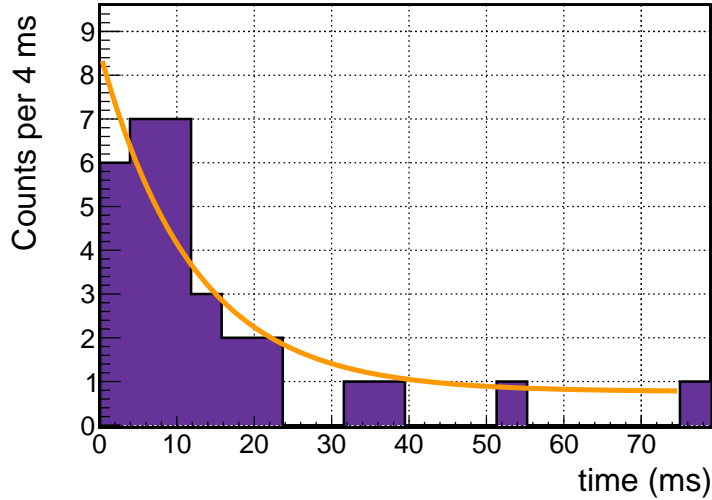


Figure 6.38: Time difference between the identified ^{49}Ni nuclei and their associated proton decays. The orange line shows the result of the fit.

Event	Energy (keV)
1	912(20)
2	1525(31)
3	1559(31)

Table 6.48: Reconstructed proton energies (when possible) from β delayed single proton emissions from ^{49}Ni events.

β delayed two proton emission

Some events are identified as β -2p emissions, from which the angles between the emitted protons and the energy of the (confined) ones could be reconstructed. The proton angular distribution of the β delayed two proton emission is shown in Figure 6.39. No particular structure is observed as predicted for a β -2p emission in which the protons are emitted sequentially. In four of the cases, the energy of one of the (confined) protons could be measured. Their energies are shown in Table 6.49. Any of them with a similar energy compared to the resolution of the detector.

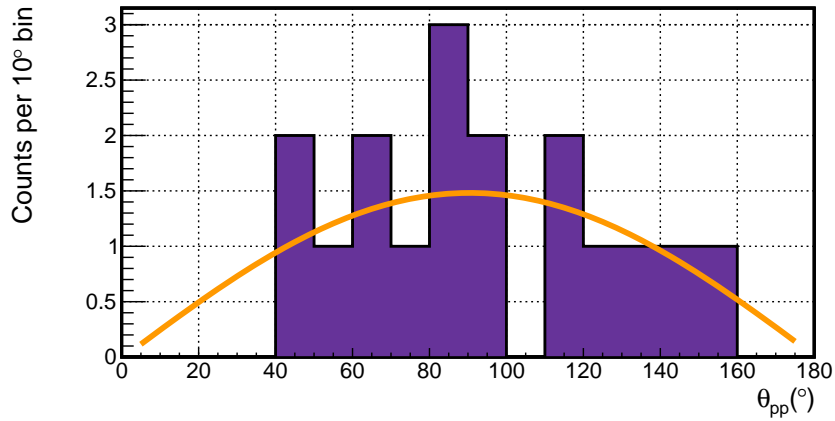


Figure 6.39: ^{49}Ni angular distribution of β delayed two proton emission and sine function normalized to the number of entries of the histogram.

Event	Energy (keV)
1	1117(24)
2	1277(27)
3	1888(36)
4	1426(30)

Table 6.49: Reconstructed proton energies (when possible) from β delayed two proton emissions from ^{49}Ni events.

β delayed three proton emission

The β delayed three proton emission decay event, emitted 0.31 ms after an implantation event identified (identification of type 2) as ^{49}Ni is shown in Figure 6.40. One of the three protons stayed confined in the detector and its energy $E_p = 908(20)$ keV has been reconstructed. The identification of this implantation event is not confirmed at the current stage, and it could be an emission from the neighbour nucleus ^{48}Ni .

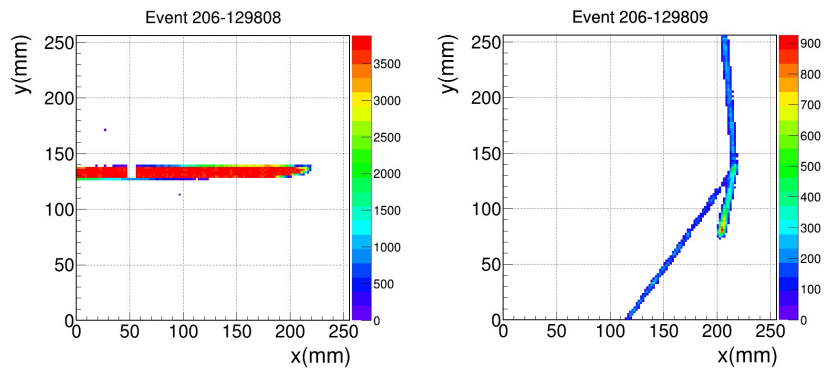


Figure 6.40: The implantation of ^{49}Ni is shown on the left and the β delayed three proton emission on the right, emitted 0.31 ms after the implantation. Only one of the three protons is not escaping the detection volume.

6.10 ⁴⁸Ni

⁴⁸Ni ($Z = 28$, $N = 20$) with $2.1^{(+14)}_{(-6)}$ ms half-life is the most exotic nucleus measured during the experiment. It decays with a branching ratio of about 70% by two proton emission. Only few nuclei have been observed and measured in previous works (see Table 6.51).

	$T_{1/2}$ (ms)	decay	BR(%)
⁴⁸ Ni	$2.1^{(+14)}_{(-6)}$	β -p	30(20)%
		2p	70(20)%

Table 6.50: Half-life, main decay mode and branching ratio

E_{p_1} (keV)	E_{p_2} (keV)	Θ_{pp} ($^\circ$)
600(70)	645(110)	66(14)
590(90)	635(90)	36(7)
580(60)	665(50)	51(8)
645(130)	680(80)	33(17)

Table 6.51: Proton energies measured for two proton emission events of ⁴⁸Ni and angles measured in a previous work [145]

^aAll values from M.Pomorski *et al.* [145]

In this work, only seven events have been identified as ⁴⁸Ni, two of them with an identification of type 1 and the rest with an identification of type 2. One of the events, initially identified as ⁴⁹Ni but with a two proton emission decay, is also included in the current results, and it will be denoted as (+1) in the presented total values in Table 6.52. The decay of one of the correctly implanted ⁴⁸Ni ions is missing, most likely due to the dead time of the detector, as further discussed in paragraph 6.10.

Seen in ACTAR	Implanted	Decays	2-p	β -1p	β -2p	β -3p
7(+1)	5(+1)	4(+1)	2(+1)(60^{+25}_{-30} %)	1(20^{+32}_{-17} %)	0 ($+21$ %)	1(20^{+32}_{-17} %)

Table 6.52: ⁴⁸Ni events reaching ACTAR TPC, those correctly implanted (not traversing the detection volume) and the detected decay events. The +1 event corresponds to one two proton emission identified as ⁴⁹Ni as discussed in the text.

The average half-life value for the correctly measured decay events is $\langle T_{1/2} \rangle = 2.19^{+3}_{-2}$ ms and the branching ratio can be estimated to be $BR(2p) = 60\%$, $BR(\beta-p) = 20\%$ and $BR(\beta-3p) = 20\%$, both values in agreement with previous results shown in Table 6.50.

The signals in the XY plane of the identified decay events from ⁴⁸Ni, together with the implantation ones and the (oftenly) measured decays from daughter nuclei, are shown in Figures 6.41 to 6.45. All the events will be described individually in the next paragraphs.

The first identified ⁴⁸Ni nuclei correctly implanted in ACTAR TPC and its decay products are shown in Figure 6.41. A two proton emission is observed 2.14 ms after the implantation event. Since both

protons are confined in the detection volume, the individual proton energies $E_{p_1} = 724(17)$ keV and $E_{p_2} = 532(12)$ keV are measured, as well as their relative emission angle $\Theta_{p_1 p_2} = 71(10)^\circ$. The total energy $E_T^{E791} = 1256(10)$ keV is in agreement with previous results in [145], with an average value of $E_L = 1260(63)$ keV. A second proton, emitted by a β -p decay of the daughter nucleus (^{46}Fe) is also registered with energy $E_{p_3} = 1422(29)$ keV, which is in agreement with the dominant proton peak reported in Section 6.7 for ^{46}Fe ($E_3^{E791} = 1404(5)$ keV).

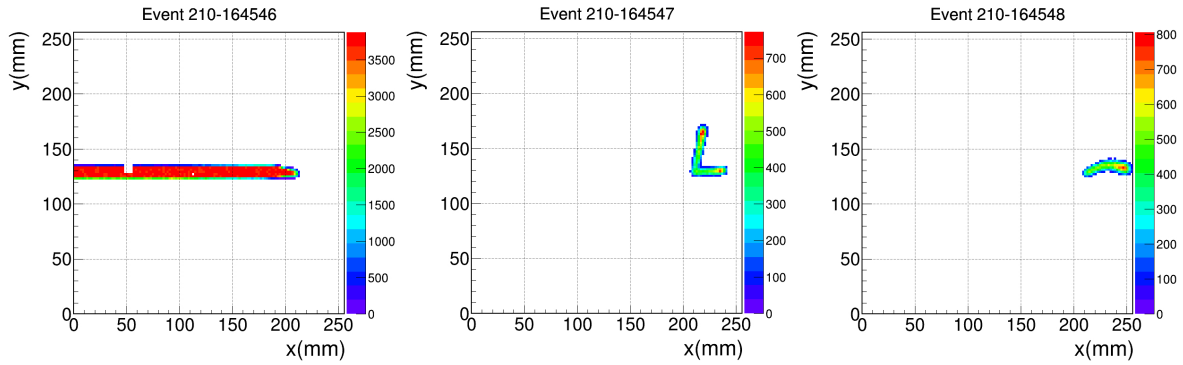


Figure 6.41: From left to right in time: the implantation of ^{48}Ni (identification of type 2), the two proton decay happening at $\Delta t = 2.14$ ms and the decay of the daughter, a β -p emission from ^{46}Fe , happening at $\Delta t = 9.8$ ms with respect to the implantation.

The second identified ^{48}Ni nucleus (identification of type 1) and its decay products are shown in Figure 6.42. In this case, the nucleus decays by β -p emission to ^{47}Fe , which further decays by β -p to ^{47}Mn . No proton energies could be estimated for any of the decays, since both escape the detection volume. In the latest case, the relatively wide track with no registered Bragg Peak and the high dispersion value in the decay point, as explained in Sections 5.3.4 and 5.3.2 respectively, indicate that the emission is happening near the cathode due to the non-neutralization of the ions in the gas. Since the proton is being emitted towards the cathode, it is thus escaping the volume.

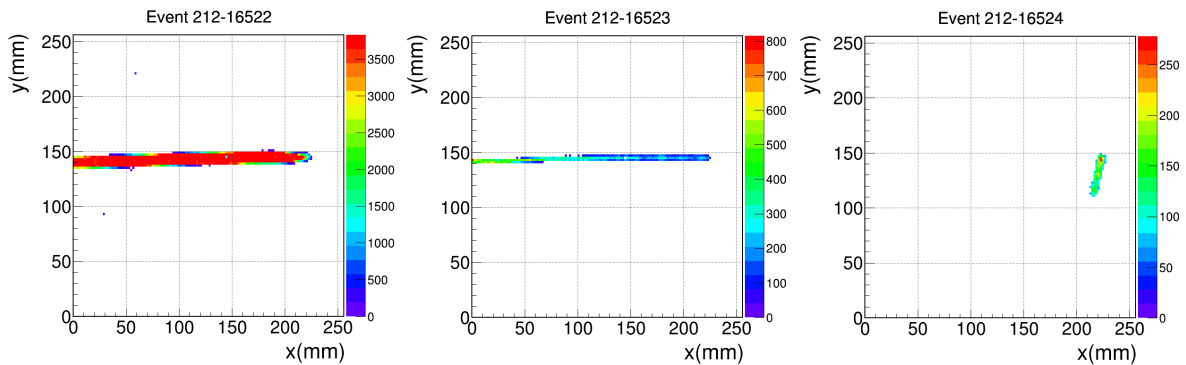


Figure 6.42: The ^{48}Ni implantation event is shown on the left. A first proton emission, from a β -p decay, is emitted at $\Delta t = 1.80$ ms (middle) The daughter nucleus ^{47}Fe decays also by β -p emission within $\Delta t = 15.8$ ms with respect to the implantation. In the latter case, the proton escapes through the cathode, as discussed in the text (right).

The third identified ^{48}Ni ion (identification of type 2) decays within 3.84 ms by β delayed three proton emission to ^{45}Cr , as shown in Figure 6.43. No further decay from ^{45}Cr is observed.

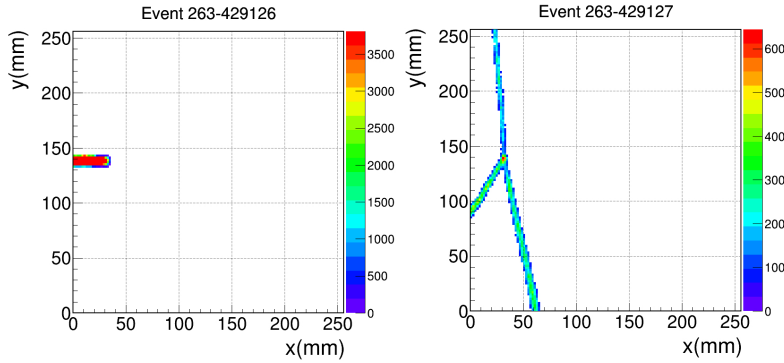


Figure 6.43: The third identified ^{48}Ni implantation event is shown on the left. This nucleus decays by β -3p emission to ^{45}Cr within $\Delta t=3.84$ ms (right) with no further observed decays.

The fourth ^{48}Ni event is initially identified as ^{49}Ni (identification of type 1). Its decay event, happening within $\Delta t=1.75$ ms although partially escaping, has been identified as a two proton emission. This nucleus has been consequently included in the ^{48}Ni group. The implantation and the decay events are shown in Figure 6.44. In the latter case, the tracks have been analysed using the reconstructed signal, obtained as explained in Section 4.1.5. First, to clarify the nature of the event and secondly, to calculate⁶ the angle of emission between the two protons $\theta_{p_1 p_2}=58\pm 7(^{\circ})$. No energies can be calculated since both protons are escaping the volume. The similar charge distribution in both tracks and the identification of the beginning of the Bragg Peak⁷ in one of the tracks with compatible charge deposit values, indicates that the proton is a low energy one. These have been the main reasons to identify this event as a two proton emission. The reconstructed signal projections in the XZ and YZ planes for this event are also shown in Figure 6.44.

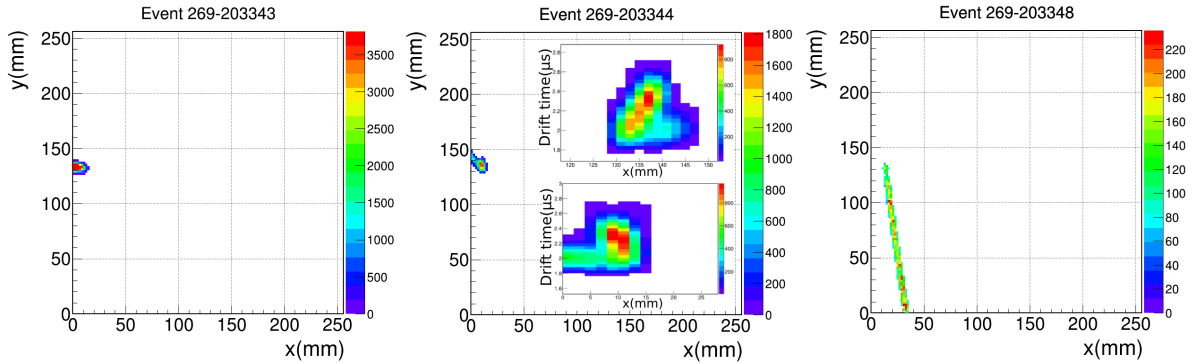


Figure 6.44: The fourth ^{48}Ni implantation event is shown on the left. The decay event, happening within $\Delta t=1.75$ ms although partially escaping, it has been classified as a two proton event. A high energy proton emission from a β -p decay of the daughter nucleus ^{46}Fe , happening at $\Delta t=57.46$ ms from the implantation event, is also observed.

⁶From the 3D fit mentioned in Section 5.3.2

⁷The lengths of the protons tracks are reduced with respect to the first event due to the change of pressure in the detector during the experiment from P=300 mbar to P=450 mbar)

The decay of the daughter nucleus ^{46}Fe , happening 57.46 ms after the implantation event, is also observed, but its energy cannot be measured since the proton is escaping the active volume. The observation of the daughter decay reinforces the hypothesis of identification of this event to be a ^{48}Ni since the daughter nucleus of ^{49}Ni after a β -2p decay (^{47}Mn) has a very low β -p branching ratio $BR_{\beta p} \ll 1.70\%$.

The fifth identified ^{48}Ni event (identification of type 2) is unfortunately also implanted very close to the entrance window. The implantation event is not shown to display the three sequential decay events measured in this case, shown in Figure 6.45. The decay of the ^{48}Ni nucleus happening within 1.45 ms has been identified as a two proton emission with a similar argument than in the previous event: similar charge distribution in both tracks and the identification of the beginning of the Bragg Peak in one of the cases. The second and third proton emissions are β -p decays of the daughter nucleus ^{46}Fe ($\Delta t=57.46$ ms) and ^{45}Cr ($\Delta t=165$ ms or $\Delta t=106$ ms with respect to the emitter) respectively. The half-lives of those nuclei are 13 ms and 61 ms, respectively. The energy of the first proton is $E_p = 1587 \pm 31$ keV and the second one $E_p = 1887 \pm 36$ keV. The dispersion of the decay points of both tracks belong to the group of events emitted from the cathode, in this case an energy correction of $\Delta E = -9$ keV and $\Delta E = -12$ keV needs to be considered as explained in Section 5.6.2. These protons could correspond to the proton groups $E_5(^{46}\text{Fe}) = 1500(20)$ keV and $E_{11}(^{45}\text{Cr})=1870(10)$ keV respectively.

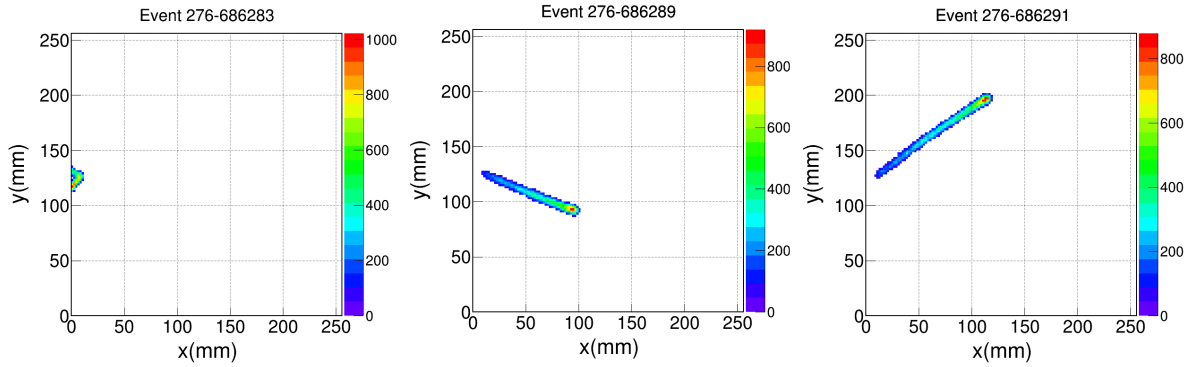


Figure 6.45: The ^{48}Ni implantation event is not shown to display the three sequential decay events measured in this case. On the left, its decay product, happening at $\Delta t=1.45$ ms, identified as a two proton emission. The second (center) and third (right) proton emissions are products of β delayed proton decays of the daughter nucleus ^{46}Fe ($\Delta t=57.46$ ms) and ^{45}Cr ($\Delta t=164.88$ ms) respectively.

A sixth ^{48}Ni event is identified with no decay products. As discussed in Section 3.6, the level 1 ACTAR TPC trigger signals are counted in the U2M scaler module. An increment of this value of two units from the ^{48}Ni implantation event and the next registered event (implantation of a another nucleus happening at $\Delta t=14$ ms) is observed, which indicates that the decay event happened most likely within the dead time of the detector from the ^{48}Ni implantation event ($194 \mu\text{s}$ for this event). The same effect is observed between the second registered event after the implantation of interest and the third one, happening at $\Delta t=26$ ms from the ^{48}Ni event with a dead time of the same order, which may indicate the loss of the decay of the daughter nuclei as well within the dead time of the detector.

The measured energy (for the non-escaping two proton event) and the reconstructed angles between the emitted protons are shown in Table 6.53. The angular distribution obtained in this work is shown together with previous results by M.Pomorski *et al.* [145] in Figure 6.46. Despite the very low number of measured events, for the moment no angles above 90° have been observed neither from the analysed 4 events in the previous work [145], nor for the three events measured in this one, which is not the case for the two proton emitter ^{54}Zn , for which only 12 two proton emission events have been reconstructed in two

different experiments: 7 events P. Ascher *et al.* [54] and 5 (preliminary), from A. Kubiela *et al.* [155] with measured angles with values distributed in the 30–150° range. Although higher statistics may be needed to conclude, the non observation of angles above 90° in the ⁴⁸Ni case can indicate the presence of a structure in the angular distribution as the one predicted by Grigorenko *et al.* [57] due to its pure configuration (double magic nucleus).

E_{p_1} (keV)	E_{p_2} (keV)	Θ_{pp} (°)
724(17)	532(12)	71(10)
-	-	58(10)
-	-	72(10)

Table 6.53: Reconstructed proton energies (when possible) and angles between emitted protons identified as decays of ⁴⁸Ni events.

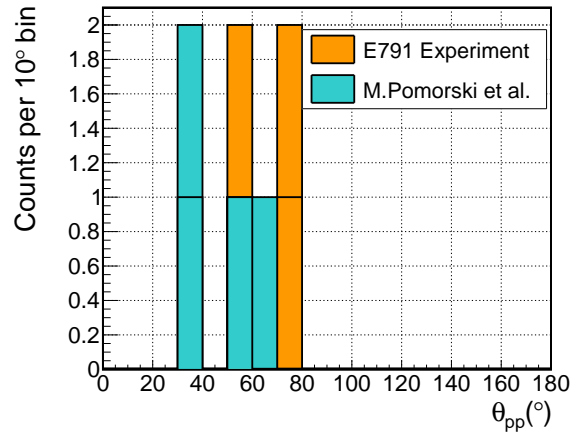


Figure 6.46: ⁴⁸Ni angular distribution obtained in this work (orange, three events) together with the results obtained in [145] (blue) (four events).

6.11 Summary of main results

A summary of the main results obtained in this chapter (half-lives, total branching ratio and branching ratio of the different emissions (β -1p, β -2p ...) and the number of implantations of all the studied nuclei, are shown in Table 6.54 and 6.55 respectively.

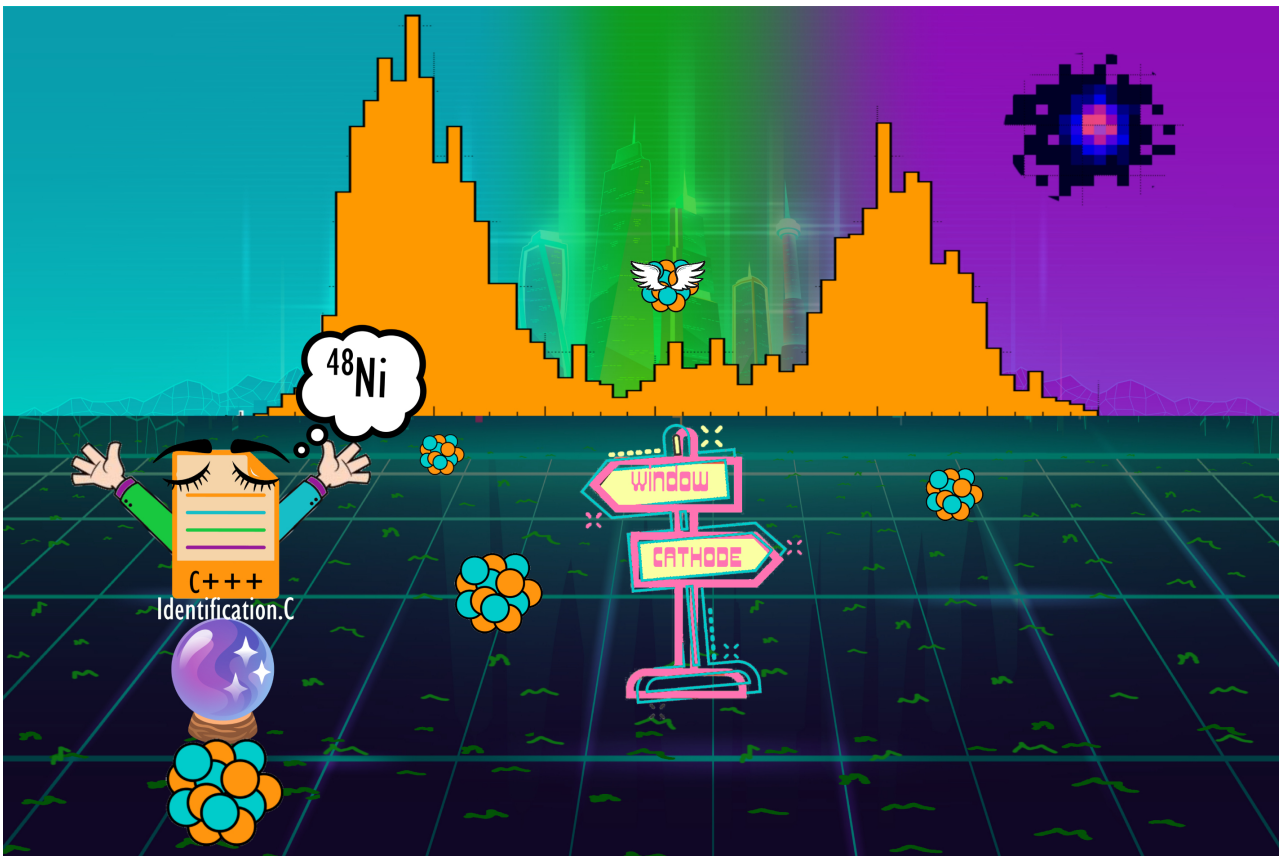
Nucleus	$T_{1/2}$		BR_p		β -1p		β -2p		β -3p		2p	
	E791	L	E791	L	E791	L	E791	L	E791	L	E791	L
^{41}Ti	81.8(4)	81.9(5)	88(4)	92.4(6)	100.0(4)	100.0(6)	7×10^{-4}	-	-	-	-	-
^{45}Cr	59(2)	60.9(4)	31(1)	34.4(8)	100(1)	100.0(8)	-	-	-	-	-	-
^{44}Cr	41(2)	42.8(6)	17.4(2)	12.2(9)	99(1)	100.0(9)	$0.67^{+0.10}_{-0.09}$	-	-	-	-	-
^{43}Cr	21(2)	21.1(4)	102(3)	91.03(3)	94.1(4)	87.1(6)	5.7(4)	12.7(6)	$0.16^{+0.1}_{-0.06}$	0.14(6)	-	-
^{46}Mn	36(3)	36.2(4)	49(2)	57.0(8)	$99.3^{+0.2}_{-0.3}$	100.0(8)	$0.7^{+0.2}_{-0.3}$	-	-	-	-	-
^{47}Fe	23(3)	21.9(2)	67(4)	88.4(9)	$99.6^{+0.2}_{-0.3}$	100.0(9)	$0.4^{+0.3}_{-0.2}$	-	-	-	-	-
^{46}Fe	11(3)	13.0(20)	77.1	70(6)	$99.2^{+0.5}_{-0.8}$	94.2(7)	$0.8^{+0.8}_{-0.5}$	0.6(7)	-	-	-	-
^{45}Fe	$1.6^{+2.0}_{-1.0}$	2.56(2)	73	100(4)	25^{+24}_{-16}	18.9(4)	-	7.8(23)	-	3.3(16)	75^{+16}_{-24}	70(4)
^{49}Ni	7(2)	7.5(10)	83	83(13)	67^{+7}_{-8}	100(13)	32^{+8}_{-7}	-	2^{+4}_{-2}	-	-	-
^{48}Ni	$2.2^{+3.0}_{-2.0}$	$2.1^{+1.4}_{-0.6}$	100	100(20)	20^{+32}_{-17}	30(20)	-	-	20^{+32}_{-17}	-	60^{+25}_{-30}	70(20)

Table 6.54: Summary of results concerning half-lives, proton branching ratio and branching ratio of the different emissions (β -1p, β -2p ...) for each of the studied nuclei.

Nucleus	Implantations
^{41}Ti	426583
^{45}Cr	16480
^{44}Cr	64517
^{44}Cr	4367
^{46}Mn	4192
^{47}Fe	2021
^{46}Fe	467
^{45}Fe	11(+10)
^{49}Ni	65
^{48}Ni	7(+1)

Table 6.55: Summary of number of implantations for each nucleus.

Chapter 7: Further analysis and setup upgrade



Contents

7.1	Identification of the nuclei	202
7.2	Drift of ions	204
7.3	Fitting of the implantation event and escaping protons	204
7.4	Proton Fitting in 3D	204
7.5	Setup upgrade (γ and β detection)	205

This chapter addresses the further analysis that needs to be performed to deal with the encountered problems discussed along this work, aiming to improve the quality and reliability of the results. (Sections 7.1 to 7.4). In the last section 7.5, an upgrade of the setup for measurements of γ rays and β particles is presented.

7.1 Identification of the nuclei

The identification process described in Section 5.2 presents some limitations. The model was built within the assumption of Gaussian distributed identification parameters. This is experimentally not the case, especially in the time of flight parameter, as it was previously discussed in Section 5.2. When projecting this parameter value in a Z line of the 2D identification matrix (Figures 7.1 and 7.2) a tail towards the lower N nucleus time of flight distribution is observed.

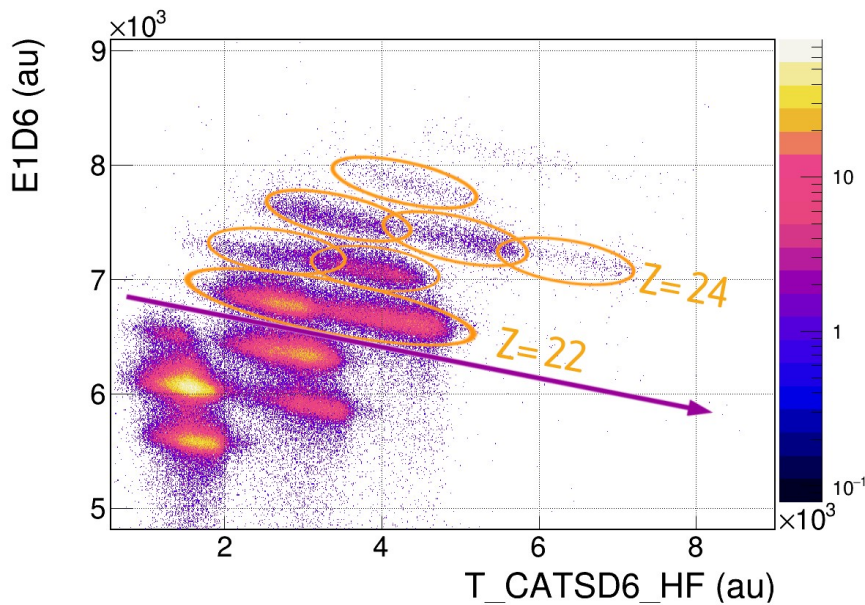


Figure 7.1: Identification 2D matrix for a single run. The purple line is used to project the time of flight values of the Z=22 group of nuclei.

This overlapping in time of flight (happening essentially from lower N values (See Section 5.2) explains the two proton emissions from ^{45}Fe and ^{48}Ni events initially identified to be (^{46}Fe and ^{49}Ni nuclei respectively, as presented in Chapter 6.

The 4-D identification method needs to be adapted by the use of other functions predicting more accurately the parameter distributions in order to better estimate the contamination between nuclei, aiming

for a better identification. The Crystal Ball function (a combination of a Gaussian with a powerlaw tail), defined in Equation 7.1 and implemented in ROOT [156] may be a good candidate. The function is defined as follows:

$$f(x, \alpha, n, \bar{x}, \sigma) = N \cdot \begin{cases} \exp\left(-\frac{(x-\bar{x})^2}{2\sigma^2}\right), & \text{for } \frac{x-\bar{x}}{\sigma} \geq -\alpha \\ A \cdot \left(B - \frac{(x-\bar{x})^2}{2\sigma}\right) & \text{for } \frac{x-\bar{x}}{\sigma} \leq -\alpha \end{cases} \quad (7.1)$$

A preliminary fit using a combination of two crystal ball functions is shown in Figure 7.2.

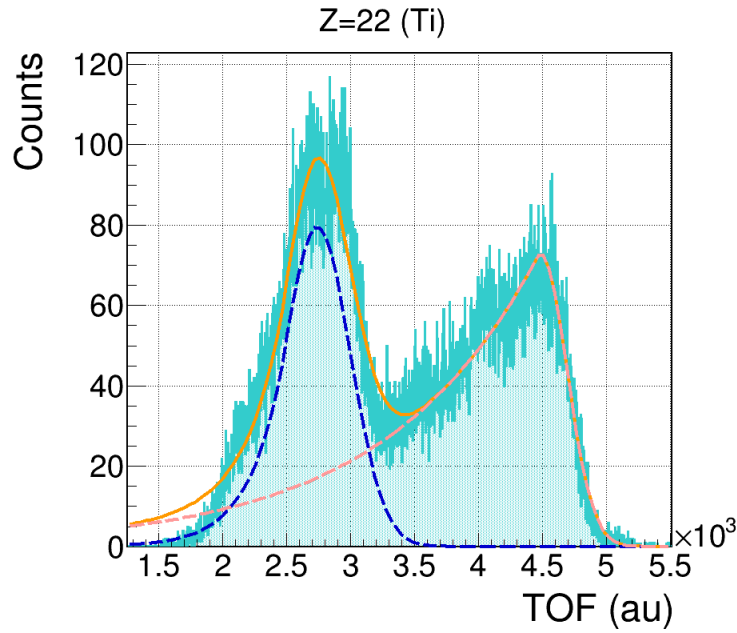


Figure 7.2: Projection of the time of flight in the Z=22 line (see Figure 7.1) for the full nuclei group without any contour conditions. The individual crystal ball functions are represented by the pink and blue dashed lines, and the total function by the orange line.

Extra helpful information can be obtained from the non-proton emitters to quantify the mixing of the species. In the example of the Z=22 line, ^{41}Ti is a proton emitter with a high branching ratio in contrast to ^{42}Ti , that decays (100%) by β/EC without proton emission. The proton decay events associated to the latter one (^{42}Ti) are thus examples of a wrong identification and their identification parameter values may be positioned in the tails of the distribution of the contaminant nucleus (^{41}Ti), giving a hint of its extension in N. The comprehension and modeling of the parameter distributions for the nuclei are essential to improve the identification analysis, especially in experiments with low statistics and large momentum acceptance settings.

7.2 Drift of ions

The drifting of the ions, consequence of the non neutralization of the nucleus in the gas as explained in Section 5.5 affects the different measurements of the observables. A full understanding of this process is thus crucial in their determination. A more accurate study can be achieved if the dispersion parameters (constant for a given gas and a fixed pressure) are fixed, and the fit is performed leaving the height parameter z free instead. This will allow for a better identification of the decay point position in the z axis in an event-by-event basis and will lead to a better estimation of the number of drifting ions, which affects all the branching ratio calculations. This will hopefully clarify the effect of the drifting of ions in the half-life measurements.

As it was discussed in Section 5.44, there is a small decay point z position dependence on the obtained reconstructed energies. For that reason, the length to energy conversion SRIM input values (see section 5.3.3) needs to be optimized only for emissions from the entrance window. A correction for events emitted from the cathode needs to be applied accordingly. This may not have critical effects in the obtained energies for the single proton distributions with a relatively long half-life presented in Chapter 6, but it will allow suppressing the systematic error for short half-life nuclei or single proton energy measurements, included in Section 5.6.2 as a provisional solution to take into account this effect.

7.3 Fitting of the implantation event and escaping protons

A systematic difference between the stopping point of the ion and the decay point of the proton track was found in Section 5.4.2. A better estimation of the stopping point in the implantation cases can be performed if the implantation track is also fitted, which was not the case in the current work.

The fit of the protons has been performed only for protons not escaping the volume in the XY plane. Fitting all the tracks can translate into a better implantation–decay event correlation, which could have an effect in the measured half-lives and the total proton branching ratio estimates.

7.4 Proton Fitting in 3D

In Section 5.3.2 some different ways of track fitting were proposed: the fit taking into account only the dispersion in the XY plane and the one taking into account also the dispersion in the Z dimension (3D). The second one, being the best choice, requires large computing times, and it was used only for the most exotic multiple emission fits in the current work. A study of the impact of the fitting method was performed for a group of proton events for which two proton distributions were built (fitted in 3D and fitted with the XY+T method). This study revealed maximum length differences of 8 mm for tracks emitted with a vertical angle above 80° (1% of the events), and 3 mm for vertical angles between 60° and 80° (11% of the events). When fitting the full energy distributions, differences in the obtained energies only of about 0.5% were found, justifying the use of the (much faster) (XY+T) fit. Nevertheless, the 3D fit can be performed in the future for a better estimation of the lengths in the case of too vertical tracks for which the highest differences between the two fits are found. By using the (XY+T) fit results as a starting point, the fitting process can be significantly speeded up.

7.5 Setup upgrade (γ and β detection)

In order to perform full proton spectroscopy experiments, the installation of gamma detection systems around the detector is required to complete the proton information, aiming for a full interpretation of the transitions as it was done for ^{44}Cr in 6 using γ information from a preliminary work by P. Ascher *et al.* [146]. Part of the ACTAR TPC collaboration (USC, Santiago) already proposed the installation of CsI(Tl) detectors around the detection volume in order to detect high-energy particles and γ rays for transfer reactions purposes (J. Lois Fuentes [157]). The proposed setup consists of four walls composed of a first Si layer (1mm from the detection volume and made out of $500\ \mu\text{m}$ Si detectors) for heavy particle detection and a second layer of CsI(Tl) for γ detection. These crystals, used for the CALIFA barrel calorimeter [158], have been tested and can achieve an intrinsic efficiency higher than 50% for γ rays. The same setup could be used for decay experiment purposes: the β particles can be detected in the Si layers and γ rays in the CsI(Tl). An illustration of the proposed setup upgrade is shown in Figure 7.3. Although this upgrade of the setup can be used for both transfer reactions and decay experiments, a more optimized setup for proton spectroscopy will require thicker silicon walls (1 mm) for β detection.

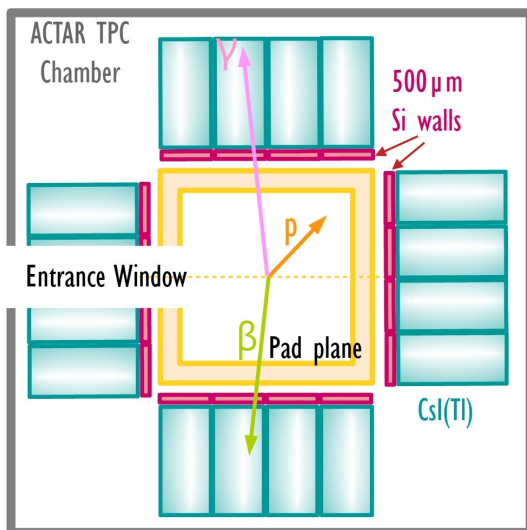


Figure 7.3: The ACTAR active volume is shown in orange (pad plane), surrounded by four walls composed by a Si detector (red) layer and a CsI(Tl) (blue) layer. Examples of a proton track (measured in ACTAR), a β track (measured by the Si wall) and γ ray (detected in the CsI(Tl)) are illustrated.

Conclusions and Perspectives



Two proton decay

Despite the very few two proton decay events measured for ^{48}Ni , a result of a production rate lower than originally expected, the angles between the two protons could be reconstructed for the correctly implanted nuclei with ACTAR TPC, allowing for a first comparison with theoretical predictions. For the moment, no angles above 90° have been observed, which can indicate the presence of a structure in the angular distribution of the ^{48}Ni protons as the one predicted by Grigorenko *et al.*. This may indicate the robustness of the $Z=28$ shell closure at the proton drip line, although a higher statistics is needed to conclude.

Some two proton emissions of ^{45}Fe could be measured as well, for which the individual proton energies and the angles between the emitted protons were also reconstructed, showing a very good agreement with previous works and a better energy resolution.

The results obtained in the current work demonstrate the high capabilities of the detector and the developed analysis techniques in order to determine the individual proton energies and reconstruct the angles between the protons despite the unfavorable pressure conditions, (resulting into very small tracks), chosen to optimize the implantation of ^{48}Ni in the detection volume. A longer version of the detector (LACTAR TPC) with the same number of pads but rectangular shape (256x64 pixels instead of 128x128) has already been built, and it is currently under tests for future decay experiments, aiming to maximize the number of implantations without worsening the angular resolution in the chamber.

Two experiments have been already accepted at RIKEN: single proton emission experiments from ^{68}Br , ^{72}Rb , ^{89}Rh , and ^{93}Ag and two proton emission from ^{67}Kr . Further two proton emitter candidates could be studied if their production becomes available in the future, or if longer experiments can be performed, increasing the production of such exotic nuclei. Studies of β -delayed direct to proton emissions (for ^{43}Cr and ^{46}Fe , from which some energy protons were found to be compatible with this emission mechanism in the current work) could also be performed in the near future. (L)ACTAR TPC is a powerful detector adapted for such measurements and ready to use for this purpose.

β delayed proton emissions

Even though the experiment was not optimized for the study of the decay products from the neighbouring nuclei in the mass region of ^{48}Ni , some of them were implanted in ACTAR TPC: ^{41}Ti , $^{45,44,43}\text{Cr}$, ^{46}Mn , $^{47,46,45}\text{Fe}$ and ^{49}Ni . Their decay products have also been analysed in this work. Due to the identification problems, some of the results are still preliminary. They are denoted with the super-index ^P in the following paragraphs:

- β delayed three proton emissions have been found for the first time for ^{48}Ni and $^{49}\text{Ni}^{\text{P}}$.
- β delayed two proton emissions have been found for the first time for ^{49}Ni , ^{46}Mn , ^{47}Fe and $^{44}\text{Cr}^{\text{P}}$.
- In the case of β delayed two proton emissions, some of the individual proton energies could be measured for the first time for ^{43}Cr , ^{46}Mn , ^{47}Fe , ^{46}Fe and ^{49}Ni . Sometimes, the two protons stayed confined in the detection volume (^{43}Cr and ^{47}Fe) and the total energy of the transition has been calculated. In some cases the proton energies, measured with very similar energy, could correspond to β -delayed simultaneous two proton emission from an excited state of the daughter nucleus. Further studies, with optimized settings for that purpose, would be quite interesting to identify the nature of these events by identifying the different transitions with higher statistics since the β delayed direct

two proton emission has never been evidenced so far.

- In the case of β delayed one proton emissions, the energy distributions associated to each nucleus could be extracted and 36^P new proton transitions have been identified and the branching ratios^P have been calculated. These results can slightly change when performing a better identification of the nuclei, as explained in the last chapter.

Despite the encountered effect of the non-neutralization of the ions and the identification problems, the obtained results demonstrate that the ACTAR TPC detector is well suited for the determination of the energy of the decay products of exotic nuclei in the neutron deficient region. The results are obtained with a very high resolution with respect to previous works performed with silicon detectors, where there exist an important β background. This opens up new experiment possibilities for proton spectroscopy purposes using ACTAR TPC. An experiment of this type using ACTAR TPC has already been proposed for ⁴⁶Mn, in which the study of low energy proton transitions has a strong astrophysical interest. These studies require the installation of a γ detection system surrounding ACTAR TPC. As explained in the last chapter, this is already an ongoing project.

In summary, various decay-mode experiment possibilities are opened for ACTAR TPC: direct proton emission studies, two proton emission (from ground and excited states) and β -(multi) proton spectroscopy. During this work, a dedicated methodology for each of the stages of the analysis has been developed, that shed light on the different problems that strongly affect some of the results. The strategies and methods proposed in this work constitute a baseline for future experiments in decay mode using ACTAR TPC.

Bibliography

- [1] E. Rutherford., *Philosophical Magazine* 6 21 (1911) 669–688
- [2] Chapman K., *Phil.Trans.R.Soc. A* 378 (2020) 20190535
- [3] Mayer M. G., *Phys. Rev.* 75(2) (1949) 1969–1970
- [4] A. Ekström et al., *Front. Phys.* 11 (2023) 3389
- [5] M. R. Pahlavani *Selected Topics in Applications of Quantum Mechanics. InTech* (2015) Chapter 8.
- [6] Bo-Anders Jönsson, *Physica Medica* 81 (2021) 144–146
- [7] E. Rutherford., *Philosophical Magazine and Journal of Sciences.* 47 284 (1899) 109–163
- [8] Luis W. Alvarez, *Phys. Rev.* 52 (1937) 134
- [9] L. Meitner and O. R.Frisch, *Det Kgl. Danske Videnskabernes Selskab. Matematisk-Fysiske Meddelelser.* 17 5 (1939)
- [10] G. N. Flerov and K. A. Petrzhak, *J. Phys. U.S.S.R.* 3, (1940) 275
- [11] Scharff-Goldhaber and G. Klaiber, *Phys. Rev.* 70 (3–4) (1946) 229
- [12] R. McPherson, R. Barton, *Phys. Canada* 19 (1963) 36
- [13] G. Gamow, *Nature* 126 (1930) 397.
- [14] R.B. Roberts et al. *Phys. Rev.* 55 (1939) 510 664
- [15] S. Hoffmann et al., *Z. Phys A* 305, (1982) 111.
- [16] J. Giovinazzo et al., *Physical Review Letters*, 89, (2002) 102501.
- [17] Rose, H., Jones, G. *Nature* 307 (1984) 245–247
- [18] S. R. Elliott et al., *Physical Review Letters* 59 (1987) 2020–2023
- [19] XENON Collaboration. *Nature* 568 (2019) 532–535.
- [20] F. Mercier et al., *Phys. Rev. Lett* 127 (2021) 012501
- [21] Ch. Theisen et al., Proposal INTC-P-616 (2022)
- [22] E.P. Wigner, Proc. Robert A.Welch Conf.Chem. Res. (Robert A. Welch Foundation, Houston, Texas 1 (1957) 67
- [23] Y.H.Lam et al., *At. Data Nucl. Data Tab* 99 (2013) 680
- [24] C. Dossat et al., *Nucl. Phys. A* 792 (2007) 18–86.
- [25] V. Goldansky., *Nucl. Physic* 19, (1960) 482–495.

- [26] M. D. Cable et al., *Phys. Rev. Lett* **50** (1983) 404.
- [27] M. D. Cable et al., *Phys. Rev C* **30** (1984) 1276
- [28] B. Blank and M.J.G. Borge., *Progress in Particle and Nuclear Physics*, **60**, (2008) 403–483.
- [29] J. C. Batchelder., *Atomic Data and Nuclear Data Tables* **132**, (2020) 101323
- [30] V. A. Karnaukhov et al., *Nucl. Phys. A* **90** (1967) 23.
- [31] A. J. Armini et al., *Phys. Rev.* **165** (1968) 1194.
- [32] B. Blank and M. Ploszajczak. *Reports on Progress in Physics*, **71**, (2008) 046301
- [33] Y. B.Zel'dovich., *Sov. Phys. JEPT* **111** (1960) 812.
- [34] V. Karnaukhov and N. Tarantin., *Sov. Phys. JEPT* **12**, (1961) 771.
- [35] J. Jänecke., *Nucl. Phys.*, **61**, (1965) 326–341.
- [36] O. Keppler et al., *Z. Phys A* **305**, (1982) 125
- [37] V. Goldansky., *Nucl. Physic* **27**, (1961) 648.
- [38] V. Goldansky., *Nuovo Cimento*. **25** suppl.2 (1962) 123.
- [39] V. Goldansky., *Phys. Lett* **14** (1965) 233.
- [40] V. Goldansky., *Nucl. Phys* **78**, (1966) 233.
- [41] V.M. Galitsky, V.F.Cheltsov., *Nucl. Phys* **56**, (1964) 86.
- [42] J. Giovinazzo et al., *Nuclear Physics A*, **722**, (2003) 434c–438c
- [43] M. Pfützner et al., *Eur. Phys. J. A*, **14**, (2002) 279–285
- [44] B. Blank et al.; *Physical Review Letters*, **94**, (2005) 232501
- [45] C. Dossat et al.; *Physical Review C*, **72**, (2005) 054315.
- [46] T. Goigoux et al.; *Physical Review Letters*, **117**, (2016) 162501.
- [47] O. Bochkarev et al., *Sovi. J. of Nucl. Phys.*, **49**, (1989) 941.
- [48] R. Kryger et al., *Phys. Rev. Lett.*, **74**, (1995) 860
- [49] G.J. KeKelis et al., *Phys. Rev. C* **17** (1978) 1929–1938,
- [50] M. Pfützner et al., *Progres in Part. and Nucl. Phys.* (2023) 104050.
- [51] L. Audirac, *Étude de la radioactivité 2p de 45Fe avec une TPC*. PhD thesis, Université Bordeaux 1, (2011)
- [52] K. Miernik et al., *Physical Review Letters*, **99**, (2007) 192501.

- [53] K. Miernik et al., *Eur. Phys. J. A*, **42**, (2009) 431
- [54] P. Ascher et al., *Phys. Rev. Lett.* **107**, (2011) 102502.
- [55] M. Pomorski et al., *Phys. Rev. C* **83** (2011) 061303.
- [56] L. Zhou et al., *Nucl. Sci. Tech.* **33** (2022) 105.
- [57] L. Grigorenko et al., *Phys. Rev. Lett.*, **85** (2000) 22.
- [58] F. C. Barker., *Physical Review C*, **63** (2001) 047303.
- [59] J. Okolowicz et al., *Phys. Rep.* **374** (2003) 271–384.
- [60] J. Rotureau et al., *Phys. Rev. Lett.*, **95** (2005) 042503.
- [61] J. Rotureau et al., *Nucl. Phys. A* **767** (2006) 13–57.
- [62] N. Michel et al., *Phys. Rev. Lett.* **89** (4) (2002) 042502
- [63] N. Michel and M. Płoszajczak., *Gamow Shell Model: The Unified Theory of Nuclear Structure and Reactions (Lecture Notes in Physics)* **983** 1st ed. 2021 Edition
- [64] S. M. Wang et al., *Phys. Rev. C* **96** (2017) 044307.
- [65] B.A. Brown et al., *Phys. Rev. C* **100** (2019) 054332
- [66] L. V. Grigorenko et al., *Phys. Rev. C* **95** (2017) 021601.
- [67] S. M. Wang, W. Nazarewicz, *Phys. Rev.* **120** (2018) 212502.
- [68] D. Thompson et al., *Nucl. Phys.* **A286**, (1977) (53).
- [69] Carl D.Anderson,*Phys. Rev.* **43 A381** (1933) 491–494
- [70] Anderson and Neddermeyer,*Phys. Rev.* **50**, **263** (1936)
- [71] D. Rochester C. C. Butler, *Nature* **160** (1947) 855–857
- [72] Arthur H. Compton *Phys. Rev.* **21 483** (1923) 483–502
- [73] Donald A. Glaser, *Phys. Rev.* **87 665** (1952)
- [74] G.Charpak et al.,*Nucl. Instrum .Methods Phys.* **62 262** (1968)
- [75] H. Geiger and W. Müller, *Phys. Zeits.* **29 839** (1928)
- [76] G.F. Knoll. *Radiation Detection and Measurement.* John Wiley Sons, 3 edition, (2000).
- [77] T.Bressani et al., *Proc. of the int. Seminar on Filmless Spark and Streamer Chambers* (1969) 275
- [78] (a) D. Nygren, *PEP-198* (1975); (b) “Proposal for a PEP Facility based on the TPC”, *PEP4* (1976)
- [79] Y. Ayyad et al., *Eur. Phys. J. A* (2018) 181

- [80] S. Beceiro–Novo et al., *Progress in Particle and Nuclear Physics* **84** (2015) 124–165.
- [81] E. Demonchy et al., *Nucl. Instrum. Methods Phys* **A583** (2007) 34
- [82] D.Suzuki et al.,*Nucl. Instrum. Methods Phys.* **A691** (2012) 39–54
- [83] B. Blank et al., *Nucl. Instrum. Methods Phys.* **B266** (2008) 4606–4611
- [84] Miernik et al., *Nucl. Instrum. Methods Phys.* **A581** (2007) 194
- [85] E. Pollacco, et al., *Nucl. Instrum. Methods Phys. A* (2013) 67–103
- [86] C.-E. Demonchy et al.,*Nucl. Instrum. Methods Phys.* **A583** (2007) 341
- [87] M. Caamano et al., *Phys. Rev. Lett.* **99** (2007) 062502
- [88] I. Tanihata et al., *Phys. Rev. Lett.* **100** (2009) 192502
- [89] T. Roger et al., *Phys. Rev. C* **79** (2009) 031603(R)
- [90] M. Caamaño et al., *Phys. Letters B* **829** (2022) 137067
- [91] B. Blank et al., *Nucl. Instrum. Methods Phys.* **A613** (2010) 65
- [92] L.Audirac *Eur. Phys. J. A* **48** (2012) 179.
- [93] J. Giovinazzo et al. *Nucl. Instrum. Methods Phys. A* **840** (2016) 15–27
- [94] J.Pancin et al., *Nucl. Instrum. Methods Phys. A* **735** (2014) 532–540
- [95] T. Roger et al., *Nucl. Instrum. Methods Phys. A* **895** (2018) 126–134
- [96] J. Giovinazzo et al., *Nucl. Instrum. Methods Phys. A* **892**, (2018) 114–121
- [97] B. Mauss et al., *Nucl. Instrum. Methods Phys. Res. A* **940**, 498 (2019).
- [98] L. Sarmiento et al. *Nature Communications* **14** (2023) 5961
- [99] Experiment S2008: B. Fernandez–Dominguez et al,
- [100] Experiment S2029: G.F. Gringer, T. Roger
- [101] (RIBF NP–PAC–23) J. Giovinazzo et al.,
- [102] (RIBF NP–PAC–22) B. Blank et al.,
- [103] I. Giomataris et al., *Nucl. Instrum. Methods Phys. Res.* **A560**, (2006) 405 .
- [104] *Fabricant de cartes et produits électroniques professionnels* <https://www.fedd.fr/>
- [105] E.Pollaco et al., *Nucl. Instrum. Methods Phys Res* **A887**, 81 (2018)
- [106] Wittwer, G et al.; *19th IEEE–NPSS Real Time Conference.* (2014)
- [107] R. Anne et al., *Nucl. Phys* **A575**, (1994) 125.

- [108] J.P.Dufour et al., *Nucl. Instr. and Meth. A* **248**, (1986) 267–281
- [109] R.Dayras *Journal de Physique Colloque C4. S8. 47* (1986)
- [110] S. Ottini et al., *Nucl. Instr. and Meth. in Phys. Res. A* **431 476** (1999)
- [111] F. Sauli, "Principle of operation of multiwire proportional and drift chambers" CERN **77-09** (1977)
- [112] lise.nscl.msu.edu
- [113] B. A. Brown, *Phys. Rev. C* **43** R1513 (1991).
- [114] W. E. Ormand, *Phys. Rev. C* **55** 2407 (1997).
- [115] B. J. Cole, *Phys. Rev. C* **54** 1240 (1996).
- [116] B. Mauss et al., *EPJ Web of Conferences* **174** (2018) 01010
- [117] T.Roger et al., *Nucl. Instr. and Meth A* textbf 895 (2018) 126–134
- [118] J.Giovinazzo et al., *Nucl. Instr. and Meth A* textbf 953 (2020) 163184
- [119] H.J.Hilke & W.Riegler *Gaseous Detectors- Particle Physics Reference Library* 91–136
- [120] S.F. Biagi, *Nucl. Instr. and Meth A* **421** (1999) 234–240
<https://magboltz.web.cern.ch/magboltz/>
- [121] R. Veenhof, Garfield. <https://garfield.web.cern.ch/garfield/>
- [122] S. Biagi *Nucl. Instr. and Meth A* **283** (1989) 716–722
- [123] Jacquelin J., *Regressions et trajectoires en 3D*, (2011).
- [124] Christoph Dalitz et al.; *Image Processing On Line* **7,184** (2017)
- [125] K.S. Roberts, *A new representation for a line, in Computer Vision and Pattern Recognition* **48** (2015) 993–1010.
- [126] M. Jeltsch, C. Dalitz, and R. Pohle-Frohlich, *Hough parameter space regularisation for line detection in 3D, in International Conference on Computer Vision Theory and Applications(VISAPP)*, 2016, 345–352.
- [127] S. Agostinelli et al., *Nucl. Instrum. Methods Phys. Res. A* **506** (2003) 250
- [128] J. Alison et al., *Nucl. Instrum. Methods Phys. Res. A* **835** (2016) 186
- [129] Hans Dembinski and Piti Ongmongkolkul et al., *scikit-hep/iminuit-Zenodo*, 2020
<https://doi.org/10.5281/zenodo.3949207>
- [130] T. Ziegler. <http://www.srim.org>
- [131] lise.nscl.msu.edu
- [132] Glen Cowan *Statistical Data Analysis* 1998

- [133] L. Sarmiento et al. *Nature Communications* (2023)
- [134] C.W. Fabjan and F. Gianotti. *Reviews of modern physics* **75** (2003)
- [135] J.Giovinazzo et al., *Nucl. Instrum. Methods Phys A* **1042** (2022) 167447
- [136] A. Honkanen et al., *Nucl. Phys. A* **621** (1997) 689
- [137] M. Bhattacharya et al., *Physical Review C* **58** (1998) 3677
- [138] W. Liu et al., *Physical Review C* **58** (1998) 2677
- [139] R.G. Sextro et al., *Nucl. Phys. A* **234** (1974) 130
- [140] C. Dossat et al., *Nucl. Phys. A* **792** (2007) 18–86
- [141] Z.Y. Zhou et al., *Phys. Rev. C* **31** (1985) 1941
- [142] W. Trinder et al., *Phys. Lett. C* **415B** (1997) 211
- [143] J. Cerny, D.R Goosman and D.E. Alburger *Phys. Lett. B* **37** (1971) 380
- [144] E. Hagberg et al., *Nuclear Physics A* **613** (1997) 183–198
- [145] M. Pomorski et al., *Phys.Rev. C* **90** (2014) 014311
- [146] P. Ascher *Private communications*
- [147] J. Giovinazzo et al., *Eur. Phys. J. A* **10** (2001) 73
- [148] V. Borrel et al., *Z. Phys. A* **344** (1992) 135
- [149] M. Wang et al., *Chin. Phys. C* **45** (2021) 030003
- [150] <http://www.nndc.bnl.gov/ensdf/>
- [151] C. Y. Fu et al., *Physical Review C* **102** (2020) 054311
- [152] D.R.Goosman and D.E.Alburger *Phys.Letters B* **37** (1971) 380
- [153] A.M.Sanchez-Bénitez et al., *Proposal GANIL PAC* Nov 2017
- [154] K.-H. Schmidt et al., *Zeitschrift für Physik A Atoms and Nuclei* **316** (1984) 19–26
- [155] A. Kubiela et al., *Private communications*
- [156] Lorenzo Moneta., https://root.cern/doc/v610/CrystalBall_8C.html
- [157] J.L. Fuentes *Complete spectroscopy of ^{12}C and ^{20}O with solid and active targets using transfer reactions*
<http://hdl.handle.net/10347/30947>
- [158] H. Alvarez-Pol et al., *Nucl. Instrum. Methods Phys. Res. A* **767** (2014) 453–466

Two proton radioactivity and other exotic decays in the ^{48}Ni region measured with ACTAR TPC

Abstract: The study of exotic nuclei near the proton drip lines is of great importance for a better understanding of nuclear structure. The two-proton radioactivity, a decay mode for neutron deficient isotopes at the proton drip line, was predicted in 1960 and experimentally evidenced in 2002. The angles between the two emitted protons and their energies are important observables keeping a trace of the interaction of the protons inside the nucleus.

An experiment at GANIL/LISE3 facility was performed in 2021 aiming to produce one of the two proton emitter nuclei from ground state known up to date, the doubly-magic ^{48}Ni nucleus, and to measure the angular distribution of their emitted protons. The ACtive TARget and Time Projection Chamber (ACTAR TPC) device was used to implant the ions and perform the tracking of the decay products (protons). In addition, other interesting exotic nuclei in the mass region of ^{48}Ni have been produced and their decay products have been measured. First evidences of exotic decays such as β -delayed three proton emission (^{48}Ni , ^{49}Ni) or two proton emission (^{46}Mn , ^{47}Fe) have been found. The current work addresses the analysis of this experiment.

Despite several issues that are covered in the manuscript, the results allowed for a first comparison of the two-proton angular distribution of ^{48}Ni to the existing theoretical models. Also, the results demonstrate that the detector is well suited for the determination of observables such as the angular distribution and the energy of the decay products, obtained with a very high resolution with respect to previous works performed at low energies with silicon detectors, opening up new experiment possibilities for proton-spectroscopy purposes using ACTAR TPC. The analysis of these decays can provide many experimental information about the structure and decay scheme of very unstable nuclei.

A dedicated methodology for each of the stages of the analysis has been developed in this work, constituting a reference for future experiments in decay mode using ACTAR TPC.

Keywords: 2-proton, Exotic nuclei, Proton drip line, Delayed proton emission, Radioactivity

Unité de recherche
UMR 5797 LP2i Bordeaux, 33170 Gradignan, France.

Étude de la radioactivité 2-protons et autres modes de décroissance exotiques dans la région d' ^{48}Ni avec ACTAR TPC

Résumé : L'étude des noyaux exotiques à la drip-line proton est importante pour mieux comprendre la structure nucléaire loin de la vallée de stabilité. La radioactivité deux protons est un mode de décroissance particulier des noyaux très déficitaires en neutrons à la drip-line proton. Ce mode de radioactivité a été prédit en 1960 et découvert expérimentalement en 2002. Les angles relatifs d'émission des deux protons lors de l'émission donnent une information sur les interactions à l'intérieur du noyau avant l'émission.

Une expérience a été réalisée au GANIL/LISE3 dans le but de produire le noyau ^{48}Ni et analyser les caractéristiques de la radioactivité deux protons. Une chambre à projection temporelle (ACTAR TPC) a été utilisée pour implanter les ions et reconstruire les trajectoires des protons émis. En plus, d'autres noyaux très exotiques dans la région de masse d' ^{48}Ni ont été produits et leurs produits de désintégration ont été mesurés également. Des émissions retardées de plusieurs protons β -2p pour (^{46}Mn , ^{47}Fe) et β -3p pour (^{48}Ni , ^{49}Ni) ont été observés pour la première fois. Ce travail de thèse concerne l'analyse de cette expérience.

Malgré quelques problèmes abordés dans le manuscrit, les résultats ont permis de comparer pour la première fois les distributions angulaires des deux protons du ^{48}Ni avec les modèles théoriques existantes. Ainsi, les résultats obtenus prouvent que le détecteur est bien adapté à la détermination d'observables telles que les distributions angulaires ou l'énergie des produits de désintégration, qui ont été mesurés avec une très bonne résolution à basse énergie par rapport aux expériences précédentes réalisées avec des détecteurs silicium. Ces résultats ouvrent de très belles perspectives pour de futures études par spectroscopie proton en utilisant ACTAR TPC. L'analyse des données peut fournir de multiples informations expérimentales concernant la structure nucléaire et les schémas de désintégration des noyaux très exotiques.

Une méthodologie dédiée à chacune des étapes de l'analyse a été développée pendant ce travail, constituant une référence pour de futures expériences en mode désintégration en utilisant ACTAR TPC.

Mots-clés : 2-protons, Noyaux exotiques, Drip line proton, Émissions retardées, Radioactivité
